MODELING PRODUCTION AND CHARACTERIZING WELL PERFORMANCE OF FRACTURED HORIZONTAL WELL IN UNCONVENTIONAL RESERVOIRS

A Dissertation

by

SHUAI LIU

Submitted to the Office of Graduate and Professional Studies of
Texas A&M University
in partial fulfillment of the requirements for the degree of

DOCTOR OF PHILOSOPHY

Chair of Committee,	Peter P. Valkó
Committee Members,	Thomas A. Blasingame
	Raytcho Lazarov
	John Lee
Head of Department,	Jeff Spath

May 2019

Major Subject: Petroleum Engineering

ABSTRACT

This dissertation presents a comprehensive study for modeling the production and characterizing the well performance for the fractured horizontal well in unconventional reservoirs. Based on the different fundamental governing equations utilized, the standard diffusivity equation for normal diffusion or the fractional diffusivity equation for anomalous diffusion, our work is separated into two main parts.

In the setting of the standard diffusivity equation, we develop an efficient algorithm to quickly assess the production performance of a specified well-fracture configuration and a section-based approach for providing a preliminarily optimized development plan (number of horizontal wells and clusters to be created in a section). According to our method, under the assumption of planar hydraulic fractures with infinite conductivity, the dimensionless total fracture length and the feasible range of fracture half-length are the two most important factors for the decision of an optimal development plan.

In the second part of our work, we employ anomalous diffusion to structurally accounting for the effect of the heterogeneity due to complex fracture networks on the production.

Firstly, by simulating the particle-wise diffusion on a graph object, complex fracture networks are formally verified as a major cause of anomalous diffusion in the reservoir scale, which compromisingly provides the fundamental mechanism for the further investigation based on the fractional diffusivity equation.

Secondly, to resolve the issues in a traditional planar fracture framework, hydraulic fractures are merged into the fracture network and the fractional diffusivity equation is solved in a domain based on a horizontal lateral. From this perspective, two fractional production decline

models are developed. Model I, without considering the influx from the matrix, successfully interprets the relevant production data of the synthetic and field cases, which manifests its capability of accurately describing the transient regime for the fracture flow. Then, after incorporating the influx and a tempering factor, Model II can describe the whole sequence of the flow regimes. According to its type curves, the essence of using hydraulic fracturing for economically developing unconventional reservoirs can be explained as reducing c while increasing ω and σ, and other insights like selecting the re-fracturing candidates are also provided.

DEDICATION

To my parents, Ling and Jianbin, and my wife, Ruobing, for their love and support.

To those who have been deprived from the freedom of thought and expression.

ACKNOWLEDGEMENTS

First of all, I would like to express my deep gratitude to my advisor and committee chair, Dr. Peter Valkó, for guiding and supervising me through the whole course of my research. His insightful thoughts and comprehensive knowledge on engineering, physics, and mathematics inspires me to keep a critical eye on any popular preconceptions and to think outside the box honoring some fundamental laws. His rigorous attitude would also benefit my entire life.

I would like to thank my committee members, Dr. Thomas Blasingame and Dr. Raytcho Lazarov for their great courses on the flow through porous media and the finite element methods, which strengthen my basic knowledge on the relevant field and generally deepen my comprehension towards reservoir engineering and mathematics.

I would also like to thank Dr. John Lee for being my committee member and for his valuable comments.

Thanks also go to my friends and colleagues for making my time at Texas A&M University an unforgettable and fruitful experience.

Finally, I would express my gratitude to my mother and father for their absolute support and encouragement, and to my wife for her trust and patience.

CONTRIBUTORS AND FUNDING SOURCES

Contributors

This work was supervised by a dissertation committee consisting of Dr. Peter Valkó, Dr. Thomas Blasingame, and Dr. John Lee of the Harold Vance Department of Petroleum Engineering, and Dr. Raytcho Lazarov of the Department of Mathematics.

The unstructured grids of the reservoir simulation models for explicitly modeling the complex fracture networks in Section 5 are kindly provided by Dr. Hongjie Xiong at University Lands.

All work conducted for the dissertation was completed by the student independently.

Funding Sources

Graduate study was supported by a graduate research assistantship from Texas A&M University.

NOMENCLATURE

A	Area of a dimensional problem domain, $[L^2]$
A_r	Aspect ratio of the rectangular problem domain, dimensionless
A_s	Area of a section, $[L^2]$
a	Characteristic length of a system
B	Formation volume factor, dimensionless
b	Aperture of a fracture in a fracture network, $[L]$
C	Concentration, $[Mol\ L^{-3}]$
c	Hemispherical skin factor, dimensionless
c_t	Total compressibility, $[M^{-1}L^1T^2]$
D	Diffusion coefficient, $[L^2T^{-1}]$
d_f	Fractal dimension
$d_{i,j}$	Distance between node i and j, $[L]$
EUR	Estimated ultimate recovery, $[L^3]$
H	Formation thickness in Section 2 and Section 3, $[L]$
h	Discretization size
h_f	Effective fractured thickness of formation, $[L]$
I	Source term due to the influx from the matrix, $[T^{-1}]$
I_x	Penetration ratio of the rectangular problem domain, dimensionless
i_u	Flux normalized by the drawdown pressure, $[TL^2M^{-1}]$
J	Productivity index, $[TL^4M^{-1}]$
k	Permeability, $[L^2]$

k^*	Anomalous Permeability, $[L^2T^{1-\alpha}]$
L	Length of a fracture segment, $[L]$
L_m	Effective width of the matrix domain, $[L]$
l	Length of a rectangular dimensional problem domain, $[L]$
l_f	Total fracture length in a section, $[L]$
N	Number of elements
N_i	Set of the neighbor states of i
n_c	Number of columns in a fracture array
n_f	Number of planar hydraulic fractures in the domain of interest
n_r	Number of rows in a fracture array
P	Pressure, $[ML^{-1}T^{-2}]$
$\vec{P}$	Stochastic vector of the existence probability for a particle starting from i
p	Probability
Q	Cumulative production, $[L^3]$
$\boldsymbol{Q}$	Transition rate matrix
q	Flow rate, $[L^3T^{-1}]$
q_{ij}	Transition rate between node i and j, $[T^{-1}]$
S	Set of all the nodes in a graph
r	Displacement of a diffusing particle, $[L]$
r_c	Radius of the approximating hemisphere, $[L]$
r_p	Radius of a perforation, $[L]$
t	Time, $[T]$
$\vec{v}_{ds}$	Vector of distance square

$\vec{v}$	Volume flux, $[LT^{-1}]$
w	Width of a rectangular dimensional problem domain, $[L]$
X	Random variable of a Markov chain
x	x coordinate, $[L]$
x_c	Average length of stage and cluster spacings, $[L]$
x_f	Hydraulic fracture half-length, $[L]$
y	y coordinate, $[L]$
y_c	Width of the convergence region near a perforation, $[L]$
y_e	Width of the formation embedded conductive fracture network on one side of a horizontal wellbore, $[L]$

Greek

α	Diffusion exponent, dimensionless
β	Ratio of d_f to v
ϵ	Mesh size controlling parameter in the finite element methods
η	Hydraulic diffusivity coefficient, $[L^2T^{-1}]$
η^*	Anomalous hydraulic diffusivity coefficient, $[L^2T^{-\alpha}]$
λ	Eigenvalue in Section 2 and 4; Tempering factor in Section 5, $[T^{-1}]$
μ	Viscosity, $[ML^{-1}T^{-1}]$
ν	Number of effective spatial degree of freedom on the fractal
ξ	ξ coordinate in matrix continuum, $[L]$
σ	Characteristic time ratio, dimensionless
τ	Characteristic time, $[T]$

φ	Eigenfunction
ϕ	Porosity, dimensionless
Ω	Problem domain
ω	Storativity ratio, dimensionless

Superscripts and Subscripts

BDS	Boundary dominated state
D	Dimensionless
f	Fracture or fracture continuum
i	Initial condition
m	Matrix continuum
PSS	Pseudo-steady state
p	Perforation
sc	Surface condition
w	Bottom-hole of wellbore

TABLE OF CONTENTS

Page

LIST OF FIGURES

Page

LIST OF TABLES

Page

1. INTRODUCTION

1.1. Background

For the first time in 75 years, the United States became back again a net oil exporter in the first week of December 2018 (Blas, 2018). Besides other political and economic factors, the continuous rise of tight oil and shale gas production (Energy Information Administration (EIA), 2017) since the dawn of "the shale revolution" (Brown and Yucel, 2013) technically paves such a path of "energy independence". In 2017, tight oil production in the U.S. was about 4.67 million b/d accounting for about 50% of total U.S. crude oil production that year (EIA, 2018a). Also, tight oil production is projected to remain the leading source of U.S. crude oil production from 2017 to 2050 (**Fig. 1.1**) accounting for about 65% cumulative domestic production (EIA, 2018b). Consequently, even though more than a decade has passed since the initial boom in production from shale/tight formations, the exploration and development in unconventional reservoirs, especially shale gas and tight oil, keeping being one of the hottest topics in the modern oil & gas industry.

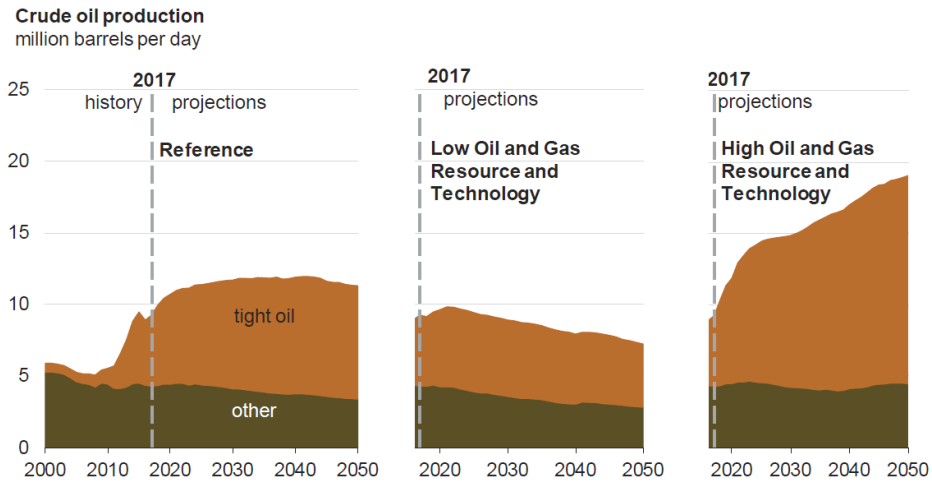

Figure 1.1 – History and projections of U.S. crude oil production from 2000 to 2050 (reprinted from EIA, 2018b)

It is the combination of horizontal drilling and multi-stage hydraulic fracturing that leads to the economic production from unconventional reservoirs (Flores et al., 2011). Compared to the horizontal drilling, hydraulic fracturing arguably plays a more important role for extracting the hydrocarbon borne in the super tight formations with ultra-low permeability. This is more or less implied by an apparently larger portion of the budget spent on completion treatment of a typical well in unconventional reservoirs (EIA, 2016). As a emerging technique effectively improving well productivity, the first fracturing experiment was conducted in 1947. The concept of "hydraulic fracturing" was introduced by Clark (1949) into the oil & gas industry and then this type of techniques was successfully commercialized and began to be wildly deployed in 1950s (Flores et al., 2011; King, 2012). Probably being the most effective approach of increasing production by far in tight and shale reservoirs (Moridis and Blasingame, 2014), more than 2.5 million fracturing treatments have been conducted world-wide and over 1 million in the U.S. (King, 2012). A typical fracturing treatment in a horizontal well is illustrated in **Fig. 1.2**.

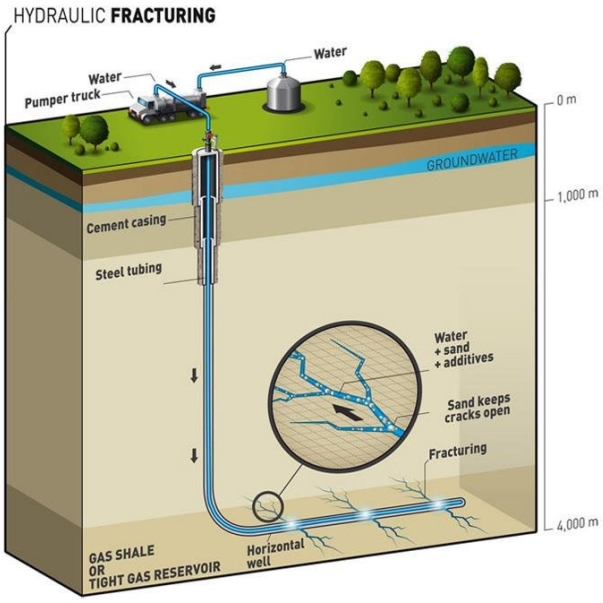

Figure 1.2 – Schematic of a fracturing treatment in a horizontal well (reprinted from Salami, 2014)

1.2. Statement of the problem

Generating conductive flow paths in the originally tight formation by massive fracturing treatment introduces new problems for modelling and interpreting the flow and production through unconventional reservoirs in the academic community despite the great success in practice.

Without much knowledge about the highly heterogenous fracture system in a typical unconventional reservoir, a preliminary model, which uses multiple stages of planar-shape fractures (**Fig. 1.3**) to drain a homogeneous formation with ultra-low permeability, is often employed to study the problem of interest. This simplified model was first proposed by Chen and Raghavan (1997) and can lead to some basic understandings at early phases of a project when only a few details about the reservoir are acquired with confidence. By further integrating more reservoir details or complex phenomena, for instance the heterogeneity of permeability and porosity, the geomechanics coupled with fluid flow, or the transport in the nano-size pore, planar-fracture model can even be used as the framework in more sophisticated simulation works (Wilson and Durlofsky, 2013; Jahandideh and Jafarpour, 2014; Olorode et al., 2017; Guo et al., 2018). Despite the multiple complex phenomena integrated in reservoir simulation, the accuracy or representativeness of the simulation results are questionable due to the quality issues for a lot of input parameters required by such sophisticated models, let alone the over-simplification of the conductive fracture geometry. Additionally, the optimization of well and cluster spacing based on this type of models often resorts to non-linear algorithms (Boulis et al., 2013; Yu and Sepehrnoori, 2013; Ma et al., 2013), which could take undesirably large amount of computational resources and hard to be applied at early phases of development due to the limited information about the reservoir of interest.

On the other hand, the planar fracture model is exactly the mental image underlying the inverse-model techniques such as rate transient analysis (RTA), which has gained popularity as a

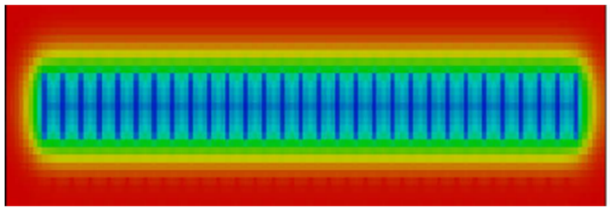

Figure 1.3 – Schematic of horizontal well with multiple stages of planar-shape fractures

useful tool for interpreting production data and estimating the relevant properties of reservoir and completion (Clarkson and Pedersen, 2010; Chu et al., 2017). The classic inverse-model techniques for analyzing production data and understanding reservoirs, for instance RTA and pressure transient analysis (PTA), are mostly based on various solutions of diffusivity equation (Blasingame et al., 1986a, 1986b, 1989a, 1989b) and mathematically obtained by the process of homogenization. The representativeness of the averaged properties out of these methods is valid to a large extent when the heterogeneity in the problem domain is mild, which corresponds to the scenario where the flow paths relevant to fluid production are spread in a relatively uniform manner. This is close to the situation in conventional reservoirs where the variance of major flow paths is small, or at least finite. However, as has been mentioned before, in unconventional reservoirs of tight formation the conductive flow paths consisting of both newly generated fractures and reactivated pre-existing natural fractures are the key to economic production. Therefore, the topology of such a complex fracture network determines the geometry of the dominant flow paths, which could be quite far away from the uniformly spreading regular lattice (**Fig. 1.4**). This discrepancy may be the main reason why the facile application of conventional techniques to unconventional reservoirs are arguably suspicious (Qanbari and Clarkson, 2016; Beohar et al., 2017; Chu et al., 2017; Aniemena and Vera, 2018; Ataei et al., 2018).

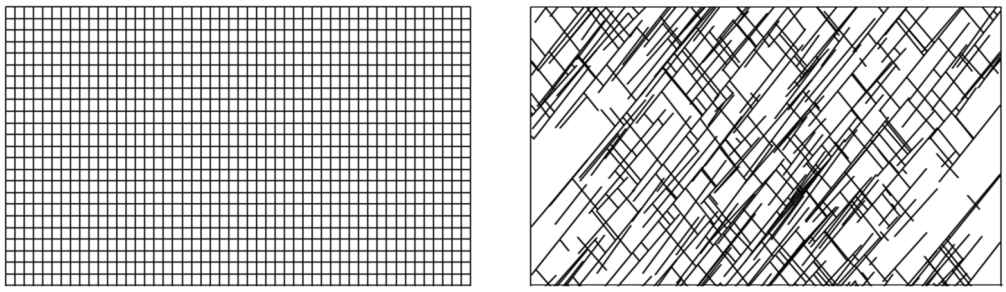

(a) (b)

Figure 1.4 – Topology of complex fracture network in comparison of regular lattice. (a) Regular lattice. (b) Complex fracture network.

1.3. Literature Review

In this section, we summarize the prior works related to modeling, interpreting, or optimizing the well performance of fractured wells either in conventional and unconventional reservoirs. Then, to focus on dealing with the heterogeneity in highly fractured formations, prior works on fractal reservoir models, reservoir models based on anomalous diffusion, and multi-continuum models (dual-porosity model) are introduced in the second half.

1.3.1. Well Performance of Fractured Well

A large amount of outstanding works has been published for the fractured well performance corresponding to either constant pressure or constant rate wellbore conditions.

Prats (1961) is one of the early works studying the fractured well performance. In this work, the shape of pressure contour near the fracture is independent of the size of the drainage area when the radius of the area is large enough. He also concluded that with some reasonable values of the properties the pressure drop along the fracture is negligible compared to that in the reservoir. Perhaps the most important result of this work is that regarding the production performance the fracture with infinite conductivity is equivalent to a well with the radius of a quarter of the total fracture length.

Russell and Truitt (1964) solved the problem of fractured well with infinite conductivity numerically, using the method of finite differences. They mainly focused on the asymptotic flow regimes during the early-time transient period and characterizing the reservoir properties with the well testing data in this early time.

By using the semi-analytical method based on instantaneous Green's function, Gringarten et. al. (1974) provided new solutions for vertical fractured well with either infinite conductivity or uniform influx from formation. It has a greater accuracy than the prior works and can be applied to analyze the short-time field data to get the information concerning the properties of the reservoir. They also found that an equivalent point of $x_D = 0.732$ on the uniform-influx fracture whose pressure transient behavior can be used to approximate that at the wellbore of the case with infinite conductivity.

Cinco-Ley et. al. (1978) extended the above semi-analytical method to the situation of finite conductivity fractures to account for the effect of the fracture conductivity on the well performance. They correlated the wellbore pressure with the dimensionless fracture conductivity and showed the existence of radial flow regime for the fracture with a finite conductivity. They concluded that the hydraulic can be regarded as infinite conductivity only if the dimensionless fracture conductivity is greater than 300. According to their work, with a small fracture conductivity one-half slope linear flow regime doesn't show up in the log-log plot.

Based on the semi-analytical solution of finite conductivity fractures, Cinco-Ley et al. (1981) identified four flow regimes that can be observed in a vertical well intercepting a planar fracture in an infinite homogeneous reservoir. From the very early time to the late time, the flow regimes are fracture linear flow (a half-slope straight line), bilinear flow (a quarter-slope straight line), formation-linear flow (a half-slope straight line), and pseudo-radial flow (a zero-slope

straight line), as shown in **Fig. 1.5**. The concept of bilinear and linear flow have been employed as a diagnostic tool for the inverse-model techniques of PTA and RTA.

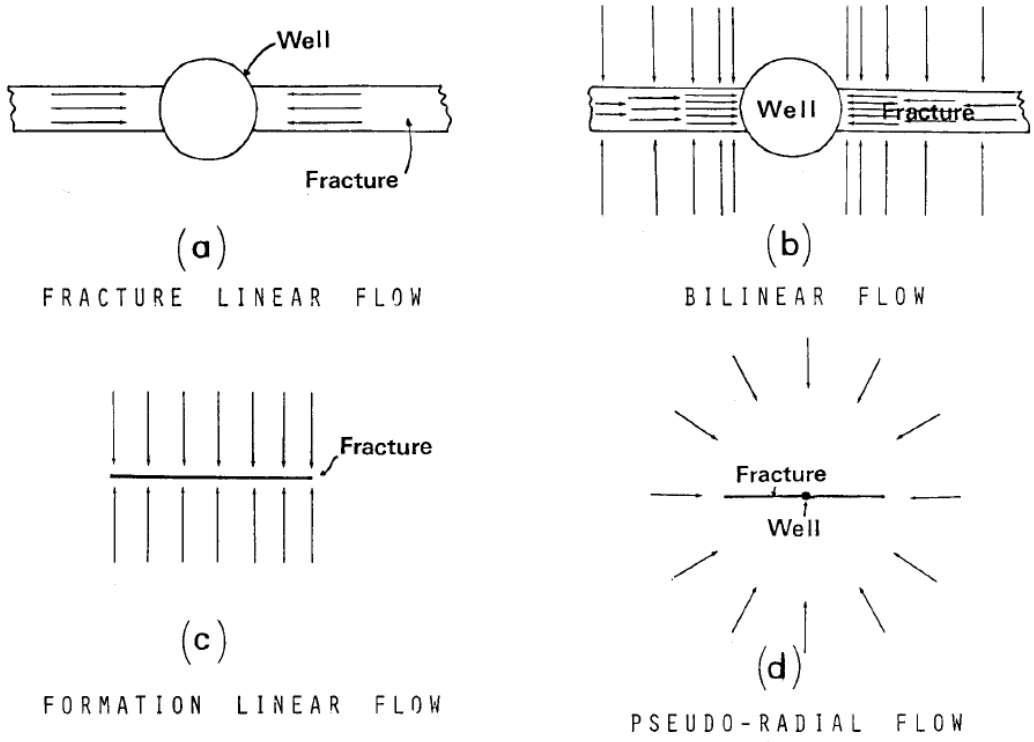

Figure 1.5 – Flow regimes for a vertically fractured well (reprinted from Cinco-Ley et al., 1981)

Using the Ozkan-Raghvan solution (Ozkan and Raghvan, 1988), Chen and Raghavan (1997) presented algorithms to efficiently compute pressure distributions for a horizontal well with multiple fracture stages in a bounded rectangular drainage area, without the need of resorting to the dubious image-well approach (Larsen and Hegre, 1991, 1994). Based on this convenient tool, the flow regimes probably occurring in this type of well-fracture configuration are summarized that their appearance depends on the characteristics of the hydraulic fractures and the formation of interest.

Based on the same mathematical tool as Chen and Raghavan (1997), Raghavan et al. (1997) focuses on the long-time performance of a horizontal well with multi-stage planar fractures. The concept of effective radius of stimulated wells (Prats, 1961) is generalized to the multi-fractured horizontal well. And a correlation of effective radius with respect to number of fractures and fracture conductivity is also presented (**Fig. 1.6**). They also conclude that the early-time well performance of such a well-fracture configuration is equivalent to a vertical well intercepting a single fracture with a sort of average conductivity and a fracture length equal to the distance between two outermost stages.

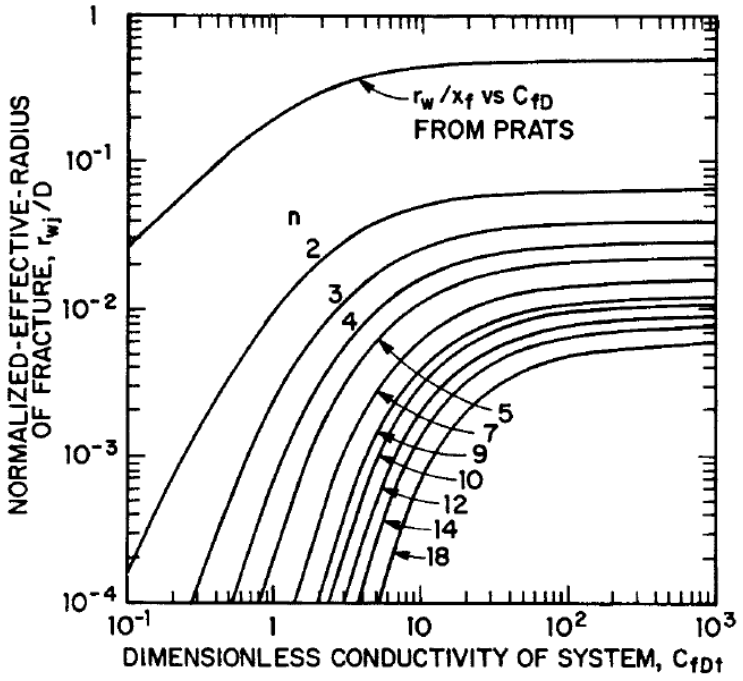

Figure 1.6 – Correlation of the effective radius of a multi-fractured horizontal well with respect to number of fractures and fracture conductivity (reprinted from Raghavan et al., 1997)

Soliman et. al. (1999) modeled the multiply fractured horizontal well and provided a solution with constant pressure conditions, which they claimed to be the most suitable condition

for producing tight gas reservoir. They investigate the productivity of different well-fracture configurations by solving the time-dependent problem introduced in Chen and Raghavan (1997) and then concentrating on the late-time performance of the solutions. Also, by using this model, they investigated the contributions to the total rate of various fractures with different positions. They also compared the well performance of longitudinal fractures with that of transverse fractures.

Hagoort (2010) used the constant bottom-hole pressure solution of a dual-porosity model with an exact transient influx function to investigate the different production performances due to the different orders of reaching the pseudo-steady state for the flow in the natural fracture and the matrix. In this work, the case of natural fracture flow becoming boundary-dominated when the matrix flow is still transient is inspiring for the study of the production in unconventional reservoirs.

Given the ultra-low permeability of the formation matrix and the extensively elongated transient regime, Lee and Brockenbrough (1983) introduces the so-called trilinear model (**Fig. 1.7**) as a simplified but useful "asymptotic" model to study the flow in unconventional reservoirs. The early-time well performance computed using the method of Cinco-Ley et. al. (1978) can be matched by the solution of this asymptotic model.

Ozkan et al. (2009) applied an analytical trilinear solution to describe the performance of the multiple fractured well and concluded that smaller fracture spacing corresponds to better productivity.

1.3.2. Optimization on Well and Cluster spacing

During the last decade, several studies have been conducted on various aspects of optimizing hydraulic fracturing design for multi-stage fractured horizontal wells in unconventional reservoirs.

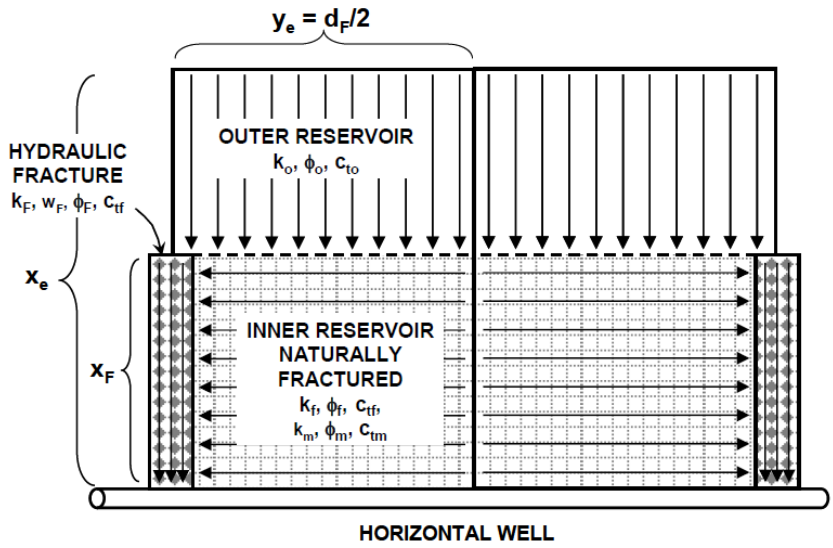

Figure 1.7 – Schematic of the trilinear model used for multiple-fractured horizontal well performance (reprinted from Ozkan et al., 2009)

Some works did the optimization based on cumulative production during a time span or overall PI of the well. Meyer et al. (2010) and Ozkan et al. (2009) both applied an analytical trilinear solution to describe the performance of the multiple fractured well. Ozkan et al. (2009) concluded that smaller fracture spacing corresponds to better productivity, while Meyer et al. (2010) used the economic indicators, Net Present Value (NPV) and Discounted Return on Investment (DROI), to get the optimum number of fracture stages and the optimum propped fracture length in one horizontal lateral. Both papers tended to provide general statements, without considering detailed reservoir specifics.

Wilson and Durlofsky (2013) used the generalized pattern search (GPS) algorithm (**Fig. 1.8**) on a reduced-physics surrogate model, which incorporated the heterogeneous geological description of Barnett Shale, to find the optimal location, lengths, and number of fracture stages of horizontal well laterals. With this tool they provided field development scenarios with much higher net present values than the base case scenario. Boulis et al. (2013) optimized the number of

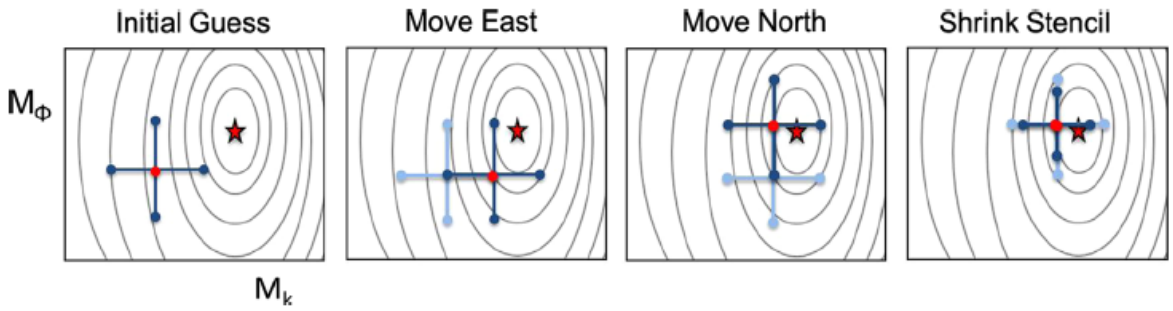

Figure 1.8 – Illustration of GPS optimization for surrogate tuning (reprinted from Wilson and Durlofsky, 2013)

wells in a section by employing a Monte-Carlo based stochastic forward modeling workflow and obtaining reasonable NPV bounds. Yu and Sepehrnoori (2013) employed Response Surface Methodology (RSM) to optimize multiple horizontal lateral placement with NPV optimization. Their work considered two horizontal laterals with aligning or alternating fracture configuration. They obtained an optimal design combination with certain reservoir and economic conditions and predicted the contribution of gas desorption during 30 years of production for an actual horizontal lateral in Barnett Shale. As illustrated in **Fig. 1.9**, Ma et al. (2013) optimized hydraulic fracture placement with the gradient-based finite difference method (FD), discrete simultaneous perturbation stochastic approximation (DSPSA), and genetic algorithm (GA), and then compared the results and computational time. As a conclusion, they suggested to use hybrid algorithms for the fracture placement optimization.

Besides, some more complex phenomena are also accounted for in the relevant optimization works. Eburi et al. (2014) conducted reservoir simulation to study the effect of well interference and fluid composition on well spacing and field development decisions in an unconventional reservoir developed by multi-fractured horizontal laterals. Their results indicated that fluid composition can have significant impact on well spacing. They outlined a workflow to

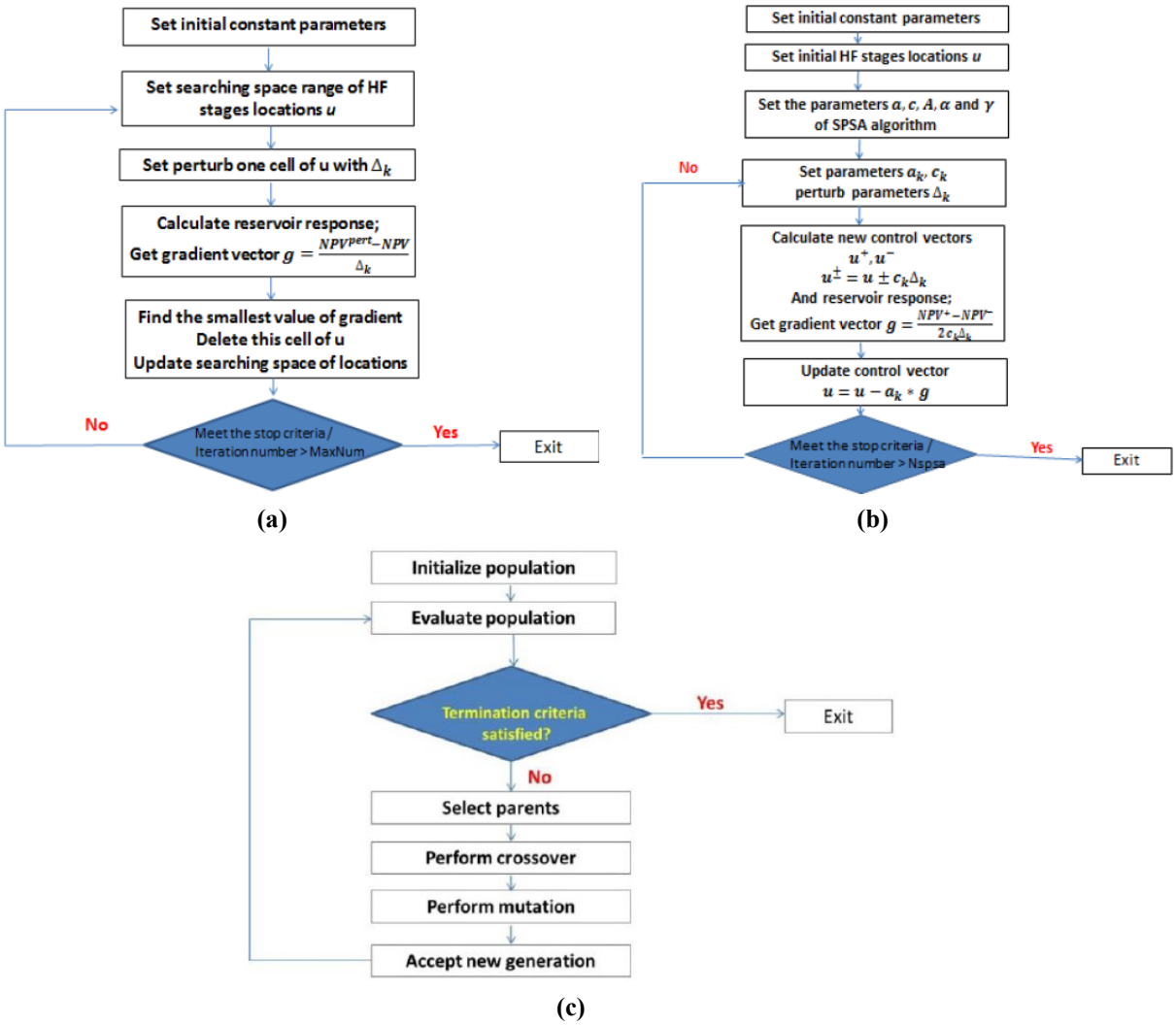

Figure 1.9 – Illustrations of non-linear optimization algorithms. (a) FD method flowchart. (b) DSPSA flowchart. (c) GA flowchart (reprinted from Ma et al. (2013))

evaluate well performance under various field development strategies. Moghanloo et al. (2015) proposed a moving boundary problem to represent the dynamic drainage volume in extremely low permeability formations and used the resultant well deliverability to optimize the fracture spacing and horizontal lateral length in a single well. One of their conclusions is that increasing the length of horizontal lateral or decreasing fracture spacing will not always enhance the production performance. Several authors emphasized the importance of geomechanics. Jahandideh and

Jafapour (2014) considered the geospatial variability in geomechanical rock properties (brittleness vs. ductile) to optimize fracture location, length and number of stages, as illustrated in **Fig. 1.10**. Roussel and Sharma (2011) considered additional constraints on fracture spacing to avoid detrimental interaction during fracture propagation.

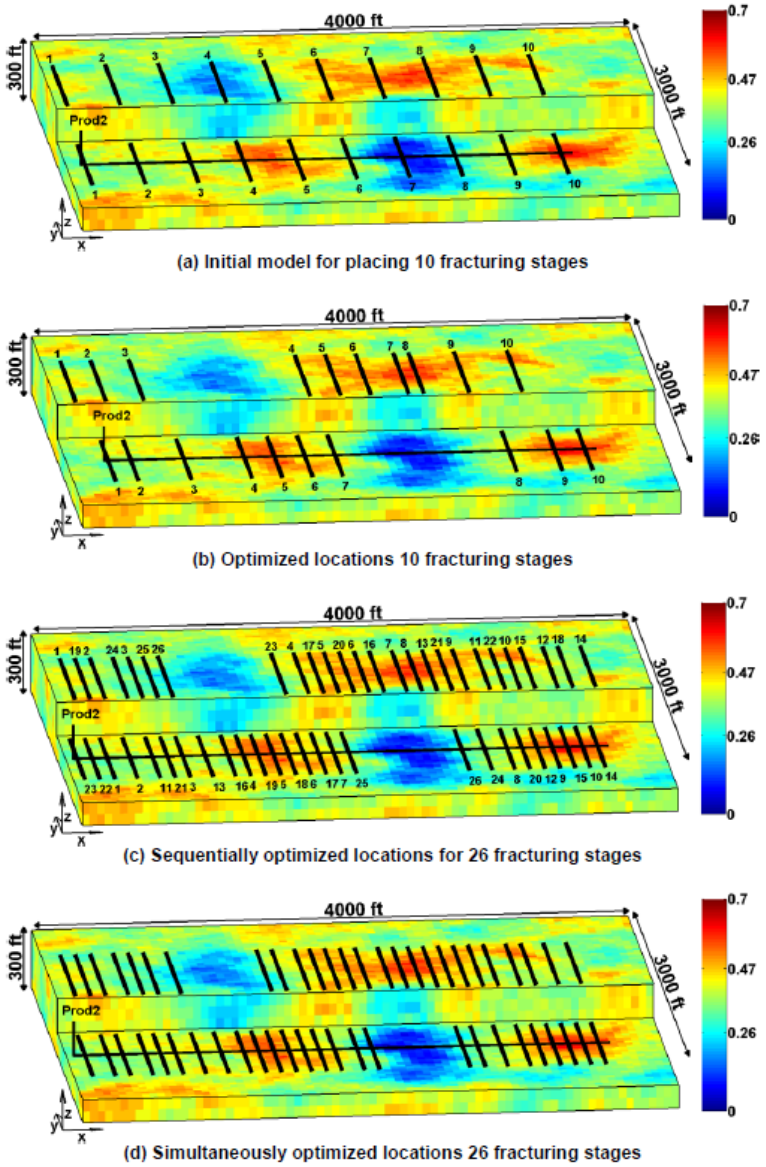

Figure 1.10 – Optimization of fracture locations and number of stages (reprinted from Jahandideh and Jafapour, 2014)

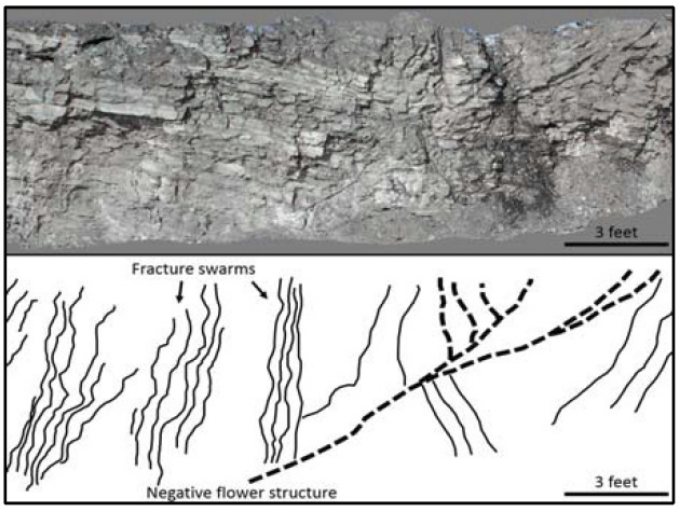

(a)

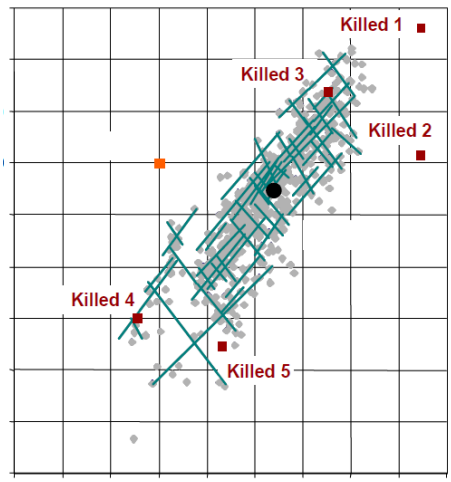

(b)

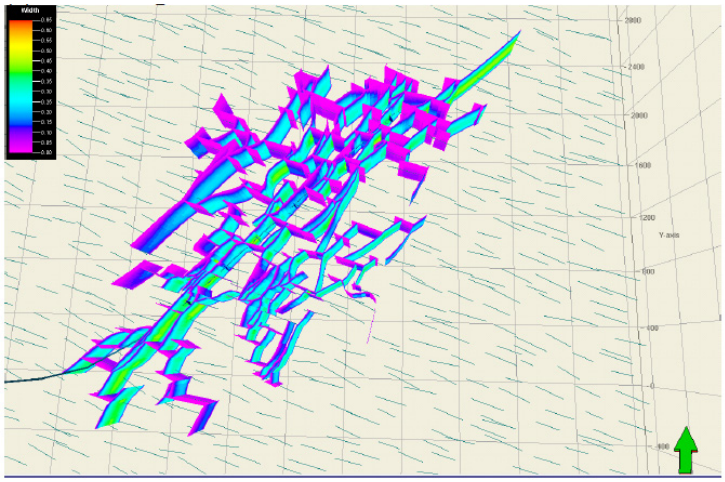

(c)

Figure 1.11– Complex fracture network (flow paths) indicated by various types of techniques. (a) Fracture swarms and listric faults embedded in an outcrop in the Niobrara unconventional play (reprinted from Grechishnikova, 2017). (b) Fracture network interpreted from micro-seismic in Barnett (reprinted from Fisher et al., 2014). (c) Fracture network from the simulation of fracture propagation modeling (reprinted from Weng et al. 2014)

1.3.3. Fractal Reservoir Models and Anomalous diffusion

In order to account for the heterogeneity due to the random flow paths/fractures (**Fig. 1.11**) in reservoirs, researchers in reservoir engineering have been resorting to fractal model to describe the impacts quantitatively. Based on the characteristics of a fractal object and the work of O'Shaughnessy et al. (1985), Chang and Yortsos (1990) first derived the fractal-controlling

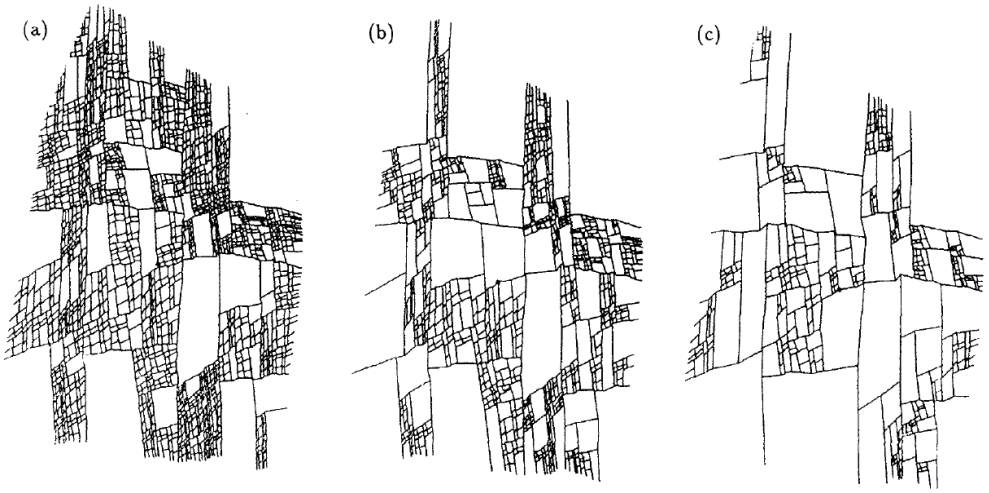

Figure 1.12– Examples of 2D fractal networks of fractures with different fractal dimensions (reprinted from Acuna et al., 1995a)

permeability and porosity distribution, which vary with respect to radial distance in a manner of power law, and integrated it into conventional dual-porosity model (Warren and Root, 1963).

Acuna et al. (1991, 1995a, 1995b) compared the model in Chang and Yortsos (1990) with some simulation results obtained from finite fractal-like networks (**Fig. 1.12**) generated with a computational geometry algorithm, called the "iteration function system" technique, and demonstrated the consistency between them as well as some deviations due to the finiteness of the computational model.

Flamenco-Lopez et al. (2003) provided asymptotic expressions for the fractal model originated from Chang and Yortsos (1990) but with either pseudo-steady-state or transient matrix influx function and then proposed to analyze both transient and pseudo-steady-state flow regime for characterizing all parameters in the fractal model.

Still in a setting of radial coordinates, Valdes-Perez and Blasingame (2018) extended the fractal dual-porosity model to account for a fractal matrix and investigated the sensitivity of fractal dimension and conductivity index towards the pressure- or rate-transient signals. Also, a formal equivalence between the fractal reservoir model and anomalous-diffusion-backed model is derived

by neglecting the storativity ratio and taking the late-time asymptotic form of influx from matrix to fracture.

Moreover, some efforts have also been made to incorporate fractal reservoir model into settings of hydraulic fractures. Following the Gringarten's method (Gringarten et al., 1974), Beier (1994) developed the pressure solution of infinite-conductivity fracture as well as uniform-flux fracture within a fractal reservoir. A semi-analytical model is built in Valdes-Perez et al. (2018) to conduct PTA and RTA of a horizontal well intercepted by finite-conductivity hydraulic fractures with various shapes. In the recent decade, many works (Cossio et al., 2013, Wang et al., 2015a, Wang et al., 2015b, Fan and Ettehadtavakkol, 2017) have been done to combine the fractal-controlled power-law-variable reservoir properties with asymptotic trilinear model to introduce fractal reservoir model into the studies on the performance of multi-fractured horizontal wells.

However, as pointed out in Beier (1994), spatial superposition doesn't rigorously apply to such type of fractal model originated from Chang and Yortsos (1990) due to its nature of coordinate dependence, so that many proposed models obtained by combining fractal reservoir structure with hydraulic fractures are questionable because of the implicitly contained superposition and coordinate transformation. Furthermore, the power-law variation of properties artificially imposes on the reservoir properties a specific pattern, which is sort of inconsistent with the significant randomness of unconventional reservoirs. Therefore, to get rid of these drawbacks, our research is focused on average properties of the underlying heterogeneous model and concentrates on a more prominent feature of this non-Euclidean object, called anomalous diffusion.

Though it hasn't aroused wide attention in the community of petroleum engineering, anomalous diffusion has been observed in abundant experiments (Adams and Gelhar, 1992; Berkowitz and Scher, 2001) and well-studied analytically (Metzler et al., 1994; Berkowitz and

Scher, 1997) and numerically (Zhang et al., 2008; Vilaseca et al., 2011) by hydrologists, biologists, and physicists. Usually, it is the tracers or the small protein molecules that undertake the anomalous diffusion in a flow field that has very high heterogeneity, such as complex fracture systems or massive large molecular as obstacles. The contrast between normal and anomalous diffusion when both are subject to the identical drift velocity is illustrated in **Fig. 1.13**. Unlike the normal diffusion that is characterized by a linear relationship between mean square displacement (MSD) and time, $\langle r^2 \rangle = \eta t$, anomalous diffusion holds a power-law relation, $\langle r^2 \rangle = \eta^* t^\alpha$. This is embodied by diffusion through highly heterogeneous media, which are partially modeled as fractal objects. In other words, anomalous diffusion characterizes the dynamics of chaotic systems like fractals in a coordinate independent way. Here α is the anomalous diffusion exponent. When α is smaller than 1, this kind of anomalous diffusion is specifically termed as sub-diffusion. In contrast, when α is greater than 1, it is called super-diffusion. The parameter η^* is anomalous diffusivity coefficient with an irregular unit of $\text{length}^2/\text{time}^\alpha$ which, in our opinion, reflects the complexity and heterogeneity of the media.

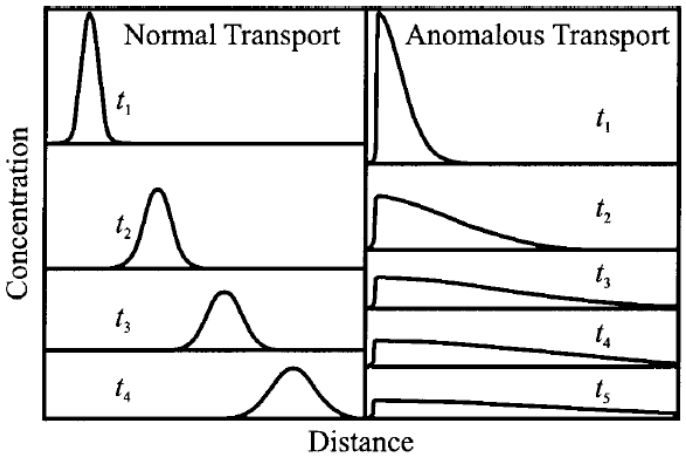

Figure 1.13– Schematic of the contrast between normal and anomalous diffusion (reprinted from Berkowitz and Scher, 2001)

Since the diffusivity equation describes both the tracers' diffusion and the flow through porous media, by analogy and similarity the flow through porous media is very likely to show characteristics of anomalous diffusion in highly heterogeneous formations, for example shales. Perhaps due to this analogy, anomalous diffusion has been considered in petroleum engineering as a possible modeling approach for highly-fractured unconventional reservoirs by some prior researchers.

Raghavan (2011) and Raghavan and Chen (2017a) generalized Darcy's law to a non-Darcy, fractional constitutive equation and combined that into their mature dual-porosity-model framework (Raghavan and Chen, 2013) for the multiple fracture horizontal well to investigate the effect of anomalous diffusion. It provides the asymptotic solutions for the long-term reservoir responses and found that power-law behaviors reflect the heterogeneity in the system. Using the same models as Raghavan and Chen (2017a) but without considering matrix influx, Raghavan and Chen (2017b) then focused on the boundary-dominated state of a constant bottom-hole pressure case only in fracture systems. They found the long-time production decline can be described by a two-parameter Mittag-Leffler function, which leads to a power-law decline behavior, and concluded that the normal exponential decline of a slightly compressible fluid is simply a subset of this generalized model. Raghavan and Chen (2019) presents a Theis-like solution using the Fox function for a sub-diffusion process with a line-source in an infinite 2D domain. Using this "master" solution, the pressure performance of a uniform-flux fracture in the setting of sub-diffusion is further investigated.

Albinali et al. (2016) used anomalous diffusion to represent flow in the naturally fractured region between hydraulic fractures for the transient, single-phase production. Based on the sensitivity analyses, they suggested to use this model on a wide range of flow heterogeneity even

without the intrinsic details of the formation properties. Albinali and Ozkan (2016) discussed the basis of anomalous diffusion and combined this new concept with the dual-porosity model to interpret the flow in the heterogeneous formation. Sub-diffusion exponents and other coefficients can be extracted from the anomalous diffusion model to help us learn more about the reservoir-rock quality and stimulation efficiency. Holy and Ozkan (2016) recently developed a 1-D numerical model for the linear, multi-phase flow undertaking anomalous diffusion. This work provides the foundation for more general multi-dimensional numerical models in the future.

Some works (Ozcan et al., 2014, Wang et al., 2016) have also been done to integrate anomalous diffusion into the so-called trilinear model in order to catch up the early transient regime. Most of the previous relevant works are fruitful in terms of mathematically formulating various models based on the theoretical concepts of fractional flux law.

Besides only considering sub-diffusion, which features fractional order time derivative, the one-dimensional reservoir models involving both sub-diffusion and super-diffusion are formulated mathematically using spatiotemporal fractional order derivatives in Chen and Raghavan (2015) and Raghavan and Chen (2018). Chen and Raghavan (2015) solves the problem in an infinite 1D domain, and Raghavan and Chen (2018) investigates the corresponding pressure performance in a finite domain by firstly solving an infinite composite-domain problem and then taking the limit of infinity for the permeability of the second region. They conclude that with the help of their 1D solution the corresponding trilinear model can be built to evaluate multi-fractured horizontal well performance. Based on the theory of power law behavior in Chen and Raghavan (2015), Chu et al. (2018) plot pressure interference test data in terms of the Chow Pressure Group (Chow, 1952) whose results are claimed to be capable of extracting the relevant diffusion exponent of the anomalous diffusion model and can be regarded as an indicator of connectivity between wells.

However, unlike the straight-forward physical meanings of the conventional concepts, like permeability and porosity, big gap still exists between the fractal-related concepts and their corresponding entities or causes in unconventional reservoirs, other than a too general concept of "heterogeneity". Such lack of physical meanings more or less restricts the corresponding models from being applied widely in practical ways.

In an inspiring previous work, Camacho-Velazquez et al. (2008) tried to approach the fractal model problem from the perspective of non-Euclidean model instead of being restricted to the spatially variable parameters (permeability and porosity). Therefore, they naturally applied the Metzler's fractional diffusivity equation (Metzler et al., 1994) in cylindrical coordinates and analyzed the pressure transient performance. Accordingly, the anomalous diffusion can be mainly attributed to the complex geometry of the efficiently conductive fracture network which is embedded in the formation. It inspires our research to relate the somewhat abstract fractional parameters of the anomalous diffusion phenomenon to the geometric-physical properties of the highly-fractured porous media.

As illustrated in **Fig. 1.14**, anomalous diffusion occurring in reality (colored data points) often shows a characteristic of scale dependence, which means that anomalous diffusion, specially sub-diffusion for a transport in porous media, only dominates during some early and intermedia period and then slowly converges to normal diffusion in the late time. This cut-off or "pre-asymptotic" phenomenon is successfully captured in Meerschaert et al. (2008) by a novel tempered anomalous diffusion model, which tempers the long waiting time of sub-diffusion particles with an exponential decline function.

Kelly et al. (2017) apply various models including regular advection-dispersion equation (ADE), fractional advection-dispersion equation (sFADE), fractional mobile-immobile model

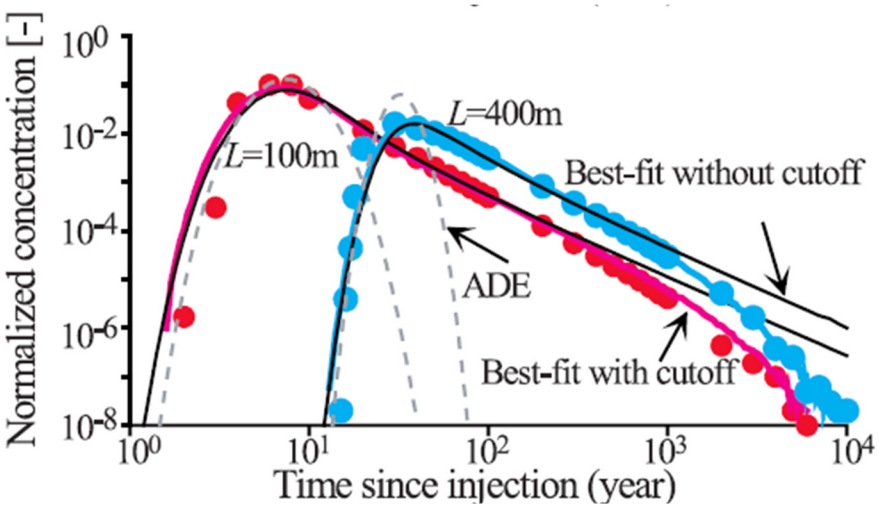

Figure 1.14 – Fitting advection-diffusion equation (ADE), fractional ADE with and without cut-off to measured data (reprinted from Meerschaert et al., 2008)

(FMIM), and temporally tempered Levy motion model (TTLM, tempered anomalous diffusion) to fit to the experimental data of in-stream pulse injection to compare the performance of these models. Tempered anomalous diffusion model is the one which best tracks the measured data among the models under study.

For the application of tempered anomalous diffusion in reservoir engineering, Yang (2018) developed a tempered sub-diffusion reservoir model in a 1D domain with a thin skin on the boundary of hydraulic fracture surface. The effects of α and the tempered factor λ on production rate, cumulative production, and productivity index are also investigated using this model.

1.3.4. Dual-Porosity Model

To take into account the existence of complex fractures in the formations, the dual-porosity model (Warren and Root, 1963; Kazemi, 1969; de Swaan, 1978), as illustrated in **Fig. 1.15** and its variants (Abdassah and Ershaghi, 1986; Liu et al., 1987) are widely employed in the study of unconventional reservoirs. Bello and Wattenbarger (2008) combined the slab matrix transient dual porosity model with RTA to study the usage of various shape factor formulations and the effect of matrix geometry on the transient linear response. Fuentes-Cruz and Valko (2015) applied the dual-

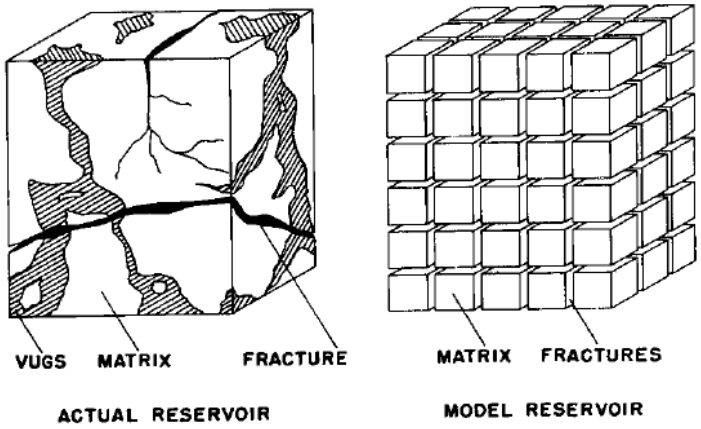

Figure 1.15 – Schematic of the actual natural-fracture reservoir and the idealization with a dual-porosity model (reprinted from Warren and Root, 1963)

porosity/dual-permeability model to study the proposed concept of variable matrix-block size and their resulting mathematical model is fundamentally different compared with the standard dual-porosity model due to the inter-porosity flow.

1.4. Research Objectives

Based on the previously identified problems and the current status of the research on them the objectives of this dissertation are set as below.

- To *develop* a method to quickly assess the efficiency of a given well-fracture configuration (the combination of well and cluster spacing) with the governing equation of standard diffusivity equation and then provide preliminarily optimized spacings for the early-time field development plan and the further detailed simulation works;
- To *attribute* the major source of anomalous diffusion in the reservoir scale to the complex topologic characteristics of conductive fracture networks using formal demonstration;
- To *develop* production decline models structurally integrating the relevant topologic characteristics of conductive fracture networks using various types of anomalous diffusion and the relevant dual-porosity model;
- To *validate* and *apply* the novel production decline models based on some synthetic and field production data.

1.5. Outline of the dissertation

With the main objects stated above, the rest of dissertation proceeds as follows.

In Section 2, based on standard diffusivity equation, the methods for quickly assessing the efficiency of a well-fracture configuration and then optimizing it are presented. An efficient algorithm for accurately calculating stabilized productivity index of a planar hydraulic fracture is developed by combining finite element method (FEM) with Richardson extrapolation. It can be applied to correlate the fractured well performance to its well-fracture configuration. Then, with the help of this algorithm, a section-based optimization method is proposed and established, which resorts to direct enumeration of the number of horizontal laterals and the number of fractures to efficiently provide a preliminarily optimized development plan for the early phase of a project, given specified fracturing treatment resources as well as the status of fracturing technique used.

In Section 3, the connection between anomalous diffusion and complex fracture networks is demonstrated formally. Firstly, the physical background of diffusivity equation is revisited by introducing the equivalence between this equation and a particle-wise Brownian movement. Next, a simulation model for the particles diffusing on a complex fracture network is built based on the concept of a continuous time Markov chain and then computationally implemented by a graph object. Finally, after post-processing the simulation results, the relationships of MSD vs. time for different cases are displayed in log-log plot, based on which distinct signature of anomalous diffusion is shown and some relevant discussions are made.

In Section 4, based on the formal demonstration of Section 3, a fracture-based model involving sub-diffusion is developed within the classic framework of horizontal well with multi-stage planar fractures. Sub-diffusion is incorporated into the governing equation by employing fractional order time derivate. Then, the problem is solved within the relevant dimensionless domain of a single hydraulic fracture and the corresponding type curves with three parameters are presented. Consistency and robustness of this fracture-based model is investigated. And after

applying this model to some deliberate synthetic cases, its feasibility, characteristics, and limitation are discussed.

In Section 5, to resolve the issues of the fracture-based model developed in Section 4, the well-based fractional production decline models are developed and investigated, which turn out to be a very helpful tool for describing in a first-principle manner the flow regimes from the early- to late-time of multi-fractured horizontal wells in unconventional reservoirs, specially shale and tight sands. Taking a horizontal wellbore as an infinite-conductivity flow channel, a 1D sub-diffusion reservoir model is built with a fractional-flux-dependent convergence skin on the wellbore boundary. After conducting data-fitting of this model on some pertinent synthetic and field data, its capability of interpreting the early- and intermediate-time production data, which is mainly due to the flow in fracture systems, is emphasized. Next, to consider the complete flow regimes from the early- to late-time, a dual-porosity model is built using tempered sub-diffusion mechanism. The corresponding type curves are finally presented, which indicate that the production of slightly compressible fluid in the setting of interest is totally characterized by 7 parameters.

Section 6 summarizes all the works in this dissertation and makes some recommendations for the future works.

2. ASSESSMENT AND OPTIMIZATION OF WELL-FRACTURE CONFIGURATION IN TIGHT FORMATIONS USING THE STANDARD DIFFUSIVITY EQUATION*

2.1. Introduction

In this section, we consider the assessment and optimization for the development plan of shale gas or tight oil with multiple multi-stage fractured laterals in a large square drainage area that we call a "section" (usually 640 acres in the U.S.).

As acknowledged in Section 1.3.2, most of the above referred works on well-fracture configuration (well and/or cluster spacing) optimization are based on sophisticated numerical simulation that requires a large number of inputs which at the early stages of development may be inaccessible or burdened by substantial uncertainty. Moreover, many of the works use quite sophisticated nonlinear search algorithms, which would be computationally expensive. In this section, however, we consider only that part of the problem that can be addressed in rather general terms. Therefore, simplifying assumptions are made to the point that numerical results can be delivered.

We propose a convenient section-based optimization of the fracture array with two integer variables, the number of columns (horizontal laterals) and rows (fractures created in a lateral), to provide some general statements regarding spacing of wells and clusters. The approach is based on a reliable and efficient productivity index (PI) calculation for boundary dominated state (BDS). The dimensionless PI is obtained by solving a time-independent eigenvalue problem using the finite element method (FEM) combined with Richardson extrapolation.

The results will provide some insight and useful bounds on achievable productivity. The methodology is based on accurate numerical solution of a well-defined eigenvalue problem, and as such, it can provide reference values for various research fields relying heavily on the diffusivity equation.

2.2. Numerical Computation for Productivity Index of a Single Planar Fracture

As the basis for the section-based optimization approach, an algorithm, which combines FEM with Richardson extrapolation, is first introduced to calculate the single fracture PI both for constant pressure and constant rate wellbore conditions.

2.2.1. Methodology

2.2.1.1. Productivity Index of a Single Fracture

The assumptions underlining the model are:

- The drainage volume of the single fracture is an isotropic, homogeneous and horizontal formation with a cuboidal shape. Each external boundary is of no flow conditions. The formation has uniform thickness H, permeability k, porosity ϕ, all of which are constants.
- The formation contains slightly compressible single-phase flow. This fluid has the constant properties of formation volume factor B, viscosity μ. The total compressibility of fluid and rock is c_t.
- An infinite-conductivity vertical planar fracture is located at the center of the drainage volume. It is parallel to one side of the rectangular. In addition, the fracture fully penetrates the formation thickness.
- The flow in the reservoir is dictated by Darcy's law. And the fluid flowing directly to the wellbore is neglected. All the produced fluid flows from formation to the fracture, and then from the fracture to the wellbore.

The above assumption regarding the fluid properties has been adopted by many papers (Gringarten et al., 1974; Cinco Ley et al., 1978) to eliminate the extra complexities of fluid state, which is out of the scope of the present work. Though the infinite conductivity fracture has been assumed and investigated by scholars (Gringarten et al., 1974; Hagoort, 2009), the infinite conductivity assumption in our work has particular meaning in the unconventional reservoirs.

Compared to conventional fracture design, in unconventional reservoirs, the value and even meaning of reservoir permeability is questionable and difficult to be used as a direct design input. This difficulty is avoided in this work by the assumption that the created propped fractures have infinite conductivity. This assumption is justified by the fact that, despite the improved capability for conducting fluids in the stimulated reservoir volume (SRV), the induced permeability of the SRV is usually lower than about 0.01 mD, even after accounting for the effect of enhanced natural fractures.

With the above assumptions, the problem reduces to a 2D single-phase flow in a bounded rectangular domain with the gravity being neglected. **Fig. 2.1(a)** illustrates the model we are investigating. We regard the symmetrical element, a quarter of the drainage area, as our problem domain which has the length l, the width w, and the fracture half-length x_f.

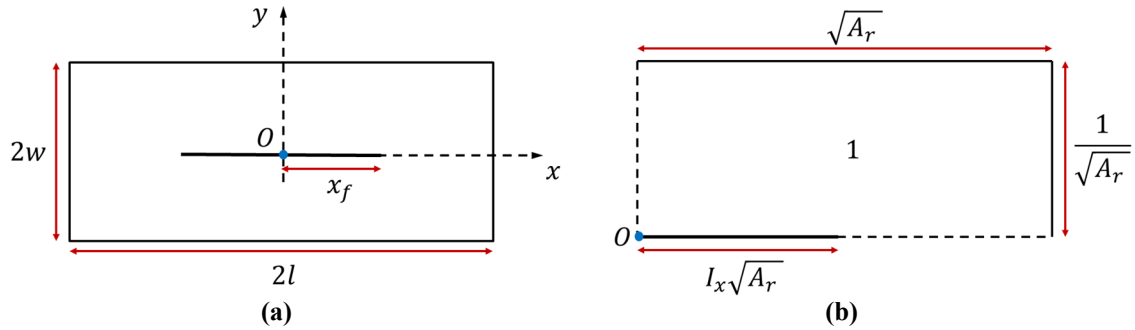

Figure 2.1 – Schematics of (a) a centrally located fracture in a drainage area and (b) the corresponding dimensionless problem domain

In the homogeneous and isotropic reservoir with constant formation and fluid properties, the pressure distribution of slightly compressible flow can be mathematically modeled by the diffusivity equation throughout all the phases of production, as Eq. (2.1) shows.

$$\frac{\partial^2 P}{\partial x^2}+\frac{\partial^2 P}{\partial y^2}=\frac{\phi c_t \mu}{k}\frac{\partial P}{\partial t} \quad \text{.....(2.1)}$$

The initial condition is a uniform initial pressure across the domain, as shown in Eq. (2.2a).

$$t=0: P=0 \quad \text{.....(2.2a)}$$

The boundary consists of the no-flow boundary, the geometry symmetry, and the infinite conductivity fracture. The first two types are the zero Neumann condition mathematically.

$$x=l, 0\le y\le w: \frac{\partial P}{\partial x}=0 \quad \text{.....(2.2b)}$$

$$y=w, 0\le x\le l: \frac{\partial P}{\partial y}=0 \quad \text{.....(2.2c)}$$

$$x=0, 0\le y\le w: \frac{\partial P}{\partial x}=0 \quad \text{.....(2.2d)}$$

$$y=0, x_f<x\le l: \frac{\partial P}{\partial y}=0 \quad \text{.....(2.2e)}$$

Along the infinite conductivity fracture, the boundary condition in the constant pressure case (BDS) is as Eq. (2.2f) shows.

$$y=0, 0\le x\le x_f: P=P_w \quad \text{.....(2.2f)}$$

Here P_f is the specified constant bottomhole pressure.

The boundary conditions in the constant rate case are as Eq. (2.2g) and Eq. (2.2h) show. Here q_{sc} is the specified constant rate in the surface condition.

$$y=0, 0\le x\le x_f: q_{sc}=\frac{4kH}{\mu B}\int_0^{x_f}\frac{\partial P}{\partial y}dx \quad \text{.....(2.2g)}$$

$$y=0, 0\le x\le x_f: \frac{\partial P}{\partial x}=0 \quad \text{.....(2.2h)}$$

After introducing the dimensionless groups shown below, the corresponding dimensionless form is shown in Eq. (2.3). In the definition of dimensionless groups, A is the area of the quarter, $A=$

wl. Also, by the definition of aspect ratio, $A_r = l/w$, and fracture penetration ratio, $I_x = x_f/l$, the length, width and fracture half-length of the dimensionless domain are $l_D = \sqrt{A_r}$, $w_D = 1/\sqrt{A_r}$ and $x_{fD} = I_x\sqrt{A_r}$ respectively, as **Fig. 2.1(b)** shows.

$$x_D = \frac{x}{\sqrt{A}} = \frac{x}{l}\sqrt{A_r}, \qquad y_D = \frac{y}{\sqrt{A}} = \frac{y}{w}\frac{1}{\sqrt{A_r}}, \qquad t_D = \frac{kt}{\phi c_t \mu A},$$

$$A_r = \frac{l}{w}, \qquad I_x = \frac{x_f}{l},$$

Constant bottom-hole pressure case:

$$P_D = \frac{P - P_w}{P_i - P_w}, \quad q_D = \frac{\mu B q}{2\pi k H (P_i - P_w)}$$

Constant rate case:

$$P_D = \frac{2\pi k H (P - P_w)}{\mu B q_{sc}}, \qquad q_D = \frac{q}{q_{sc}}$$

$$\frac{\partial^2 P_D}{\partial x_D^2} + \frac{\partial^2 P_D}{\partial y_D^2} = \frac{\partial P_D}{\partial t_D} \quad \text{(2.3a)}$$

$$t_D = 0 : P_D = 1 \quad \text{(2.3b)}$$

$$x_D = \sqrt{A_r}, 0 \le y_D \le \frac{1}{\sqrt{A_r}} : \frac{\partial P_D}{\partial x_D} = 0 \quad \text{(2.3c)}$$

$$y_D = \frac{1}{\sqrt{A_r}}, 0 \le x_D \le \sqrt{A_r} : \frac{\partial P_D}{\partial y_D} = 0 \quad \text{(2.3d)}$$

$$x_D = 0, 0 \le y_D \le \frac{1}{\sqrt{A_r}} : \frac{\partial P_D}{\partial x_D} = 0 \quad \text{(2.3e)}$$

$$y_D = 0, I_x\sqrt{A_r} \le x_D \le \sqrt{A_r} : \frac{\partial P_D}{\partial y_D} = 0 \quad \text{(2.3f)}$$

The boundary condition on the hydraulic fracture in the constant bottom-hole pressure case (BDS):

$$y_D = 0, 0 \le x_D \le I_x\sqrt{A_r} : P_D = 0 \quad \text{(2.3g)}$$

The boundary condition on the hydraulic fracture in the constant rate case:

$$y_D = 0, 0 \le x_D \le I_x\sqrt{A_r} : \frac{\partial P_D}{\partial x_D} = 0 \quad \text{(2.3h)}$$

$$q_{scD} = -\frac{2}{\pi}\int_0^{I_x\sqrt{A_r}} \frac{\partial p_D}{\partial y_D} dx_D = -1 \quad \text{(2.3i)}$$

The dimensionless PI is defined as the flow rate normalized by the drawdown pressure as shown in Eq. (2.4). The PI can be extracted from the behavior of the previous systems. Since the stabilized PI is directly related to the long-time pressure distribution, we modify the above systems into some kind of "stabilized" form. For the two cases the modifications are not the same.

$$J_D = \frac{q_{wD}}{\bar{P}_D - P_{wD}} \quad \text{(2.4)}$$

2.2.1.1.1. BDS PI

The long-time flow regime with constant wellbore pressure in a bounded reservoir is called the boundary dominated state. In the BDS, although the wellbore flow rate keeps changing as well as the difference between the average reservoir pressure and the wellbore pressure, the ratio of the flow rate to the pressure difference converges to a stabilized value. A convenient and elegant way to calculate BDS PI is to use the eigenvalue with the minimum absolute value of the relevant eigensystem (Eq. (2.5)). The derivation details can be found in Appendix A.

$$J_{D,BDS} = \frac{2}{\pi}\,|\lambda_1| \quad \text{(2.5)}$$

In Eq. (2.5), λ_1 is the eigenvalue with the minimum absolute value of the corresponding eigensystem.

2.2.1.1.2. PSS PI

In constant rate condition, the reservoir is "stabilized" into the pseudo steady state (PSS) in the late time of production, which means that each point has identical time rate of pressure change. A usual way to analyze PSS is to combine the diffusivity equation with the material

balance to get a Poisson equation. The Poisson equation along with the corresponding boundary conditions is a fully time-independent boundary value problem. The reciprocal of the average dimensionless variable P_D is the PSS PI (Eq. (2.6)). The derivation details can be found in Appendix B.

$$J_{D,PSS} = \frac{1}{\bar{P}_D} = \frac{1}{\int_{\Omega_D} P_D dX} \quad \text{.....(2.6)}$$

The approach in this work considers stabilized dimensionless PI (in BDS and PSS) as reasonable measure of the overall productivity of a configuration. In unconventional reservoirs, however, due to the ultra-low matrix permeability the transient flow regime lasts much longer than in conventional reservoirs. Therefore, it might look unwise to tailor the system to perform well only "at late time". But other factors may decrease the time to reach the stabilized flow regime. For instance, the individual drainage area of a fracture is much smaller, and its shape is elongated. Under such conditions the pressure distribution reaches some kind of stable shape in months or in one or two years, as often indicated by the characteristic behavior of the production decline. While the transient PI is larger than the stabilized PI, the basic decisions to be made by the section-based approach, which will be introduced later, can still be based on a convenient measure of stabilized productivity. The idea, that in an unconventional reservoir the boundaries of the fracture drainage area are not felt for decades (Brown et al. 2011; Moghanloo et al. 2015) is somewhat questionable. In fact, the boundaries are "reached" during the hours or days of the stimulation treatment itself and this is acknowledged by the term "Stimulated Volume". In reality, the simple concepts of transient and stabilized states are less applicable and the time to reach stabilized flow certainly cannot be calculated from nano-darcy order of matrix permeability. Actually, a more realistic description for the flow regimes from the early to the late time of production from fractured unconventional reservoirs will be provided in Section 5.

The eigenvalue problem and the boundary value problem are both numerically solved by the FEM since this type of methods can readily handle the geometric complexity due to the arbitrary aspect ratio and penetration ratio. The FEM package in Mathematica (Wolfram Research, Inc., 2018) is used to implement the solution. We conduct the calculations both with linear or quadratic triangular elements. For both mesh types, a specific mesh refinement procedure is used and then extrapolation to infinite resolution provides the final value of the productivity index.

2.2.1.2. Mesh Refinement and Extrapolation

Just like other semi-analytical or numerical methods, simply solving the problem numerically with FEM doesn't guarantee the accuracy of the results. With the numerically attained PI at hand, we cannot tell how many digits are reliable and how many are not. Thus, some treatments need to be imposed on the primary results, in order to refine them and strengthen our confidence.

Richardson extrapolation is a widely used method to improve the order of truncation errors for numerical solutions. However, a successful extrapolation heavily depends on the trend of error change with the discretization size h, namely the size of the mesh. In detail, only when a straight line with its slope very close to a positive integer shows up on a $\log - \log$ plot of error vs. h, the numerical solution in this interval can be used to do the extrapolation successfully.

Although the rigorous error is not available since the exact solution is certainly unknown, two ways are proposed to approximate the error. The first option is that a numerical solution with small enough h is taken as a "true solution", and then the difference between the "true solution" and a sequence of solutions with decreasing h are regarded as the errors. Another option is to use "pseudo error", defined by Soroushian (2010) as the difference between two consecutive numerical results in a series with decreasing h. In this work, we use the second option, because it requires less subjective judgment.

The success of Richardson extrapolation relies on the manner in which the mesh is refined (Burg and Erwin 2009; Lin and Xie 1987). Generally speaking, a sequence of geometrically similar meshes is necessary for a successful extrapolation. In this work, the unstructured triangle elements are used to deal with the arbitrary A_r and I_x. The refinement with self-similarity for the unstructured mesh is guaranteed by the so-called *h*-refinement, in the process of which new nodes are inserted at the midpoint of each edge in the primary mesh, and then connected to generate new edges. As a result, this method subdivides each triangle element into 4 similar triangles. **Fig. 2.2** illustrates the *h*-refinement process.

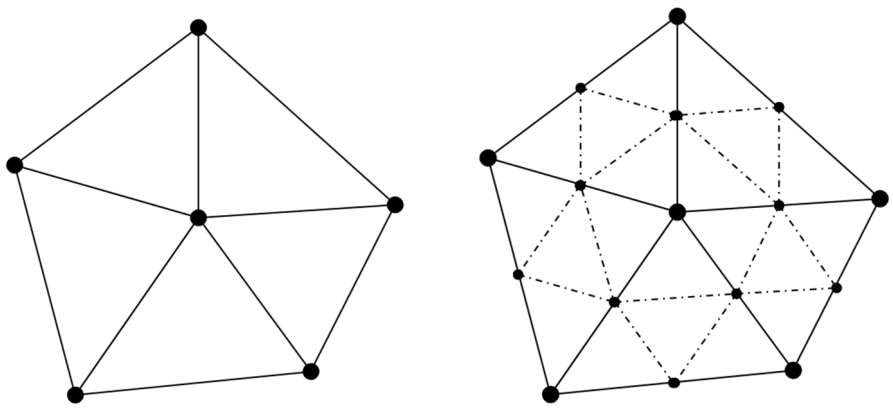

Figure 2.2 – Plot illustrating the *h*-refinement process for 5 meshes. (a) Origin mesh. (b) Refined mesh.

The full steps of the algorithm are the following. And the flowchart of the algorithm is shown in **Fig. 2.3**.

1. Primarily solve the system for $J_{D,BDS}$ and $J_{D,PSS}$ by using FEM with an arbitrarily chosen mesh size controlling parameter.
2. Extract the primary mesh, do the h-refinement on it and then solve for the new $J_{D,BDS}$ and $J_{D,PSS}$ with the refined mesh; repeat Step 2 for several times to get a sequence of $J_{D,BDS}$ and $J_{D,PSS}$ corresponding to a sequence of refined meshes.
3. Make the $\log - \log$ plot of "pseudo error" vs average mesh size $\bar{h}$ (Eq. (2.7) where N is the number of meshes) and then do the linear regression for these points to

check whether the value of R^2 is close to 1.0 and the slope of the straight line is close to a positive integer, if not, adjust the mesh size controlling parameter used in Step 1 and then repeat Step 2 to Step 4.

4. By using the leading convergence order obtained from the straight-line slope, Richardson extrapolation is imposed on PIs with the last two meshes to get an accurate result.

$$\bar{h} = \sqrt{\frac{1}{N}} \quad \text{.....(2.7)}$$

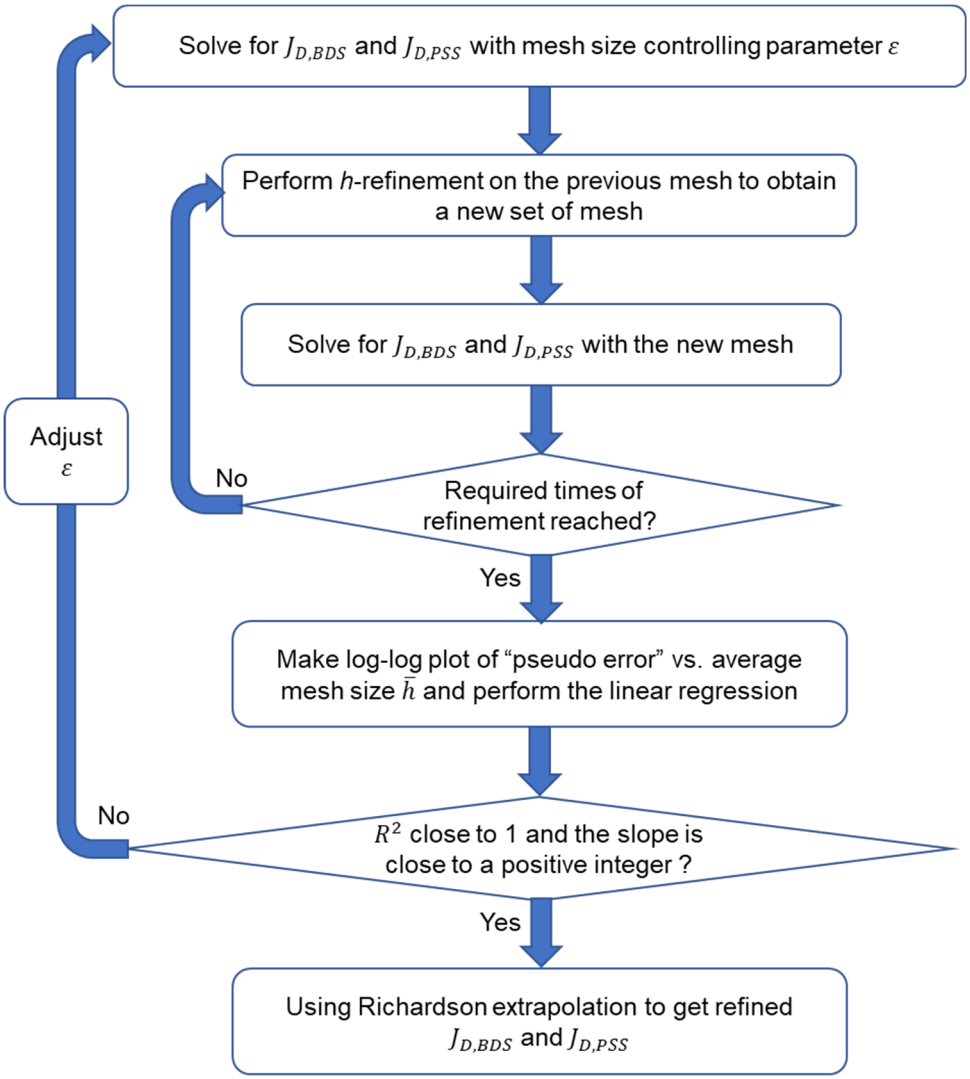

Figure 2.3 – Flowchart of the algorithm for obtaining accurate PI with Richardson extrapolation

Table 2.1 – Table of pseudo-error plot, linear expression and R^2 value for BDS and PSS

BDS	
Pseudo-error plot	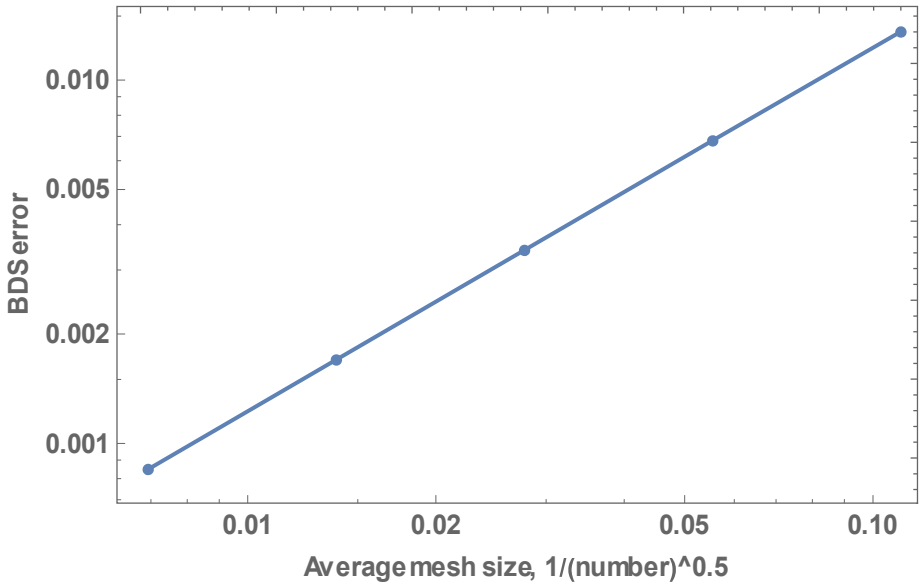
Linear expression	$-2.09753 + 1.00007x$
R^2	0.999999

PSS	
Pseudo-error plot	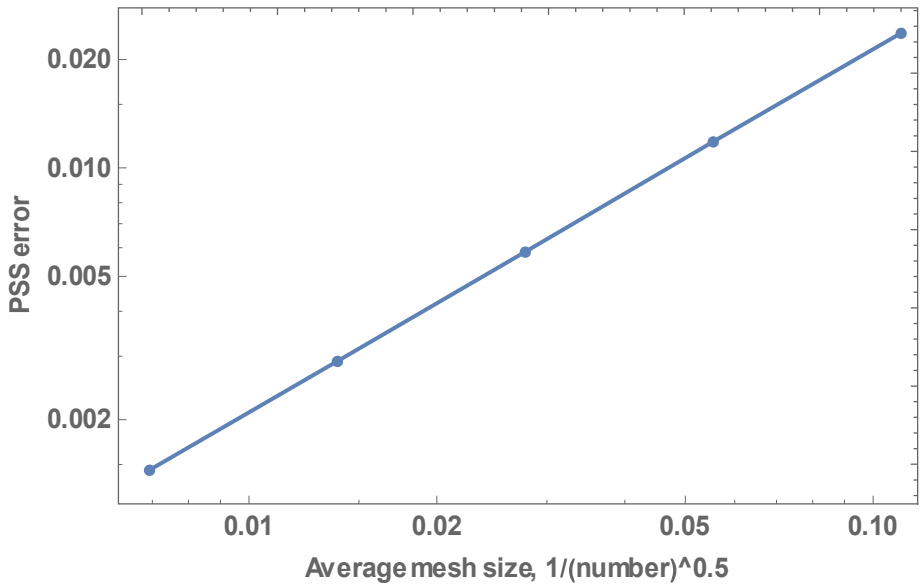
Linear expression	$-1.52439 + 1.0083x$
R^2	0.999995

2.2.2. Results of PI Calculation

2.2.2.1. Calculation Example by the Proposed Algorithm

The extrapolation is implemented on each pair of neighboring PIs in the sequence of refined meshes. By comparing all the refined results, it becomes apparent to us how many digits for the refined PIs are stable and thus accurate.

The algorithm is implemented in Mathematica (Wolfram Research, Inc., 2018). The calculation using the above algorithm is demonstrated in **Fig. 2.4**, **Table 2.1** and **Table 2.2** for a case with $A_r = 3.2$, $I_x = 0.43$. In this case, **Fig. 2.5 (a)** is the plot of the eigenfunction corresponding to the eigenvalue used in BDS. For comparison, we also show the distribution of the dimensionless variable P_D for the PSS case in **Fig. 2.5 (b)**.

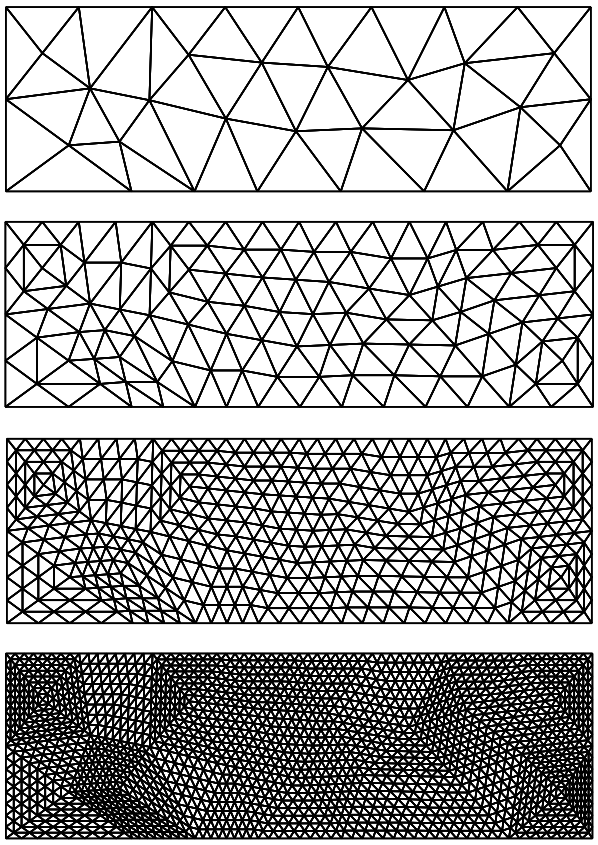

Figure 2.4 – Plots of the original mesh and the meshes refined 3 times

Table 2.2 – Primary and refined PI with $A_r = 3.2$, $I_x = 0.43$

	Element Number N	$J_{D,BDS}$	Refined $J_{D,BDS}$	$J_{D,PSS}$	Refined $J_{D,PSS}$
1	81	0.979279	0.952051	1.38137	1.33418
2	324	0.965664	0.952004	1.35764	1.33407
3	1296	0.958834	0.952010	1.34579	1.33414
4	5184	0.955422	0.952014	1.33993	1.33413
5	20736	0.953718	0.952014	1.33701	1.33412
6	82944	0.952866	-	1.33556	-

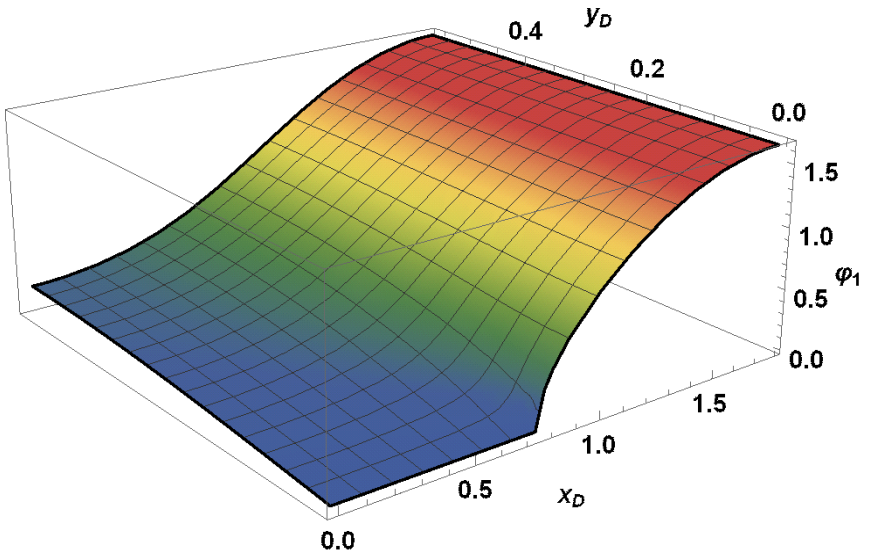

(a)

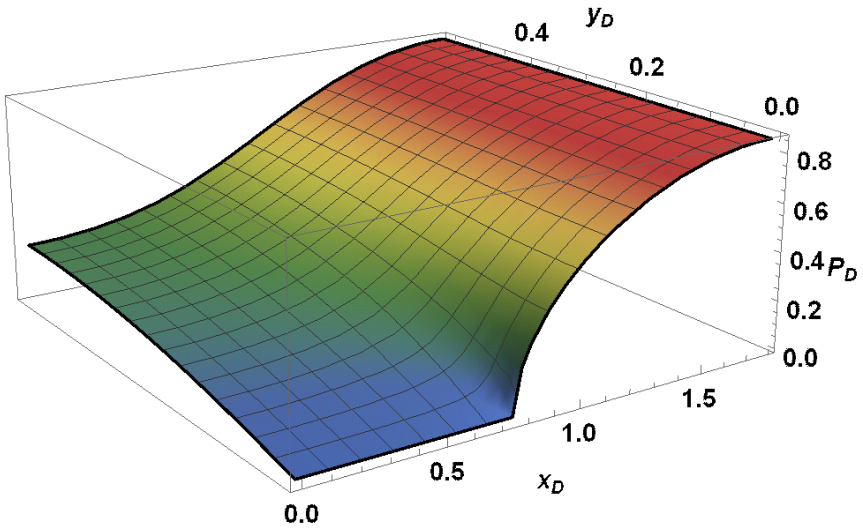

(b)

Figure 2.5 – Plots of the relevant function related to the calculation of BDS and PSS PI. (a) Plot of the eigenfunction corresponding to the first eigenvalue. (b) Plot of the dimensionless variable P_D.

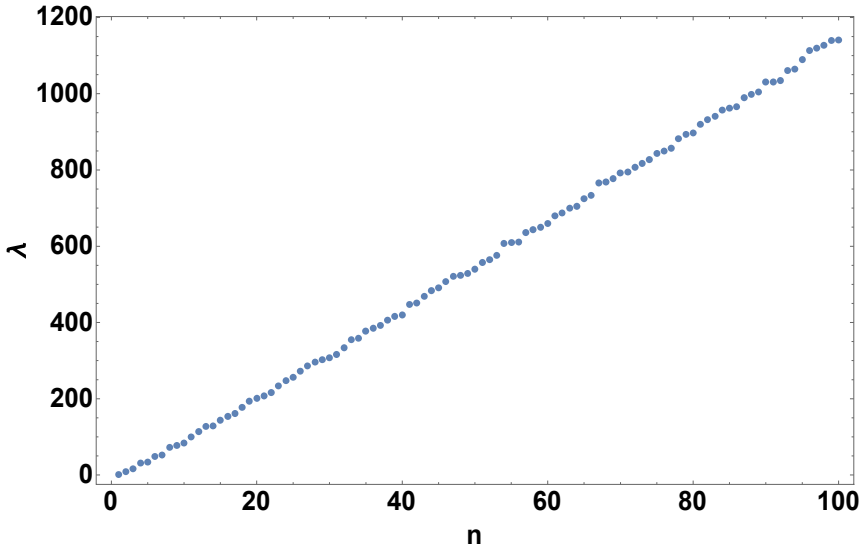

Figure 2.6 – Eigenvalues for the case of $A_r = 3.2$, $I_x = 0.43$

Fig. 2.6 illustrates the increasing eigenvalues with respect to n for the calculation case.

2.2.2.2. Comparison with Published Results

In order to accelerate the convergence, second order triangular elements are chosen. In **Table 2.3** the PSS PIs obtained are compared to the results of Hagoort (2009). The particular case of $x_{wD} = y_{wD} = 0.5$ is considered.

For $A_r = 1.0$ and 0.5 the deviations are less than 0.2%, the stated accuracy in Hagoort's work. For $A_r = 2.0$ the deviations are somewhat bigger but still below $0.4\ \%$. Apparently, the results from our work and the referred one are in good agreement up to the third significant digit. Based on the feature of our method, we can tell unambiguously how many digits are stable. In contrast, the accuracy of the results of the conventional semi-analytical methods (Gringarten et al. 1974; Raghavan et al. 1997; Hagoort 2009) is usually over-estimated. While our PSS productivity indexes are near to previously published results, such comparison cannot be made for the stabilized BDS PI, because previous reliable results are not available for non-square drainage areas partially penetrated by the fracture.

Table 2.3 – Comparison with Hagoort (2009)

I_x	$A_r = 1.0$			$A_r = 2.0$			$A_r = 0.5$		
	PI		Deviation (%)	PI		Deviation (%)	PI		Deviation (%)
	Our work	Hagoort		Our work	Hagoort		Our work	Hagoort	
0.1	0.41977	0.4194	0.0881	0.45363	0.4532	0.0948	0.34456	0.3443	0.0755
0.2	0.58788	0.5872	0.1157	0.66192	0.6610	0.1390	0.45013	0.4498	0.0733
0.3	0.76009	0.7590	0.1434	0.90224	0.9006	0.1818	0.54440	0.5438	0.1102
0.4	0.94644	0.9448	0.1733	1.20267	1.1997	0.2470	0.63347	0.6327	0.1216
0.5	1.14797	1.1457	0.1977	1.58581	1.5812	0.2907	0.71748	0.7166	0.1227
0.6	1.35873	1.3560	0.2009	2.06464	2.0578	0.3313	0.79420	0.7933	0.1133
0.7	1.56455	1.5615	0.1949	2.62469	2.6157	0.3425	0.86014	0.8592	0.1093
0.8	1.74273	1.7400	0.1567	3.19693	3.1876	0.2918	0.91126	0.9105	0.0834
0.9	1.86571	1.8641	0.0863	3.64643	3.6402	0.1709	0.94376	0.9434	0.0381
1.0	1.90986	1.9098	0.0031	3.81972	3.8197	0.0005	0.95493	0.9549	0.0031

2.2.2.3. Summary of PI for a Single Fracture

With the method introduced above, the accurate PIs for both BDS and PSS are calculated as a function with respect to two variables, aspect ratio A_r and penetration ratio I_x. The results are presented in **Table 2.4** and **Table 2.5**. Given that these PIs have 4 to 5 accurate significant digits, they can be confidently taken as a benchmark for the PI calculation, or fracture design and evaluation.

For extreme aspect ratios, there is a huge difference between the BDS and PSS PIs. This underlines the importance of using the BDS values in optimization.

2.3. Optimal Development Plan for Hydraulic Fractures in a Section

With the tool we have developed in Section 2.2, PI for a single fracture centrally located in a bounded drainage area can be calculated with at least 4 significant digits, and the calculation is done within 4 seconds (if the mesh is refined 3 times).

Table 2.4– PI table for BDS and PSS for $A_r = 1.0, 2.0, 0.5, 4.0, 0.25$

	$A_r = 1.0$		$A_r = 2.0$		$A_r = 0.5$		$A_r = 4.0$		$A_r = 0.25$	
I_x	BDS	PSS	BDS	PSS	BDS	PSS	BDS	PSS	BDS	PSS
0.1	0.40914	0.41970	0.43032	0.45363	0.33352	0.34456	0.34585	0.39584	0.23817	0.25320
0.2	0.56250	0.58788	0.60323	0.66192	0.42659	0.45013	0.45734	0.57114	0.28015	0.30592
0.3	0.71392	0.76009	0.79120	0.90224	0.50484	0.54440	0.58828	0.80158	0.31026	0.34673
0.4	0.87247	0.94644	1.02043	1.20267	0.57430	0.63347	0.76851	1.14169	0.33382	0.38084
0.5	1.03789	1.14797	1.31663	1.58581	0.63566	0.71748	1.03789	1.66724	0.35260	0.40968
0.6	1.20277	1.35873	1.70647	2.06464	0.68800	0.79420	1.46999	2.48946	0.36740	0.43359
0.7	1.35301	1.56455	2.19538	2.62469	0.73006	0.86014	2.21817	3.73140	0.37862	0.45253
0.8	1.47171	1.74273	2.69891	3.19693	0.76069	0.91126	3.59538	5.37638	0.38649	0.46629
0.9	1.54596	1.86571	3.03720	3.64643	0.77922	0.94376	5.63273	6.96242	0.39115	0.47466
1.0	1.57080	1.90986	3.14159	3.81972	0.78540	0.95493	6.28319	7.63944	0.39270	0.47747

Table 2.5 – PI table for BDS and PSS for $A_r = 10.0, 0.1, 20.0, 0.05$

	$A_r = 10.0$		$A_r = 0.1$		$A_r = 20.0$		$A_r = 0.05$	
I_x	BDS	PSS	BDS	PSS	BDS	PSS	BDS	PSS
0.1	0.17512	0.22262	0.12587	0.14102	0.09236	0.12141	0.07004	0.08112
0.2	0.22031	0.31233	0.13604	0.15599	0.11621	0.17113	0.07299	0.08586
0.3	0.28354	0.45277	0.14241	0.16595	0.15063	0.25200	0.07474	0.08880
0.4	0.37832	0.68944	0.14697	0.17339	0.20294	0.39267	0.07595	0.09088
0.5	0.52990	1.14797	0.15036	0.17912	0.28811	0.65966	0.07684	0.09243
0.6	0.79457	1.96143	0.15292	0.18355	0.44074	1.22960	0.07749	0.09359
0.7	1.31990	3.78040	0.15480	0.18687	0.75664	2.66170	0.07797	0.09445
0.8	2.59880	7.85400	0.15608	0.18917	1.58915	7.11500	0.07829	0.09503
0.9	7.00821	14.96440	0.15683	0.19054	5.19760	22.26146	0.07848	0.09538
1.0	15.70796	19.09859	0.15708	0.19099	31.41593	38.19718	0.07854	0.09549

2.3.1. Considerations for Well-based Optimization

For a horizontal lateral with evenly distributed multi-stage fractures in a formation with constant permeability k, thickness H and produced liquid of constant viscosity μ and formation volume factor B, the PI is simply expressed as

$$J = \frac{2\pi kH}{B\mu} n_f J_{D,f}(A_r, I_x), \quad (2.8)$$

where n_f is the number of fractures in a well and $J_{D,f}$ is the dimensionless PI for a single fracture, which is a function of the aspect ratio of the single fracture's drainage area and of the penetration ratio. The objective function of optimization is the dimensionless PI:

$$J_D = n_f J_{D,f}(A_r, I_x), \quad (2.9)$$

subject to some constraints that the penetration ratio should be between 0 and 1 (or a constant a bit smaller than 1, say 0.95, to avoid fracture communication between adjacent laterals). An additional constraint should express the limitation on resources. For instance, from a given amount of proppant used in a well, only a certain total fracture length can be created (assuming average fracture width and average propped height are given).

To solve the constrained nonlinear optimization problem is not a trivial task. The optimization process is undesirably time-consuming and sensitive to the starting estimates of the decision variables.

2.3.2. Considerations for Section-based Optimization

However, if we widen our horizon from a well to a section, the optimization process can be simplified to a large extent. With the assumption that all the fractures are created with the same length and distributed evenly, the fracture array becomes regular, as shown in **Fig. 2.7** for a two horizontal lateral case. The configuration of the fracture array is defined by the number of columns n_c and the number of rows n_r. According to the basic configuration, the fractures in a single column can be transvers fractures stemming from a single horizontal lateral. Only in the last couple of years has it become possible to drill and complete a horizontal lateral almost as long as a typical section side. Previously, such a column of fractures was realized with the help of two horizontal laterals. From the productivity point of view the number of laterals in one column is irrelevant. The wells only collect the production from the fractures, they do not affect productivity. The

number of columns is just another way to express well spacing. The suggested terminology attempts to put the emphases on the important variables.

The dimensionless PI for the whole section is still $n_f J_{D,f}$, but here n_f is the total number of fractures in the section. Even though $J_{D,f}$ is still a function of the aspect ratio and penetration ratio, these two parameters are well defined by n_c, n_r, and the given total fracture length in the section, which represents the available "fracturing resources". Therefore, if the total fracture length is specified in a section, the dimensionless PI can be well determined by using two variables, n_c and n_r. As these two variables are positive integers, a sequence of integer pairs satisfying the constraints can be easily generated and the corresponding dimensionless PI can be calculated for each pair. In other words, the objective function can be maximized by total enumeration. We would also like to emphasize that the statement that $J_{D,f}$ is a function of n_c and n_r is implicitly based on a few assumptions: the SRV covers the whole section and the induced properties within the SRV

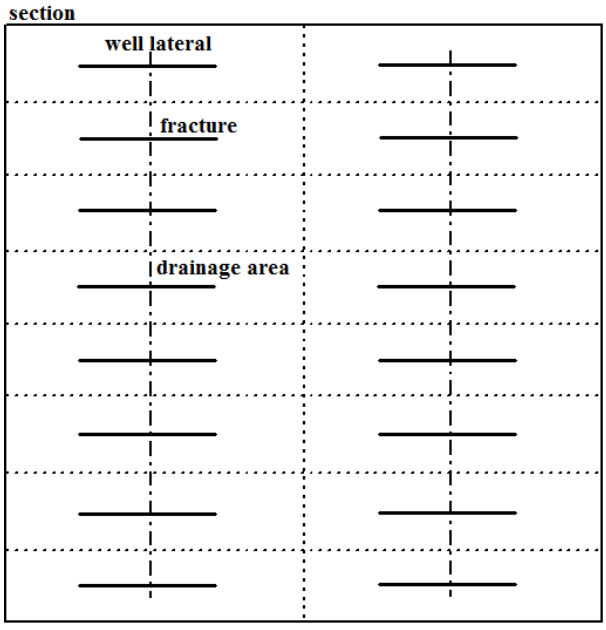

Figure 2.7 – Plot of an evenly distributed fracture array with two horizontal laterals in a section ($n_c = 2$, $n_r = 8$)

do not depend on the choice of n_c, n_r once the total fracture length for the whole section is fixed.

Under the simplifying assumptions Eq. (2.9) can be written in a section-based form:

$$J_D = n_c n_r J_{D,f}\left(\frac{n_r}{n_c}, \frac{l_{fD}}{n_r}\right) \quad (2.10)$$

According to Eq. (2.10) the dimensionless PI for the whole section is determined by three numbers, number of columns n_c, number of rows n_r, and the dimensionless number l_{fD} defined by

$$l_{fD} = \frac{l_f}{\sqrt{A_s}} = n_c n_r \frac{2x_f}{\sqrt{A_s}}. \quad (2.11)$$

Here l_f is the total fracture length in a section (the sum of all $2x_f$), A_s is the area of the section, x_f is the half-length of each fracture. Ultimately, the total fracture length is a consequence of available proppant, but it also depends on average propped fracture width (necessary to consider the fractures of infinite conductivity) and average propped fracture height. We name l_{fD} dimensionless total fracture length. It represents the fracturing treatment size relative to the size of the section. Also, the product $n_c n_r$ is the total number of fractures and the ratio n_r/n_c is the aspect ratio of the drainage area of a single fracture. In dimensioned terms, well spacing is $\sqrt{A_s}/n_c$, cluster spacing is $\sqrt{A_s}/n_r$ and fracture half-length is $l_f/(2n_c n_r)$.

2.3.3. Lower bound on the objective function

If we consider integer l_{fD} values, it is easy to see that the section can be divided into l_{fD}^2 squares and the total fracture length is sufficient to place a wall-to-wall fracture in the middle of each square. The dimensionless BDS PI of one such square is $\pi/2$ (Wattenbarger at al., 1998). Therefore, we constructed a feasible solution with the objective function

$$J_{D,lower-bound} = 0.5\,\pi\, l_{fD}^2. \quad (2.12)$$

For instance, in **Table 2.6**, $J_{D,lower-bound} = 0.5\,\pi\, l_{fD}^2 = 2253.9$. We see that the lower bound is indeed smaller than all the actual Total J_D values in the 4th column of the table. It is also clear, that the lower bound is rather sharp. The actual value in the **Tables 2.6 – 2.9** (which will be described in detail later) is usually only 2-11% more than the lower bound.

2.3.4. Results for a 640-acre section

As a case study, we consider a 1 mile by 1 mile section, ($\sqrt{A_s} = \sqrt{640\ \text{acre}} = 5280$ ft), with various total fracture lengths, such as 200,000 ft, 240,000 ft, 280,000 ft, and 300,000 ft. For simplicity, we temporarily neglect the concern about fracture communication and use 1.0 as the upper boundary for penetration ratio.

Table 2.6 – Optimization for total fracture length 200,000 ft, $l_{fD} = 37.88$

n_c	n_r	n_f	Total J_D	Single Lateral J_D	I_x	x_f, ft
5	39	195	2350.3	470.06	0.97	512.8
6	39	234	2362.8	393.80	0.97	427.4
7	40	280	2403.0	343.29	0.95	357.1
8	40	320	2433.0	304.13	0.95	312.5
9	41	369	2459.7	273.30	0.92	271.0
10	41	410	2498.3	249.83	0.92	243.9

Table 2.7 – Optimization for total fracture length 240,000 ft, $l_{fD} = 45.45$

n_c	n_r	n_f	Total J_D	Single Lateral J_D	I_x	x_f, ft
5	47	235	3320.2	664.04	0.97	510.6
6	47	282	3383.7	563.95	0.97	425.5
7	47	329	3411.6	487.37	0.97	364.7
8	48	384	3437.6	429.70	0.95	312.5
9	48	432	3485.2	387.24	0.95	277.8
10	48	480	3512.9	351.29	0.95	250.0

Table 2.8– Optimization for total fracture length $280,000$ ft, $l_{fD} = 53.03$

n_c	n_r	n_f	Total J_D	Single Lateral J_D	I_x	x_f, ft
5	54	270	4538.0	907.60	0.98	518.5
6	54	324	4552.4	758.73	0.98	432.1
7	55	385	4597.2	656.74	0.96	363.6
8	55	440	4644.6	580.58	0.96	318.2
9	55	495	4669.6	518.84	0.96	282.8
10	56	560	4720.7	472.07	0.95	250.0

Table 2.9 – Table for the case with total fracture length $300,000$ ft, $l_{fD} = 56.82$

n_c	n_r	n_f	Total J_D	Single Lateral J_D	I_x	x_f, ft
5	58	290	5193.3	1038.66	0.98	517.2
6	58	348	5230.5	871.75	0.98	431.0
7	58	406	5245.8	749.40	0.98	369.5
8	59	472	5304.6	663.08	0.96	317.8
9	59	531	5348.0	594.22	0.96	282.5
10	59	590	5372.8	537.28	0.96	254.2

Using the method suggested above, the total dimensionless BDS PIs of reasonable of n_c and n_r are calculated and shown in the 3D plots with contours, as shown in **Fig. 2.8 (a)** to **Fig. 2.8 (d)**. In each 3D plot, it is apparent that the dimensionless PI decreases significantly with increased number of fractures for a given number of well. The reason for this feature is that with the specific total fracture length, the increase for the number of fractures leads to the decrease in penetration ratio. In the condition of infinite conductivity fracture, the reduction in the dimensionless PI per fracture due to the decreased penetration ratio outweighs the increase in the number of fractures. Thus, this phenomenon mainly results from the limited total fracture length and infinite conductivity assumption.

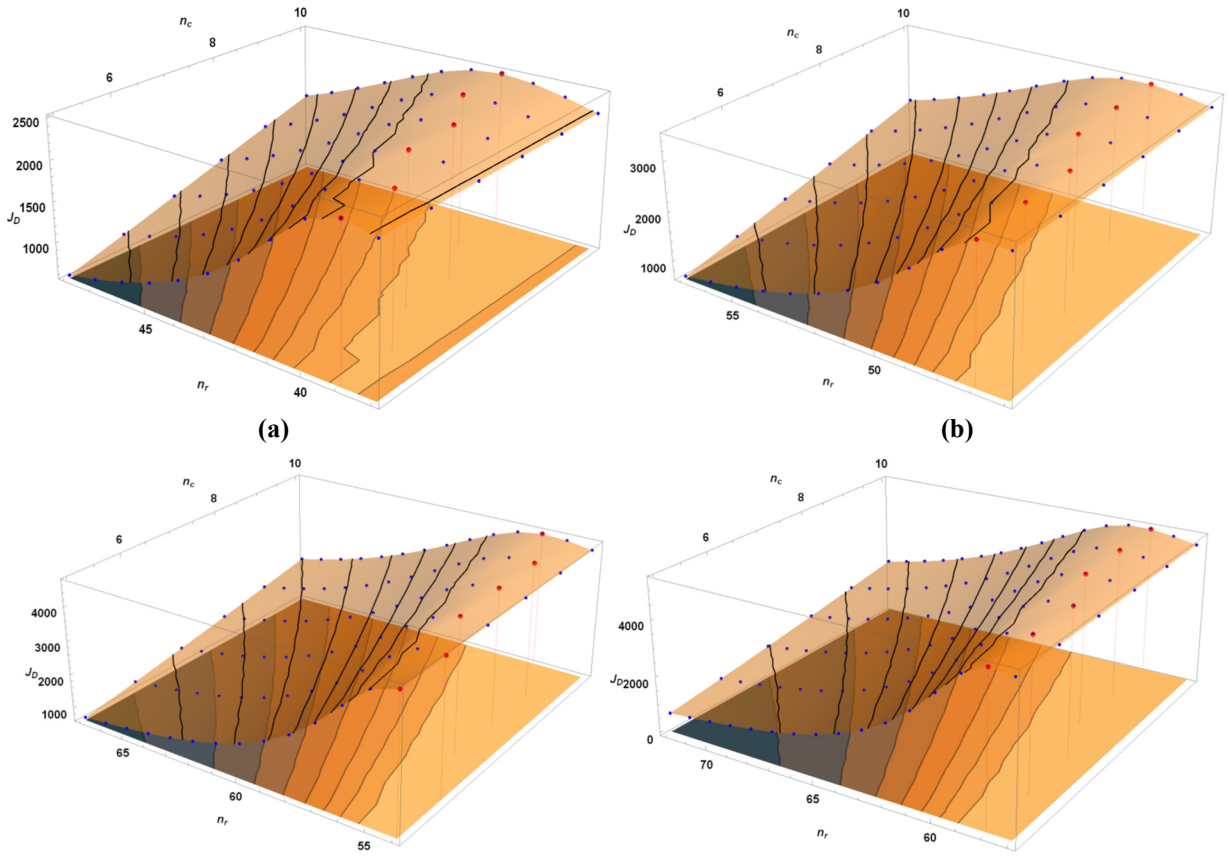

Figure 2.8 – Plot of total J_D in a section with specified total fracture lengths (l_f, l_{fD}). (a) $l_f = 200,000$ ft, $l_{fD} = 37.88$. (b) $l_f = 240,000$ ft, $l_{fD} = 45.45$. (c) $l_f = 280,000$ ft, $l_{fD} = 53.03$. (d) $l_f = 300,000$ ft, $l_{fD} = 56.82$.

The maximum total dimensionless BDS PI corresponding to specified number of columns, n_c, are highlighted with red color in these figures. **Table 2.6** to **Table 2.9** list the maximum total J_Ds corresponding to some practical column numbers. Each row is obtained by a one variable enumeration. In earlier developments a typical column could be realized drilling two horizontal laterals in the Barnett and Eagle Ford shales. In view of recent developments, one column can be realized drilling one horizontal lateral.

The most striking feature of the results is, that the maximum total J_D increases only moderately with n_c, but the improvement is not substantial at a fixed l_{fD}. In other words, what

ultimately matters is the total amount of proppant, not the number of laterals. Indeed, the single-lateral J_D is always decreasing with increasing n_c under the constraint of fixed l_{fD}.

The second important observation is, that the necessary penetration ratio (I_x) is near to one. Therefore, the "optimal" fracture half-length is only slightly less than the half-distance between the laterals. In essence, this means that the laterals should be drilled near enough for the fractures to penetrate the space between them *repeatedly* and *reliably*.

Despite the overall feature of these dimensionless PI tables, we also prefer to obtain an individual optimal choice. Generally, the steps to reach the optimum are:

1. With the given total fracture length in a section (which results from the total proppant mass per section, average fracture height, average fracture width for infinite conductive fracture, proppant density and proppant pack porosity) we can obtain the maximum dimensionless PI for specific numbers of wells with some constrains on the penetration ratio;
2. In the dimensionless PI table, some configurations with small numbers of wells can be excluded because they would require longer half-length than the feasible range. Among the candidates, the one with the minimum number of wells is reasonable to pick because the marginal increase of dimensionless PI is certainly not enough to justify the extra cost associated with one more lateral.

In view of the above remarks we can say that in addition to the total (infinite conductivity) fracture length available, the other decisive factor is the technologically feasible range of fracture half-lengths. In unconventional reservoirs the x_f becomes crucial. The calculations show that if the actual x_f is only 10 % less than the indicated, the total productivity might suffer 50 % reduction. Increasing the number of fractures in one lateral cannot compensate for the lost lateral penetration.

2.4. Discussions about the Section-based Optimization Approach

If we could create an $x_f = 520$ ft infinite conductivity fracture repeatedly and reliably, we could select the first row from each table, as shown from **Table 2.6** to **Table 2.9**. The slight improvement of overall productivity could never justify the additional cost of drilling more than 5 laterals.

However, in typical shale gas and tight oil formations targeting an $x_f = 520$ ft infinite conductivity fracture is not realistic. In practice, there is a feasible interval for such x_f. As an example, let us assume, that the feasible range of x_f is $300 - 360$ ft. Then in **Table 2.6** there are two potential candidates ($n_c = 7$ or 8) and the obvious optimal choice is $n_c = 7$. However, from each of the other tables we can pick only $n_c = 8$. In other words, the realistic feasible range of x_f dictates our choice, once the total fracture length is fixed.

Along an individual horizontal lateral, the effect of cluster spacing is implicitly taken into account by the aspect ratio, which is furtherly a function of n_c and n_r, of the drainage volume. A cluster spacing derived from an unoptimized n_r is much likely to lead to an aspect ratio that results a pretty low total dimensionless productivity. That is, the cluster spacing is optimized interactively with well spacing, which is the rationale of the section-based method. This effect is enlarged by the constraint on the "feasible range of x_f-s". For instance, if we consider the feasible range to be 300 – 360 ft for infinite conductivity fractures, then a well spacing of more than 800 ft will ultimately suffer from low lateral penetration ratio of the fractures. Therefore, the total dimensionless fracture length and the feasible range of individual fracture length together completely specifies the optimization problem. In addition, if the implicit assumptions for our section based method are accepted, that the SRV covers the whole section and the induced properties within the SRV do not depend on the choice of n_c, n_r for a given l_{fD}, then the optimal lateral and cluster spacing are independent of the "original" and even of the "induced" reservoir permeability.

As noted before, the total fracture length is proportional to the amount of proppant given the average fracture width and height. Eq. (2.12) and the results from **Table 2.6** to **Table 2.9** indicate that the maximum total J_D increases quadratically with the total available proppant. Even

if more proppant (and fluid, etc.) costs at least proportionally more, this fact underlines the potential of the "new" unconventional technology. Of course, the actual total fracture length is ultimately an economic decision, and our preliminary calculations cannot substitute the detailed analysis taking into account prices, risks, etc. Such an analysis is, however, out of the scope of the present work.

Of course, the results are no longer valid if the basic assumptions for the present approach are not valid. For example, if the individual fracture cannot be regarded as infinite conductivity, the maximum J_D for a single fracture may happen at less lateral penetration (but larger fracture width) and the actual dimensionless productivity will be much less than the "lower bound" of Eq. (2.12). Or if the radial flow convergence in the fracture still causes substantial "convergence skin", our results are again not applicable.

In this work we use the BDS J_D as the objective function. We think it is more justified as a measure of productivity, than the PSS J_D. In unconventional reservoirs the production rate declines substantially in the early production phase and usually continues to decline later on with a relatively slow pace. Under such conditions, the constant rate assumption is quite unrealistic. An even more important reason to use BDS J_D is the fact that it has a mathematically clearer meaning. The first eigenvalue together with the first eigenfunction captures the very essence of the configuration. The fact that to reach a fully established BDS takes long time does not automatically mean that the decision on n_r and n_c will be wrong. The BDS J_D will still well characterize the relative productivity advantage of the configuration, even if the actual transient rate will be different from the calculable stabilized rate.

Admittedly, we offer only a first pass method for decision making in the early stages of unconventional field development, when detailed inputs are not yet available. The method can

provide reasonable starting configurations for more detailed stimulation studies. The calculated results also help to establish bounds on productivity and might help to focus on parameters that are the decisive ones.

2.5. Section Summary

1. A method combining the FEM with Richardson extrapolation is introduced in this section to calculate accurate dimensionless productivity indexes (J_D) in both constant pressure condition (boundary dominated state, BDS) and constant rate condition (pseudo steady state, PSS);
2. By using the proposed method, a J_D table with different aspect ratios (A_r) and fracture penetration ratios (I_x) is presented with at least 4 significant digits;
3. A convenient section-based optimization approach is proposed for determining the optimal development plan;
4. The dimensionless total fracture length (l_{fD}) and the feasible range of fracture half-length are the two most important input parameters dictating the number of columns and rows of the optimum fracture array. Other parameters (lateral spacing, cluster spacing, individual fracture penetration) all follow from these main decisions.
5. In the development plan of unconventional reservoirs, the amount of proppant available for the whole section is more important than the number of laterals. In fact, the productivity potential is determined first of all by the dimensionless total fracture length l_{fD}. The required number of laterals is basically determined by the technologically feasible range of infinite conductivity fracture half-length.

3. ANOMALOUS DIFFUSION DUE TO A COMPLEX FRACTURE NETWORK*

3.1. Introduction

Though some simplifying assumptions are involved, the rationale of the work done in Section 2 exactly follows the mainstream methodology of modeling and analyzing production from highly fractured unconventional reservoirs, which is applying the concepts and tools in conventional reservoir engineering as a special scenario of ultra-low permeability. Basically speaking, these concepts and tools are more or less constructed on the governing equation of the standard diffusivity equation with some representative parameters averaged over the whole reservoir of interest. Naturally, due to the inconsistency between this kind of "naive" averaging and the highly heterogeneity in almost all scales for unconventional reservoirs, the applications of these concepts and tools originating from conventional reservoir engineering to unconventional reservoirs can hardly be considered satisfactory (indicated by the relevant referred works in Section 1.2), and the computationally costly reservoir simulation seems to be undoubtably superior to the efficient reservoir engineering calculations in this setting.

However, in the rest of our work, we would like to investigate the possibility of structurally accounting for the heterogeneity due to complex fracture networks by integrating its effects on production or the flow in the reservoir scale to the governing equation through a phenomenon called anomalous diffusion.

As has been mentioned in Section 1.3.3, the anomalous diffusion has been introduced into the field of petroleum engineering to try to solve some challenges in the highly heterogeneous unconventional reservoir. Besides formulating and solving the new models mathematically,

researchers are also tending to attribute it either to a broad concept of heterogeneity or to some small- or micro-scale heterogeneous structures of the rock. In contrast, we would like to investigate another probable reservoir-scale source for the anomalous diffusion in unconventional reservoirs, which is the complex topology of the conductive fracture network.

As an engineering work, the rigorous mathematical derivation for the connection between the normal diffusion (Darcy's flow) in discrete fracture network and continuum-backed anomalous diffusion in the whole domain of interest has been temporarily put on hold. On the other hand, this connection will be demonstrated formally by simulating the normal diffusion on complex fracture networks to display the non-linear relationship between the mean square displacement (MSD) of diffusing particles and time, which is the content of this section.

3.2. Revisiting Diffusivity Equation

Single-phase flow of slightly compressible fluid in porous media is always the primary and most essential problem for petroleum industry (Dake, 1983). Although it may be called as one of the thoroughly investigated topics in this field, we would like to propose a new perspective for this equation when the porous media has a micro-structure in the form of complex fracture network. For simplicity and without losing generality, we will concentrate on the problem in a 2-D domain.

The assumptions for the discussion and the model in this paper are listed as follows.

1. The fluid is of single phase and slight compressibility. The formation volume factor B and viscosity μ can be considered essentially constant. The total compressibility of fracture rock and matrix rock saturated with the fluid are c_{tf} and c_{tm}, respectively. In addition, only isothermal flow is considered.
2. The formation is horizontal and its thickness H is constant. Its upper and lower boundary is of no flow conditions.
3. The porous media consists of two main parts: the fractures and the matrix. The schematic graph in **Fig. 3.1 (a)** illustrates the domains of our model.
    - Although, in reality, the unconventional reservoir formations have the strong heterogeneity due to fractures in nearly all scales (Gale et al., 2014;

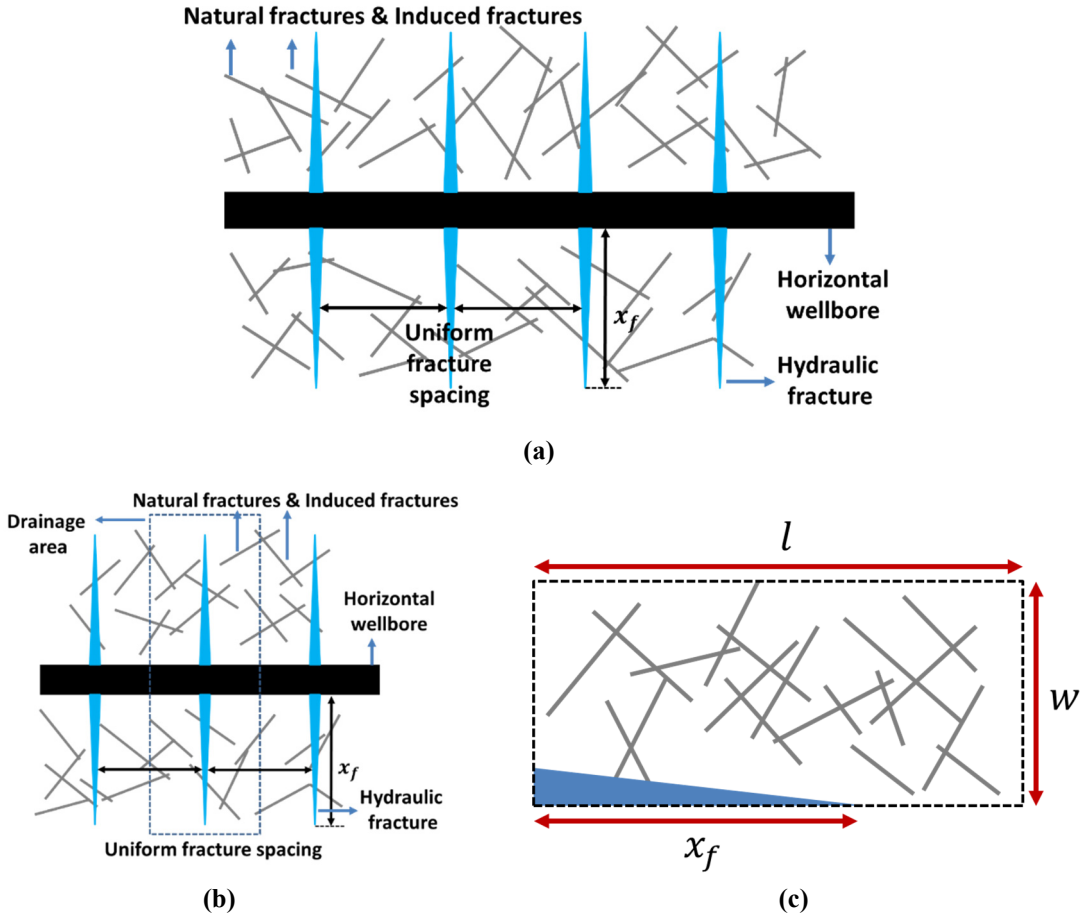

Figure 3.1 – Schematics of (a) the fracture system & matrix, (b) the drainage area of an individual hydraulic fracture, and (c) the problem domain

Grechishnikova, 2017), for the purpose of this work we only take into account the macroscopic fractures (larger than $\sim 10^{-3}$ft). The fracture system consists of natural fracture sets, induced fractures and hydraulic fractures, all of which are interconnected to form a "fracture network" and capable of directly contributing to the flow into the wellbore. The natural fractures and induced fractures have the same formation properties: constant fracture permeability k_f, constant fracture porosity ϕ_f and constant aperture b. The hydraulic fractures are assumed to be of planar shape and have infinite conductivity. All the fractures have the same height as the formation thickness and are perpendicular to the horizontal bedding plane.

- The matrix is isotropic and homogeneous. This means that we neglect the small-scale fractures, and isolated fractures that have no connections to the interconnected fracture system as mentioned previously. The matrix has constant parameters: permeability k_m, porosity ϕ_m.
- Based on the nature of the unconventional reservoir that the fractures have pretty much higher permeability than matrix, it is assumed that the fluid

initially located in fractures only transports in the fracture system, and that the fluid initially located in the matrix firstly transports slowly through the matrix into the fracture system, after which it continues transporting only in the fracture system.

4. Based on the above assumptions, the flow in both domains is dictated by Darcy's law. Due to the pretty small size of aperture b compared to H we can assume laminar flow in the fracture system.

The hydraulic fractures are of uniform spacings, as shown in **Fig. 3.1 (b)**, so that each one is located in the center of its own drainage volume. By the geometric and physical symmetry, we regard the symmetrical element, a quarter of the drainage area for one hydraulic fracture, as our problem domain. As shown in **Fig. 3.1 (c)**, it has the length l, the width w, and the hydraulic fracture half-length x_f. Furthermore, the drainage area's outer boundaries are of no flow conditions, except for the part of infinite-conductivity fracture that is at constant pressure condition. For simplicity, we also neglect the flow in fractures across the drainage area boundary, if any.

By the above assumptions, the problem has been reduced to a 2-D single phase flow problem with the gravity being neglected. In either the homogeneous and isotropic domains, the matrix or the fracture system, the pressure distribution of slightly compressible flow can be mathematically modeled by the diffusivity equation, as Eq. (3.1) shows.

$$\frac{k_i}{\phi_i c_{ti} \mu} \Delta P_i = \frac{\partial P_i}{\partial t} \quad \text{.....(3.1)}$$

where $i = f, m$ and P_i is the pressure in domain i.

As a regular step, we wrap up into a single parameter the parameters on the left-hand-side before the Laplace operator. In Eq. (3.2), the parameter η_i is usually called the hydraulic diffusivity coefficient with the unit of $\text{length}^2/\text{time}$. Obviously, η_i is also a constant parameter in either the fracture system or the matrix. Substituting η_i back into Eq. (3.1) gives us a result which has the form of the equation dictating the general diffusion process (Eq. (3.4)), as shown in Eq. (3.3).

$$\eta_i = \frac{k_i}{\phi_i c_{ti} \mu} \quad (3.2)$$

$$\eta_i \Delta P_i = \frac{\partial P_i}{\partial t} \quad (3.3)$$

$$D \Delta C = \frac{\partial C}{\partial t} \quad (3.4)$$

Since D and η_i have the same dimension and the above two equations share the same form, there should be some physical analogy between pressure P_i and concentration C. With the assumption of slightly compressible fluid, the relation between pressure and density is linear, which means that pressure is equivalent to density in this case. Thus, pressure can be taken as some type of "density" or "concentration" for the single-phase fluid particles. From this perspective, Eq. (3.3) describes the aggregate behavior of the huge number of fluid particles in the porous media. By the theory of normal diffusion (Vlahos, 2008), which has been investigated since Einstein (1905)'s work on Brownian motion, the MSD, $\langle r^2 \rangle$, of the fluid particles is related to the time t by the diffusion coefficient D, as shown in Eq. (3.5). Eq. (3.3) can be derived from Eq. (3.5) (Vlahos, 2008), which means Eq. (3.3) is only valid for the aggregate behavior of those particles whose relationship of MSD vs. t is dictated by Eq. (3.5). That is, the validity for using Eq. (3.3) for a flow on the domain of interest in a specified scale depends on the validity of Eq. (3.5) describing the fluid particles in the same domain.

$$\langle r^2 \rangle \sim t \quad (3.5)$$

According to the above analysis, the reason why Eq. (3.3) can be successfully applied to the conventional reservoir's flow in multiple scales is that the fluid particles moves approximately in a Euclidean space due to the relatively homogeneous porous media, and that the average motion of the particles is dictated by Eq. (3.5). And for the same reason, Eq. (3.3) is also valid for the flow

in some tight sands with very low permeability but no well-developed fracture networks, except for a quite small η_i.

However, this isn't the case for the unconventional reservoirs with complex fracture systems. By the assumptions, all the produced fluid comes directly from the fracture system. And the high production rate during the early period (several months to years) after the beginning of production all comes from the fluid initially located in the fracture system because of the ultra-low matrix permeability. Thus, the major fluid flow and the production in this period can be readily modeled by solving Eq. (3.3) with the fracture parameters on the fracture domain, only if the span, shape, and other details of the fracture network are available, which is basically impossible by the current state-of-the-art technology. Consequently, we are forced to model the fracture flow based on the composite domain consisting of both matrix and fractures, since we have much more information and confidence to determine the drainage area (like what has been done in Section 2). Using the perspective of diffusing fluid particles, it is obvious that the particles only move in the fracture network instead of the full Euclidean space. Therefore, although the particle motion is described by Eq. (3.5) using the 1-D coordinate attached to the fracture, this relationship of MSD vs. t needs to be transferred to the 2-D coordinate attached to the whole drainage area. This is illustrated in **Fig. 3.2**. In this figure, a particle diffuses from point 1 to point 2 along the yellow path in the fracture. Its displacement with respect to the fracture coordinate is $|r_1| + |r_2| + |r_3| + |r_4|$, while that with respect to the drainage area coordinate is $|d|$, which is much smaller than the previous one. Apparently, this transferring should take into account the topologic characteristics of the fracture network, which means the transferred relation of MSD vs. t might not follow the linear relation as Eq. (3.5). According to some prior works (Berkowitz and Scher, 2001; Vlahos, 2008), it can be intuitively proposed that the modified relation should have the power law form as

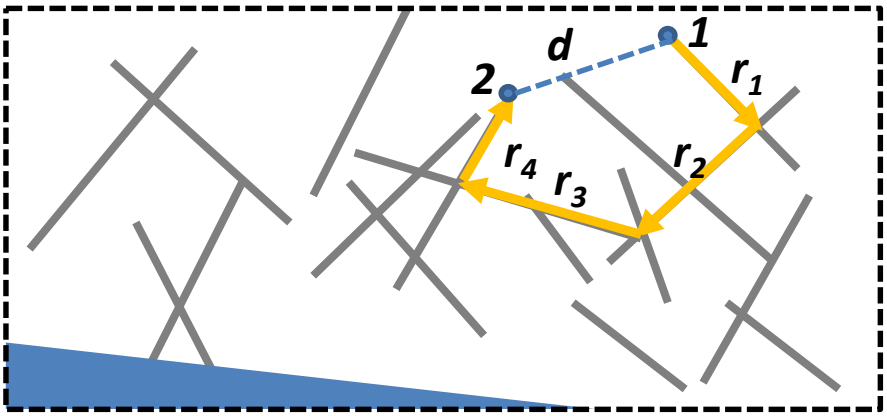

Figure 3.2 – Schematic of the displacements with respect to different coordinates

shown in Eq. (3.6).

$$\langle r^2 \rangle \sim t^{\alpha} \quad (3.6)$$

If α, the diffusivity exponent, doesn't keep unit, the corresponding process is named as the anomalous diffusion. To demonstrate this phenomenon in highly fractured formation is the main task of the rest of this paper. As a consequence, due to the possible invalidity of Eq. (3.5) when α isn't the unity anymore, using Eq. (3.3) to model the flow and production *based on the whole drainage area* may be only a very rough simplification and fails to capture some features of the flow through the unconventional reservoir with complex fracture networks.

3.3. Simulation Model for Particle Diffusing on a Complex Network Using Markov Chain

3.3.1. Continuous Time Markov Chain

To simulate the fluid particle's motion in the fracture network, which is embedded in a 2-D Euclidean space, we take advantage of its normal diffusion. As has been studied in many publications (Itô and McKean, 1996; Rogers and Willianms, 1994), the fluid particles under normal diffusion can be mathematically modeled to have Markov property. In more details, denoting the location of a single particle at time t as $X(t)$, we have a continuous-time stochastic

process $\{X(t): t \geq 0\}$, which is considered to have Markov property only if the conditional probability satisfies Eq. (3.7) (Itô and McKean, 1996; Rogers and Willianms, 1994).

$$p[X(t) = j \mid X(s) = i, X(t_{n-1}) = i_{n-1}, X(t_{n-2}) = i_{n-2}, \cdots, X(t_1) = i_1] = p[X(t) = j \mid X(s) = i] \quad \text{.....(3.7)}$$

where $0 \leq t_1 \leq t_2 \leq \cdots \leq t_{n-2} \leq t_{n-1} \leq s \leq t$ is any non-decreasing sequence of $n+1$ times and $i_1, i_2, \cdots, i_{n-2}, i_{n-1}, i, j$ are any $n+1$ states in the state space of Markov chain. It means that each step of stochastic "jump" only depends on the current states, and the particle acts as it "forgets" the states it has previously experienced.

Since in this work the particles only move in the fracture network, the state space of the Markov chain only contains the points belonging to the fractures. For simplicity and the limitedness of our computational resources, we only take the endpoints and the intersection points of the fracture segments as the states in the state space of Markov chain, as illustrated in **Fig. 3.3**. When a particle occupies a state at a given time, it will "jump" after some "waiting time" at the next step to one of the neighbor states. The target of the "jumping" is chosen randomly according to the probability distribution determined by the diffusivity coefficient, the length, and the aperture of all the fracture segments directly connected to the current state, as shown in Eq. (3.8).

$$p[X(t) = j \mid X(s) = i] = \begin{cases} \dfrac{\eta_i b_i L_i^{-1}}{\sum_{k \in N_i} \eta_k b_k L_k^{-1}}, & j \neq i \\ 0, & j = i \end{cases} \quad \text{.....(3.8)}$$

where $p[X(t) = j \mid X(s) = i]$ is the probability for jumping from the current state i to the neighbor state j, N_i is the set of the neighbor states of i, and η_k, b_k and L_k are respectively the diffusivity coefficient, aperture and length of the fracture segment connecting i and one of its neighbor state k. Only if this kind of probability distribution is applied will the resulting expectation of the stochastic process hold consistency with the solution of the diffusivity equation.

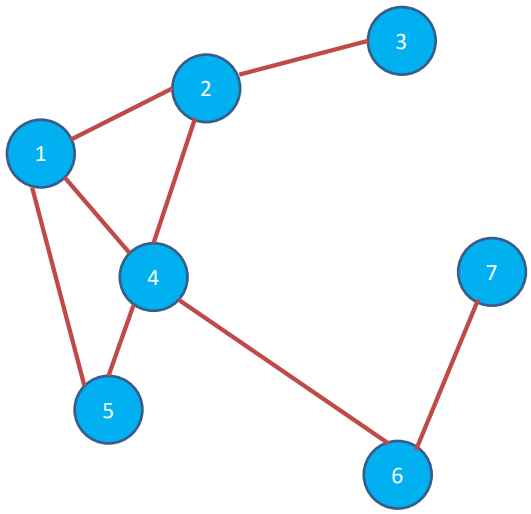

Figure 3.3 – Schematic of endpoints and intersection points as states

However, the above probability distribution only applies to the states corresponding to regular points, not to those points located on the hydraulic fracture. As stated in the assumptions, the hydraulic fracture has infinite conductivity, which is translated into total absorbing states for the particle stochastic motion. It means that whenever a particle jumps into these states, it will stay there forever and won't jump to other states again. Apparently, the probability distribution of these absorbing states is

$$p[X(t) = j \mid X(s) = i] = \begin{cases} 0, & j \neq i \\ 1, & j = i \end{cases} \quad \text{.....(3.9)}$$

This definition of absorbing state is consistent with the constant pressure condition on the hydraulic fracture boundary. No matter what type the state is, its probability distribution satisfies the normalization condition that

$$\sum_{j \in N_i} p[X(t) = j \mid X(s) = i] = 1. \quad \text{.....(3.10)}$$

Both definitions in Eq. (3.8) and Eq. (3.9) use only the information of current state i, which manifests this process as a Markov chain. Besides the spatial increment, the temporal increment (the "waiting time") should also keep the Markov property, which means that only the

"memoryless" Poisson distribution should be applied to the temporal increment. While the Markov property of time will later be considered implicitly by the Kolmogorov forward equation, we state the temporal increment's Poisson distribution here for completeness.

3.3.2. Implementation Using a Graph Object

By the above concepts, we have implicitly described the fracture network as a graph object, which has the endpoints and the intersection points of the fracture segments as the nodes and the fracture segments between these nodes as edges. This graph is certainly related to the corresponding fracture network, so the graph is classified to be a geometric graph with Euclidean coordinates as one of the node attributes and length as one of the edge attributes. Besides, another critical attribute for each edge is the weight, which defines the transition rate of continuous time Markov chain (CTMC) and is related to the probability distribution previously discussed. The edge weight is naturally defined as $\eta b L^{-1}$. Briefly speaking, introducing the graph definition and terminologies explicitly will make our simulation easier to be implemented by programming.

So far, we have reduced our problem to a feasible task that a CTMC is to be simulated on a geometric graph object, whose set of nodes is taken as the finite state space, and the weight ($\eta b L^{-1}$) of the edge between node i and j as the major part of transition rate q_{ij}. By the Kolmogorov forward equation (Itô and McKean, 1996), for the node i as the initial node, we have

$$\frac{dp_j(t)}{dt} = \sum_{k \in S} p_k(t) q_{kj}. \quad (3.11)$$

In Eq. (3.11), $p_j(t) = p[X(t) = j \mid X(0) = i]$ is the probability for the particle occurring at node j at time t after it starts moving from the initial node i. q_{kj} is the transition rate between node k and node j. And S is the set of all the nodes in the graph. The entry of the transition rate matrix $\{q_{ij}\}$ for a node i not located on the hydraulic fracture is as Eq. (3.12) shows.

$$q_{ij} = \begin{cases} \eta_{ij} b_{ij} L_{ij}^{-1} / a^2 & j \neq i \text{ and } j \in N_i \\ -\dfrac{\sum_{j \in N_i} \eta_{ij} b_{ij} L_{ij}^{-1}}{a^2} & j = i \\ 0 & Otherwise \end{cases} \quad \text{.....(3.12)}$$

where the subscript ij represents the property of the fracture between node i and j, and a is only a characteristic length of the system for making the unit consistent. Other denotations in Eq. (3.12) have the same meaning as the corresponding ones in Eq. (3.8). On the other hands, the corresponding entry of the transition rate matrix $\{q_{ij}\}$ for a node i located on the hydraulic fracture is as Eq. (3.13) shows.

$$q_{ij} = \begin{cases} 1, & j = i \\ 0, & Otherwise \end{cases} \text{.....(3.13)}$$

Writing the ordinary differential equation (ODE) of Eq. (3.11) into the matrix form, we have

$$\frac{d\vec{P}(t)}{dt} = \vec{P}(t)\boldsymbol{Q} \text{.....(3.14)}$$

where $\vec{P}(t)$ is a stochastic vector of the existence probability for a particle initially starting from a specified node i, and $\boldsymbol{Q} = \{q_{ij}\}$ is the transition rate matrix. From graph theory, we know ("Transition rate matrix", 2019) that for a well-defined weighted graph, each entry of $\boldsymbol{Q}$ is the opposite of the corresponding entry in the graph's Laplacian matrix, which can be readily obtained. With the help of matrix exponential, the solution of Eq. (3.14) can be symbolically expressed as

$$\vec{P}(t) = \vec{P}(0)\exp(\boldsymbol{Q}t) \text{.....(3.15)}$$

where $\vec{P}(0)$ is the particle's initial distribution among all nodes.

If we temporarily assume that the matrix exponential in Eq. (3.15) can be successfully evaluated, we can obtain the probabilities for a particle occurring at each node at any time t after

it starts to move from node i. The initial stochastic vector for this case is given by Eq. (3.16). 1 is the ith entry of this vector.

$$\vec{P}(0) = [0 \quad \cdots \quad 0 \quad 1 \quad 0 \quad \cdots \quad 0] \tag{3.16}$$

These probabilities are equivalent to the particle distribution at time t when massive particles all start from i to undertake the stochastic process. After attaining the evolution of probability, a vector of distance square $\vec{v}_{ds}$, which is defined in Eq. (3.17), is incorporated using the node attribute of coordinates to get the MSD of the diffusing particle in the embedding Euclidean plane.

$$\vec{v}_{ds} = \left[d_{1,i}^2 \quad \cdots \quad d_{i-1,i}^2 \quad 0 \quad d_{i+1,i}^2 \quad \cdots \quad d_{n,i}^2\right] \tag{3.17}$$

where $d_{j,i}$ is the Euclidean distance between the node i and j, $d_{j,i} = \left[\left(x_i - x_j\right)^2 + \left(y_i - y_j\right)^2\right]^{1/2}$. Finally, the relation of MSD vs. t is calculated by taking the dot product between $\vec{P}(t)$ and $\vec{v}_{ds}$ as shown in Eq. (3.18).

$$\langle r^2 \rangle(t) = \vec{P}(t) \cdot \vec{v}_{ds} \tag{3.18}$$

3.3.3. Details of the Simulation Process

Theoretically, we have provided the solution to our problem, but in practice the stable evaluation of the matrix exponential is problematic. Since usually the longest fractures ($\sim 10^2$ft) are several orders of magnitude longer than the shortest ones ($\sim 10^{-3}$ft), the value range of the non-zero entries in the matrix $\boldsymbol{Q}$ is quite large, which makes $\boldsymbol{Q}$ a very stiff matrix. Some common methods (Padé approximation, Krylov space methods (Moler and Van Loan, 2003)) and packages (expokit (Sidje, 1998), MatrixExp in Mathematica (Wolfram Research, Inc., 2018)) for evaluating matrix exponential do not work very well for the cases encountered in this paper. So, we had to resort to numerical methods solving the ODE Eq. (3.14) directly (Basically, any "stiff" ODE solver

can be used). We have used Mathematica's NDSolve function (Wolfram Research, Inc., 2018), which integrates many "stiff" ODE solvers into its options, to solve Eq. (3.14) numerically for getting $\vec{P}(t)$.

The flowchart of the whole simulation process is shown in **Fig. 3.4**. Several software and packages are applied to do the pre-processing before the simulation is conducted. The 2-D discrete fracture network (DFN) is created using FRACGEN, which is a module for generating fracture networks stochastically in a fractured reservoir modeling software, FRACGEN/NFLOW (McKoy and Sams, 1997). The DFN is processed by an open-source python package, lsi (splichte, 2013) based on the Bentley-Ottmann algorithm. And the graph object is created by a module, networkx (Hagberg et al., 2008), which is designed for the problems of graph theory.

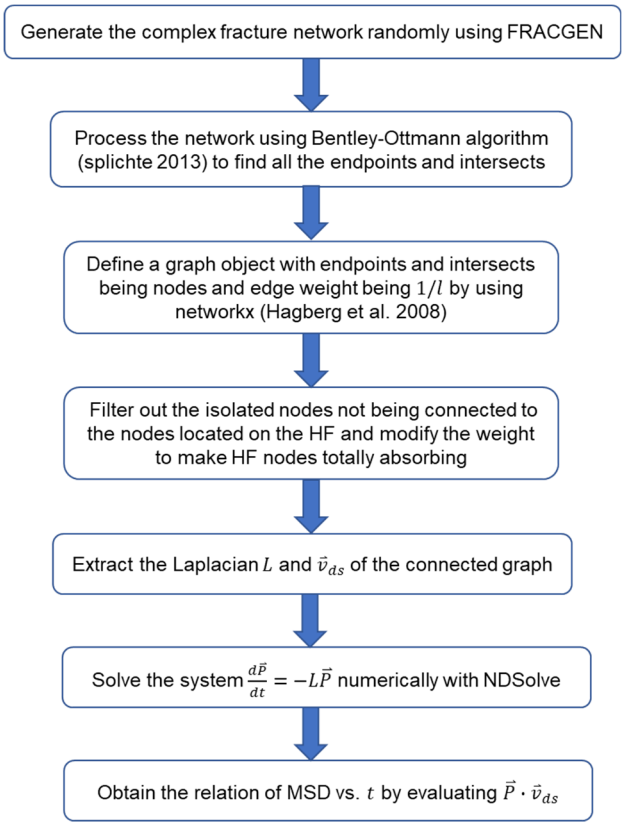

Figure 3.4 – Flowchart of simulating the diffusion on the complex fracture network to get the relation of MSD vs. t

3.4. Simulation Results

Using the described model in Section 3.3, we conduct the simulation to the flow in the fracture networks with different scenarios: Case 0 uses the regular meshes with uniform grid size in both x and y axis; Case 1 uses the fracture network with two orthogonal sets which are randomly generated by FRACGEN; Case 2 also uses the fracture network with two orthogonal sets, but the overall network rotates 45°; Case 3 uses the fracture network with two sets having 40° between them, and all the upper domain ; Case 4 uses a very complex fracture network, which has 4 sets of fractures and is the sample, "MWX4f", in FRACGEN. The domain of the first 4 cases all have the dimensions of $500\text{ ft} \times 250\text{ ft}$ coming from the well spacing 1000 ft and fracture spacing 500 ft. And all cases have a hydraulic fracture half-length of 400 ft ($I_x = 0.8$) which is represented by the blue line on the boundary. Since each case contains hundreds and even thousands of nodes, the comprehensive investigation is impossible without the help of some statistical methods, which is out of the scope of this paper. So, we only select 10 nodes randomly in each case to do the simulation on them and to show the relation of MSD vs. t. The plots and parameters of the fracture networks, and the results are shown below.

3.4.1. Case 0

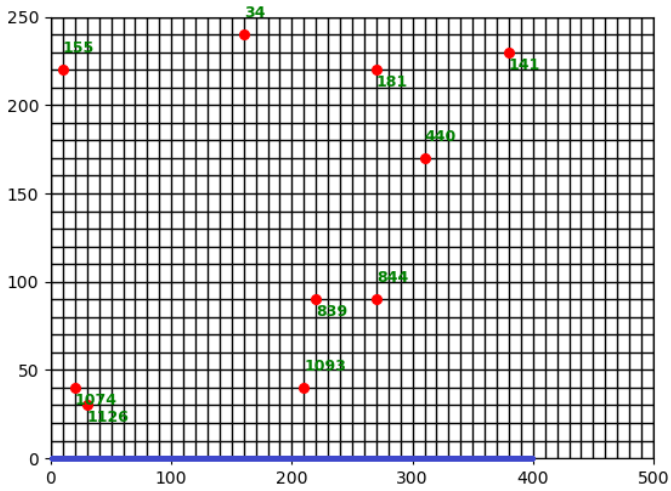

Figure 3.5 – Plot of the fracture network and 10 sampled nodes in Case 0

Table 3.1 – Statistics of the fracture network in Case 0 (ft)

Max	Min	Mean	Median	Number of fractures	Number of nodes
10	10	10	10	2525	1285

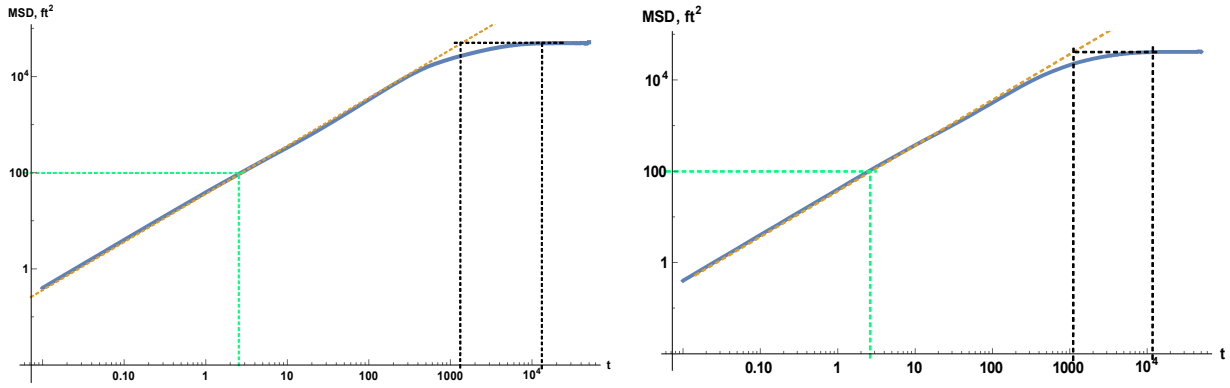

Node 34 Node 141

Figure 3.6 – Log-log plots of MSD vs. time for 10 sampled nodes in Case 0

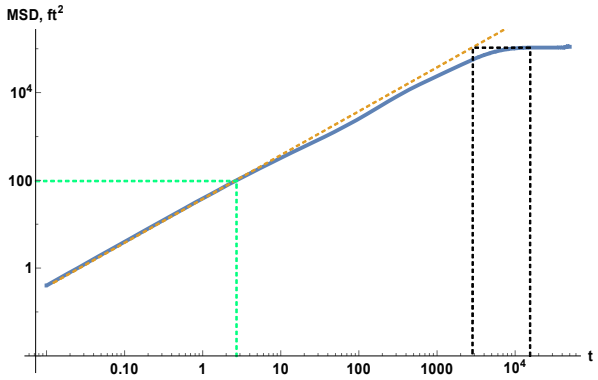

Node 155

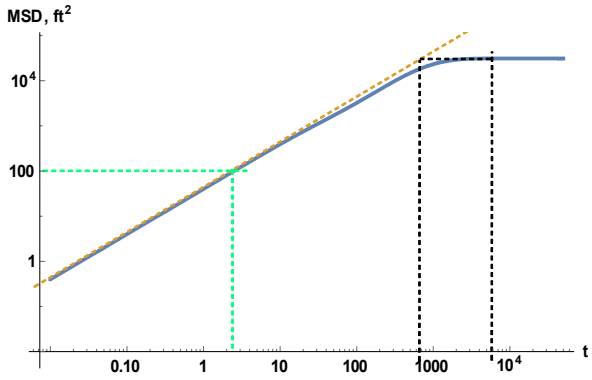

Node 181

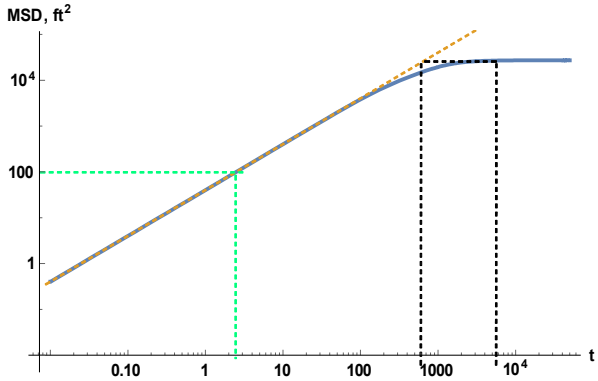

Node 440

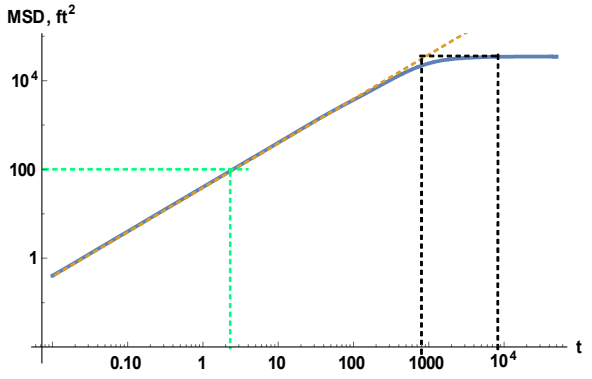

Node 839

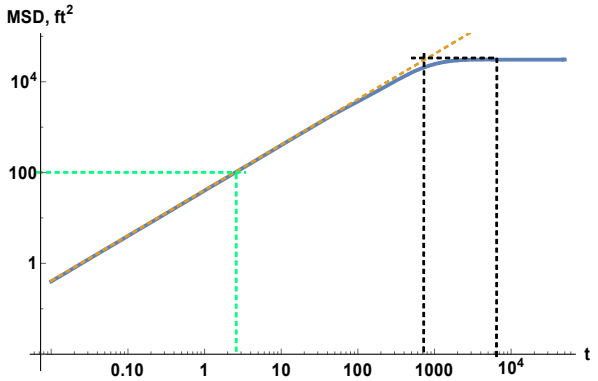

Node 844

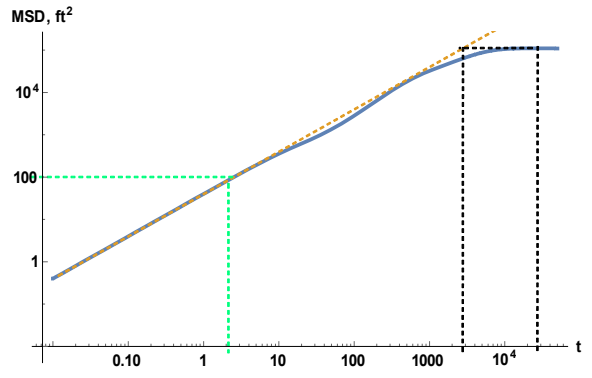

Node 1074

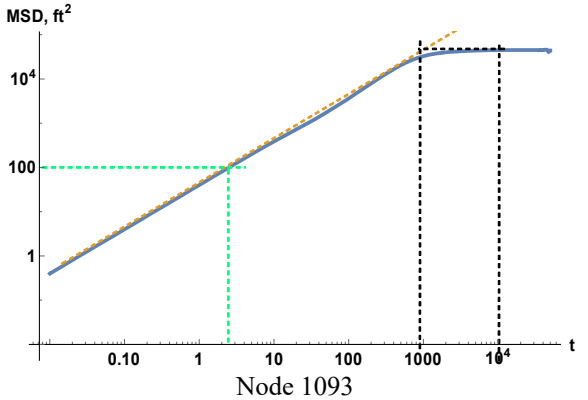

Node 1093

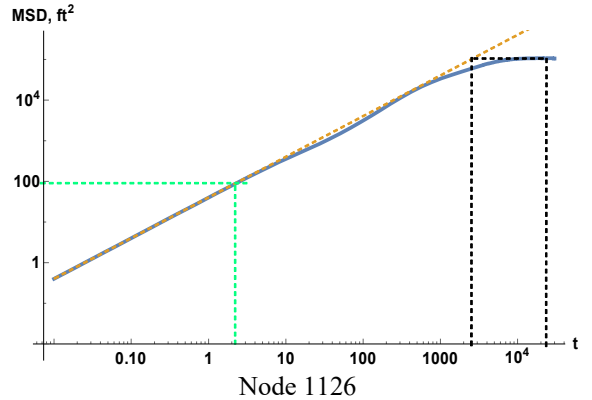

Node 1126

Figure 3.6 Continued

3.4.2. Case 1

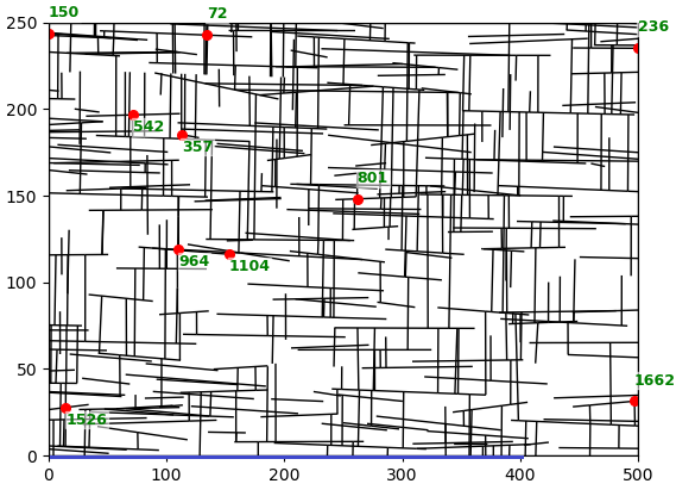

Figure 3.7 – Plot of the fracture network and 10 sampled nodes in Case 1

Table 3.2 – Statistics for the fracture network in Case 1 (ft)

Max	Min	Mean	Median	Number of fractures	Number of nodes
92.4	1.7E-3	11.0	7.6	1969	1753

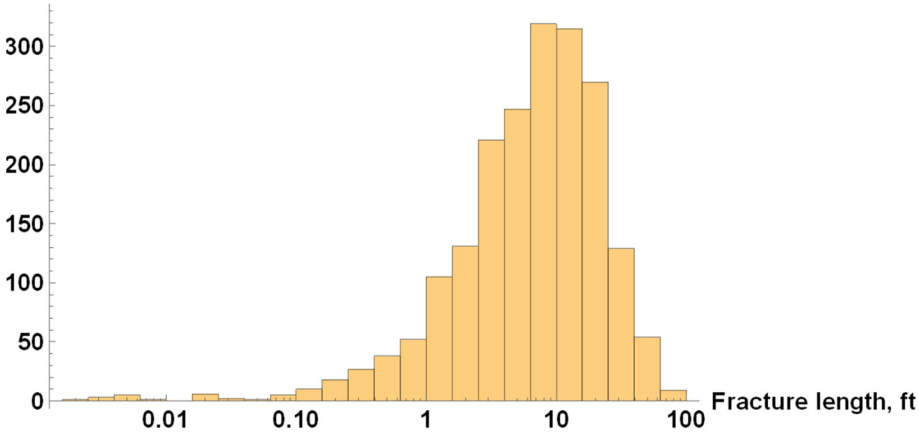

Figure 3.8 – Histogram of the fracture length in Case 1

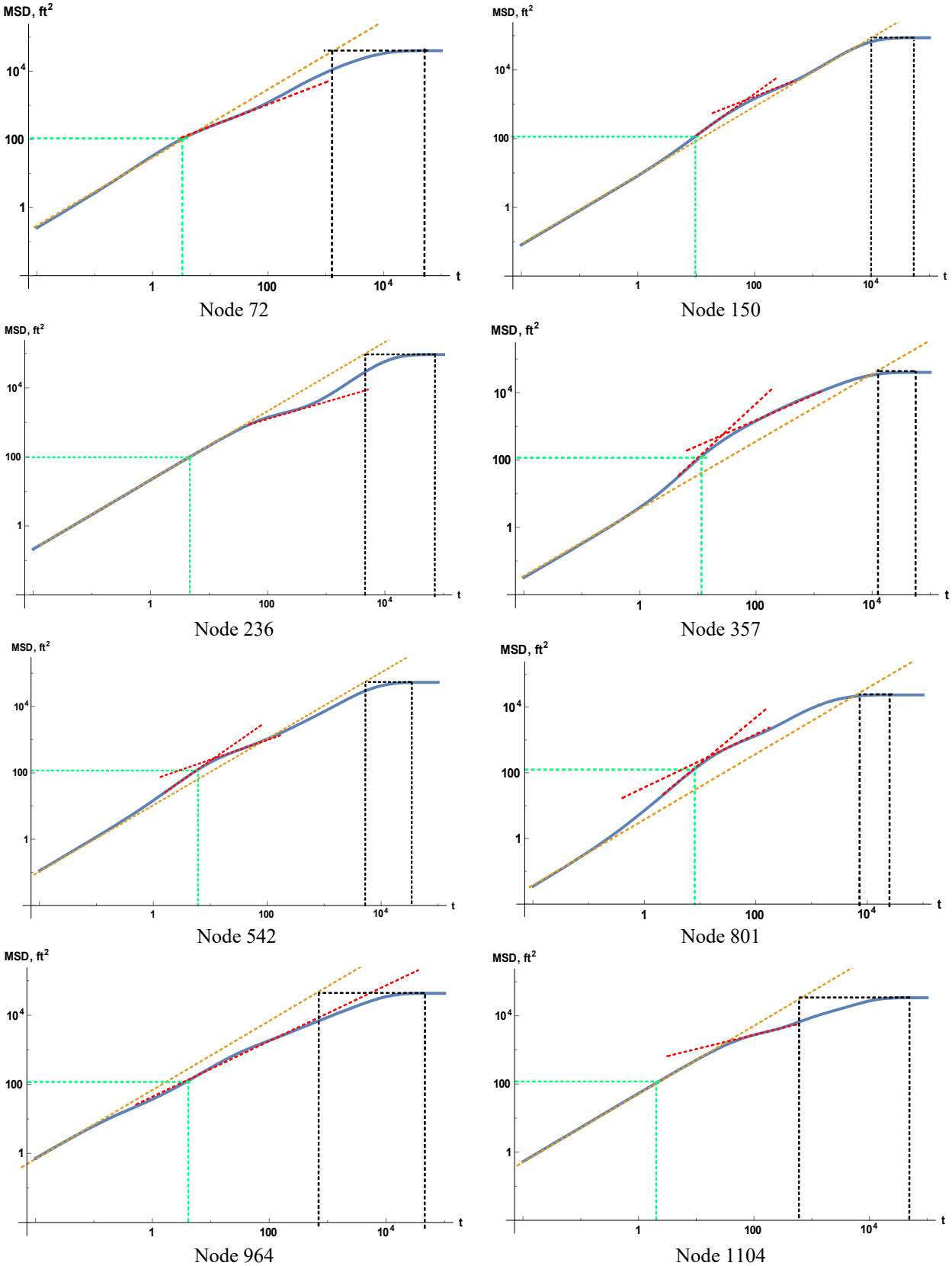

Figure 3.9 – Log-log plots of MSD vs. time for 10 sampled nodes in Case 1

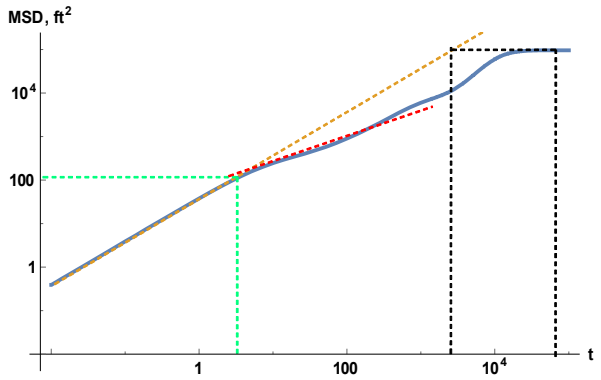

Node 1526

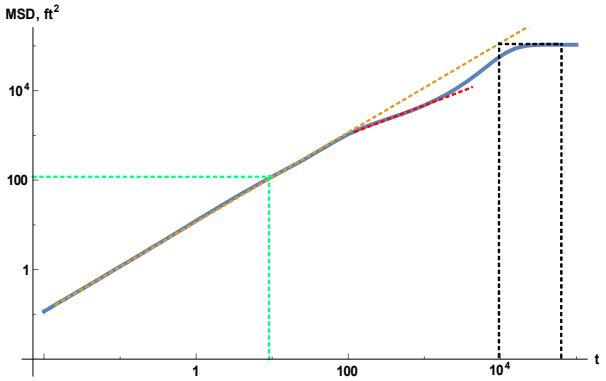

Node 1662

Figure 3.9 Continued

3.4.3. Case 2

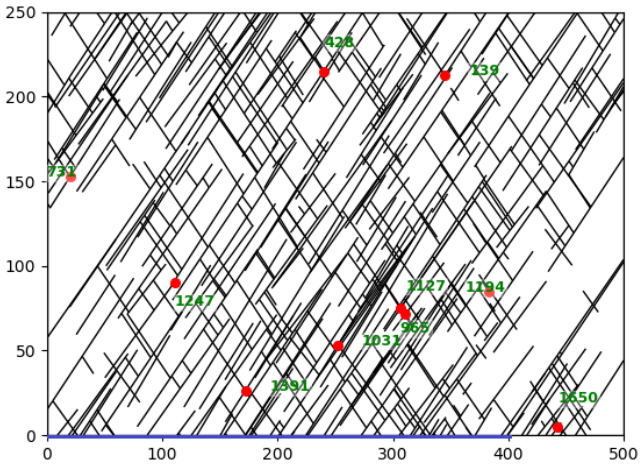

Figure 3.10 – Plot of the fracture network and 10 sampled nodes in Case 2

Table 3.3 – Statistics for the fracture network in Case 2 (ft)

Max	Min	Mean	Median	Number of fractures	Number of nodes
83.8	1.0E-3	10.5	7.5	1940	1690

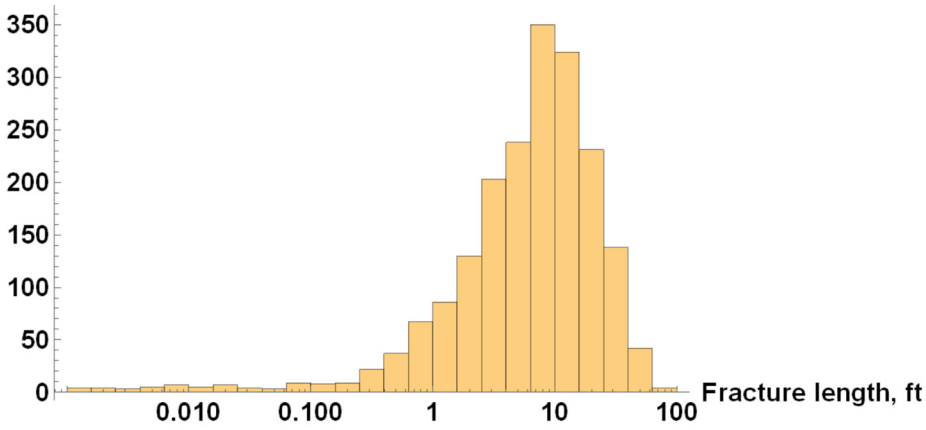

Figure 3.11 – Histogram of the fracture length in Case 2

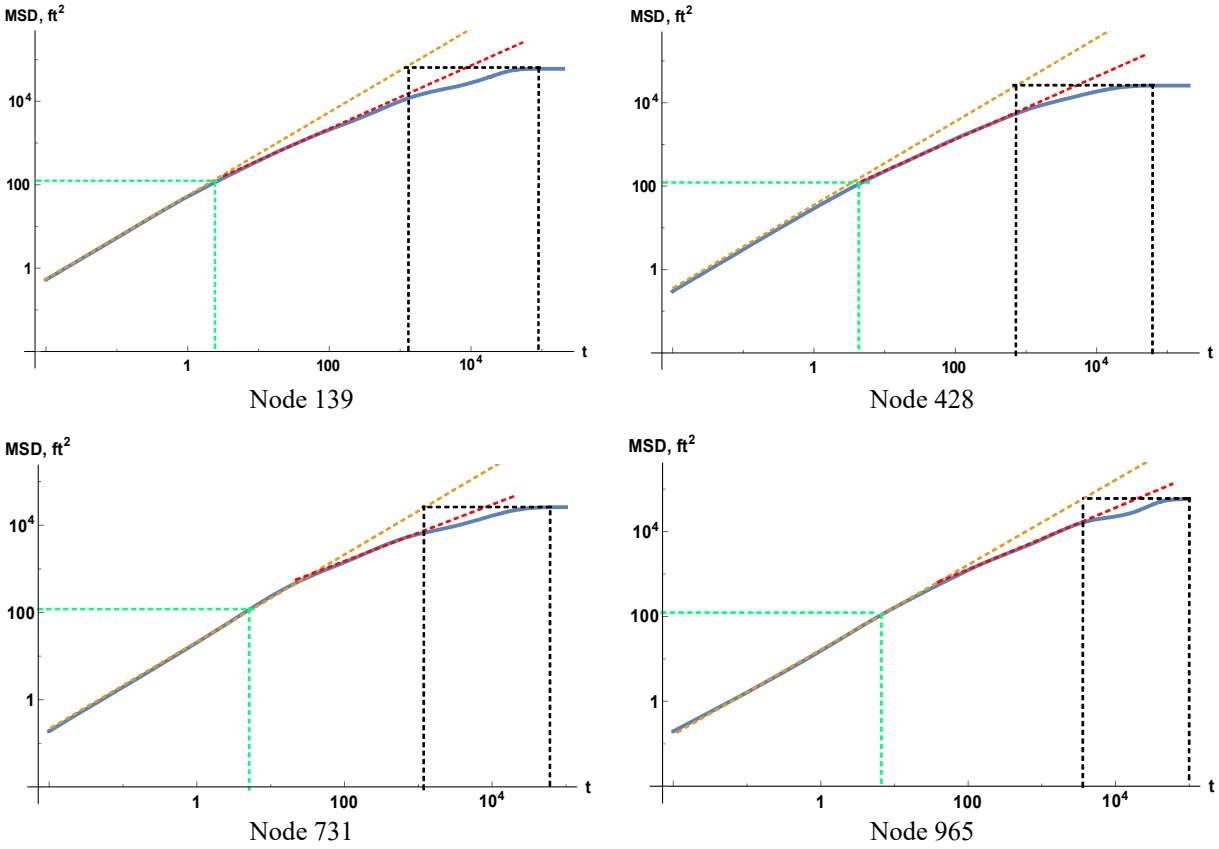

Figure 3.12 – Log-log plots of MSD vs. time for 10 sampled nodes in Case 2

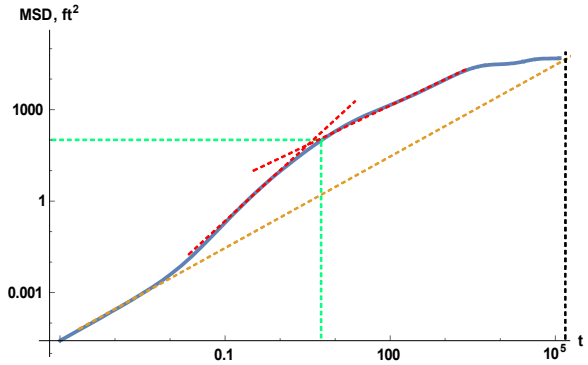

Node 1031

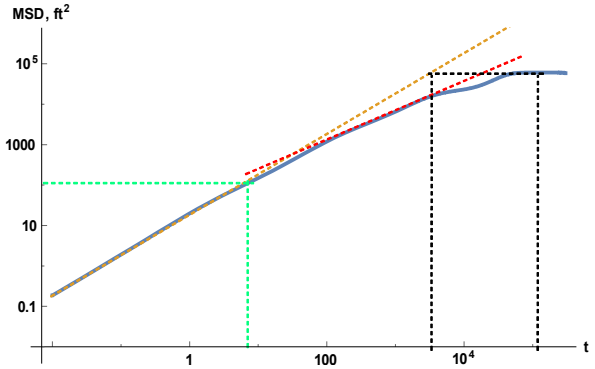

Node 1127

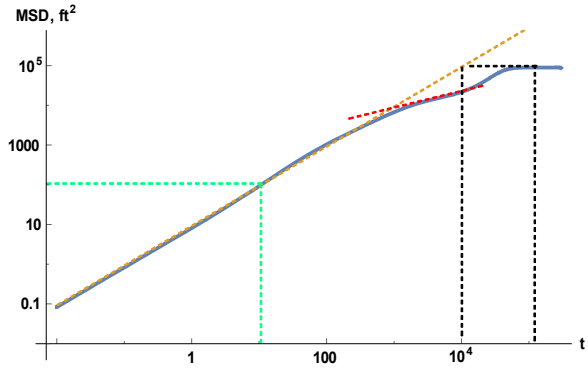

Node 1194

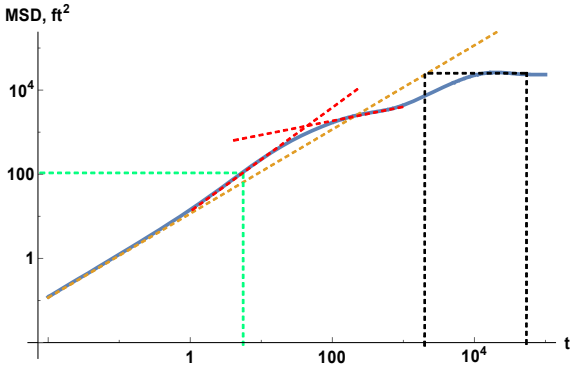

Node 1247

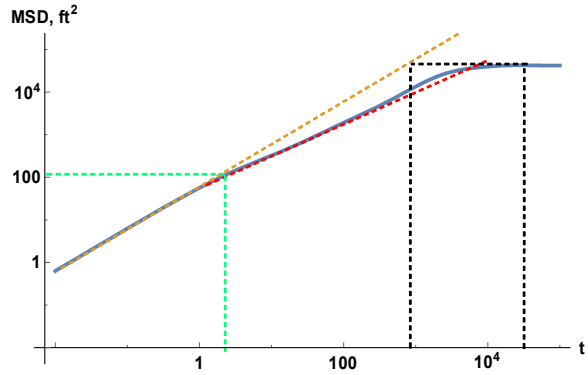

Node 1391

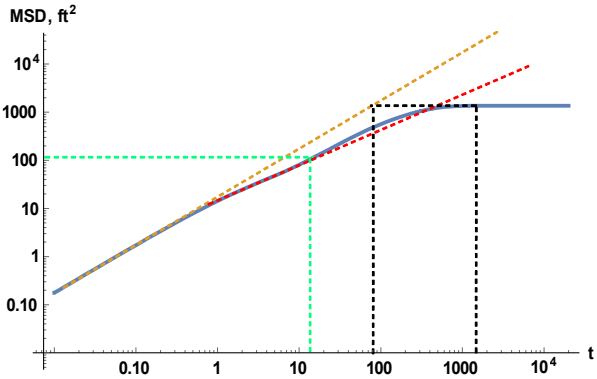

Node 1650

Figure 3.12 Continued

3.4.4. Case 3

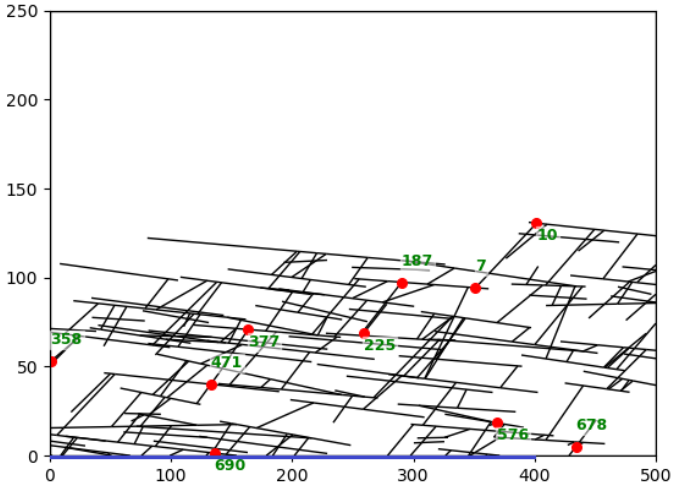

Figure 3.13 – Plot of the fracture network and 10 sampled nodes in Case 3

Table 3.4 – Statistics for the fracture network in Case 3 (ft)

Max	Min	Mean	Median	Number of fractures	Number of nodes
123.7	1.0E-3	13.1	8.5	753	698

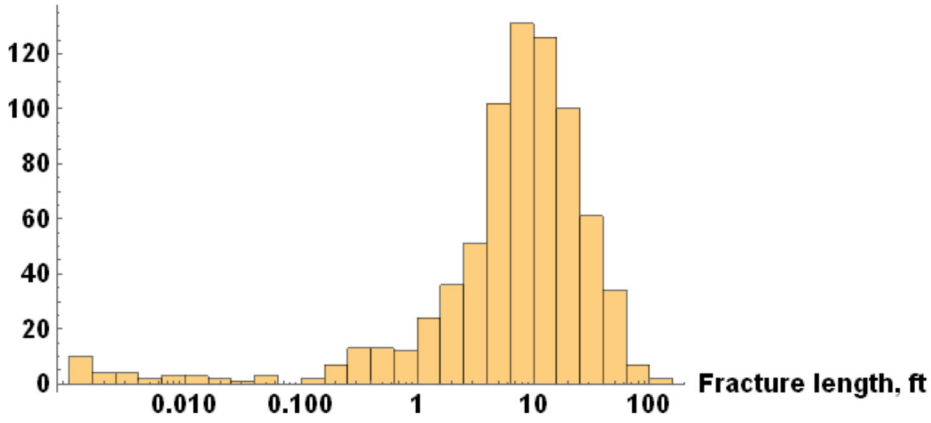

Figure 3.14 – Histogram of the fracture length in Case 3

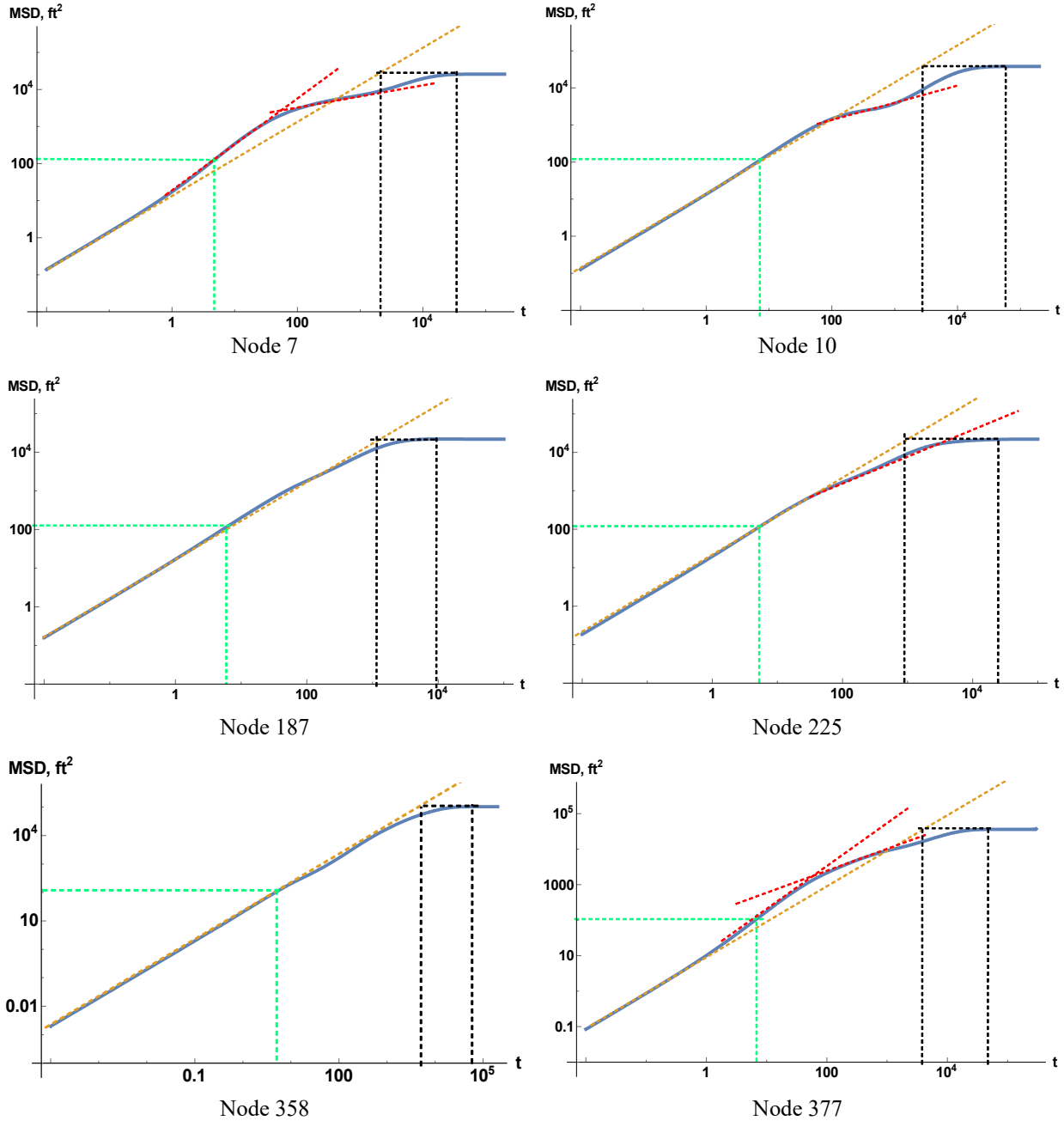

Figure 3.15 – Log-log plots of MSD vs. time for 10 sampled nodes in Case 3

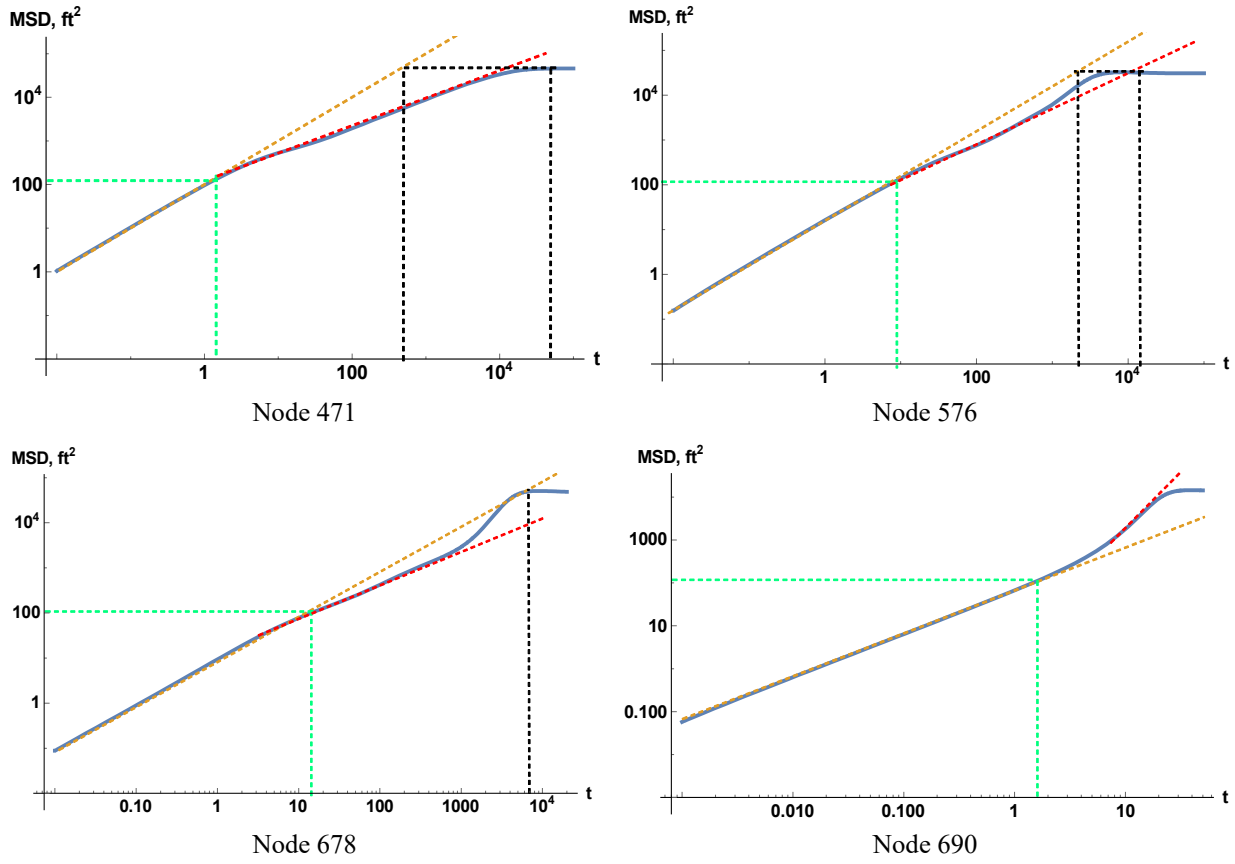

Figure 3.15 Continued

3.4.5. Case 4

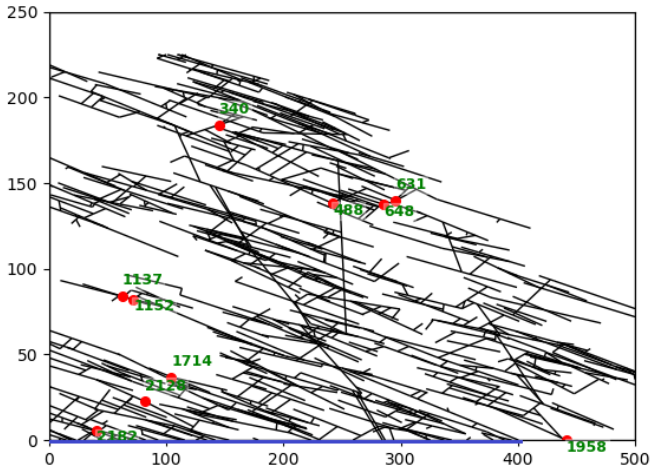

Figure 3.16 – Plot of the fracture network and 10 sampled nodes in Case 4

Table 3.5 – Statistics for the fracture network in Case 4 (ft)

Max	Min	Mean	Median	Number of fractures	Number of nodes
81.6	1.0E-3	10.0	5.9	2572	2214

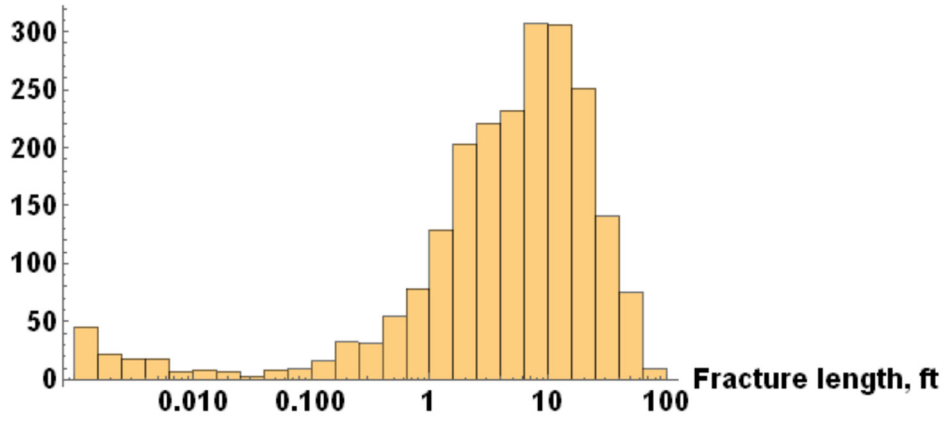

Figure 3.17 – Histogram of the fracture length in Case 4

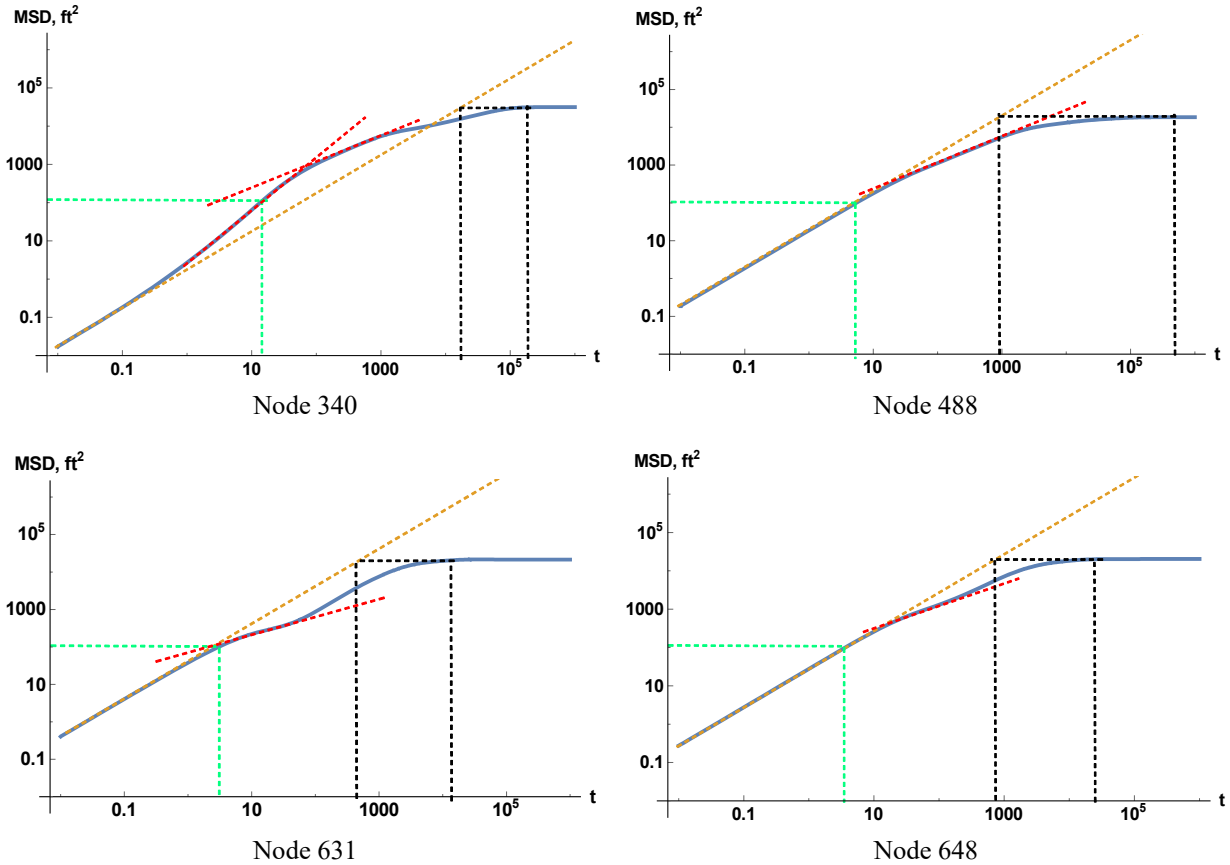

Figure 3.18 – log-log plots of MSD vs. time for 10 sampled nodes in Case 4

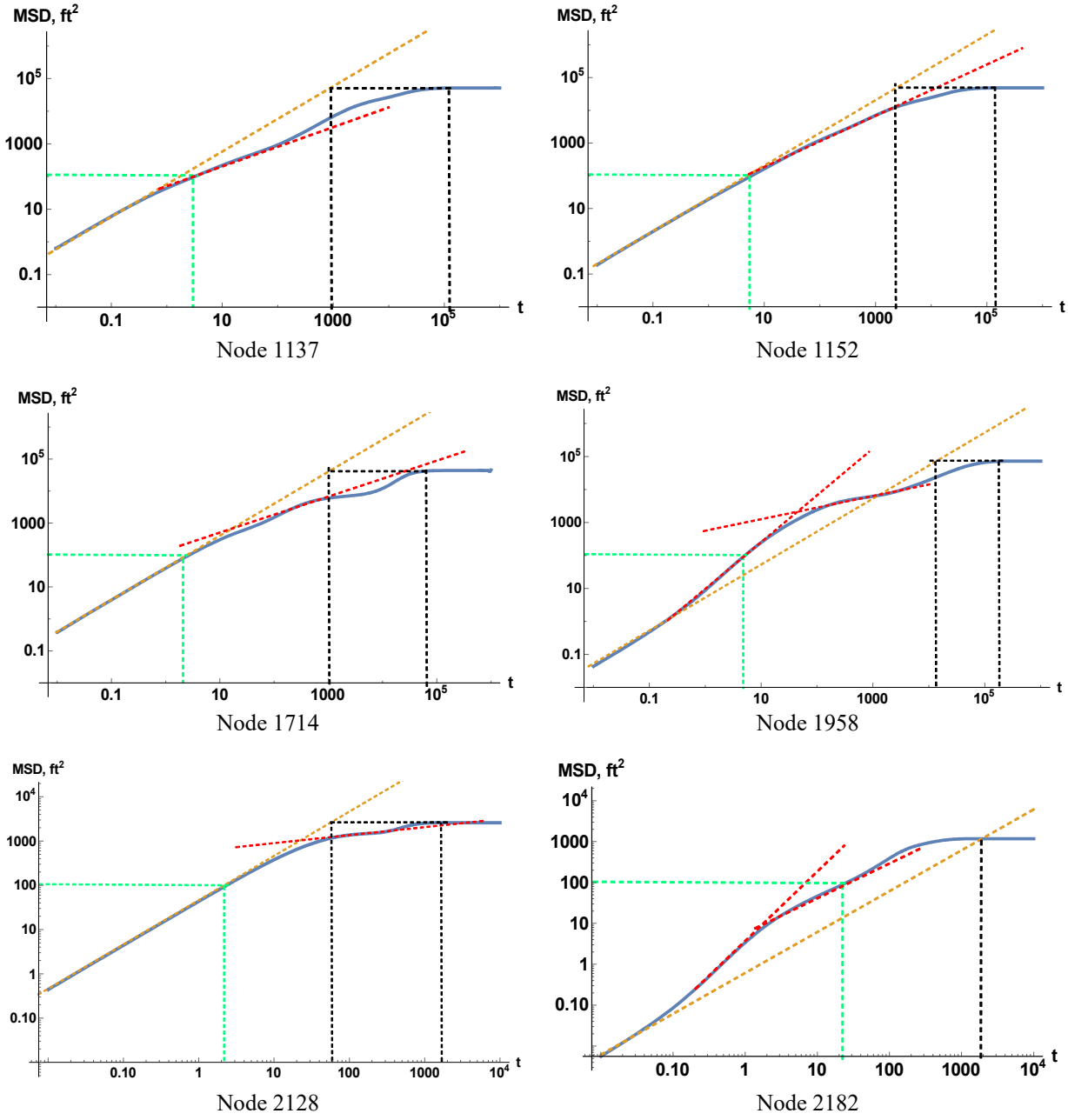

Figure 3.18 Continued

3.5. Relevant Discussions

When performing the above 5 case studies, for simplicity we assign the unit value to the diffusivity coefficient η, the aperture b, the fracture height H, and the characteristic length a and only use L^{-1} as the weight of the edges to construct the weighted graph's Laplacian matrix. Since

by our assumptions η, b and H are all constants, only a constant factor is needed to transfer the "time" t in the above plots to the real time, and the phenomena displayed aren't affected by the values of these parameters as far as they fall into the ranges guaranteeing the basic assumptions of this work.

In each of the above plots, besides the resulting relations of MSD vs. t presented in log-log plot, some dash lines with different colors are added to accommodate our analysis. Firstly, the most straight-forward one is the orange dash line, which has exactly the unit slope. Because Case 0 uses the regular grid to do the simulation, it is exactly the same thing as conducting numerical simulation to the homogeneous reservoirs with the most common spatial discretization. Thus, Case 0's result should be expected to show the nature of normal diffusion, as we have discussed in the previous section. It is exactly what we see in Case 0's plots (Fig. 3.6). The unit-slope orange line tracks firmly the resulting curve until deviation happens at the late time, when most of the particles have been "locked" in the absorbing nodes and MSD levels out. Some very small deviations occur at the early or intermediate time of some nodes, Node 155, Node1074, and Node 1126. This is due to the boundary effect of our finite graph on these nodes that are relatively close to the boundaries. Then, using Case 0 as a reference, we can immediately notice the discrepancies between other cases (Fig. 3.9, Fig. 3.12, Fig. 3.15, Fig. 3.18) and the normal diffusion. Although it seems that every node in Case 1 to Case 4 has its unique relation due the various local characteristics of the random created DFN, an obvious common phenomenon is that most of the curves deviate from the unit-slope orange in quite early time. Many of them are concave downwards displaying sub-diffusion, with some of them being concave upwards corresponding to super-diffusion.

The pair of green dash lines in each plot give us some sense of the scale of heterogeneity. Roughly speaking, the average fracture length in all 5 cases is about 10 ft, which corresponds to

$100\ \text{ft}^2$ for distance square. So, the green line pair shows the point where the MSD reaches a value that can be taken as characteristic size of heterogeneity. In Case 0 where the fracture segments are all 10 ft long, the slope keeps the unit value before and after $100\ \text{ft}^2$ MSD is reached due to the totally homogeneous fracture distribution. In other cases, most deviations happen within the range $10\ \text{ft}^2 \sim 10^3\ \text{ft}^2$ MSD, or $1\ \text{ft} \sim 10\ \text{ft}$, again roughly speaking. Moreover, we can see that each plot has the exact unit-slope section in the very early time when MSD is very small. Recall that only fractures longer than 10^{-3} ft are modeled in our work, and the number of fractures with length less than 10^{-1} ft is very small from all the four histograms. This means that the flow domain with its characteristic dimensions less than the average fracture length can be considered homogeneous to some extent. However, since only 10 nodes have been sampled out of thousands for each case, this point can only be taken as a reasonable suggestion. It should also be noted that this observation has been made while neglecting all other types of heterogeneity.

Although currently we cannot connect the fracture network characteristics (fracture density, fracture length distribution, fracture sets and clusters, and so on) to the properties of the diffusion due to the limited number of sampled nodes, we are capable to summarize some common diffusion patterns when looking at the results from various DFNs comprehensively. We have already noted the early time concave period. Similarly, the absorbing boundary domination at the late time is quite apparent. From the homogeneous Case 0, it is apparent that the absorbing boundary has the effect of greatly leveling out the curve. Bearing this in mind, we roughly draw the red straight dash line by hand to try to catch up its average deviating trends in early or intermediate times, and to try to rule out the absorbing boundary effects. So, these handmade trendlines are to some extent secant lines of the resulting curves. Consequently, the slope of these trendlines, which is exactly the diffusivity exponent α in Eq. (3.6), tells the types of anomalous diffusion in a given range of

scale: sub-diffusion for $\alpha < 1$ and super-diffusion for $\alpha > 1$. Generally speaking, there are two diffusion patterns for the flow in the fracture network, if the anomalous diffusion does happen. Type 1 is that after the early normal diffusion section, the curve directly concaves downward, and the flow begins to undertake sub-diffusion until the absorbing boundary dominates. The typical examples for this type are Node 964, 1104 in Case 1 (Fig. 3.9), Node 139, 428, 731, 965, 1650 in Case 2 (Fig. 3.12), Node 10, 471 in Case 3 (Fig. 3.15), and Node 1137, 1714, 2128 in Case4 (Fig. 3.18). Type 2 is characterized with a hump-like shape, which means the curve concaves upward to undertake super-diffusion firstly, and then becomes sub-diffusion in a larger MSD range. The typical examples for this type are Node 150, 357, 801 in Case 1 (Fig. 3.9), Node 1031 in Case 2 (Fig. 3.12), Node 7, 377 in Case 3 (Fig. 3.15), and Node 340, 1958, 2182 in Case 4 (Fig. 3.18). Only if the absorbing boundary begins to dominate, the undertaking diffusion is overwhelmingly affected and even totally hidden. These two patterns are kind of intuitive for a flow into hydraulic fractures (the absorbing nodes). We feel that more complex patterns can be expected in some highly heterogeneous formations, possibly alternating sub-diffusion and super-diffusion time periods.

Based on our prior discussions, we now try to answer our major question in this section: Is it valid enough to apply the classical diffusivity equation on the reservoir scale to model single-phase flow and to analyze the production? In our opinion, the diffusion pattern classification provides a perspective for the answer. Looking back again at Case 0, we make a tangential line (the horizontal black dash line) from the final plateau of the curve, and the tangential point and the intersection point with the unite-slope trendline both correspond to a time (the vertical black dash lines). Not so surprisingly, we find that in the normal diffusion case, the differences between these two times for different nodes are always around 1 log cycle. So, this can serve as a standard to tell

the validity of the averaged model (or homogenization) with the classical diffusivity equation. The type 1 pattern, when only sub-diffusion happens, obviously enlarges this time difference to around $1\,1/2$ or even 2 log cycles, and hence disproves the validity. On the other hand, the super-diffusion and sub-diffusion in type 2 pattern counteract with each other to some extent and can lead to the time difference around 1 log cycle, such as Node 150 in Case 1 (Fig. 3.9), Node 7, Node 377 in Case 3 (Fig. 3.15), and Node 340 in Case 4 (Fig. 3.18). So, if both type of nodes exist in a situation, we should determine or estimate which type dominates. It would require massive simulation conducted, or some advanced statistical tool employed. However, type 2 pattern can also lead to confusion by substantially shortening the time difference, which displays a super-diffusion on average, like the Node 357, 542, 801 in Case 1 (Fig. 3.9), Node 1031 in Case 2 (Fig. 3.12), Node 2181 in Case 4 (Fig. 3.18). Actually, depending on the relation between super-diffusion, sub-diffusion and absorbing boundary effects, type 2 pattern can manifest itself as "apparent" super-diffusion, sub-diffusion or normal diffusion on average. The above observations provide further supportive argument for using the fractional diffusivity equation for modeling flow in porous media and production behavior in highly fractured unconventional reservoirs.

In the end, we can also make some discussions about the common dual-porosity model from the perspective of anomalous diffusions. Regarding one of the modeled continua, fracture system, it implicitly makes assumption that the flow particles in the fracture continuum undertake the diffusion in a Euclidean space. Thus, although it considers matrix supplementing fluid into fracture correctly, it still fails to capture the heterogeneity due to the geometry of fracture network, which may limit the model's application in highly fractured unconventional reservoirs. In this dissertation, a modified dual-porosity model accounting for the complex geometry of fracture network is developed in Section 5.

3.6. Section Summary

1. The physical background of the single-phase diffusivity equation is revisited. Combining the characteristics of single particle diffusion with complex fracture geometry, it is indicated that anomalous diffusion phenomenon will be dominant on the reservoir scale, even for single phase production behavior;
2. A Markov-chain-based model is presented to model single particle diffusion and it is demonstrated that anomalous diffusion characteristics emerge from considering normal diffusion on a graph that is embedded in a 2-D Euclidean space;
3. The fractional diffusivity equation have advantages over the standard diffusivity equation in characterizing flow and production in highly fractured unconventional reservoirs.

4. FRACTIONAL PRODUCTION DECLINE MODEL BASED ON A PLANAR HYDRAULIC FRACTURE*

4.1. Introduction

According to the formal demonstration of particle-wise anomalous diffusion due to complex fracture networks, fractional diffusivity equation, as a description of the aggregate behavior of massive diffusing particles, has got some supportive arguments for structurally incorporating the effects of the embedding heterogeneous micro-structure of the formation into modeling production and flow in the reservoir scale.

As has been referred to in Section 1.3.3, many relevant works with fractional diffusivity equation have been done for its application to reservoir engineering. However, because many of the prior works just replace Darcy's law with the relevant fractional flux law literarily within the traditional framework of multi-stage planar fractures along a horizontal well (Chen and Raghavan, 1997), many hard-to-determine (even hard-to-comprehend) parameters are contained in the resulting models, which make them a sort of compromise type of model between the forward modeling (reservoir simulation) and inverse modeling (PTA, RTA). In other word, these prior models, in our opinion, are inconvenient to be applied in either settings.

In this section, by deploying fractional diffusivity equation to the traditional setting of multi-stage planar fractures along a horizontal well and further simplifying the problem given some characteristics of highly fractured unconventional reservoirs with tight formation, we will develop a corresponding inverse-problem model and then investigate its features and feasibility in the relevant applications.

4.2. Model Description

Despite the fact that both types of anomalous diffusion (sub-diffusion and super-diffusion) could happen depending on the geometrical characteristics of a highly-conductive fracture network according to the simulation results of Section 3, we focus only on the sub-diffusion in this work, based on the observations of many previous works (Berkowitz and Scher, 1997; Havlin and Ben-Avraham, 1987) indicating that sub-diffusion is the dominating diffusion type in the case of porous media drained by complex fracture systems. In addition, as will be shown later, this restriction allows considerable simplifications in the mathematical treatment.

Within the traditional setting of modeling multi-fracture horizontal well, we first focus on developing a simplified 3-parameter model mainly based on the drainage area of an individual fracture in order to get a feasible model to be used in inverse problems. The underlying assumptions of the model are as follows:

- The formation is isotropic and homogeneous with respect to the diffusion exponent α and "anomalous" hydraulic diffusivity coefficient η^*. It stretches horizontally with the thickness h_f. All the above values are constant.
- The slightly compressible flow considered is of single phase. The fluid properties keep constant, such as the formation volume factor B, the viscosity μ, and the total compressibility c_t. The constancy of μ and c_t are consistent with the above assumption of constant hydraulic diffusivity coefficient η^*.
- The hydraulic fractures (HF) have infinite conductivity and are of planar shape with the uniform half-length as x_f (**Fig. 4.1 (a)**). Also, the HFs fully penetrate the formation thickness.
- The horizontal well spacings are uniform, so are the hydraulic fracture spacings, as shown in **Fig. 4.1 (a)**. Thus, each hydraulic fracture is located at the center of its drainage area due to the physical and geometric symmetry (**Fig. 4.1 (b)**).
- The flow is described by a fractional flux law, which is a consistent consequence of the fractional diffusivity equation and will be derived later.

The assumption on the isotropy and homogeneity of the formation seems to contradict with our motivation of introducing fractional diffusivity equation, because the latter is applied on purpose to account for the heterogeneity. This issue is resolved by taking the constant formation

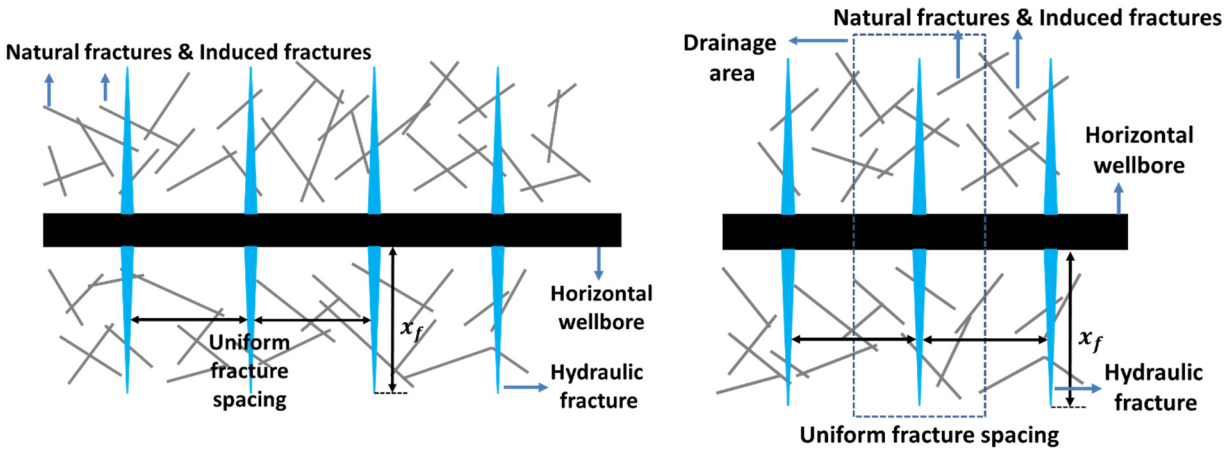

Figure 4.1 – Schematics of the fracture system and the drainage area of an individual hydraulic fracture

properties, such as α and η^*, as the average values of the complex system, which consists of the fracture network and the embedding ultra-low-permeability formation. Compared to the homogenization using normal diffusivity equation, the homogenization using fractional diffusivity equation is directly performed to the specific and prominent properties of the highly fractured formation, rather than to some ambiguous concepts (such as reservoir permeability) inherited from conventional reservoir engineering. Moreover, the assumptions regarding the fluid properties and the hydraulic fracture are justified by the same reasoning for the counterparts in the normal diffusivity equation model in Section 2.2.1.1. Additionally, the planar-shape HF is further justified by the notion that the effect of branches of induced fractures are accounted for constitutively with the model parameters α and η^* even if, in reality, the distinction between HF and induced fractures might be blurred in unconventional reservoirs.

Since sub-diffusion is considered, fractional time derivative is employed as the temporal operator in the governing equation. On the other hand, the spatial operator is selected with a view to mapping flow in discrete fractures to continuous drainage area. Balankin, who has done a lot of

works mapping the physical problems on fractals onto the continuum framework of the embedding Euclidean space, conducts a comprehensive investigation in one of his recent papers (Balankin, 2018) and provides the informative form of fractal Laplacian operator in Cartesian coordinates as Eq. (4.1) shows.

$$\Delta_F = \sum_{i=1}^{n} \frac{x_i^{2(1-\beta_i)}}{\beta_i^2} \left[\frac{\partial^2}{\partial x_i^2} + \frac{(1-\beta_i)(1-\nu_i) + (\nu_i - \beta_i)}{x_i} \frac{\partial}{\partial x_i} \right] \quad \text{.....(4.1)}$$

where n is the dimension of the embedding Euclidean space, x_i is the ith coordinate in a Cartesian system, ν_i is the ith component of the number of effective spatial degree of freedom on the fractal (Balankin, 2015), and $\beta_i = d_{fi}/\nu_i$ is the ratio of ith component of fractal dimension d_{fi} to the corresponding ν_i. Arithmetically combining the relevant value on each coordinate yields the total value for the specific space, as shown in Eq. (4.2) and Eq. (4.3).

$$d_f = \sum_{i=1}^{n} d_{fi} \quad \text{.....(4.2)}$$

$$\nu = \sum_{i=1}^{n} \nu_i \quad \text{.....(4.3)}$$

Then, if we apply Eq. (4.1) to our 2-D problem by imposing the assumptions of homogeneity and isotropy on it, it can be simplified to Eq. (4.4).

$$\Delta_F = \sum_{i=1}^{2} \frac{x_i^{2(1-\beta)}}{\beta^2} \left[\frac{\partial^2}{\partial x_i^2} + \frac{(1-\beta)(1-\nu/2) + (\nu/2 - \beta)}{x_i} \frac{\partial}{\partial x_i} \right] \quad \text{.....(4.4)}$$

where $\beta = d_f/\nu$.

According to Table 1 in Balankin (2018), most of the named path-connected fractals embedded in 2-D space, such as Vicsek snowflack, Sierpiński gasket, Sierpiński carpet, and percolation cluster, have both the ratio β and $\nu/2$ very close to 1.0, which makes the coefficient

of the second term in the bracket of Eq. (4.4) close to 0, especially for some problems of "large" scale. Following the above discussions, we take $\beta = \nu/2 = 1.0$ and get rid of the convection term in the fractal Laplacian operator in this work for the purpose of simplifying the mathematical treatment. Consequently, we obtain

$$\Delta_F = \sum_{i=1}^{2} \frac{\partial^2}{\partial x_i^2} = \frac{\partial^2}{\partial x^2} + \frac{\partial^2}{\partial y^2} = \Delta = \nabla \cdot \nabla \quad (4.5)$$

which is the normal Laplacian operator. Combined Eq. (4.5) with the fractional order time derivate in (Metzler et al., 1994), we finally obtain the governing equation of our problem as shown in Eq. (4.6).

$$\frac{1}{\eta^*} \frac{\partial^\alpha}{\partial t^\alpha} P = \nabla \cdot \nabla P \quad (4.6)$$

where P is the mapped fluid pressure, and η^* has the unit of $\text{length}^2/\text{time}^\alpha$. The fractional time derivative term is defined in the Riemann-Liouville manner with $0 < \gamma \leq 1$ (Eq. (4.7)).

$$\frac{d^\gamma}{dt^\gamma} f(t) := \frac{1}{\Gamma(1-\gamma)} \frac{d}{dt} \int_0^t \frac{f(\tau)}{(t-\tau)^\gamma} d\tau \quad (4.7)$$

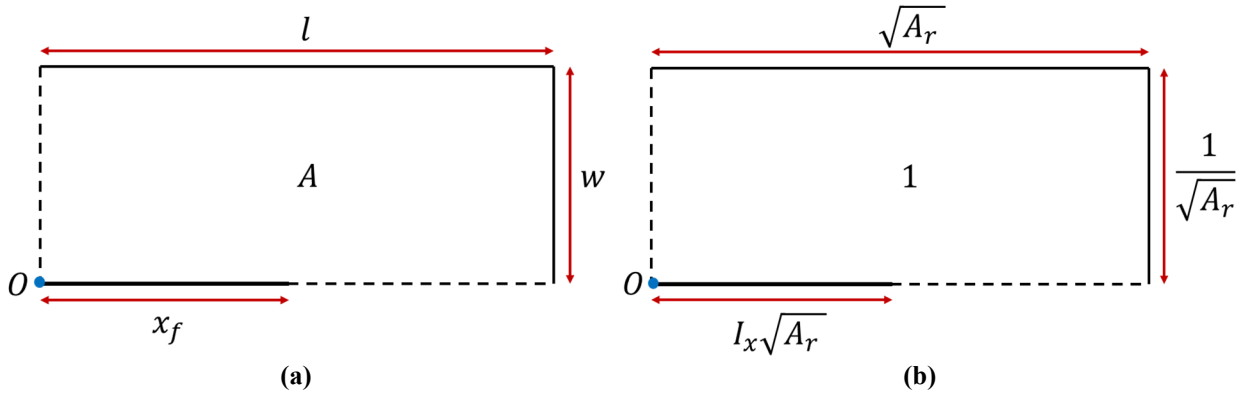

Figure 4.2 – Schematic of (a) a symmetric element of a drainage area and (b) the corresponding dimensionless problem domain

By the assumptions of homogeneity and geometric symmetry, we can take a quarter of the drainage area for an individual HF as the problem domain, as **Fig. 4.2** shows. Then it is evident that the boundaries are of no-flow type except for the part $0 \le x \le x_f$. Thus, we have

$$x = l, 0 \le y \le w : \frac{\partial P}{\partial x} = 0 \quad \text{.....(4.8a)}$$

$$y = w, 0 \le x \le l : \frac{\partial P}{\partial y} = 0 \quad \text{.....(4.8b)}$$

$$x = 0, 0 \le y \le w : \frac{\partial P}{\partial x} = 0 \quad \text{.....(4.8c)}$$

$$y = 0, x_f < x \le l : \frac{\partial P}{\partial y} = 0 \quad \text{.....(4.8d)}$$

Given the fact of the formation with ultra-low permeability in the unconventional reservoir, producing with constant bottom-hole pressure is presumably a more realistic production scheme than constant flow rate. Therefore, our work focuses on the problem with constant bottom-hole pressure, namely the constant Dirichlet condition along the infinite HF, as shown in Eq. (4.8e).

$$y = 0, 0 \le x \le x_f : P = P_w \quad \text{.....(4.8e)}$$

where P_w is a specific constant value.

The initial condition is uniform initial pressure, as shown in Eq. (4.9).

$$P(x, y, 0) = P_i \quad \text{.....(4.9)}$$

After substituting the dimensionless groups defined below into the above equations, the problem to be solved is well formulated as Eq. (4.10).

$$P_D = \frac{P - P_w}{P_i - P_w}, \qquad A_r = \frac{l}{w}, \qquad I_x = \frac{x_f}{l},$$

$$x_D = \frac{x}{\sqrt{A}} = \frac{x}{l}\sqrt{A_r}, \qquad y_D = \frac{y}{\sqrt{A}} = \frac{y}{w}\frac{1}{\sqrt{A_r}}, \qquad t_D = \left(\frac{\eta^*}{A}\right)^{\frac{1}{\alpha}} t = \frac{t}{\tau},$$

$$l_D = \frac{l}{\sqrt{A}} = \sqrt{A_r}\,, \qquad w_D = \frac{w}{\sqrt{A}} = \frac{1}{\sqrt{A_r}}\,,$$

$$q_D = \frac{\mu B q_{sc}}{k^* h_f (P_i - P_w)} \left(\frac{A}{\eta^*}\right)^{\frac{1-\alpha}{\alpha}} = \frac{\tau}{EUR} q_{sc}\,, \qquad Q_D = \int_0^{t_D} q_D \, \mathrm{d}t_D = \frac{B Q_{sc}}{h_f A c_t \phi (P_i - P_w)} = \frac{Q_{sc}}{EUR}$$

$$\frac{\partial^\alpha}{\partial t_D^\alpha} P_D = \Delta_D P_D \quad \text{.....(4.10a)}$$

$$P_D(x_D, y_D, 0) = 1 \quad \text{.....(4.10b)}$$

$$x_D = \sqrt{A_r}, 0 \le y_D \le 1/\sqrt{A_r} : \frac{\partial P_D}{\partial x_D} = 0 \quad \text{.....(4.10c)}$$

$$y_D = 1/\sqrt{A_r}\,, 0 \le x_D \le \sqrt{A_r} : \frac{\partial P_D}{\partial y_D} = 0 \quad \text{.....(4.10d)}$$

$$x_D = 0, 0 \le y_D \le 1/\sqrt{A_r} : \frac{\partial P_D}{\partial x_D} = 0 \quad \text{.....(4.10e)}$$

$$y_D = 0, I_x\sqrt{A_r} < x_D \le \sqrt{A_r} : \frac{\partial P_D}{\partial y_D} = 0 \quad \text{.....(4.10f)}$$

$$y_D = 0, 0 \le x_D \le I_x\sqrt{A_r} : P_D = 0 \quad \text{.....(4.10g)}$$

where the dimensionless drainage area is a rectangle of unit area, A_r is the aspect ratio, $A_r = l/w$, and I_x is the penetration ratio of the infinite-conductivity HF in the x-direction, $I_x = x_f/l$.

Fractional flux law implicitly employed in Eq. (4.6) is as Eq. (4.11) shows.

$$\vec{v} = -\frac{k^*}{\mu} \frac{\partial^{1-\alpha}}{\partial t^{1-\alpha}} \nabla P \quad \text{.....(4.11)}$$

where k^* represents the "anomalous" permeability of the fracture-network embedding formation with the irregular dimension of $\text{length}^2/\text{time}^{1-\alpha}$. The detailed derivation can be found in Appendix C. This relation between pressure and volumetric flux takes the place of Darcy's law in the normal diffusivity equation to manifest the property of "memory" or "path dependence", which is out of the underlying heterogeneous fracture network. Many works (Albinali and Ozkan, 2016;

Raghavan and Chen, 2017a, 2017b) tend to directly combine the fractional flux law with the ordinary continuity equation to get the governing equation like Eq. (4.6). However, since we view the problem as a mapping between different spaces as mentioned above, the fractional flux law isn't handy *a priori* and the direct combination not quite intuitive. Furthermore, according to our model, the fractional flux law in the form of Eq. (4.11) is a simplified version in which the impacts of fractal geometry are ignored on the spatial operator. Perhaps more importantly, as we will see in Section 5, when tempered anomalous diffusion is accounted for to model the flow through fracture systems in a more realistic manner, the implicitly contained flux law does not have a close form in time domain and can only be derived from the corresponding governing equation, not the other way around.

4.3. Solutions and Type Curves of Fracture-based Model

By the method of separation of variables (Appendix D), the solution of our problem (Eq. (4.10)) can be expressed in the form of infinite series, as shown in Eq. (4.12).

$$P_D(x_D, y_D, t_D) = \sum_{i=1}^{\infty} E_\alpha(-\lambda_i t_D^\alpha)\varphi_i(x_D, y_D) \int_\Omega \varphi_i(x_D, y_D) dX_D \quad \text{.....(4.12)}$$

where λ_i is the ith eigenvalue of the relevant eigenproblem with φ_i the corresponding normalized eigenfunction, and Ω denotes the dimensionless 2-D problem domain with unit area. $E_\alpha(z)$ is the Mittag-Leffler function of one parameter with the definition (Haubold et al., 2011) in Eq. (4.13).

$$E_\alpha(z) := \sum_{k=0}^{\infty} \frac{z^k}{\Gamma(\alpha k + 1)} \quad \text{.....(4.13)}$$

By the relationship between dimensionless rate and pressure as well as some recursive properties of Mittag-Leffler function, the declining production rate is expressed as Eq. (4.14). The detailed derivations for the relation and for Eq. (4.14) are included in Appendix E.

$$q_D(t_D) = \frac{1}{t_D^{1-\alpha}} \sum_{i=1}^{\infty} \lambda_i E_{\alpha,\alpha}(-\lambda_i t_D^{\alpha}) A_i \quad \text{.....(4.14)}$$

where A_i denotes the group $\left(\int_{\Omega} \varphi_i(x_D, y_D) dX\right)^2$. And the following relation holds due to the normalized eigenfunction.

$$\sum_{i=1}^{\infty} A_i = 1 \quad \text{.....(4.15)}$$

Since the eigenpairs (λ_i, φ_i) are determined by the geometry of the problem domain, that is, A_r and I_x, λ_i, and A_i are functions with respect these two parameters. Thus, $q_D(t_D)$ is well defined by three dimensionless parameters, A_r, I_x, and α, compared to the two-parameter model (A_r, I_x) of the normal diffusivity equation over the same domain, which has been investigated by the work in Section 2. This allows us to model the production performance of the highly fractured formation with an additional factor, the highly heterogeneous fracture network.

The dimensionless cumulative production can be obtained from Eq. (4.14), as Eq. (4.16) shows.

$$Q_D(t_D) = \int_0^{t_D} q_D(\tau) d\tau = 1 - \sum_{i=1}^{\infty} E_{\alpha}(-\lambda_i t_D^{\alpha}) A_i \quad \text{.....(4.16)}$$

A truncated version of the series in Eq. (4.14) and Eq. (4.16) has been used for generating the type curves. Based on our experience, 100 terms are enough to achieve a fair accuracy for practical applications. Mathematica (Wolfram Research, Inc., 2018) with its powerful built-in functions, such as NDEigensystem and MittagLefflerE, is employed in the generation. In **Fig. 4.3**, the type curves of production rate and cumulative production corresponding to $A_r = 1.0, 4.0, 7.0$ are shown with various α and I_x.

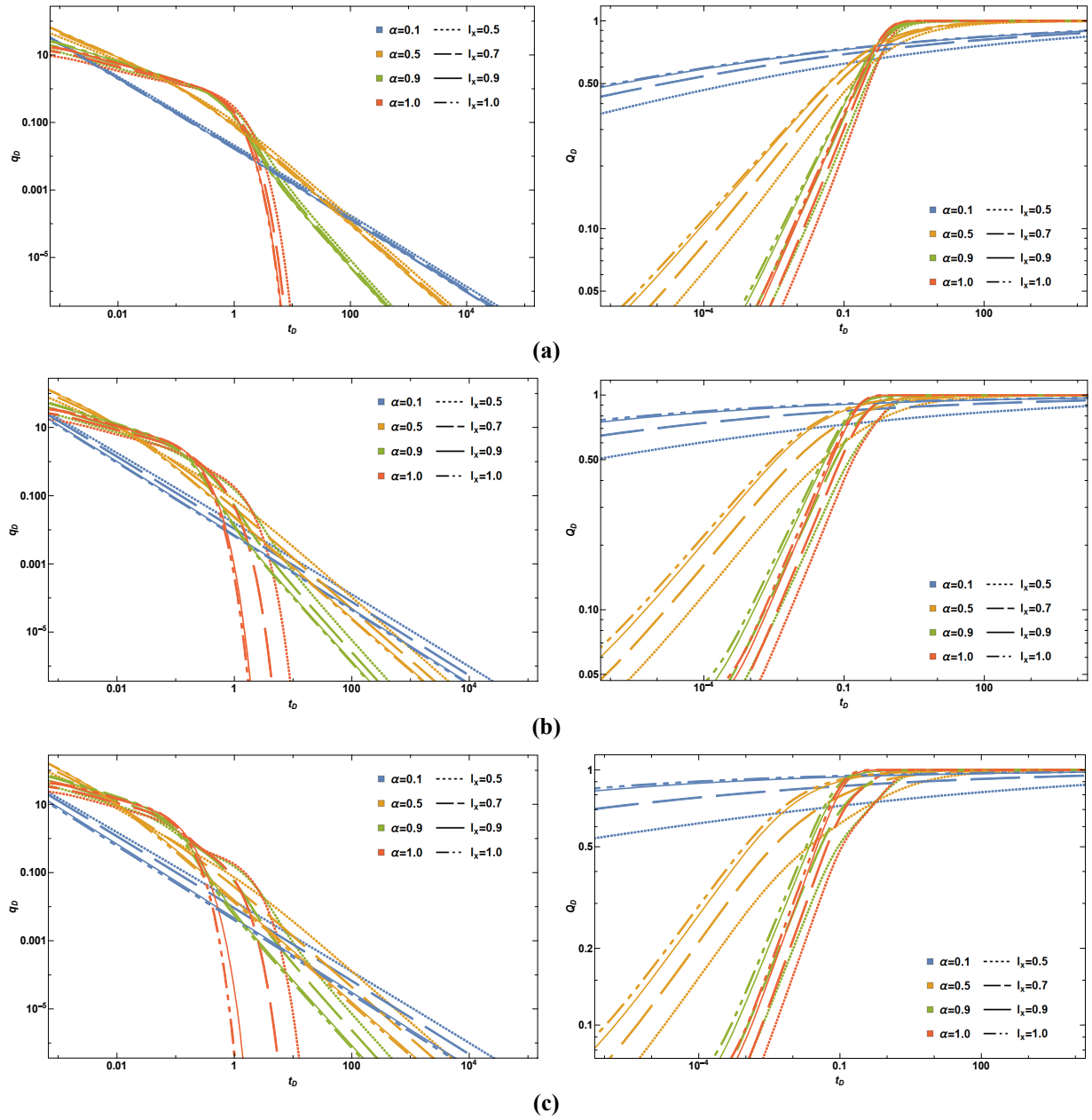

Figure 4.3 – Type curves of rate and cumulative production with various A_r, I_x, and α. (a) $A_r = 1.0$. (b) $A_r = 4.0$. (c) $A_r = 7.0$.

It is evident in the type curves of **Fig. 4.3** that the anomalous diffusion exponent α has significant impact on the trends according to which the declining production rate and cumulative production evolve, especially compared to the effects of A_r and I_x. Taking the cases of $\alpha = 1$, corresponding to normal diffusion, as reference, when $\alpha < 1$ the production rate declines faster in

the early time and slower in late time. In fact, the late-time performance manifests itself as straight lines in the log-log plot due to the long-time asymptotic behavior of the Mittag-Leffler function. Additionally, on the curves of $\alpha = 1$, we can find the well-known linear flow regime with the slope of $1/2$ in the early time. On the curves of $\alpha < 1$ the asymptotically linear segments also occur, but with the slope larger than $1/2$. This slope increases monotonically with α approaching 0, that is with anomalous diffusion behavior becoming more prominent.

The dimensionless cumulative plots indicate that different αs result in distinct "rate" of cumulation. In general, the cumulative process of α closer to unity have a steeper slope regardless of the values of A_r and I_x.

As has been mentioned previously, the shape of the type curves largely depends on α, in the following section we address the issues of consistency and robustness of the fractional decline model when applied to production performance analysis of fractured wells.

4.4. Consistency and Robustness

By consistency we mean that knowing only a limited number of production rates (or cumulative production values) will introduce only a limited error in the estimated key parameters.

However, consistency is not the only property we need to consider. As has been shown in Eq. (4.14) and Eq. (4.16), our type curves are completely determined by A_r, I_x, and α, where α is introduced to account for the structural characteristics of the embedded complex fracture network, so that it cannot be obtained *a priori* and is one of the parameters to be determined by data-fitting. On the other hand, A_r and I_x are related to the fracture-well configuration and can be estimated from the (horizontal) well spacing and cluster spacing within the well in addition to designed propped fracture x_f, as have been shown in Section 2. Therefore, in a typical type-curve fitting procedure a family of type curves based on estimated A_r and I_x are generated to determine α. In

such a usage, the assumed A_r and I_x inevitably introduce errors into the data-fitting process from the beginning, which necessitates investigating the robustness of identifying α in the presence of uncertainty regarding A_r and I_x.

For the purpose of studying consistency and robustness, we generate sets of synthetic production data using such a fractional decline model, and then perform data fitting on them to extract the estimated the key parameters: the time scale (τ) and anomalous diffusion parameter (α) ultimately needed to determine estimated ultimate recovery (EUR).

If the processing of the synthetic data leads to limited deviation between estimated parameters and their "true value", even if the available production history is limited to a certain time interval and number of points, we call the parameter estimation consistent. If the limited deviation between estimated parameters and their "true value" occurs even if A_r and I_x parameters used in the processing have a certain error, we call the procedure robust.

We assume a horizontal well with a perforated interval of 4,694 ft drilled in a shale formation and that the well spacing is 1,320 ft. In this well, we have 12 fracturing stages, each of which has two HFs created with the half-length of 500 ft. Thus, A_r and I_x for each fracture drainage area are 6.75 and 0.76, respectively. We also assume the EUR for the well is 250 Mbbl, the time scale, τ, 4000 d and $\alpha = 0.5$. From the definitions of dimensionless variables, we know

$$t = \left(\frac{A}{\eta^*}\right)^{1/\alpha} t_D = \tau\, t_D \quad \text{.....(4.17)}$$

$$Q = \frac{Q_D \phi c_t A h (P_i - P_w)}{B} = EUR\, Q_D \quad \text{.....(4.18)}$$

$$q = \frac{q_D k^* h (P_i - P_w)}{\mu B} \left(\frac{A}{\eta^*}\right)^{(\alpha-1)/\alpha} = \frac{EUR}{\tau} q_D \quad \text{.....(4.19)}$$

Using the type curve of $A_r = 6.75$, $I_x = 0.76$, and $\alpha = 0.5$ along with Eq. (4.17) to Eq. (4.19), we generate the production rate and cumulative production with various schemes of sampling time. To account for the impacts of early-time and late-time sampling points, the following sampling scheme is applied: in the early time the sampling points are in the manner of 2^{n_1} d ($n_1 \in$ Integer) up to 2^4 d $= 16$ d; then, starting from 20 d, an increment of 40 d is used to represent the monthly reported production data until a terminal of $n_2\tau$ is reached. By using various values of n_1 in $\{-5, -3, -1, 0\}$ and n_2 in $\{1, 2\}$, data sets of different early time resolution and late time duration can be generated. An example set of sampling points with $n_1 = -3$ and $n_2 = 1$ is shown in **Fig. 4.4**.

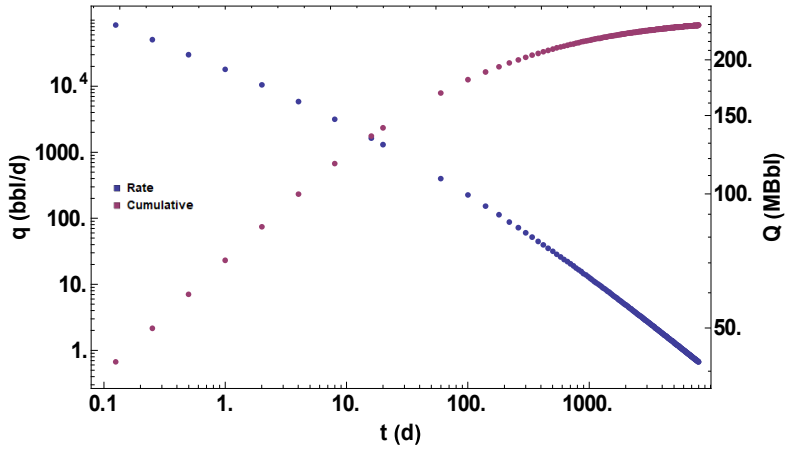

Figure 4.4 – A set of sampling points with the sampling scheme (n_1, n_2) of $(-3, 1)$

4.4.1. Consistency

In the first part of the study, A_r and I_x are assumed to be known accurately. Therefore, $A_r = 6.75$ and $I_x = 0.76$ are used to create a family of type curves with $0 < \alpha \leq 1$, as shown in **Fig. 4.5**. Then, a data fitting algorithm (Mathematica function FindFit (Wolfram Research, Inc., 2018)) with simply a constrain of $(0,1]$ on α is run to achieve the best fit for a specific set of

sampling points in the family. The data fitting yields the fitted α, τ, and EUR. **Table 4.1** shows the results and comparison with the inputs of $\alpha = 0.5$, $\tau = 4000$ d and $EUR = 250$ Mbbl.

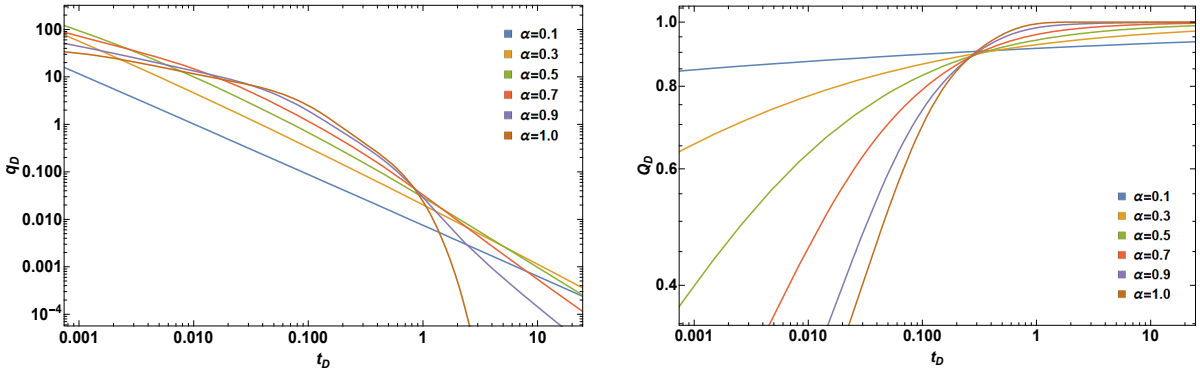

Figure 4.5 – Type curves of rate and cumulative production with various $A_r = 6.75$, $I_x = 0.76$

Table 4.1 – Fitted parameters and corresponding deviations in the consistency study

Rate								
(n_1, n_2)	α	Dev (%)	τ (d)	Dev (%)	τ^α (d^α)	Dev (%)	EUR (Mbbl)	Dev (%)
(0,1)	0.419	16	1806	54.9	23.2	63.3	379.8	51.9
(−1,1)	0.415	17	1604	59.9	21.4	66.2	395.1	58.0
(−3,1)	0.519	3.9	2571	35.7	59.0	6.7	282.7	13.1
(−5,1)	0.529	5.7	2615	34.6	64.0	1.2	276.9	10.7
(0,2)	0.500	2.6E-5	4000	2.5E-4	63.2	2.4E-4	250.0	1.2E-4
(−1,2)	0.500	1.4E-5	4000	2.0E-4	63.2	1.6E-4	250.0	9.0E-5
(−3,2)	0.500	1.1E-6	4000	1.4E-4	63.2	7.6E-5	250.0	6.0E-5
(−5,2)	0.500	5.7E-6	4000	1.2E-4	63.2	3.8E-5	250.0	4.7E-5
Cumulative								
(n_1, n_2)	α	Dev (%)	τ (d)	Dev (%)	τ^α (d^α)	Dev (%)	EUR (Mbbl)	Dev (%)
(0,1)	0.430	14	15732	293.3	63.6	0.5	268.5	7.4
(−1,1)	0.461	7.8	8452	111.3	64.6	2.2	259.8	3.9
(−3,1)	0.467	6.7	8197	104.9	67.0	5.9	259.6	3.8
(−5,1)	0.455	8.9	12008	200.2	72.1	14.0	265.6	6.2
(0,2)	0.456	8.8	8316	107.9	61.4	3.0	257.9	3.2
(−1,2)	0.460	8.1	8210	105.3	63.0	0.4	257.8	3.1
(−3,2)	0.465	7.0	8030	100.8	65.5	3.6	257.6	3.1
(−5,2)	0.469	6.1	7873	96.8	67.4	6.5	257.5	3.0

In each set of sampling points, the deviation of fitted α is quite small with the maximum of 17%. The fitted EURs for most cases are close to the true value, especially for the rate-fitting cases with longer late-time duration. For the time scale, τ, although the fitted values all largely deviate from the true value 4000 d, the combination of fitted parameters, τ^{α}, has limited errors for most cases. Since by Eq. (4.17) τ^{α} coincides with the quotient of A/η^{*}, it indicates that the fitted anomalous diffusivity coefficient $\eta^{*}$is also quite comparable to its true value. To sum up, in most cases the data fitting with the type curves based on fractional decline model yields consistent results with the corresponding true values.

Even without further comprehensive investigations, we can arguably conclude that increasing the sampling points in the early time doesn't contribute to as much accuracy as extending the late-time sampling period does, given the fact that in either cumulative production or production rate case the sampling point sets with 2τ generally have more accurate fitted values and stable performances. However, notice the disappointing results of sampling cases with very few early-time points (the first two rows of **Table 4.1**).

4.4.2. Robustness

Besides the consistency issue, the robustness of the fractional decline model needs to be investigated, considering the effect of uncertainty in the A_r and I_x parameters, as mentioned above. In the second part of the study, some errors are introduced to A_r and I_x, that is the fitting is performed using the family of type curves generated with the distorted A_r and I_x.

We distort the aspect ratio $A_r = 6.75$ with errors from $\pm 10\%$ to $\pm 60\%$, and then the penetration ratio $I_x = 0.76$ with errors of $\pm 10\%$, $\pm 20\%$, $\pm 30\%$, -40% and -50%. In addition, the sampling scheme of $(n_1, n_2) = (-2, 2)$ is used throughout the robustness study. The fitted values and the corresponding deviations are shown in **Table 4.2** and **Table 4.3**.

Table 4.2 – Fitted parameters and corresponding deviations in the robustness study with errors on A_r

Rate							
Error on A_r	α	Dev (%)	τ (d)	τ^{α} (d$^{\alpha}$)	Dev (%)	EUR (Mbbl)	Dev (%)
10%	0.511	2.2	4161	70.7	11.8	249.7	1.4E-1
-10%	0.489	2.2	3788	56.3	10.9	250.0	3.2E-3
20%	0.522	4.4	4284	78.8	24.6	248.5	6.1E-1
-20%	0.480	4.1	3453	49.8	21.3	252.1	8.3E-1
30%	0.534	6.8	4300	87.0	37.6	245.1	2.0
-30%	0.471	5.9	3069	43.7	30.9	254.7	1.9
40%	0.545	9.0	4319	95.9	51.6	246.2	1.5
-40%	0.463	7.5	2581	37.9	40.1	255.5	2.2
50%	0.530	6.0	2698	65.8	4.1	302.2	20.9
-50%	0.456	8.8	2052	32.4	48.7	256.5	2.6
60%	0.537	7.5	2633	68.9	9.0	305.4	22.2
-60%	0.451	9.7	1477	26.9	57.4	257.0	2.8
Cumulative							
Error on A_r	α	Dev (%)	τ (d)	τ^{α} (d$^{\alpha}$)	Dev (%)	EUR (Mbbl)	Dev (%)
10%	0.454	9.3	12205	71.3	12.8	262	4.8
-10%	0.435	13	11612	58.8	7.0	263	5.2
20%	0.457	8.7	13984	78.1	23.6	263	5.2
-20%	0.421	16	12076	52.5	16.9	265	6.0
30%	0.470	6.1	12637	84.4	33.4	261	4.6
-30%	0.406	19	12912	46.7	26.2	268	7.1
40%	0.481	3.8	11795	90.9	43.7	260	4.1
-40%	0.388	22	14250	40.7	35.6	272	8.8
50%	0.492	1.5	10877	97.3	53.8	259	3.7
-50%	0.372	26	14155	34.9	44.8	276	10
60%	0.508	1.5	9377	103.7	64.0	257	3.0
-60%	0.349	30	16011	29.2	53.8	285	14

From **Table 4.2** and **Table 4.3**, it is evident that even though some errors are introduced into A_r and I_x, the fitted αs from either cumulative or rate fitting fall into a limited error range with the maximum deviation of 30% for the case of even -60% error in A_r. The fitted EURs showremarkable robustness in the sense that their deviations are much less than the related errors in A_r or I_x. Even though the deviations for τ^{α} are not as small as those for α and EUR, they increase gradually along with the increasing errors in A_r and I_x and show no evidence of

Table 4.3 – Fitted parameters and corresponding deviations in the robustness study with errors on I_x

Rate							
Error on I_x	α	Dev (%)	τ (d)	τ^{α} (d$^{\alpha}$)	Dev (%)	EUR (Mbbl)	Dev (%)
10%	0.466	6.8	6044	57.9	8.5	302.2	20.9
-10%	0.523	4.6	1776	50.0	20.9	245.1	2.0
20%	0.445	11	7368	52.4	17.2	368.4	47.4
-20%	0.539	7.8	913	39.4	37.7	231.0	7.6
30%	0.439	12	8017	51.5	18.6	400.9	60.3
-30%	0.583	17	821	49.9	21.1	175.7	29.7
-40%	0.487	2.7	116	10.1	84.0	280.8	12.3
-50%	0.471	5.9	48	6.2	90.2	292.3	16.9
Cumulative							
Error on I_x	α	Dev (%)	τ (d)	τ^{α} (d$^{\alpha}$)	Dev (%)	EUR (Mbbl)	Dev (%)
10%	0.457	8.6	12935	75.7	19.7	254	1.6
-10%	0.423	15	13913	56.6	10.4	278	11
20%	0.476	4.9	12409	88.5	40.0	248	0.73
-20%	0.412	18	12677	48.9	22.6	295	18
30%	0.430	14	45717	101.0	59.7	257	2.9
-30%	0.427	15	5095	38.2	39.6	297	19
-40%	0.399	20	6090	32.2	49.0	327	31
-50%	0.379	24	4787	24.7	60.9	351	40

divergence. In conclusion, we can say that data fitting based on the fractional decline model has the property of robustness with respect of uncertainty in A_r and I_x if the sampling scheme is acceptable.

Another interesting phenomenon displayed in **Table 4.2** and **Table 4.3** is that rate fitting is much more sensitive to positive error on either A_r or I_x, while the cumulative fitting is much more sensitive to negative error. In general, it seems advantageous to use rates and cumulative production simultaneously during the computerized type curve fitting because of this specific behavior.

4.5. Application of Fractured-based Model on Reservoir Simulation Results

Due to the significant complexity of fractured unconventional reservoirs plus sophisticated production systems, the unusual production decline performance in field cases may be attributed to the effects of many elements, like the choke management scheme (Chu et al., 2017) and the temporal variation of reservoir and fluids properties (Yuan et al., 2018). Therefore, to concentrate on the effects purely belonging to the fracture network, we analyze the production data from a couple of simulation cases in which only a single-phase fluid is contained.

Three sets of simulation grids are built to represent different types of fracture network topology, containing an orthogonal evenly distributed network, an orthogonal unevenly distributed network, and a complex fracture network, as illustrated in **Fig. 4.6**. The first two sets are implemented by structured girds, while the complex network is generated by the Schlumberger Kinetix stimulation software suit and then converted to unstructured reservoir simulation grids.

Table 4.4 – Parameters of the reservoir simulation models with three types of fracture networks

	Orthogonal even case	Orthogonal uneven case	Complex fracture case
Model length / ft	4500	4500	4000
Model width / ft	750	750	690
Model height / ft	304	304	210
No. of layers		1	
Grid volume / ft^3	1.30E+8	1.37E+8	1.29E+8
Rock compressibility / psi^{-1}		7.00E-6	
Water compressibility / psi^{-1}		2.74E-6	
Water viscosity / cP		0.3985	
Water formation volume factor / RB/STB		1.0132	
Initial pressure / psi	4876	4876	4919
Initial S_w		1.0	
Porosity		0.01	
Permeability k_f / mD		1.5	
Bottom-hole pressure / psi		4000	
EUR / STB	1970	2078	2058
Ratio of fracture grid volume to bulk volume	0.126	0.133	0.223

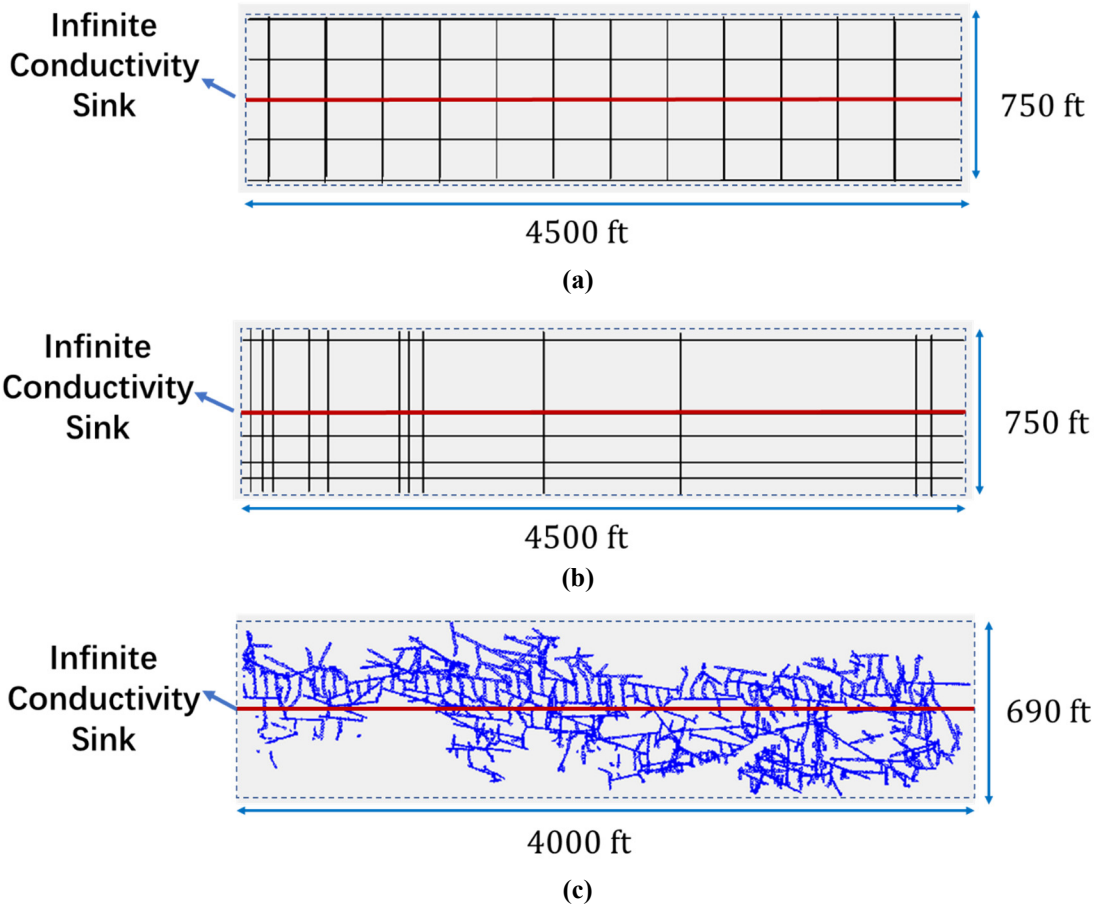

Figure 4.6 – Map views of the three types of fracture network used in the reservoir simulation models. (a) Orthogonal evenly distributed fracture network. (b) Orthogonal unevenly distributed fracture network. (c) Randomly distributed fracture network.

And all the three models only have 1 layer of grids in the vertical direction. In each model, all grids are flagged as inactive grids except those belonging to the fracture networks, so that only the flow within the fractures is simulated without any matrix influx. Additionally, in order to rule out the impact of multiphase flow and variable bottom-hole pressure, only water is initially contained in the model and the production scheme is set as bottom-hole pressure control with a constant value of 4000 psi. The relevant parameters of the simulation models are shown in **Table 4.4**. As shown in **Fig. 4.6**, perforations are set in all girds of the middle row for each case so that the

penetration ratio I_x equals the unity. All the cases are simulated using the Schlumberger INTERSECT reservoir simulator.

Fig. 4.7 shows the rate and cumulative results in log-log coordinates. Regarding the rate curves, apparently different production decline trends occur for different fracture types, especially comparing the third one with the other two. Given the identical fluid, rock properties, and bottom-hole pressure as well as the similar initial pressure and pore volume, this prominent distinction can be reasonably attributed to the different network topology.

At the first glimpse of the rate and cumulative curves in **Fig. 4.7**, even the case with complex fracture network lacks several distinctive characteristics predicted in the proposed model. But this seemingly inconsistency can be explained by the finiteness of the computational models and the average nature of our proposed model. First of all, all the rate curves in **Fig. 4.7** end up with an exponential decline, while the proposed model indicates a power-law decline for $\alpha < 1$ in the late time. The late-time exponential decline is due to the finiteness of the computational models in which the heterogeneity of scales finer than the model's resolution is totally truncated, while in the proposed model heterogeneity is modeled with infinite spatial resolution. So, in order to investigate the heterogeneity of the models, it is reasonable to only focus on the period before the exponential decline. Additionally, by manually doing curve fitting with cumulative production data, we find in the early time, say 1 to 2 days, the data fails to follow the trend of the corresponding type curves to which the data of later time fits perfectly. The reason for this is probably that initially the production is mainly affected by the local characteristics of the flow close to the producing grids. Therefore, because of the above reasons, before performing data-fitting, the data of the first 2 days is excluded for all three cases based on manually fitting the cumulative curve, and the data of late exponential decline period is screened out for the complex fracture cases based on the rate

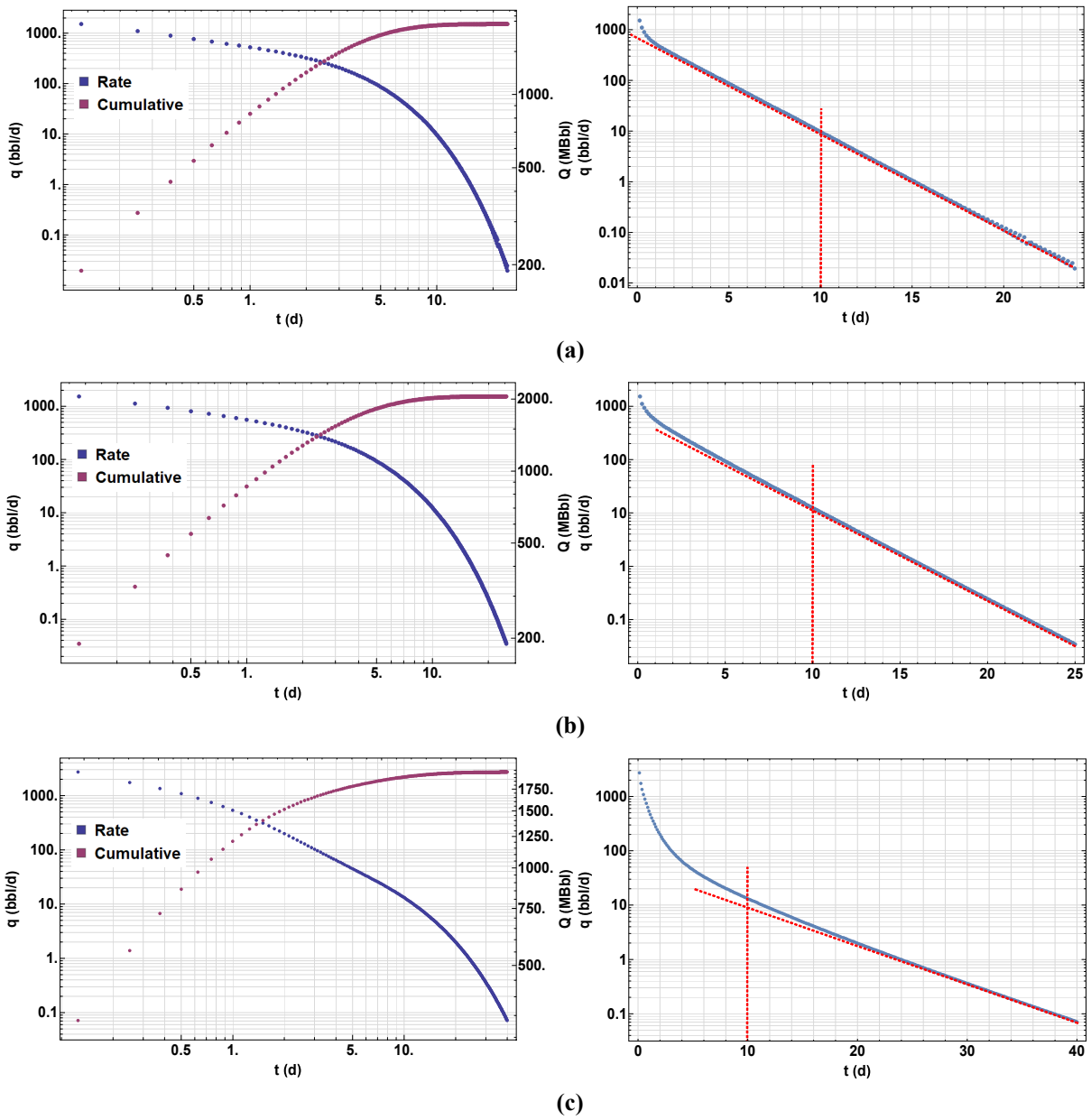

Figure 4.7 – Plots of production rate and cumulative production of three simulation cases in log-log and semi-log coordinates. (a) Evenly distributed fracture. (b) Unevenly distributed fracture. (c) Complex fracture network.

curve in the semi-log coordinates (Fig. 4.7 (c)). Because of the relatively high extent of homogeneity, the two orthogonal fracture cases begin exponential decline at a very early time (Fig. 4.7 (a), (b)). And according to our expectation, these cases are supposed to correspond to α close to the unity, the normal diffusion, so that screening out late exponential decline data isn't

performed to the first two case. Accordingly, for each case the production data within the range of $t \in (2, 10]$ (64 data points) is used.

The aspect ratio for each case is estimated according to the dimensions of the smallest rectangle whose longest side is parallel to the horizontal wellbore. That is, $A_r \approx \frac{4500}{750} = 6.0$ for the first two cases and $A_r \approx \frac{4000}{690} \approx 5.8$ for the last case. In addition, according to the settings of the models, we have the penetration ratio $I_x = 1.0$ approximately for all.

For each case the data-fitting is performed on both rate and cumulative type curves using the optimization functions in Mathematica (Wolfram Research, Inc., 2018). According to the definitions of dimensionless group, rate fitting would result into three parameters of $\left(\alpha, \tau, \frac{EUR}{\tau}\right)$, while the cumulative fitting into (α, τ, EUR). The fitted values are displayed in **Table 4.5**. And the fitted plots are shown in **Fig. 4.8**, in which the excluded early-time data is also included as gray dots for the purpose of comparison.

Table 4.5 – Fitted and calculated parameters of applying the fracture-based model to simulated production data

	Cumulative fitting							
	α	τ / d	EUR		η^* / $\text{ft}^2/\text{sec}^\alpha$	k^* / $\text{ft}^2/\text{sec}^{\alpha-1}$	ϕ	
			Fitted / STB	Dev / %			Fractal	ϕ/ϕ_f
Even	1	36.68	1957	0.66	1.05	7.62E-16	1.27E-3	0.127
Uneven	1	37.84	2056	1.06	1.03	7.76E-16	1.33E-3	0.133
Complex	0.7157	57.21	2064	0.29	44.67	5.69E-14	2.26E-4	0.226
	Rate fitting							
	α	τ / d	EUR		η^* / $\text{ft}^2/\text{sec}^\alpha$	k^* / $\text{ft}^2/\text{sec}^{\alpha-1}$	ϕ	
			Fitted / STB	Dev / %			Fractal	ϕ/ϕ_f
Even	0.9989	33.87	2174	10.36	1.17	9.32E-16	1.41E-3	0.141
Uneven	0.9864	36.43	2290	10.20	1.31	1.10E-15	1.49E-3	0.149
Complex	0.6660	40.43	3137	52.42	121	2.34E-13	3.44E-3	0.344

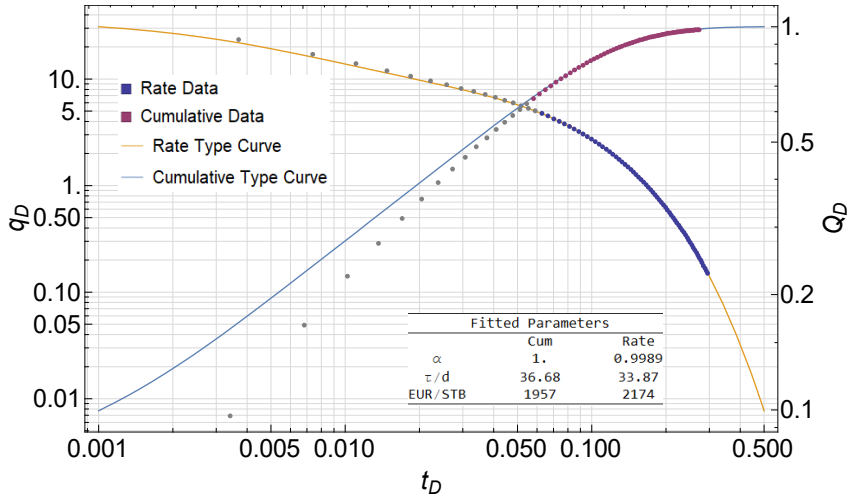

(a)

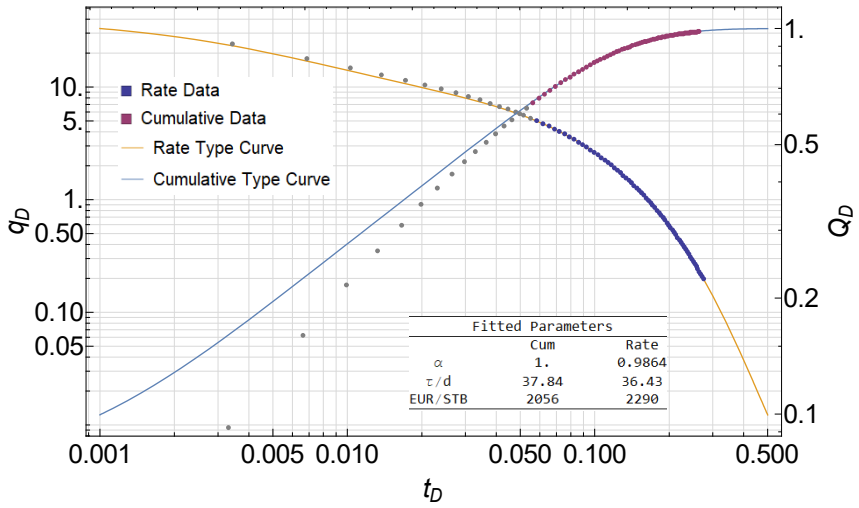

(b)

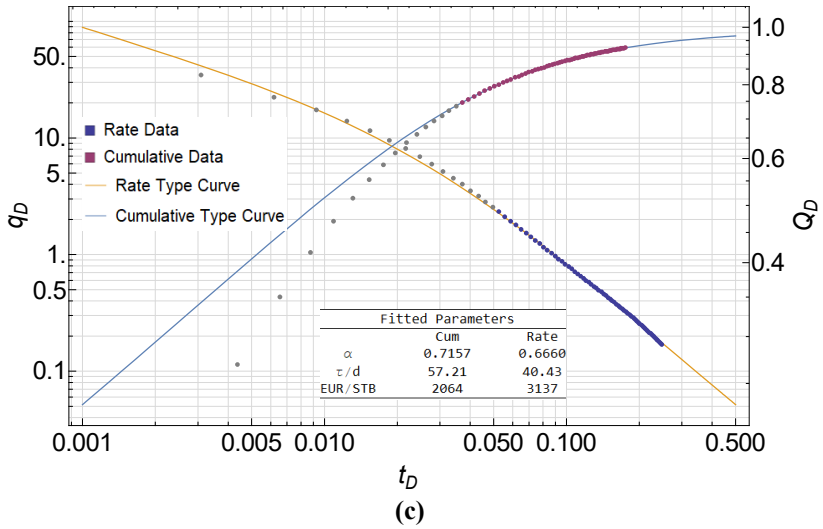

(c)

Figure 4.8 – Results of fitting simulated production data to the corresponding fracture-based type curves. (a) The evenly distributed fracture case. (b) The unevenly distributed fracture case. (c) The complex fracture case.

As a signature of anomalous diffusion, the descent of the fitted αs in **Table 4.5** from Even to Complex fits our expectation about the escalation of anomalous diffusion in more and more complex fracture networks.

Table 4.5 indicates different characteristics between cumulative fitting and rate fitting. Regarding α, rate fitting tends to be more sensitive for catching the trace of anomalous diffusion. For the two orthogonal fracture cases, cumulative fitting yields $\alpha = 1$ for both, while rate fitting results into slightly different αs. Also, despite orthogonality and even distribution, the regular lattice in the first case still owes a trace of heterogeneity due to its discrete nature, so that a non-unity number that is very close to the unity is more satisfactory than an exact one. On the other hand, regarding EUR estimation, cumulative fitting is apparently much superior to rate fitting. In all, a comprehensive consideration of both cumulative and rate fitting results can perhaps yield the information closer to the true values. Or a data-fitting combining both types is suggested.

After gaining the fitted parameters, more information about the reservoir of interest can be extracted from them. According to the definitions, the anomalous diffusivity coefficient η^* can be calculated in the way of Eq. (4.20) based on the estimated drainage area.

$$\eta^* = \frac{A}{\tau^\alpha} \quad \text{.....(4.20)}$$

And if we assume that the process of "mapping flow from discrete to continuum" only somehow "distorted" the topology-related intrinsic properties, like permeability and porosity, while the physical properties, like compressibility, viscosity, and formation volume factor, keep intact, the anomalous permeability and then the porosity in the homogeneous fractal reservoir can be obtained via Eq. (4.21) and Eq. (4.22).

$$k^* = \frac{\mu\, B\, EUR}{\tau^\alpha\, h_f (P_i - P_w)} \quad \text{.....(4.21)}$$

$$\phi = \frac{k^*}{\mu\, c_t\, \eta^*} \quad (4.22)$$

In **Table 4.5**, the values of (η^*, k^*, ϕ) based on Eq. (4.20) to Eq. (4.22) are also shown.

According to **Table 4.5**, in these cases, the calculated η^* and k^* don't show apparent patterns when compared to their regular counterparts of the fractures. But, with our above assumptions about topology-related and physical intrinsic properties, the ratios of ϕ/ϕ_f in all cases are close to the ratio of the fracture system's bulk volume to that of the estimated drainage volume (drainage area times h_f). This might provide some insights to the effects of homogenization on fracture porosity: the total fracture pore volume keeps unchanged but is divided by a much larger bulk volume, the bulk volume of the estimated drainage area, which actually has been implied by in the definition of EUR, as shown in Eq. (4.23).

$$\phi = \frac{B\ EUR/c_t(P_i - P_w)}{h_f A} \quad (4.23)$$

Because of such kind of "self-consistency", the fitted parameters such as η^*, k^* and the product $h_f c_t \phi$ are completely compatible with an arbitrary drainage area A, which means that without more information from other separate resources, trying to obtain an "objective" drainage area A only by iterations between data-fitting and type-curve generation is meaningless. And this "self-consistency" is probably the reason for the consistency and robustness of this model discussed in Section 4.4.

Even though the fracture-based model proposed previously can accurately reflect the occurrence of anomalous diffusion in the mid-time of production and estimate the EUR of the fracture system at least with noise-free simulation data, some obvious drawbacks exist reducing the feasibility of such model. First, all the above cases are done with a clearly specified $I_x = 1$, which is not the case in a practical application. Unlike in conventional reservoirs, creating

hydraulic fractures in unconventional reservoirs are known to be subject to the impacts of widely distributed natural fractures and stress-shadow effect (Fisher et al., 2004; Wu and Olsen, 2015), which makes the planar-fracture assumption unrealistic. Even though, according to the assumptions of the previous model, the pair (α, η^*) has accounted for the "tree-like branches" of hydraulic fractures (combined with other connected conductive fractures), it is hard, if not impossible, to credibly determine I_x in field cases. Moreover, as have been shown in the above data-fitting process, the fracture-based model lacks explanatory power to the data in the early period. The model with this shortcoming undesirably makes less use of the early-time flowback data, which to a large extent satisfies our model's assumptions and is supposed to reveal useful information about fractured reservoirs. In conclusion, though being concretely simplified to only having 3 parameters, the model based on the traditional multiple planar fracture framework still cannot be effectively applied in practice. In Section 5, all these drawbacks are resolved by viewing the fracture-well system from a new perspective based on an entire horizontal well.

4.6. Section Summary

1. The fracture-based model of fractional production decline is formulated by solving the diffusivity equation with temporal fractional order derivative within the traditional framework of a horizontal well with multi-stage planar fractures;
2. The corresponding type curves of this model are presented with 3 independent parameters (A_r, I_x, and α). The consistency and robustness of the parameter estimation procedure by such type curves is investigated using a synthetic case;
3. The trace of anomalous diffusion is identified when applying this fractured-based model to the intermediate-time synthetic production data of a pertinent reservoir simulation, with the early-time data being neglected;

4. Due to the "self-consistency" of this model as well as the request of estimating the parameters A_r and I_x and then iterating on them, the issue of non-uniqueness for applying this model is identified, which to some extent implies the limitations of such a traditional framework of a horizontal well with multi-stage planar fractures and will be resolved by the well-based models developed in Section 5.

5. FRACTIONAL PRODUCTION DECLINE MODEL BASED ON A HORIZONTAL WELL

5.1. Introduction

As discussed before, though the fracture-based model developed in Section 4 does capture some traces of anomalous diffusion due to the complex fracture network in the reservoir scale, practically applying this model for interpreting production data encounters some intractable difficulties rooted in the fundamental setting of this model (horizontal well intercepting multi-stage planar fractures), including the inconsistency between the complex fracture network, from which the component related to hydraulic fractures is hard to distinguish, and the planar fracture setting in the model, and the "self-consistency" of the model that makes iterations on the uncertain parameters almost impossible. Also, the screen-out of the early-time data is sort of subjective, which leads the fitting of the intermediate-time data subject to be questioned.

To resolve these difficulties and develop a more feasible inverse-problem tool, we will inherit the sub-diffusion governing equation but recast the problem domain into one based on the whole horizontal well. Firstly, no source terms are accounted for, which results in a model (Model I) that characterizes the production performance with 4 parameters and is very useful for interpreting the production data mainly due to the flow only through fracture systems, such as the flow-back data in the initial one to two months of production. Then, a source term based on standard diffusivity equation is incorporated into the model of tempered sub-diffusion, which leads to a 7-parameter model (Model II) capable of modeling the whole sequence of flow regimes of the production from a multi-fractured horizontal well in unconventional reservoirs.

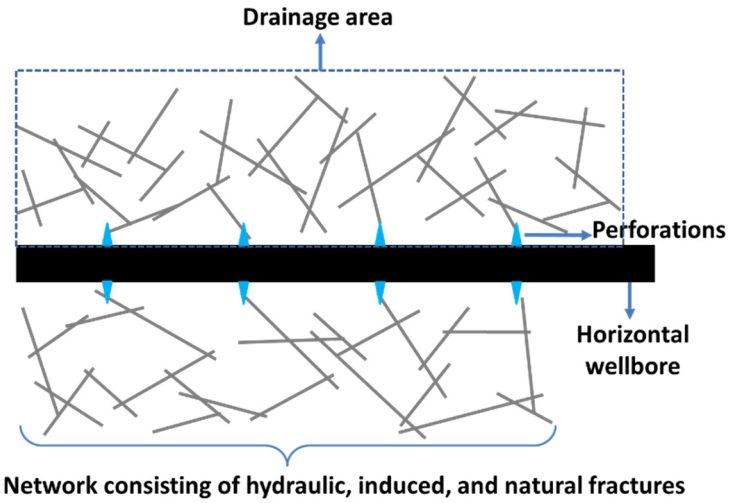

Figure 5.1 – Schematic of the well-based model with hydraulic fractures merged into fracture networks and horizontal wellbore to be an infinite conductivity flowing channel

5.2. Well-Based Model for the Flow Only Through Fracture Systems (Model I)

As illustrated in **Fig. 5.1**, given the significantly non-planar hydraulic fractures in unconventional reservoirs, they are merged into complex fracture networks and their effects on flow or production are structurally accounted for in (α, η^*). Compared to both matrix and fractures in a reservoir, a horizontal wellbore perfectly serves as an infinite conductivity flow channel. Furthermore, because of the elongated length of a typical horizontal well and the ultra-low permeability of matrix in unconventional reservoirs, the flow through the formation beyond the range of a horizontal well can be neglected compared to the amount of flow within the range. Therefore, this flow channel is regarded as a fully penetrating one, that is $I_x = 1.0$. Consequently, we have formulated a simplified 1-D problem, whose dimensional domain is shown is **Fig. 5.2**.

5.2.1. Model Description

This well-based model takes all the assumptions for the fracture-based model in Section 4.2 except the third and fourth items about hydraulic fractures. Also, it only models the flow through fracture systems.

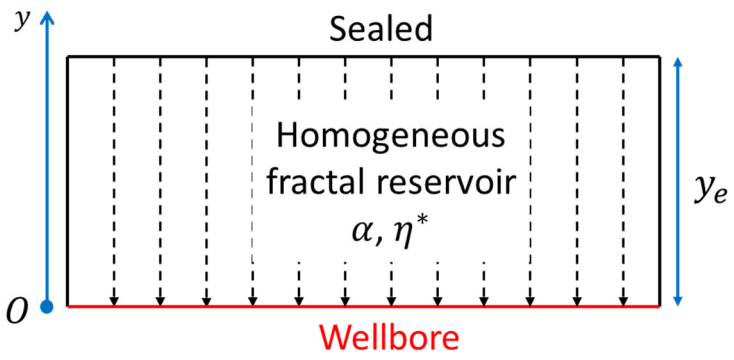

Figure 5.2 – Dimensional problem domain of the 1D well-based model

In the 1D problem domain as **Fig. 5.2** shows, the governing equation involving sub-diffusion takes fractional order derivative as temporal operator and Laplacian as spatial operator as Eq. (5.4a), similar to Eq. (4.6).

$$\frac{1}{\eta^*}\frac{\partial^\alpha}{\partial t^\alpha}P = \frac{\partial^2}{\partial y^2}P \quad \text{(5.4a)}$$

Regarding the boundary conditions, on the upper boundary zero Neumann condition still holds, while more concerns should be given to the boundary of wellbore. Compared to the part of formation far away from the wellbore, the flow in the region adjacent to the wellbore is characterized by the convergence into perforations, which would cause significant extra pressure drop in this small region (**Fig. 5.3 (a)**). This extra pressure drop is accounted for conventionally by adding it into the corresponding boundary condition acting as a thin skin. An analogy of this extra pressure drop can be made to the convergence skin proposed by Mukherjee and Economides (1991). As shown in **Fig. 5.3 (b)**, with respect to an individual perforation, the flow in the adjacent formation occurs in a manner close to a hemisphere. The length, width, and height of this convergence region are denoted as x_c, y_c, and h_f. x_c is an average length of stage and cluster spacings along a horizontal well. y_c is the estimated distance between the edge of perforation and the end of convergence region. And h_f can be regarded as the effective height of the fractured

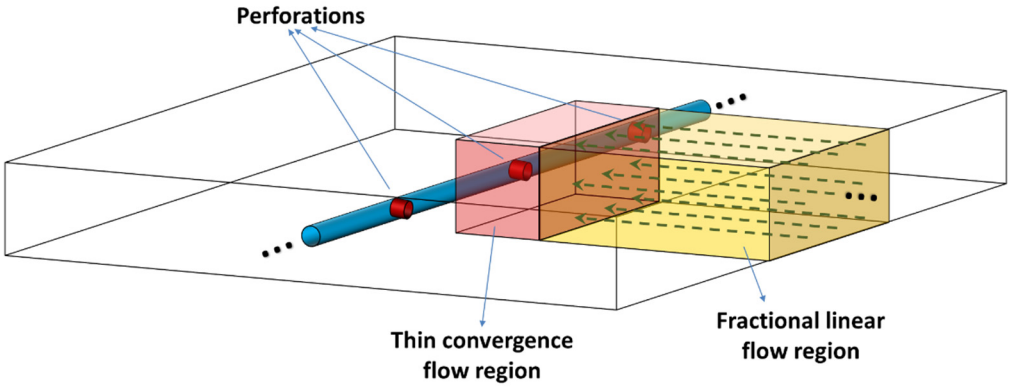

(a)

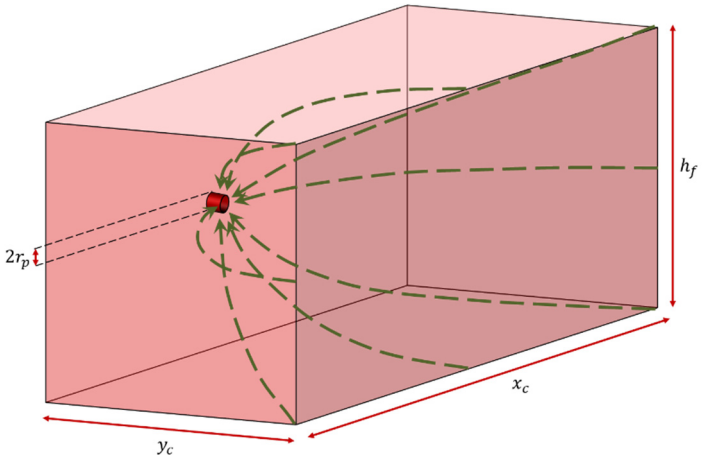

(b)

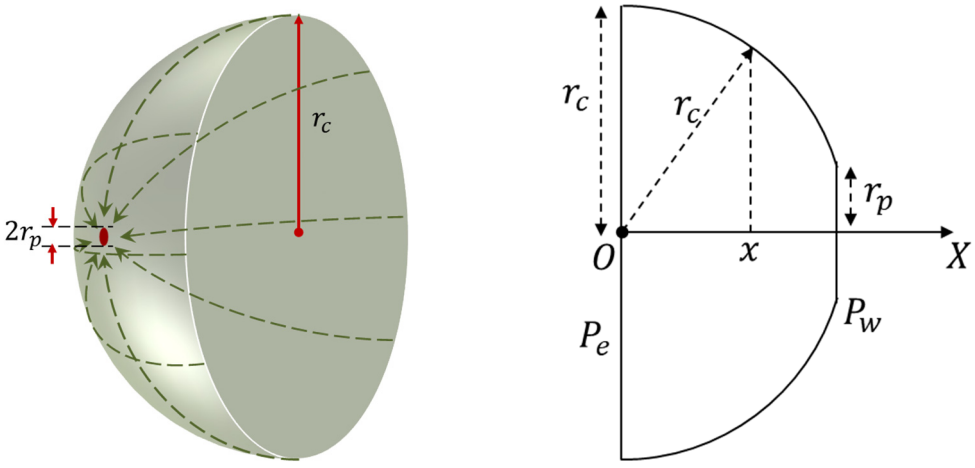

(c) (d)

Figure 5.3 – Schematics of the convergence region close to an individual perforation and the stabilized hemispherical flow to model this region

formation. Based on the state-of-the-art completion design and fracturing model results (Xiong et al., 2019), the cluster spacing is close to the height of majority fractures, which means x_c roughly equals h_f. Therefore, for simplicity, we model the convergence flow on such domain as a stabilized flow through a hemisphere whose radius is $r_c = \sqrt[3]{2\,x_c y_c h_f}/2$, as shown in **Fig. 5.3 (c)**. Also, Darcy's law is employed in this region because the limited volume and concentrated massive flow in this region would vastly shorten the fractional transient period. More importantly, in this region, due to the finiteness of the fracture network, the complete sequence of flow regimes is better off being physically described by the tempered anomalous diffusion (Meerschaert et al., 2008; Yang, 2018), which shows characteristics of regular anomalous diffusion in the early and intermediate time, but ends up with an exponential decline in the late time corresponding to a memoryless flux law like the regular Darcy's law. Therefore, Darcy's law can be logically used during the stabilized flow regime in a homogenized fractal reservoir. According to the derivation in Appendix F. the extra pressure drop is related to the flow rate as shown in Eq. (5.1).

$$\Delta P_c = q_p \frac{\mu}{\pi k_f r_c} \operatorname{arctanh}\left(\sqrt{1-\frac{r_p^2}{r_c^2}}\right) \quad \text{.....(5.1)}$$

where ΔP_c is the extra pressure drop, q_p is the flow rate through a typical perforation, μ is the fluid viscosity, r_p is the radius of such perforation, r_c is the radius of the hemisphere ($r_c = \sqrt[3]{2\,x_c y_c h_f}/2$), and k_f is the permeability of a typical fracture adjacent to perforations. And k_f can be estimated by the permeability of propped fractures under stress.

From the perspective of the fractal reservoir, the flow rate q_p is related to the fractional flux (Eq. (4.11)) through the lower boundary of the 1D domain, as shown as Eq. (5.2).

$$\vec{v} = -\frac{k^*}{\mu}\frac{\partial^{1-\alpha}}{\partial t^{1-\alpha}}\nabla P \quad \text{.....(4.11)}$$

$$q_p = |\vec{v}|_{y=0} x_c h_f = x_c h_f \frac{k^*}{\mu} \frac{\partial^{1-\alpha}}{\partial t^{1-\alpha}} \left(\frac{\partial P}{\partial y} \right)_{y=0} \quad \text{.....(5.2)}$$

Therefore, the extra pressure drop is finally expressed as a function of P by substituting Eq. (5.2) into Eq. (5.1) to obtain Eq. (5.3).

$$\Delta P_c = \frac{k^*}{k_f} \frac{x_c h_f}{\pi r_c} \operatorname{arctanh}\left(\sqrt{1 - \frac{r_p^2}{r_c^2}} \right) \frac{\partial^{1-\alpha}}{\partial t^{1-\alpha}} \left(\frac{\partial P}{\partial y} \right)_{y=0} \quad \text{.....(5.3)}$$

Based on the above discussions, in the dimensional domain the governing equation as well as the initial and boundary conditions is as Eq. (5.4) shows.

$$\frac{1}{\eta^*} \frac{\partial^\alpha}{\partial t^\alpha} P = \frac{\partial^2}{\partial y^2} P \quad \text{.....(5.4a)}$$

$$P(y, t = 0) = P_i \quad \text{.....(5.4b)}$$

$$\frac{\partial P}{\partial y}(y = y_e, t) = 0 \quad \text{.....(5.4c)}$$

$$P(y = 0, t) = P_w + \Delta P_c = P_w + \frac{k^*}{k_f} \frac{x_c h_f}{\pi r_c} \operatorname{arctanh}\left(\sqrt{1 - \frac{r_p^2}{r_c^2}} \right) \frac{\partial^{1-\alpha}}{\partial t^{1-\alpha}} \left(\frac{\partial P}{\partial y} \right)_{y=0} \quad \text{.....(5.4d)}$$

New dimensionless groups are introduced in this 1D model. In the definitions of dimensionless flow rate q_D and cumulative production Q_D, N_p stands for the number of effective perforations and the factor 2 for the spread of fracture networks on both sides of a horizontal well. EUR represents the ultimate recovery from the conductive fracture network, which directly corresponds to the effective volume of a fracture system. After substituting these definitions into Eq. (5.4), the corresponding dimensionless form is shown in Eq. (5.5).

$$P_D = \frac{P_i - P}{P_i - P_w}, \qquad y_D = \frac{y}{y_e}, \qquad t_D = \left(\frac{\eta^*}{y_e^2} \right)^{\frac{1}{\alpha}} t = \frac{t}{\tau},$$

$$c = \frac{k^*}{k_f}\left(\frac{y_e^2}{\eta^*}\right)^{\frac{\alpha-1}{\alpha}} \frac{x_c h_f}{\pi r_c y_e} \operatorname{arctanh}\left(\sqrt{1-\frac{r_p^2}{r_c^2}}\right),$$

$$q_D = \frac{\mu B q_{sc} y_e}{2\,k^* x_c h_f N_p (P_i - P_w)}\left(\frac{y_e^2}{\eta^*}\right)^{\frac{1-\alpha}{\alpha}} = \frac{\tau}{EUR} q_{sc}, \qquad Q_D = \int_0^{t_D} q_D \, \mathrm{d}t_D = \frac{BQ_{sc}}{2 y_e x_c h_f N_p c_t \phi (P_i - P_w)} = \frac{Q_{sc}}{EUR}$$

$$\frac{\partial^\alpha}{\partial t_D^\alpha} P_D = \frac{\partial^2}{\partial y_D^2} P_D \quad \text{.....(5.5a)}$$

$$P_D(y_D, t_D = 0) = 0 \quad \text{.....(5.5b)}$$

$$\frac{\partial P_D}{\partial y_D}(y_D = 1, t_D) = 0 \quad \text{.....(5.5c)}$$

$$P_D(y_D = 0, t_D) = 1 + c\frac{\partial^{1-\alpha}}{\partial t_D^{1-\alpha}}\left(\frac{\partial P_D}{\partial y_D}\right)_{y_D=0} \quad \text{.....(5.5d)}$$

After being transformed into Laplace domain, the above equations take the form shown in Eq. (5.6).

$$s^\alpha \tilde{P}_D = \frac{\partial^2}{\partial y_D^2}\tilde{P}_D \quad \text{.....(5.6a)}$$

$$\frac{\partial \tilde{P}_D}{\partial y_D}(y_D = 1, s) = 0 \quad \text{.....(5.6b)}$$

$$\tilde{P}_D(y_D = 0, s) = \frac{1}{s} + c s^{1-\alpha}\left(\frac{\partial \tilde{P}_D}{\partial y_D}\right)_{y_D=0} \quad \text{.....(5.6c)}$$

In Laplace domain, the boundary value problem in Eq. (5.6) is solved (Appendix G) to gain the solution $\bar{P}_D$, as shown in Eq. (5.7).

$$\tilde{P}_D(y_D, s) = \frac{\cosh\left(s^{\alpha/2}(y_D - 1)\right)}{s\cosh(s^{\alpha/2}) + c\, s^{2-\alpha/2}\sinh(s^{\alpha/2})} \quad \text{.....(5.7)}$$

A relationship between flow rate and integral of pressure, similar to Eq. (C9), still holds except without a minus sign. And Similar derivation can be done by following the steps in Appendix E. Thus, in Laplace domain, we have the expressions as Eq. (5.8) and Eq. (5.9).

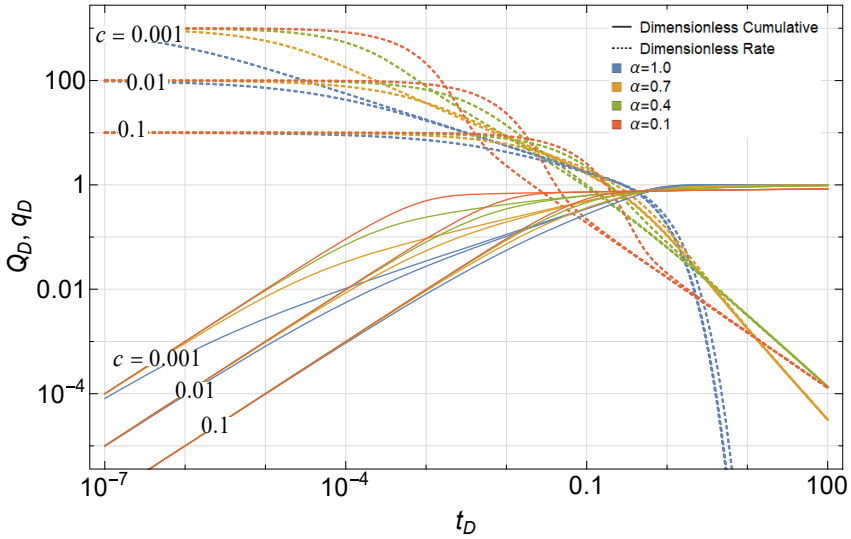

Figure 5.4 – Type curves of dimensionless rate and cumulative for the well-based fractional production decline model without source terms

$$\tilde{Q}_D = \mathcal{L}\left\{\int_0^{t_D} q_D \, \mathrm{d}t_D\right\} = \mathcal{L}\left\{\int_0^{t_D}\left(\frac{d}{dt'_D}\int_0^1 P_D \, \mathrm{d}y_D\right)\mathrm{d}t'_D\right\} = \mathcal{L}\left\{\int_0^1 P_D \, \mathrm{d}y_D\right\}$$

$$= \int_0^1 \tilde{P}_D \mathrm{d}y_D = \frac{1}{c\, s^2 + s^{1+\alpha/2}\coth(s^{\alpha/2})} \quad \text{.....(5.8)}$$

$$\tilde{q}_D = \mathcal{L}\{q_D\} = \mathcal{L}\left\{\frac{d}{dt_D}\int_0^1 P_D \mathrm{d}y_D\right\} = s\int_0^1 \tilde{P}_D \mathrm{d}y_D = \frac{1}{c\, s + s^{\alpha/2}\coth(s^{\alpha/2})} \quad \text{.....(5.9)}$$

Q_D and q_D in physical domain are obtained by conducting numerical inverse Laplace transform on the above $\tilde{Q}_D$ and $\tilde{q}_D$. Gaver-Wynn-Rho (GWR) algorithm (Valkó and Abate, 2004) is employed to guarantee a reliable inverse transformation. And the resulting type curves are displayed in **Fig. 5.4**.

Unlike the previous type curves in **Fig. 4.3** whose generation depends on some other parameters, the current well-based type curves are universal, which means that they are directly used to fit any sets of production data satisfying the model's assumptions and then the horizontal shift, the vertical shift, and the parameters of the best-fitted curve reasonably provide some relevant

information for a specific fractured reservoir as well as its completion. The steps of applying these type curves are showcased in the following case studies.

After completing a typical data-fitting process, four fitted parameters are gained, which are α, c (both from the characterization parameters of the best-fitted curve), τ (from the horizontal shift), and EUR (from the vertical shift). Based on these parameters, other useful average information can be extracted. If we still assume the compressibility of the homogeneous fractal reservoir is identical to that of the original one, and the product $x_c N_p$ is the lateral length of a horizontal wellbore, L_H, the pore volume of a typical cross section of the SRV orthogonal to the wellbore can be estimated by Eq. (5.10).

$$2y_e h_f \phi = \frac{B\ EUR}{L_H c_t (P_i - P_w)} \quad \text{.....(5.10)}$$

And if somehow the average effective height of the fracture network is obtained, we can get the product of $y_e \phi$ by Eq. (5.11).

$$y_e \phi = \frac{B\ EUR}{2h_f L_H c_t (P_i - P_w)} \quad \text{.....(5.11)}$$

Then by combining the definition of η^* and τ, the quotient of y_e/k^* is gained by Eq. (5.12).

$$\frac{y_e}{k^*} = \frac{\tau^{\alpha}}{c_t\ \mu\ (y_e \phi)} \quad \text{.....(5.12)}$$

Finally, by submitting the above relevant values in to the definition of c and recalling the relation $r_c = \sqrt[3]{2\ x_c y_c h_f}\ /2$, the range of the convergence region, y_c, can be estimated by solving the transcendental equation in Eq. (5.13) if x_c is approximated with some type of average cluster and stage spacings.

$$\frac{\pi}{2^{2/3}} \left(\frac{y_e}{k^*}\right) \tau^{1-\alpha} k_f c \ = \ \sqrt[3]{\frac{x_c^2 h_f^2}{y_c}} \operatorname{arctanh}\left(\sqrt{1 - \frac{4\ r_p^2}{\left(2x_c y_c h_f\right)^{2/3}}}\right) \quad \text{.....(5.13)}$$

In the next section, the application of the new type curves is going to be shown on some synthetic and field data. And when other information is available the corresponding parameters are calculated following the procedure through Eq. (5.10) to Eq. (5.13).

5.2.2. Application to Data from Different Sources

In this section, using our new well-based type curves we first analyze the three synthetic cases previously analyzed by the fracture-based model. And then more synthetic cases with different complex fracture networks are analyzed with the new model. At last, this model is applied to some field cases to test its feasibility.

5.2.2.1. Previous Three Synthetic Cases

Without the need of estimating or specifying A_r and I_x, the production data of the previous synthetic cases used in Section 4.5 is directly fitted to the universal well-based type curves. And due to the introduction of the convergence term, the early-time local effects are also accounted for to some extent. Thus, only the late exponential decline data needs to be screened out in the complex fracture case. The time range of the used production data is $t \in (0, 10]$ with 80 data points.

Both rate fitting and cumulative fitting are conducted. The fitted plots are shown in **Fig. 5.5**, in which the data used in fitting process is colored with blue or purple and some subsequent data is shown by gray dots.

By comparing **Fig. 4.8** and **Fig. 5.5**, the improvement of the new well-based model is apparent. The early-time data which is unable to be fitted by the fracture-based model is desirably tracked by the new type curve. That is, the new model is capable of interpreting both the early- and intermediate-time production performance and to some extent accurately catch the transient behavior of the flow in discrete fracture networks. Also, in **Fig. 5.5** all the gray parts of rate data, the data beyond 10 d and not used in data-fitting, follow the fitted type curves for a while and then

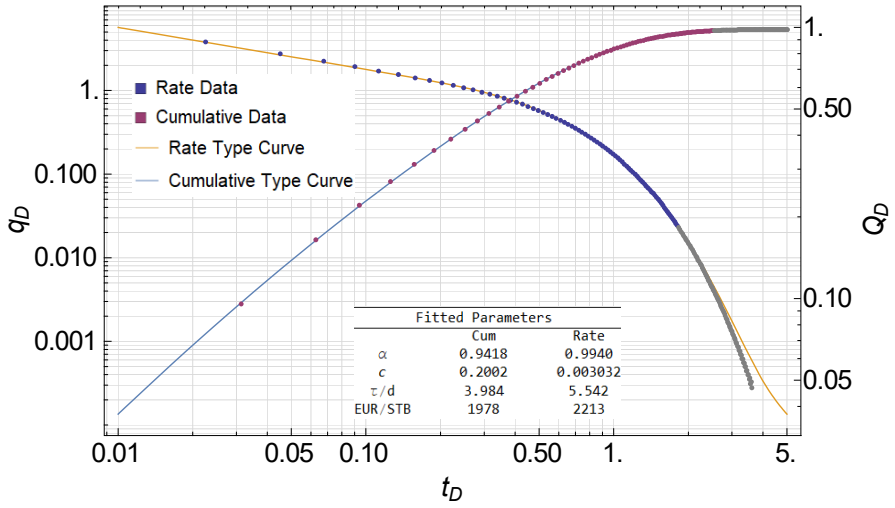

(a)

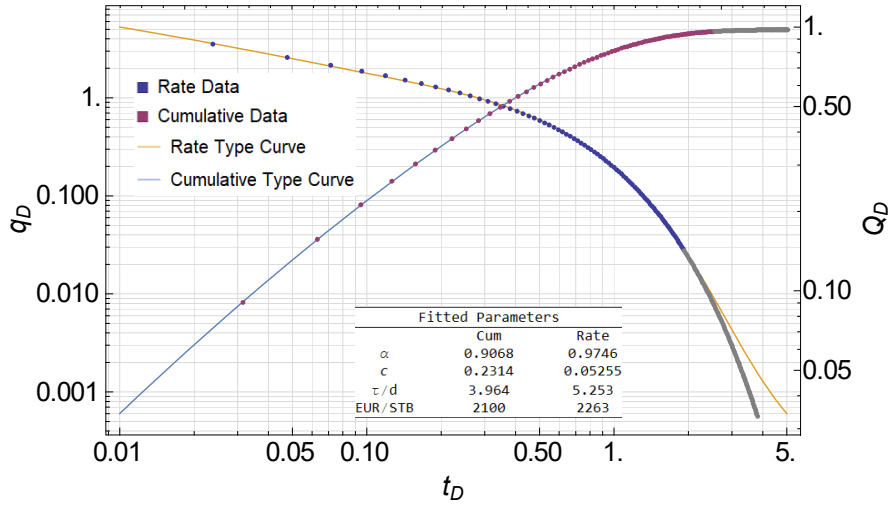

(b)

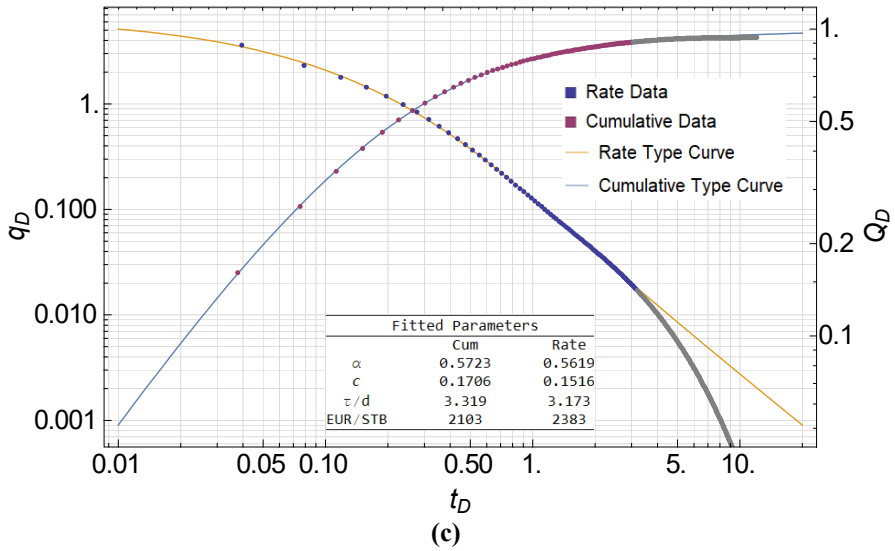

(c)

Figure 5.5 – Results of fitting synthetic data of previous cases to the corresponding well-based type curves. (a) Evenly distributed fracture case. (b) Unevenly distributed fracture case. (c) Complex fracture case.

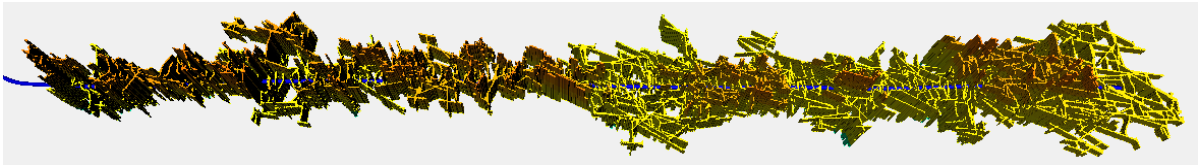

(a)

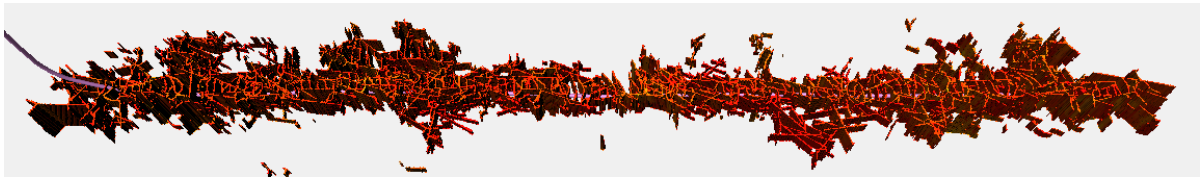

(b)

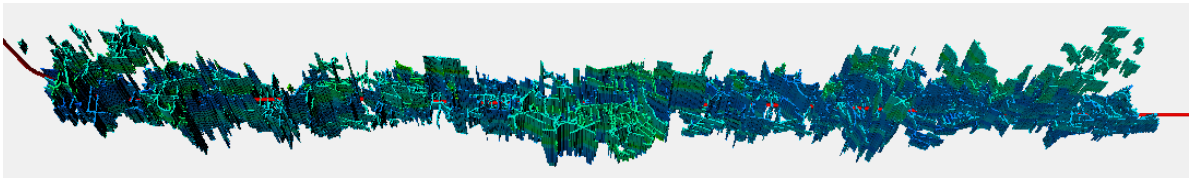

(c)

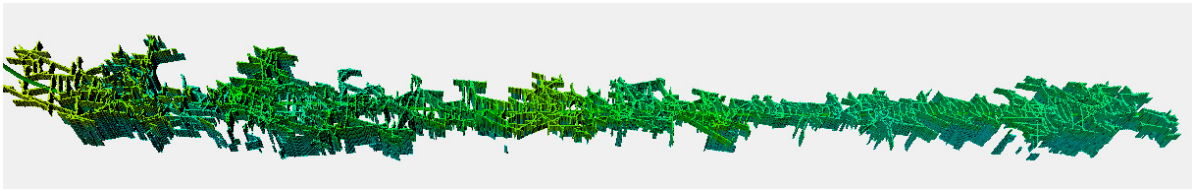

(d)

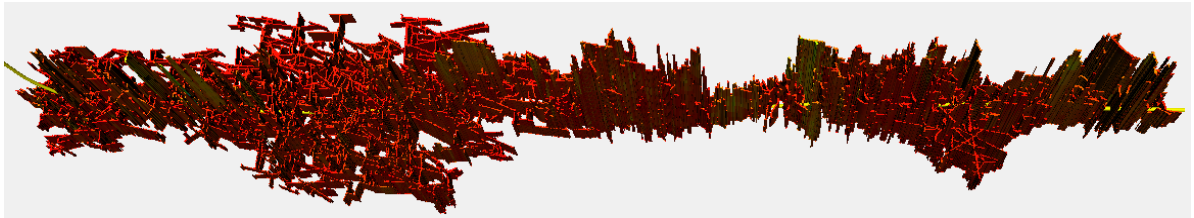

(e)

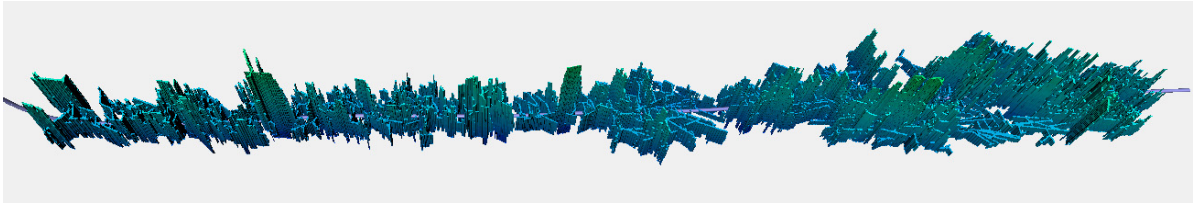

(f)

Figure 5.6 – 3D views of the complex fracture grids for the reservoir simulation models of 6 wells. (a) Well A. (b) Well B. (c) Well C. (d) Well D. (e) Well E. (f) Well F.

gradually transition to faster decline than what predicted by the type curves. This phenomenon has been expected and discussed previously as the late exponential decline due to the system's finiteness.

By comparing the fitted parameters, the cumulative fitting of two orthogonal cases results in smaller αs than the rata fitting results, which is opposite to the results of fracture-based model. Given the fact of one-layer grids and the flow paths normal to the infinite conductivity sink, the rate fitting of these two cases seems to yield more credible results, whose α is close to the unity and convergence term c is relatively small. Additionally, data-fitting for the complex fracture case yields satisfactory results because the fitted parameters of both ways are close to each other, which does provide us a reliable set of parameters to characterize the corresponding fracture network. The uniform over-estimation of EUR by using the current version of fractional model is also expectable due to the negligence of the late exponential decline.

5.2.2.2. Other Complex Fracture Cases

To apply the well-based type curves (**Fig. 5.4**) to the scenarios of producing from a whole horizontal well, we first run six reservoir simulation cases with different complex fracture networks, whose 3D views are shown in **Fig. 5.6**. Like the settings of the previous simulations, only the grids of fractures are activated to only simulate flow through fractures, and all 6 models simply contains water to implement single-phase flow. Also, the well condition is set as constant bottom-hole pressure. The detailed parameters of the 6 models are listed in **Table. 5.1**.

With the simulated production data, the well-based type curves are applied to them to interpret the corresponding anomalous diffusion due to complex fracture networks. In each case, the production data of the first 20 d (160 points) is used in the fitting process. The fitted curves with corresponding data are displayed in **Fig. 5.7** and the fitted parameters are summarized in

Table 5.1 – Model and fitted parameters of applying well-based model to 6 wells with complex fracture networks

		Well A	Well B	Well C	Well D	Well E	Well F
Model	Grid volume / ft^3	3.538E+8	3.320E+8	2.891E+8	3.288E+8	4.737E+8	2.564E+8
	Rock c_f / psi^{-1}	7.000E-6					
	Water c_w / psi^{-1}	2.744E-6					
	Water μ / cP	0.3985					
	Water B / RB/STB	1.0132					
	ϕ_f	0.01					
	k_f /mD	0.5					
	Initial S_w	1.0					
	Initial pressure / psi	4206	4308	4445	4149	4788	4837
	BHP / psi	3700	3700	3700	3700	4000	4000
	EUR / STB	3069	3460	3692	2531	6399	3679
Cum fitting	α	0.8377	0.7103	0.754	0.7053	0.7629	0.65
	c	0.1618	0.149	0.1565	0.113	0.1074	0.1319
	τ / d	5.299	9.060	5.654	6.533	12.02	8.197
	Fitted EUR / STB	3127	3484	3530	2534	6677	3862
	EUR dev / %	1.89	0.68	4.39	0.12	4.35	4.98
Rate fitting	α	0.9009	0.5866	0.5374	0.6151	0.7641	0.6247
	c	0.03849	0.1453	0.2527	0.123	0.07525	0.1138
	τ / d	6.742	9.981	5.432	6.74	12.86	8.659
	Fitted EUR / STB	3362	3833	3890	2793	7076	4153
	EUR dev / %	9.55	10.77	5.36	10.36	10.58	12.89

Table. 5.1. As before, the colored points represent the data used in data-fitting, while the gray dots are the subsequent production beyond the first 20 d.

Except the first rate point of Well B, C, and D, almost all the data points used are firmly tracked by the fitted curves, which displays the explanatory power of our model regarding the production during transient regime of the flow through fracture systems. And compared to the rate data, the cumulative data well tracks the curves even from 0.125 hr, which is a reflection of the average nature of our model. Also, most of the subsequent gray parts follow the fitted curve until they begin the transition into exponential decline. The relatively early begin of the transition like Well A and F may indicate a limited pore volume in the fracture system. In contract, the gray part

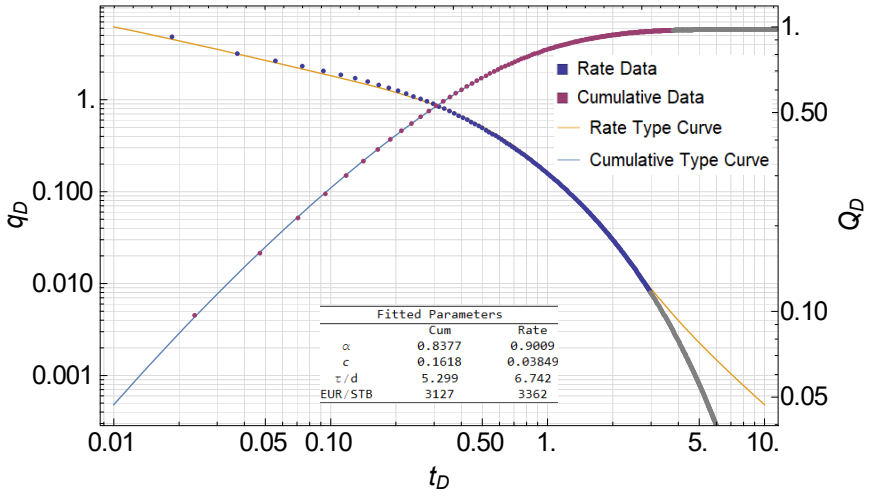

(a)

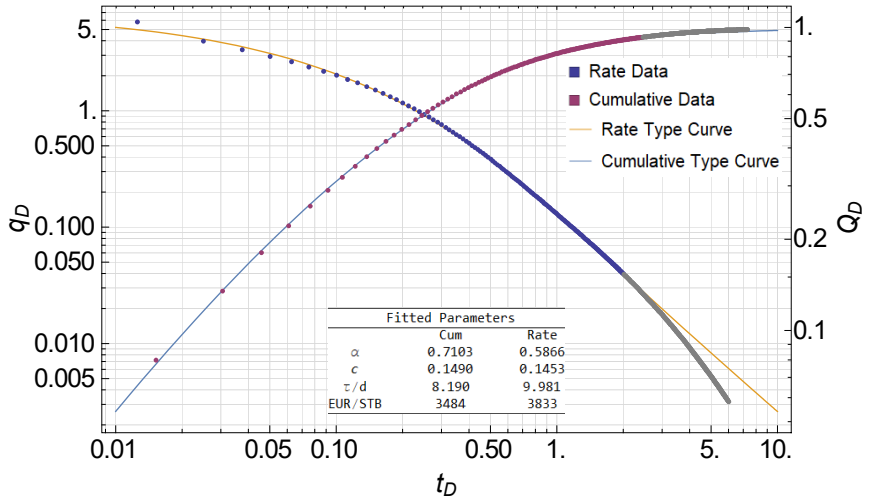

(b)

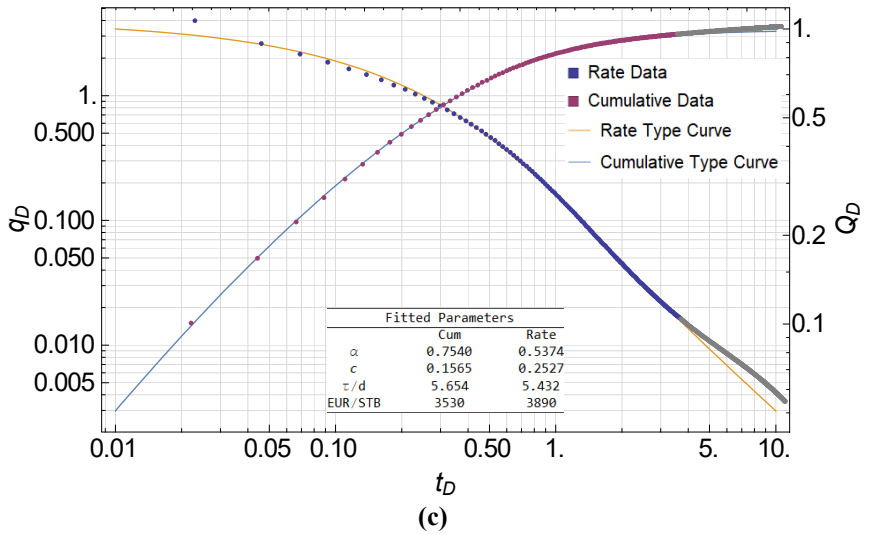

(c)

Figure 5.7 – Results of fitting simulated production data of 6 models with complex fracture networks. (a) Well A. (b) Well B. (c) Well C. (d) Well D. (e) Well E. (f) Well F.

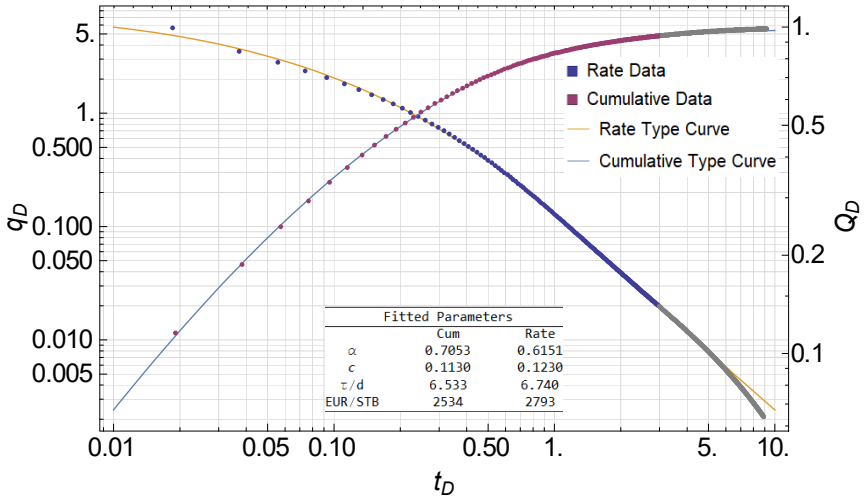

(d)

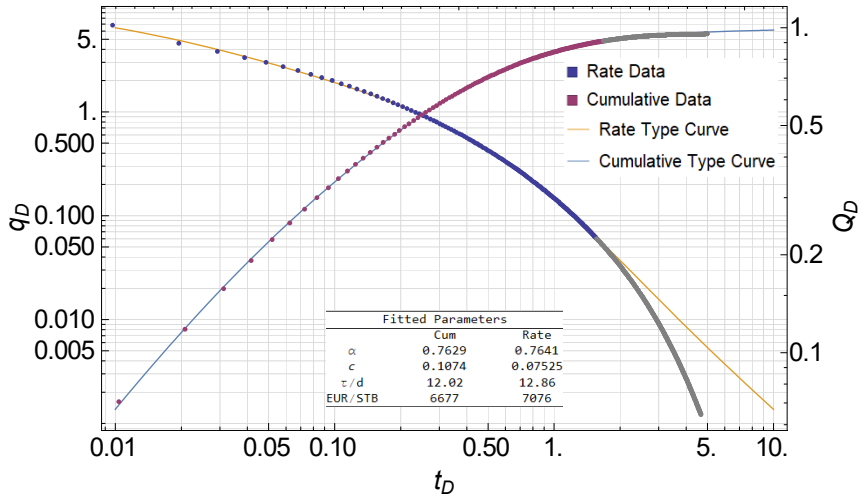

(e)

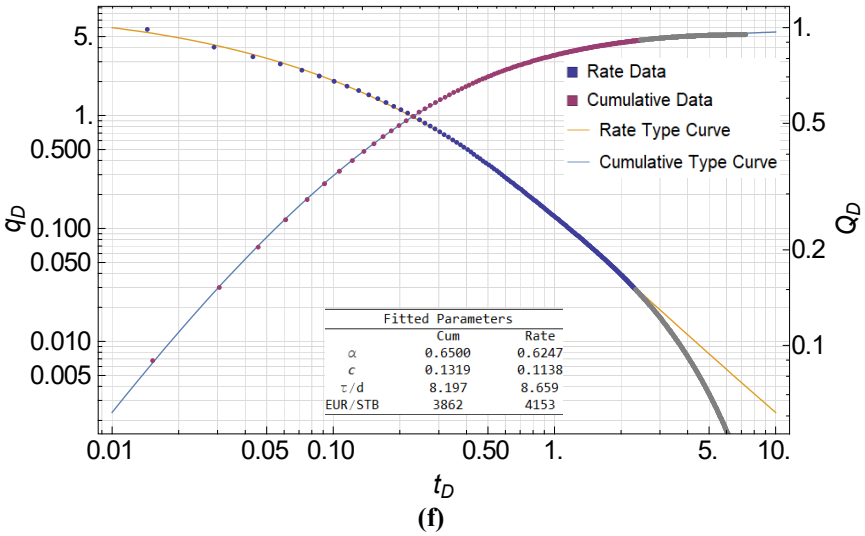

(f)

Figure 5.7 Continued

of Well D follows the fitted curve for nearly $1/3$ log cycle, which perhaps due to the relatively larger pore volume or higher complexity of its fracture network.

The most interesting well is Well C, which uniquely shows a concave-up in its gray part. This phenomenon is attributed to a refilling effect from a relatively isolated section of its fracture system, which is embodied like a dual-porosity signature on the rate plot. The refilling effect can be also seen from cumulative data. The gray part of cumulative data finally passes through the asymptotic unit line, which results into a unique underestimate of EUR by cumulative fitting in this case (**Table. 5.1**). Because Well D is located close to another well, their fracture network grids directly connect to each other. When we were dividing the whole network into well-based ones, a part of grids, which mainly belongs to another well but has some connections to Well D, was accidentally assigned to D. That's the source of the "relatively isolated section".

Among the 6 wells, Well E and Well F have a relatively consistent fitted parameters between the two ways, which may indicate a more credible characterization for the corresponding fractures. And despite the discrepancies in other parameters c and τ are consistent in most cases. Especially for c, which is an indicator to the quality of completion by our definition, its consistency rises the possibility of using this model as a direct tool for evaluating completion quality with respect to production.

Because the only complexity in the used simulation model comes from their complex grid topology, which represents complex fracture networks, the incredibly good fitting in the transient regime as well as the resulting anomalous diffusion related parameters from the back calculation provides a strong support for our proposal about the major source of anomalous diffusion in the reservoir scale. And for the limited space, the further calculations based on Eq. (5.10) to Eq. (5.13) aren't included in the current manuscript.

5.2.2.3. Field Cases

We choose two multi-fractured horizontal wells in the Permian Basin to showcase the application of the proposed model. Even though various elements may have impacts on the anomalous production performance as mentioned previously, during the initial 1 to 2 months of production the performance, in our opinion, is to a large extent relevant to the complex fracture network, because this period is mostly covered by flowback whose natural-flow scheme is relatively simple. Also, many wells experience two-phase flow of oil and water during this period. Compared with the multi-phase flow involving gas, this two-phase flow just introduces relatively slight non-linearity and is often lumped together to be considered as single-phase flow in many RTA calculations. Therefore, the application of the proposed model is focused on the well's production in this period.

First, by observing the evolution of gas oil ratio (GOR) (**Fig. 5.8**), the GOR of both well is maintained on a stable level before 40 d. Therefore, we can regard the flow in the formation as oil-water two phase flow. During this period, the bottom-hole pressure keeps decreasing. This variable pressure is roughly got rid of by normalizing the daily liquid production by drawdown pressure. In the calculation of drawdown pressure, it is the pressure in the fracture right before the production that is employed, which is supposed to be higher than the reservoir initial pressure due to the fracturing treatment. The normalized daily liquid production is then summed up to be used in the place of cumulative production. The plots of normalized daily production vs. time for the two wells in the first 40 d are shown in **Fig. 5.8**. For Well 1, two outliers occur at 15 d and 25 d, which are excluded in the rate fitting process.

The fitted curves with corresponding data are shown in **Fig. 5.9**. Due to the noise contained, the limited number of points, and the tolerant drawdown normalization, the representativeness of

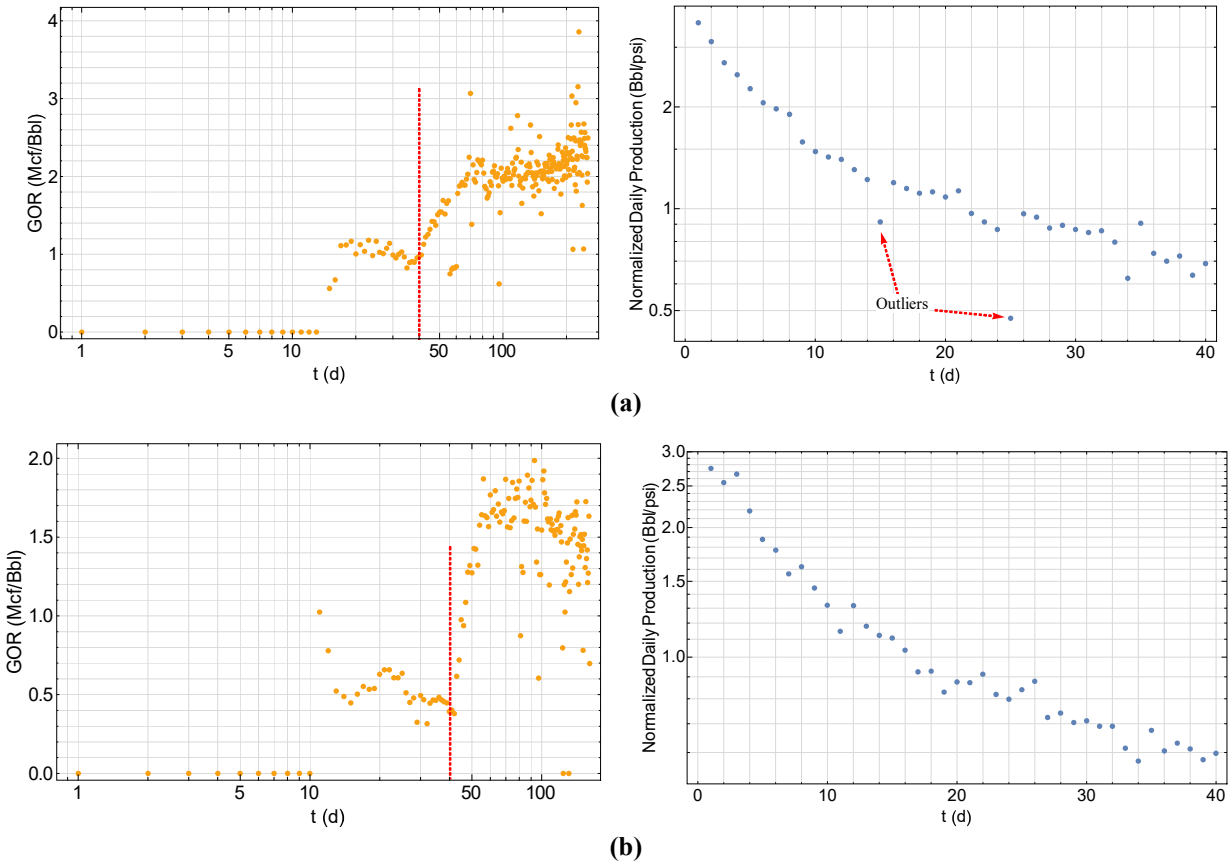

Figure 5.8 – GOR evolution and normalized daily liquid production for the two Permian Basin wells. (a) Well 1. (b) Well 2.

the fitted parameters isn't guaranteed. However, the mentioned consistency of c between two fitting methods still holds to some extent, which may tell us something about the effects of completion on production and can be used to make correlations with fracturing treatment designs.

5.2.3. Relevant Discussion

Based on the results of the above case studies on different kinds of production data, the well-based type curves of fractional decline model gain some possibilities for the application to real-world problems. As illustrated in **Fig. 5.10**, a primary workflow can be: analyze the evolution of GOR with respect to production time of the well of interest to get the period when only liquid flow occurs in the formation; screen out the production data of late exponential decline, if occurs, during the liquid flow period in semi-log production rate plot, or just select the data in the initial

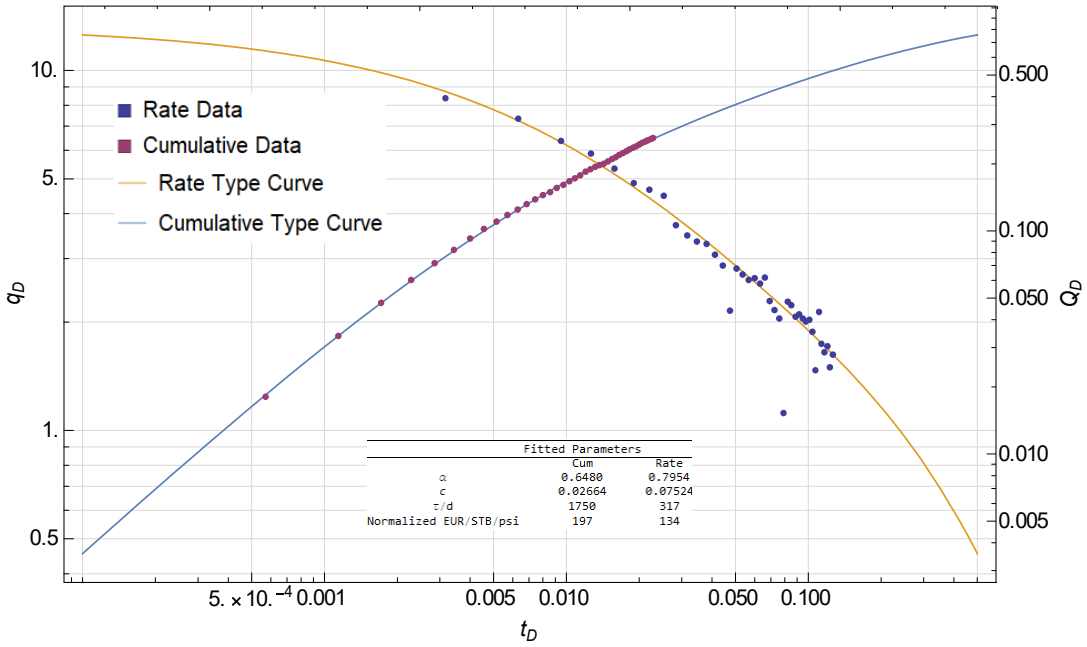

(a)

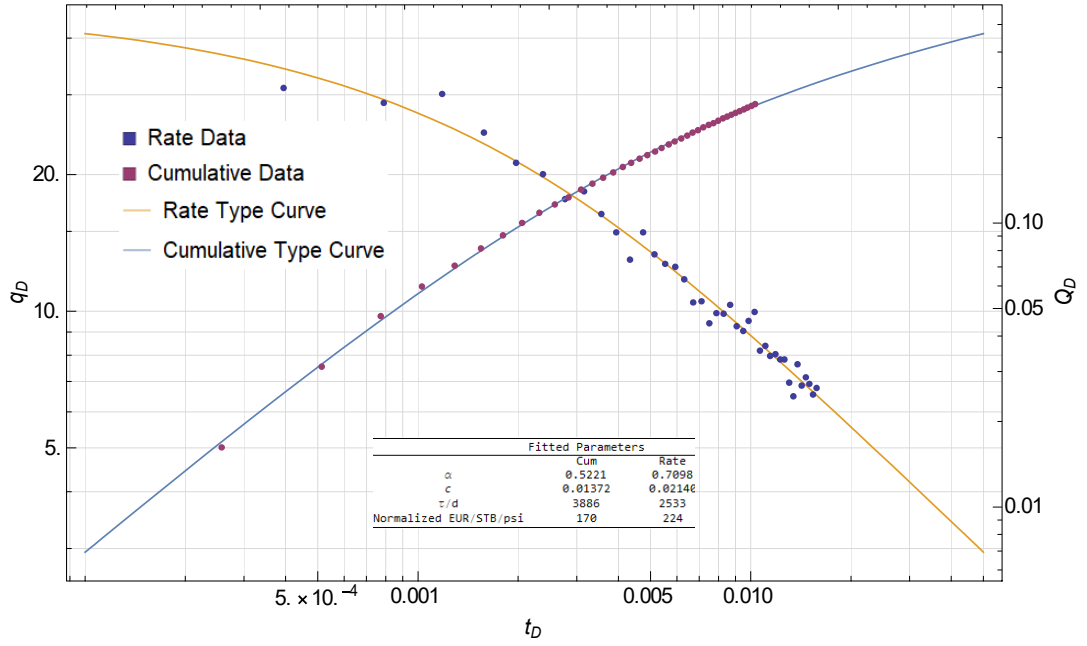

(b)

Figure 5.9 – Results of fitting field production data of the two Permian Basin wells. (a) Well 1. (b) Well 2.

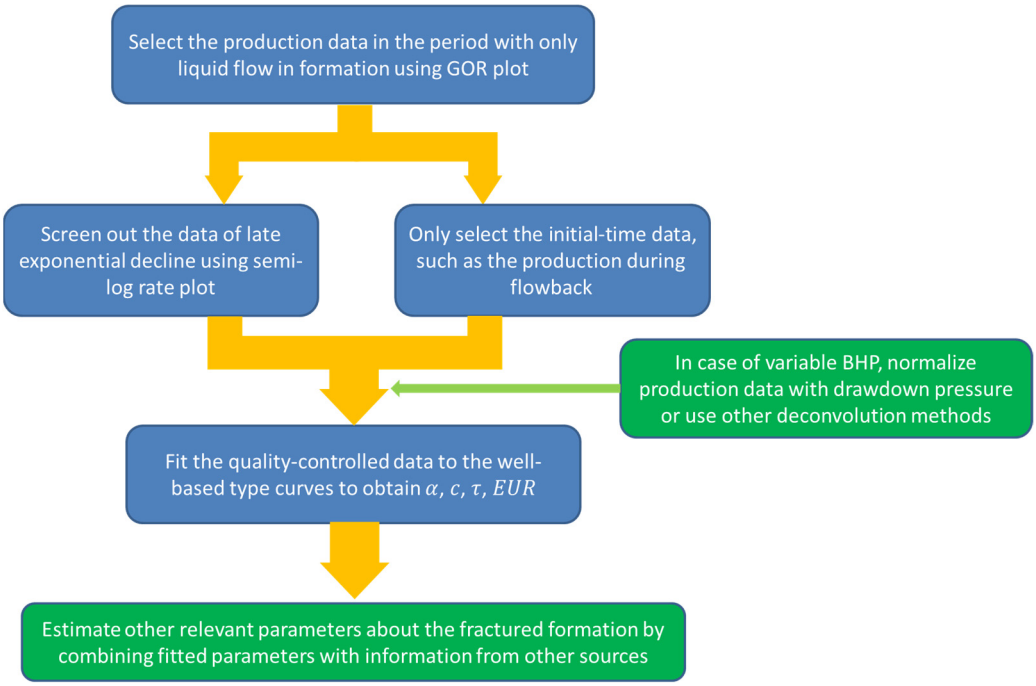

Figure 5.10 – A typical workflow of applying the well-based model to interpret production data

time of this period, such as the data during flowback; conduct data-fitting on the quality-controlled production data with the well-based type curves to get 4 fitted parameters; other relevant information about the highly fractured formation is estimated by combining the fitted parameters with parameters from other sources. If the bottom-hole pressure is not constant during the production, an approximate approach is using the production data normalized by drawdown pressure like we did in the field case study, if no other more rigorous deconvolution methods are available.

In some case studies above and the proposed workflow, we have constantly suggested to screen out the data of the late exponential decline because of the conflict between our model's infinite spatial resolution and the finiteness of real fracture systems or numerical models. Actually, as we have mentioned above, the late exponential decline can be readily incorporate into the fractional model using tempered anomalous diffusion (Meerschaert et al., 2008; Yang, 2018). If

this modification was made, then the whole production period should be able to be fitted to the modified type curves, if the assumption of single-phase flow and the condition of no source terms are satisfied. However, to our experience, for real flow occurring in fractured unconventional reservoirs, the influx from matrix would dominate probably before the late exponential decline begins in the fracture system, let alone the occurrence of gas flow in the late time of production. Thus, in order to develop a feasible tool for analyzing the early-time singe-phase/liquid flow, we choose not to bother introducing one more parameter to be fitted with considering tempered anomalous diffusion. Furthermore, the tempering factor will be considered in the model with source terms that is to be developed in Section 5.3.

As we have discussed in Section 4.5 about fracture-based model, "mapping" flow in discrete fractures onto the embedding drainage area (or drainage volume) is self-consistent. This feature is also embodied in the well-based model. As shown by the definitions of new dimensionless group and Eq. (5.10), with the fitted α, c, τ, EUR and L_H, $(P_i - P_w)$, the easily determined parameters, we can only confidently obtain the group $2h_f c_t y_e \phi/B$. Without more knowledge about how the mapping influences each property of rock, fluid, and domain and if, as before, we intuitively assume that it only distorts the topology-related intrinsic properties, such as porosity (from ϕ_f to ϕ) and permeability (from k_f to k^*), we can only get the value of $y_e\phi$ and y_e/k^* by incorporating the values of h_f, c_t, B, and μ from other sources. So, if we would like to go further to determine the range of the rectangular drainage area specifically containing the fracture network of interest, which can be well defined as SRV, more information on the distortion of ϕ and k^* is needed.

Unlike k^* with a "weird" unit containing time dimension, ϕ shows a kind of simple proportional characteristic, which may be taken advantage of to further estimate y_e from $y_e\phi$.

$$\phi = \frac{B\ EUR/c_t(P_i - P_w)}{h_f A} \quad \text{.....(4.23)}$$

As we have shown in **Table 4.5** and according to Eq. (4.23), ϕ is a ratio of the total pore volume of fracture network to the volume of the rectangular solid. So, it is smaller than the porosity ϕ_f in the fracture network by a factor which is the ratio of rectangular solid volume to the bulk volume of fracture network. Thus, in practice, this factor of a specific well can be estimated by analyzing the results of natural fracture investigation and the fracturing treatment design. Then by dividing the average porosity ϕ_f in the fracture network by this factor, ϕ and then y_e are finally determined. Compared to the range of different kinds of SRV determined by other methods (micro-seismic, fracture propagation modeling, etc.), y_e from our well-based model is reasonably considered to reflect such SRV that is most relevant to production, because it is directly gained through the back-calculation using a physical-driven model based on production data.

If other information is correctly combined with the fitted parameters, 4 informative parameters would result from the interpretation. The parameters α and η^* reflect the capacity of conducting fluid as well as the heterogeneity of the conductive fracture network embedded in the tight formation and they are average intrinsic properties. The parameter y_e represents the range of the stimulated formation. And the parameter c generally characterizes the effects of close-to-wellbore region on production. Generally speaking, four parameters are all subject to the effects of both pre-existing natural fractures and fracturing treatment but with different extent. Due to the fact that proppants cannot transport deeply into the zig-zag-shaped complex fracture network by state-of-the-art hydraulic-fracturing techniques, α, η^*, and y_e are mainly determined by the characteristics of natural fractures and the transport of fracturing fluid which re-activates many natural fractures deep into the formation. On the other hand, in our opinion, c is predominantly

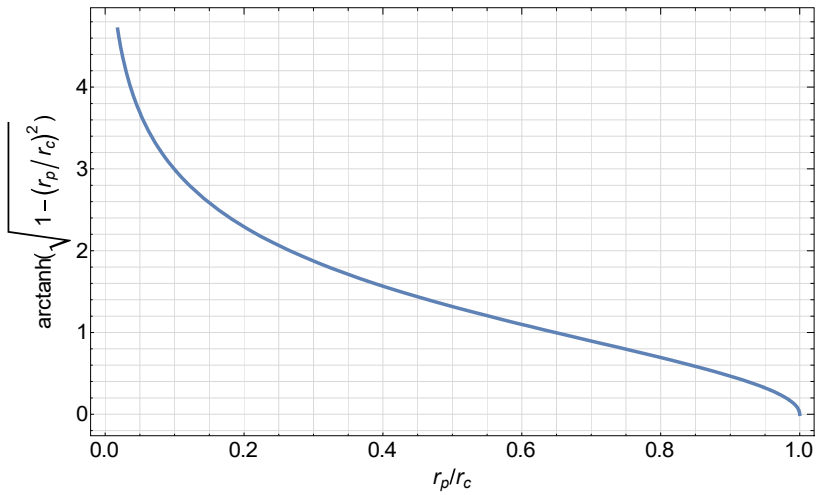

Figure 5.11 – A typical workflow of applying the well-based model to interpret production data

affected by fracturing treatment and can be roughly regarded to stand for the propped parts of fracture networks.

Some minor features of the well-based model are discussed for completeness. c, the convergence flow term has significantly impact on the production performance. According to the type curves in **Fig. 5.4**, when c is around or greater than the unity, all the corresponding type curves are mostly "compressed" to a single curve, which means that in the overwhelmingly large c cases, the pressure drop in the convergence region dominates all flow regimes and no information about the reservoir, (α, η^*), can be extracted. This case prevents any massive flow occurring towards the wellbore. From this perspective, this scenario right corresponds to a situation of drilling a horizontal well in an unconventional reservoir but without fracturing treatment. Therefore, such well-based model provides a reasonable explanation for why hydraulic fracturing is necessary for economic development of unconventional reservoirs. Furthermore, due to the steepness of function $\operatorname{arctanh}(\sqrt{1-(r_p/r_c)^2})$ when r_p/r_c is close to 0 (**Fig. 5.11**), a seemingly promising measure for

efficiently improving the production from unconventional wells is using slightly larger perforations.

5.3. Well-Based Model for the Whole Sequence of Flow Regimes (Model II)

In order to obtain such a production decline model, which is capable of describing all the flow regimes from the early to the late time for slightly compressible fluid through highly fractured unconventional reservoirs, in this section we incorporate a source term into the diffusivity equation of tempered sub-diffusion based on the previous model and discussion in Section 5.2.

5.3.1. Model Description

We denote the operator of the tempered fractional order derivative with respect to a variable t as $D_t^{\alpha,\lambda}$, where α is the fractional order and λ the tempering factor. Since λ dictates the transfer from sub-diffusion to normal diffusion, from intuition it is supposed to correspond to the finest scale of heterogeneity in the fracture network or system. When $\lambda = 0$, no transfer happens meaning heterogeneity exists in any scales. And the larger is the value of λ, the earlier the late exponential decline happens. The diffusivity equation of tempered sub-diffusion is formally written as Eq. (5.14) (Yang, 2018; Sabzikar et al., 2015).

$$\frac{1}{\eta_f^*} D_t^{\alpha,\lambda} P_f = \nabla \cdot \nabla P_f \quad \text{.....(5.14)}$$

where $\eta_f^* = k_f^* / \left(\mu (\phi c_t)_f\right)$ is the anomalous diffusivity coefficient of a composite system with the fracture system being embedded in the tight formation (assumingly impervious for the tempered sub-diffusion model). k_f^* and $(\phi c_t)_f$ denote the anomalous permeability and the product of porosity and total compressibility of such a composite system. P_f is the mapped pressure from the fracture system onto the continuous problem domain. η_f^*, P_f and ∇ have the same definitions or meanings as their counterparts in Eq. (4.6) and Eq. (5.4).

$$\frac{1}{\eta^*}\frac{\partial^\alpha}{\partial t^\alpha}P = \nabla\cdot\nabla P \quad (4.6)$$

For physically incorporating a source term into the tempered model, Eq. (5.14) needs to be recast to the explicit form of continuity equation plus a relevant flux law. To this end, the tempered fractional flux law should be derived.

5.3.1.1. Fractional Flux Law with a Tempering Factor

For the convenience in mathematical treatments and given the uniform initial condition of P_i in the problem domain, Eq. (5.14) is modified to describe the behavior of pressure drop, $\Delta P_f = P_i - P_f$, as Eq. (5.15). ΔP has the initial condition of 0.

$$\frac{1}{\eta_f^*}D_t^{\alpha,\lambda}(\Delta P_f) = \nabla\cdot\nabla(\Delta P_f) \quad (5.15)$$

Regarding $D_t^{\alpha,\lambda}$ when $0<\alpha<1$, we adopt the definition of the tempered fractional derivative in Meerschaert et al. (2013), as Eq. (5.16) shows. The tempering factor λ has the unit of time^{-1}.

$$D_t^{\alpha,\lambda}f(t) \coloneqq e^{-\lambda t}\frac{1}{\Gamma(1-\alpha)}\frac{d}{dt}\int_0^t \frac{e^{\lambda\tau}f(\tau)}{(t-\tau)^\alpha}d\tau - \lambda^\alpha f(t) \quad (5.16)$$

With the Laplace transform of Riemann-Liouville fractional derivative and the shift property of Laplace transform, the Laplace transform of $D_t^{\alpha,\lambda}f(t)$ is displayed in Eq. (5.17) (Meerschaert et al., 2013).

$$\mathcal{L}\{D_t^{\alpha,\lambda}f(t)\} = [(s+\lambda)^\alpha - \lambda^\alpha]\tilde{f}(s) \quad (5.17)$$

Accordingly, Laplace transform is performed on both sides of Eq. (5.14) to get Eq. (5.18).

$$\frac{1}{\eta_f^*}[(s+\lambda)^\alpha - \lambda^\alpha]\widetilde{\Delta P_f} = \nabla\cdot\nabla\widetilde{\Delta P_f} \quad (5.18)$$

After re-organizing the terms in Eq. (5.18), we can obtain Eq. (5.19).

$$s\widetilde{\Delta P_f} = \nabla \cdot \left[\eta_f^* \frac{s}{(s+\lambda)^\alpha - \lambda^\alpha} \nabla \widetilde{\Delta P_f}\right] \quad \text{.....(5.19)}$$

Due to $\Delta P_{fi} = 0$, the left-hand side of Eq. (5.19) has the inverse Laplace transform as $d(\Delta P_f)/dt$. Consequently, after performing inverse Laplace transform on both sides of Eq. (5.19), the continuity equation with an explicit form is expressed as Eq. (5.20), given $\nabla \widetilde{\Delta P_f} = \nabla \frac{P_i}{s} - \nabla \widetilde{P_f} = -\nabla \widetilde{P_f} = -\widetilde{\nabla P_f}$.

$$(\phi c_t)_f \frac{dP_f}{dt} = -\nabla \cdot \left[-\frac{k_f^*}{\mu} \mathcal{L}^{-1}\left\{\frac{s}{(s+\lambda)^\alpha - \lambda^\alpha} \widetilde{\nabla P_f}\right\}\right] \quad \text{.....(5.20)}$$

Based on Eq. (5.20), the tempered fractional flux law is *defined* as $\vec{v}_{\alpha,\lambda}$, whose Laplace transform is

$$\mathcal{L}\{\vec{v}_{\alpha,\lambda}\} = -\frac{k_f^*}{\mu} \frac{s}{(s+\lambda)^\alpha - \lambda^\alpha} \widetilde{\nabla P_f} \quad \text{.....(5.21)}$$

As primarily an engineering work at present, we leave the rigorous proof of the existence and uniqueness of the function $\vec{v}_{\alpha,\lambda}$ in physical domain to future works, and assume it as being well defined in this dissertation.

Finally, Eq. (5.14) is modified into a form (Eq. (5.22)) ready for further manipulations.

$$(\phi c_t)_f \frac{dP_f}{dt} = -\nabla \cdot \vec{v}_{\alpha,\lambda} \quad \text{.....(5.22)}$$

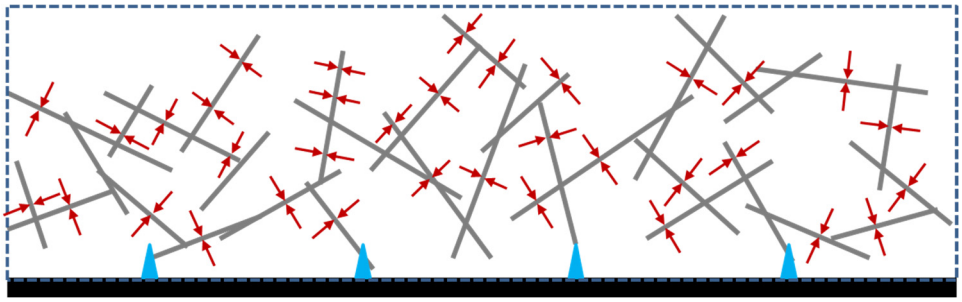

Figure 5.12– Schematic of the influx from matrix into a fracture network

5.3.1.2. Formulating the Model with a Source Term

As the model previously developed in Section 5.2, the current model still takes all the assumptions for the fracture-based model in Section 4.2 except the third and fourth items about the hydraulic fractures. In contrast to the previous model, the influx from the matrix into fractures is accounted for by a source term, which is illustrated in **Fig. 5.12**.

Within the problem domain as of **Fig. 5.2**, the corresponding governing equation with a source term as well as the corresponding initial and boundary conditions is as Eq. (5.23) shows.

$$(\phi c_t)_f \frac{\partial P_f}{\partial t} = -\frac{\partial}{\partial y} v_{\alpha,\lambda} + I \quad \text{.....(5.23a)}$$

$$P_f(y, t = 0) = P_i \quad \text{.....(5.23b)}$$

$$\frac{\partial P_f}{\partial y}(y = y_e, t) = 0 \quad \text{.....(5.23c)}$$

$$P_f(y = 0, t) = P_w + \Delta P_c = P_w + \frac{\mu}{k_f} \frac{x_c h_f}{\pi r_c} \operatorname{arctanh}\left(\sqrt{1 - \frac{r_p^2}{r_c^2}}\right) \left|\vec{v}_{\alpha,\lambda}\right|_{y=0} \quad \text{.....(5.23d)}$$

where the relevant denotations in Eq. (5.23) have the same definitions as their counterparts in Eq. (5.4) and μ is the viscosity of the fluid.

The selection of the type of governing equation for the flow within the matrix, namely I, is based on the statement, that "reservoir permeability enhancement in the SRV results principally from hydraulic fractures and that matrix damage is extremely limited or absent" (Raterman et al., 2017), from the observation of cores from the Eagle Ford Shale. In other words, even after fracturing treatments, the rock beyond the highly conductive fracture networks is left to be barely stimulated. Regarding the flow within the tight unstimulated formation, we assume the flow paths within the intact rock have relatively uniform lengths and spread homogeneously relative to the conductive fracture network in the reservoir scale. It means that in this scenario the characteristics

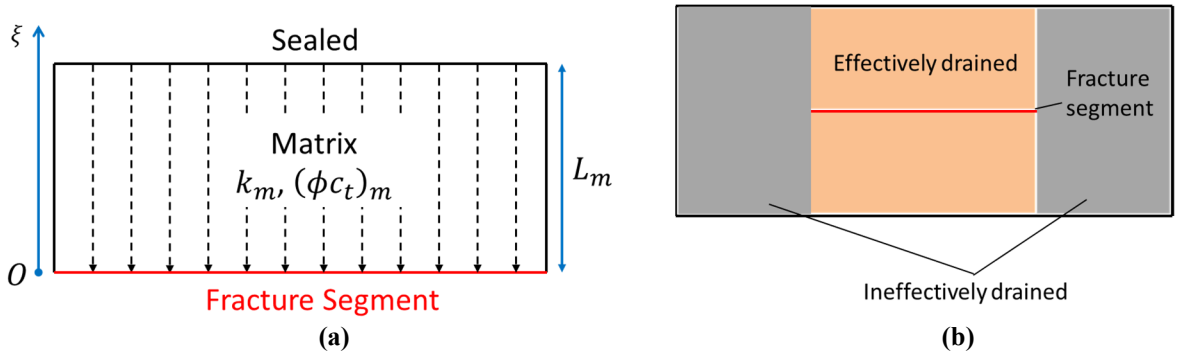

Figure 5.13 – Problem domain and schematic of the linear flow within matrix in a finite domain

of flow in the matrix are roughly close to the case described by the standard diffusivity equation. Therefore, I can be reasonably modeled by the standard diffusivity equation. Also, using the standard diffusivity equation saves us the effort to introducing one more tempering factor for the matrix system, which is supposed to lead to a more feasible and robust model.

In regard to the geometry of the domain for the flow in the matrix, we consider a situation of linear flow in a finite domain as illustrated in **Fig. 5.13 (a)**. We justify this kind of influx by the fact that the fracture can only efficiently drain the formation within the its own range when the matrix permeability is ultra-low, as illustrated in **Fig. 5.13 (b)**. Therefore, our model equivalently uses the slab-shaped matrix source whose width L_m characterizes the average effective size of the intact matrix surrounded by conductive fractures.

Based on the above settings and the assumption of slightly compressible flow, the governing equation, as well as the corresponding initial and boundary conditions for the case of constant pressure on the fracture segment boundary, is as Eq. (5.24) shows.

$$(\phi c_t)_m \frac{\partial P_m}{\partial t} = \frac{k_m}{\mu} \frac{\partial^2 P_m}{\partial \xi^2} \quad \text{(5.24a)}$$

$$P_m(\xi, t = 0) = P_i \quad \text{(5.24b)}$$

$$\frac{\partial P_m}{\partial \xi}(\xi = L_m, t) = 0 \quad \text{(5.24c)}$$

$$P_m(\xi = 0, t) = P_w \quad \text{(5.24d)}$$

where k_m, $(\phi c_t)_m$, P_m is the permeability, the product of viscosity and total compressibility, and ("mapped") pressure of the matrix system. By "mapped" pressure we mean that it is only a *proxy* in the ideal homogeneous domain for modeling the actual pore pressure in the highly heterogeneous matrix rock. And as of the mapped pressure P_f of the fracture system, the "mapped" pressure only makes sense in the cases of describing the global or macroscopic performance in the scale of interest and is of little physical significance point-wisely. And for convenience, we take the constant bottom-hole pressure P_w as the reference pressure on the fracture segment boundary.

Based on Eq. (5.24), the flux i_u on the boundary of the fracture segment normalized by the drawdown pressure is expressed as Eq. (5.25). And, we assume no skin exists on the fracture surface, which means the pressure continuity condition applies on the interface between the fracture and matrix system, as shown in Eq. (5.26).

$$i_u = \frac{1}{P_i - P_w}\frac{k_m}{\mu}\left(\frac{\partial P_m}{\partial \xi}\right)_{\xi=0} \quad \text{(5.25)}$$

$$P_m(\xi = 0, t) = P_f(y, t) \quad \text{(5.26)}$$

According to Duhamel's principle and Eq. (5.26), the relationship between I and i_u is

$$I = \frac{2}{L_m}\int_0^t i_u(t-\tau)\frac{\partial\left(P_i - P_f\right)}{\partial \tau}d\tau \quad \text{(5.27)}$$

where the factor 2 represents that a fracture segment receives influx from both of its surfaces.

By now, the whole problem has been completely formulated in a dimensional domain. The dimensionless groups are defined below. Some of them have the same definitions as the counterparts in Section 5.2 and some are newly defined to characterize new mechanisms. In the

following definitions, since two continuums exist at each point, which modifies the point-wise storativity from $(\phi c_t)_f$ to $(\phi c_t)_f + 2(\phi c_t)_m$, anomalous diffusivity coefficient has a slightly different form of $\eta_f^* = k_f^*/\left[\mu\left((\phi c_t)_f + 2(\phi c_t)_m\right)\right]$. And in the definition of σ, η_m has the definition of $\eta_m = k_m/(\mu(\phi c_t)_m)$. ω is named as storativity ratio, similar to the classic dual-porosity model. Unlike the interporosity flow coefficient that includes some dimensions of wells or hydraulic fractures, σ only contains the information of the corresponding domains and hence is named as characteristic time ratio.

$$P_D = \frac{P_i - P}{P_i - P_w}, \qquad y_D = \frac{y}{y_e}, \qquad \xi_D = \frac{\xi}{L_m} \qquad t_D = \left(\frac{\eta_f^*}{y_e^2}\right)^{\frac{1}{\alpha}} t = \frac{t}{\tau},$$

$$\lambda_D = \left(\frac{y_e^2}{\eta_f^*}\right)^{\frac{1}{\alpha}} \lambda = \tau\lambda, \qquad \omega = \frac{(\phi c_t)_f}{(\phi c_t)_f + 2(\phi c_t)_m}, \qquad \sigma = \frac{\left(y_e^2/\eta_f^*\right)^{\frac{1}{\alpha}}}{L_m^2/\eta_m},$$

$$c = \frac{k_f^*}{k_f}\left(\frac{y_e^2}{\eta_f^*}\right)^{\frac{\alpha-1}{\alpha}} \frac{x_c h_f}{\pi r_c y_e} \operatorname{arctanh}\left(\sqrt{1 - \frac{r_p^2}{r_c^2}}\right), \qquad \vec{v}_{\alpha,\lambda D} = \frac{\mu y_e \vec{v}_{\alpha,\lambda}}{k_f^*(P_i - P_w)}\left(\frac{y_e^2}{\eta_f^*}\right)^{\frac{1-\alpha}{\alpha}},$$

$$q_D = \frac{\mu y_e B q_{sc}}{2\, k_f^* x_c h_f N_p (P_i - P_w)}\left(\frac{y_e^2}{\eta_f^*}\right)^{\frac{1-\alpha}{\alpha}} = \frac{\tau}{EUR} q_{sc},$$

$$Q_D = \int_0^{t_D} q_D \, \mathrm{d}t_D = \frac{BQ_{sc}}{2 y_e x_c h_f N_p \left((\phi c_t)_f + 2(\phi c_t)_m\right)(P_i - P_w)} = \frac{Q_{sc}}{EUR}$$

After substituting the above dimensionless group definitions into Eq. (5.23) to Eq. (5.27), we can get Eq. (5.28).

$$\omega \frac{\partial P_{fD}}{\partial t_D} = \frac{\partial}{\partial y_D} v_{\alpha,\lambda D} + (1-\omega)\,\sigma \int_0^{t_D} \left(\frac{\partial P_{mD}}{\partial \xi_D}\right)_{\xi_D = 0} (t_D - \tau_D) \frac{\partial P_{fD}}{\partial \tau_D} d\tau_D \quad \text{.....(5.28a)}$$

$$P_{fD}(y_D, t_D = 0) = 0 \text{.....(5.28b)}$$

$$\frac{\partial P_{fD}}{\partial y_D}(y_D = 1, t_D) = 0 \text{.....(5.28c)}$$

$$P_{fD}(y_D = 0, t_D) = 1 - c\left|\vec{v}_{\alpha,\lambda D}\right|_{y_D=0} \quad (5.28d)$$

$$\frac{\partial P_{mD}}{\partial t_D} = \sigma \frac{\partial^2 P_{mD}}{\partial \xi_D^2} \quad (5.28e)$$

$$P_{mD}(\xi_D, t_D = 0) = 0 \quad (5.28f)$$

$$\frac{\partial P_{mD}}{\partial \xi_D}(\xi_D = 1, t_D) = 0 \quad (5.28g)$$

$$P_{mD}(\xi_D = 0, t_D) = 1 \quad (5.28h)$$

Then Laplace transform is performed to the whole system of Eq. (5.28) to obtain Eq. (5.29), which is the system to be solved

$$\omega s\widetilde{P_{fD}} = \frac{s}{(s+\lambda_D)^\alpha - {\lambda_D}^\alpha}\frac{\partial^2}{\partial y_D^2}\widetilde{P_{fD}} + (1-\omega)\,\sigma\, s\widetilde{P_{fD}}\left(\frac{\partial \widetilde{P_{mD}}}{\partial \xi_D}\right)_{\xi_D=0} \quad (5.29a)$$

$$\frac{\partial \widetilde{P_{fD}}}{\partial y_D}(y_D = 1) = 0 \quad (5.29b)$$

$$\widetilde{P_{fD}}(y_D = 0) = \frac{1}{s} + \frac{c\,s}{(s+\lambda_D)^\alpha - {\lambda_D}^\alpha}\left(\frac{\partial \widetilde{P_{fD}}}{\partial y_D}\right)_{y_D=0} \quad (5.29c)$$

$$s\widetilde{P_{mD}} = \sigma \frac{\partial^2 \widetilde{P_{mD}}}{\partial \xi_D^2} \quad (5.29d)$$

$$\frac{\partial \widetilde{P_{mD}}}{\partial \xi_D}(\xi_D = 1) = 0 \quad (5.29e)$$

$$\widetilde{P_{mD}}(\xi_D = 0) = \frac{1}{s} \quad (5.29f)$$

5.3.1.3. Solutions and of Model II

Following the steps in Appendix G, the system of Eq. (5.29) is solved to obtain the expression of $\widetilde{P_{fD}}$ as shown in Eq. (5.30).

$$\tilde{P}_D(y_D, s)$$

$$= \frac{\cosh\big((y_D - 1)\, f(\alpha, \lambda_D, s)\, g(\omega, \sigma, s)\big)}{s \cosh\big(f(\alpha, \lambda_D, s)\, g(\omega, \sigma, s)\big) + c\, s^2 \sinh\big(f(\alpha, \lambda_D, s)\, g(\omega, \sigma, s)\big) \frac{g(\omega, \sigma, s)}{f(\alpha, \lambda_D, s)}} \quad \text{.....(5.30)}$$

where $f(\alpha, \lambda_D, s) = \sqrt{(s + \lambda_D)^{\alpha} - \lambda_D{}^{\alpha}}$ and $g(\omega, \sigma, s) = \sqrt{\omega + (1 - \omega) \tanh\left(\sqrt{s/\sigma}\right)/\sqrt{s/\sigma}}$.

$f(\alpha, \lambda_D, s)$ represents the type of model for the fracture system and $g(\omega, \sigma, s)$ for the continuums. When $\lambda_D = 0$ and $\omega = 1$, namely the fracture system has heterogeneity in all scales and the matrix has no pore volumes, $f(\alpha, \lambda_D, s) = s^{\alpha/2}$ and $g(\omega, \sigma, s) = 1$. In this case, Eq. (5.30) is reduced to Eq. (5.7), so that Model I is a special case of the more generalized Model II.

Introducing a source term results in a slightly different relationship between production rate and pressure from Eq. (5.8) and Eq. (5.9). The expressions of dimensionless cumulative production and rate are obtained as shown in Eq. (5.31) and Eq. (5.32).

$$\tilde{Q}_D = \frac{1}{c\, s^2 + s\, \frac{f(\alpha, \lambda_D, s)}{g(\omega, \sigma, s)} \coth\big(f(\alpha, \lambda_D, s)\, g(\omega, \sigma, s)\big)} \quad \text{.....(5.31)}$$

$$\tilde{q}_D = \frac{1}{c\, s + \frac{f(\alpha, \lambda_D, s)}{g(\omega, \sigma, s)} \coth\big(f(\alpha, \lambda_D, s)\, g(\omega, \sigma, s)\big)} \quad \text{.....(5.32)}$$

Gaver-Wynn-Rho (GWR) algorithm (Valkó and Abate, 2004) is still used to get Q_D and q_D in physical domain. The resulting type curves are displayed in the next section.

5.3.2. Type Curves and Effects of Parameters

In contrast with Model I, there are 5 parameters (α, c, λ_D, ω, σ) in Model II, which prevents an effective comprehensive visualization of the type curves in a 2D log-log coordinates like **Fig. 5.4**. Therefore, we will visualize the model in a couple of separate plots with different focuses and discuss the effects of these parameters on the well performance.

First several subsections are for the cases without source terms ($\omega = 1$), that is, only the flow in the fracture system is considered. Due to the introduction of tempering factor λ_D, this type of flow is now described closer to the reality, since the finiteness of the physical fracture systems or the cut-off of the scale of heterogeneity is accounted for. Next, the source term is involved in the type curves. The effects of λ_D, ω, and σ on the whole sequence of flow regimes are discussed.

In the following subsections, we term the early power-law decline period of the fracture flow as "first power-law regime", the late power-law decline period of the fracture flow as "second power-law regime", and the exponential decline of the fracture flow as "fracture exponential decline regime". Both the second power-law regime and the fracture exponential decline regime represent the boundary dominated state within the fracture system. When the effect of influx emerges, we term the apparent power-law decline period after the deviation as "late power-law regime", and the final exponential decline regime as "late exponential decline regime".

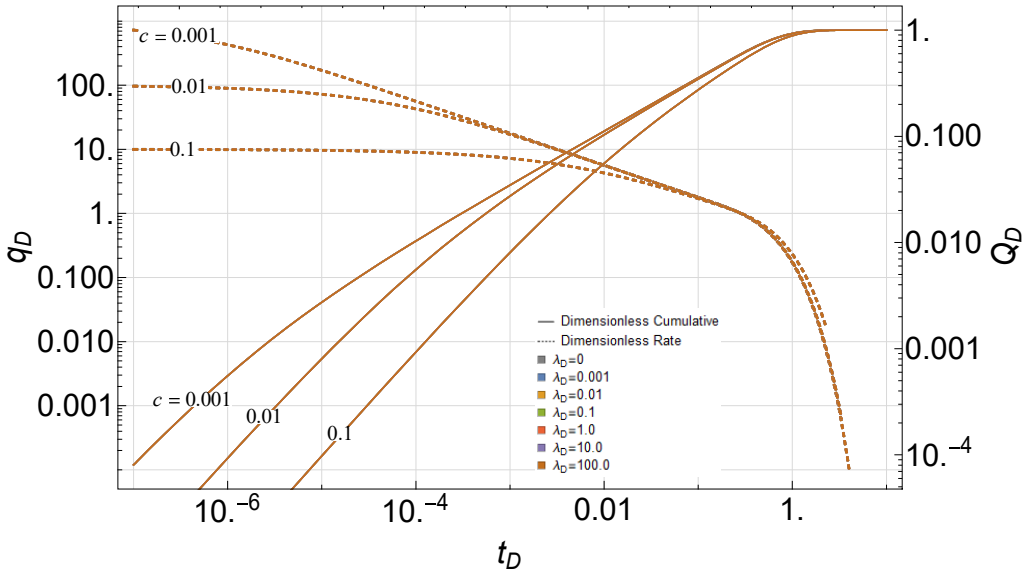

Figure 5.14 – Type curves of Model II with $\alpha = 1$ and $\omega = 1$

5.3.2.1. Effects of λ_D When $\alpha = 1$ and $\omega = 1$

When $\alpha = 1$ and $\omega = 1$, we have the expressions that $\tilde{Q}_D = 1/\left(c\, s^2 + s^{3/2}\coth\left(s^{1/2}\right)\right)$ and $\tilde{q}_D = 1/\left(c\, s + s^{1/2}\coth\left(s^{1/2}\right)\right)$, which are exactly the corresponding expression of Model I with $\alpha = 1$ in Laplace domain.

The resulting type curves are shown in **Fig. 5.14**. In the figure, it is apparent that the curves with different values of λ_D but the identical c all overlap together, including the cases with $\lambda_D = 0$, corresponding to Model I. This is consistent with our observation above based on the expressions and means that in a scenario of pure normal diffusion from the beginning the effect of λ_D vanishes, which is definitely aligned with the rationale of introducing this tempering factor.

Though a trivial verification, the type curves in **Fig. 5.14** at least demonstrates some internal consistency of our models.

5.3.2.2. Effects of λ_D When $\alpha < 1$ and $\omega = 1$

$\alpha = 0.7$ is used to generate the type curves with different values of λ_D in this subsection. Since the value of c significantly influences the performance of the early and intermediate time, the plots are made at 3 different values of c, $\{0.001, 0.01, 0.1\}$. The type curves are as displayed in **Fig. 5.15**.

In each plot of **Fig. 5.15**, the black dash curve has the value of λ_D as 0, which represents the corresponding case of Model I. Using this as a reference, the transition from subdiffusion-related decline to exponential decline can be observed. The point at which the transition becomes noticeable depends on the value of λ_D. When λ_D is small, say 0.001 or 0.01, the curve displays the whole first power-law regime and then deviates from the second power-law trend at some point to become the fracture exponential decline. When λ_D is relatively large, say 10.0 or 100.0, such a transition happens in the first power-law regime. Though without rigorous derivation, the plots

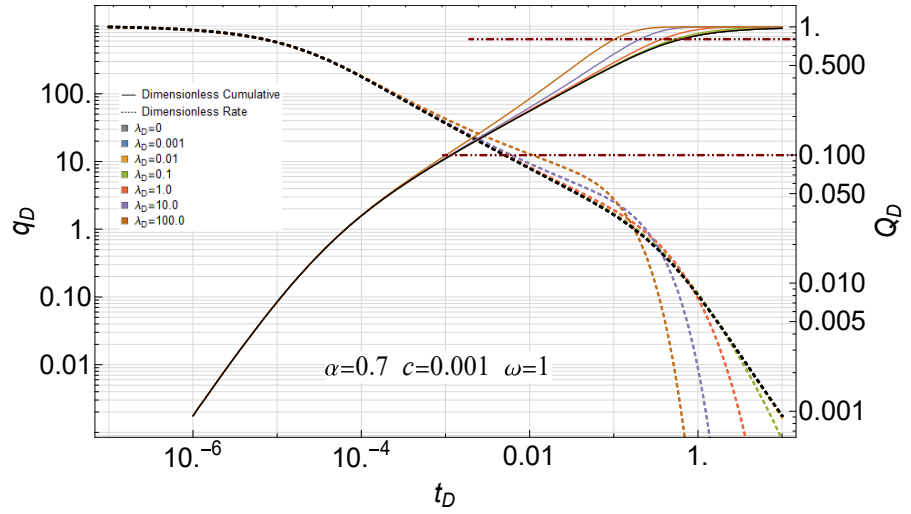

(a)

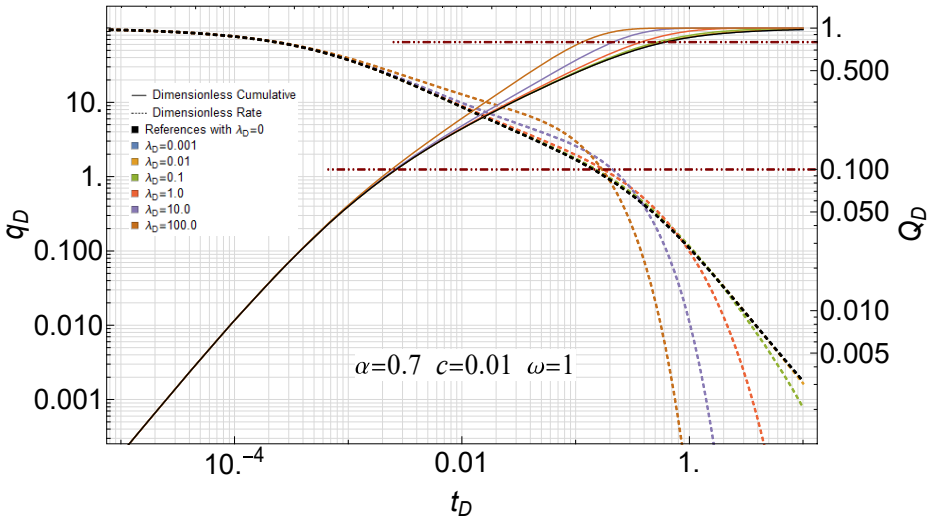

(b)

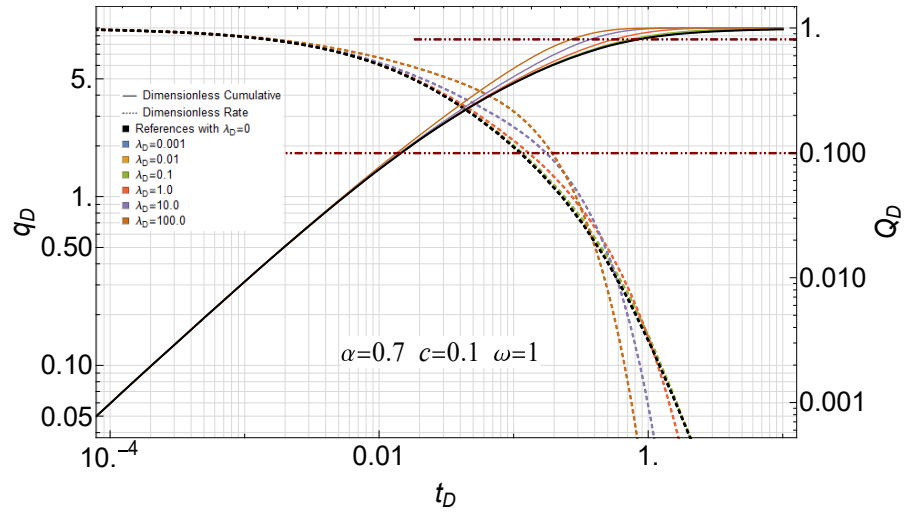

(c)

Figure 5.15 – Type curves of Model II with $\alpha = 0.7$ and $\omega = 1$. (a) $c = 0.001$. (b) $c = 0.01$. (c) $c = 0.1$.

seemingly indicate that $\lambda_D = 1$ is sort of a "critical point" at which the transition to fracture exponential decline happens right after the whole first power-law regime ends. Recalling that the tempering factor stands for the relative scale of the finest heterogeneity, $\lambda_D = 1$ probably corresponds to a typical scenario of a heterogeneous system in which the dynamics exactly consists of three parts of skin-dominated plateau regime, sub-diffusion-dominated first power-law regime, and fracture-boundary-dominated exponential regime, and the distortion of the second regime due to the third one can be neglected.

In each plot, two auxiliary lines are made to provide some insights on the cumulative curves. These two lines respectively correspond to $Q_D = 0.1$ and $Q_D = 0.8$, so the interval between these represents the time needed for increasing the recovery from 10% EUR to 80% EUR. In each case, the interval of large λ_D is shorter than that of small λ_D. For instance, in **Fig. 5.15 (a)**, the interval of $\lambda_D = 100.0$ is about 2 log cycles, while that of $\lambda_D \leq 0.1$ is about 2.8 log cycles. Apparently, the former one takes about only $1/6$ time of the later to get the same production results. Larger λ_D means a larger scale of the finest heterogeneity relative to the whole system, which roughly stands for a relatively more homogeneous system. In other words, when α is constant, a relatively homogeneous system (relatively larger cut-off) can make faster recovery than a more heterogeneous one (relatively smaller cut-off), agreeing with our intuition.

Comparing the three plots in **Fig. 5.15**, the effects of the skin c can be summarized as that it controls the length of the duration of the intermediate regime. The larger value is the skin c, the shorter is the span between the initial plateau and the fracture boundary dominated regime (either power law or exponential). In **Fig. 5.15 (c)** with $c = 0.1$, the plateau directly joins to the boundary dominated regime. In the cases with $\lambda_D \geq 1.0$ when the plateau joins directly to the exponential decline, the signature of sub-diffusion is hidden. Therefore, it implies that large c plus large λ_D

would suppress the occurrence of sub-diffusion and that some combinations of c and λ_D would manifest the dynamics as the normal diffusion even though the actual α is smaller than the unity. According to our observation, the criterion seemingly happens to be $c\lambda_D = 1$.

5.3.2.3. Effects of the Product $c\lambda_D$ When $\omega = 1$

To investigate the effect of $c\lambda_D = 1$, the type curves with $c\lambda_D = 1$ but different values of c and λ_D, are generated at three values of α, $\{0.7, 0.4, 0.1\}$, as shown in **Fig. 5.16**. In all three plots, the type curves look like describing the dynamics of the normal diffusion and α cannot be extracted in these scenarios. When α is relatively large and c small, there exists a regime with a half-slope straight line between the initial plateau and the fracture exponential decline, a well-known signature for the transient regime of the standard diffusivity equation. As α decreases or c increases, the duration of the transient regime reduces and finally the plateau directly joins to the exponential decline regime. Note that in these limiting cases of $c\lambda_D = 1$, the exponential decline is hardly truncated by the plateau and shows a complete exponential variation. In such a system, the production rate is maintained at a stable level for a while after which it begins to decline exponentially behaving like a sizeless homogeneous system that reaches boundary-dominated state instantaneously.

Using $c\lambda_D \approx 1$ as a reference, it indicates that when $c\lambda_D$ is far less than the unity, the signature of sub-diffusion appears for the flow through fracture system, which can be made use of to characterize the actual α of the system. However, when $c\lambda_D$ is around or greater than the unity, the characteristics of sub-diffusion is totally suppressed in the fracture flow regimes, and it cannot distinguish between $\alpha = 1$ or $\alpha < 1$. If it is the case, the influx from matrix is needed for re-displaying the effects of α.

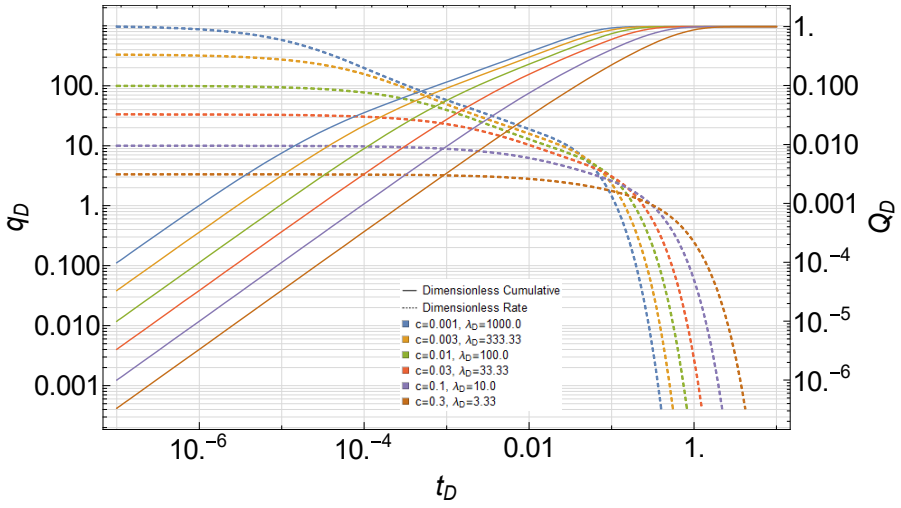

(a)

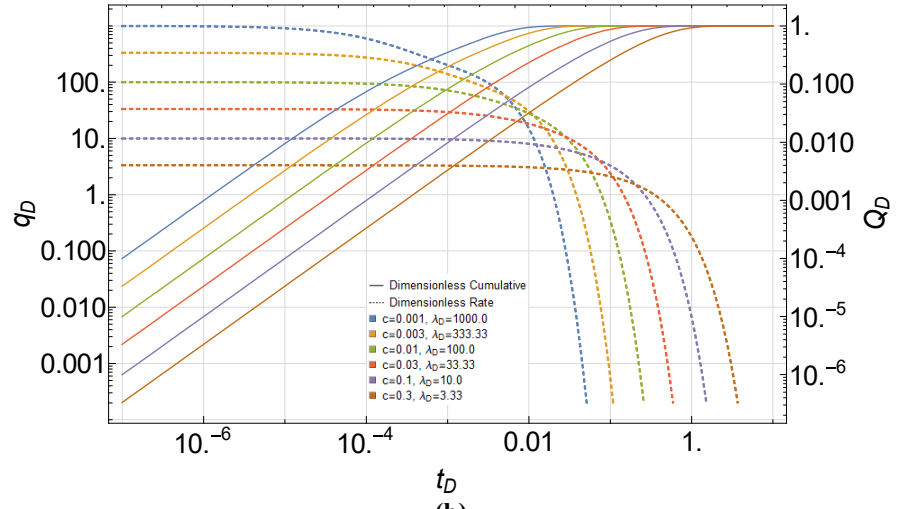

(b)

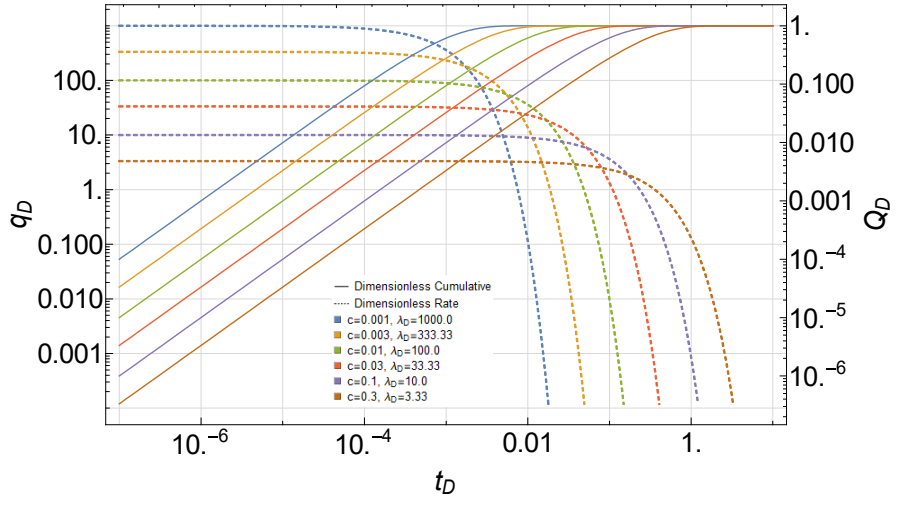

(c)

Figure 5.16 – Type curves of Model II with $c\lambda_D = 1$ and $\omega = 1$. (a) $\alpha = 0.7$. (b) $\alpha = 0.4$. (c) $\alpha = 0.1$.

5.3.2.4. Effects of λ_D When $\alpha < 1$ and $0 < \omega < 1$

From this section, the influx from matrix is added in Model II by a positive value of ω. At the beginning, a minute experiment is done in which the source term is added to a sub-diffusion model without the tempering factor. This experiment is for qualitatively understanding the pure effects of the influx to the fractional production decline model. The results are shown in **Fig. 5.17**.

Fig. 5.17 indicates that the influx from the matrix leads to a period of slightly faster decline during the early to intermediate time, after which the decline becomes slower than the pure sub-diffusion case probably because the support from the matrix begins to dominate. Finally, the case with influx ends up with a power-law decline with the same slope as that of the pure sub-diffusion. Such a late power-law decline regime is consistent with our intuition that the fluid originally borne in matrix is produced through the fracture system which is supposed to project some of its own characteristics to the production performance.

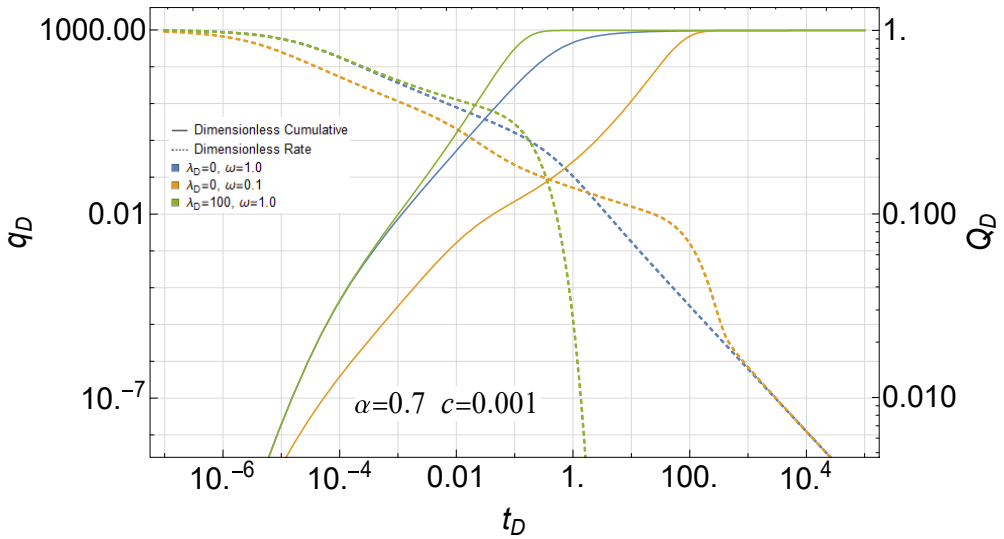

Figure 5.17 – Comparison between Model I, Model II with $\lambda_D = 0$, $\omega < 1$, and Model II with $\lambda_D \neq 0$, $\omega = 1$

Taking the three curves in **Fig. 5.17** as references, the type curves with $\alpha = 0.7$, $c = 0.001$, $\omega = 0.1$, and $\sigma = 0.01$ are displayed in **Fig. 5.18**. Generally speaking, the effect of λ_D is relatively small. All of the rate curves under study roughly track the reference of $(\lambda_D, \omega) = (0, 0.1)$ from the very beginning to the intermediate-to-late time and then deviate the reference starting the late decline exponential. When λ_D is small, like $\lambda_D = 0.001$ and 0.01, the late exponential decline would not occur immediately after the deviation and the rate curves show a sort of middle state between the late exponential and the late power-law decline. On the other hand, as λ_D increases, all the corresponding rate curves overlap during the late exponential decline regime right after the deviation.

λ_D with large values (larger than the unity according to **Fig. 5.18**) has the distinctive effect during the early-to-intermediate time that supports the rate to decline a slightly slower. This effect is more discernable on the cumulative curves. The auxiliary lines of $Q_D = 0.01$ and $Q_D = 0.1$ are made to analyze the cumulative curves. The time interval between $Q_D = 0.01$ and 0.1 of the case of $\lambda_D = 1000.0$ is about 2.1 log cycles, while that of $\lambda_D \leq 1.0$ is around 3 log cycles. It means

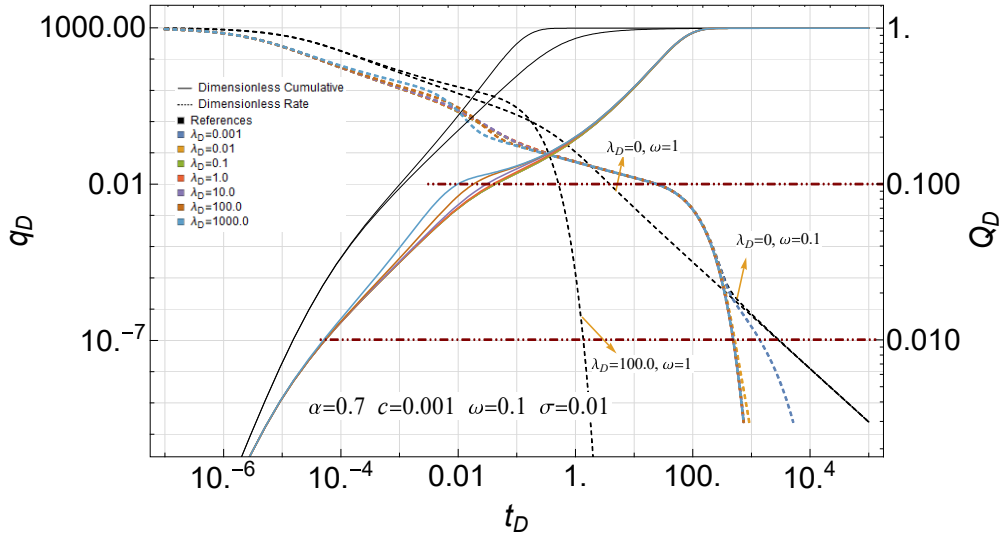

Figure 5.18 – Type curves of Model II with $\alpha = 0.7$, $c = 0.001$, $\omega = 0.1$ and $\sigma = 0.01$

that cases with $\lambda_D \leq 0.1$ would take more than 8 times as much time as that of the case with $\lambda_D = 1000.0$ to increase the recovery from 1% EUR to 10% EUR, which is aligned with our previous discussions about the drainage behavior of relatively homogeneous systems in Section 5.3.2.2. In addition, even after the influx is taken into consideration, the effect of λ_D on recovery is mainly limited to the fracture flow period.

According to **Fig. 5.18,** the effects of λ_D can be summarized as guaranteeing the occurrence of the late exponential decline and slightly accelerate the recovery during the fracture flow period when its value is large. But, as mentioned above, the general effect of λ_D is small.

5.3.2.5. Effects of ω

$\alpha = 0.7$ is still used to generate the type curves with different values of ω in this subsection. Due to the relatively insignificant effects of λ_D discussed in the last subsection, the type curves are generated only using $\lambda_D = 1.0$. The type curves are displayed in **Fig. 5.19**. In the plot, the curves colored black are the reference curves of $(\lambda_D, \omega) = (1, 0)$ and $(\lambda_D, \omega) = (1, 1)$, respectively.

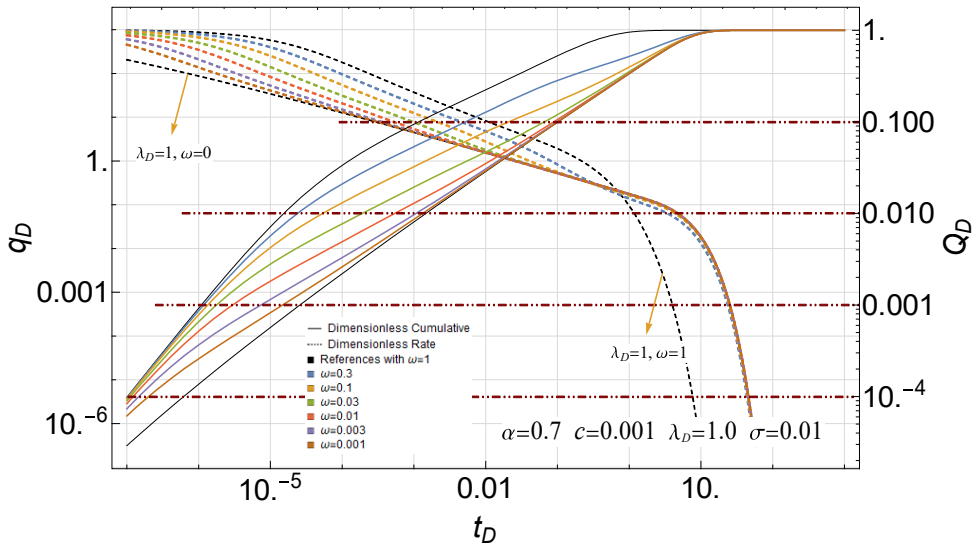

Figure 5.19 – Type curves of Model II with $\alpha = 0.7$, $c = 0.001$, $\lambda_D = 1.0$ and $\sigma = 0.01$

Each rate curve in **Fig 5.19** has the similar sequence of flow regimes. First comes the convergence dominated plateau. Then, the rate shows the first power-law regime with the slope identical to that of the first power-law regime of the corresponding Model I curve ($(\lambda_D, \omega) = (0, 1)$). Next, after a transition period comes another power-law regime with the slope of $1/2$, which is apparently dominated by the matrix flow. Finally, the production ends up with the late exponential decline. It indicates that the cases with larger value of ω would have larger flow rate in the early-to-intermediate time, though the decline rate is the same.

To investigate the effect of ω on recovery, two auxiliary lines of $Q_D = 0.0001$ and $Q_D = 0.1$ are made to analyze the cumulative curves. At $Q_D = 0.0001$, all curves roughly start from the same point. In the procedure of increasing the recovery from 0.01% EUR to 10% EUR, the time needed for the case of $\omega = 0.001$ is about 6.6 log cycles, while that for the case of $\omega = 0.3$ is about 4.5 log cycles. The former would take $10^{6.6}/10^{4.5} \approx 126$ times as much time as the later ones. This observation, that increasing ω is a significantly effective method for shrinking the time needed for achieving the same increment of recovery, explains the necessity of massive hydraulic fracturing for the economic development of unconventional reservoirs from a different perspective besides lowering the skin c (which has been discussed in Section 5.2.3). According to the definition of ω, it can be regarded as the portion of the total pore volume belonging to the fracture system. So, for a given reservoir, a larger ω corresponds to a case with more pore volume in the fracture system, namely, more pre-existing fractures and micro-fractures are re-activated by massive fracturing treatments. Actually, the two reference curves in **Fig. 5.19** corresponds two limiting cases given the other parameters invariant. The curve of $(\lambda_D, \omega) = (1, 0)$ stands for the worst case whose formation is not stimulated at all, while the curve of $(\lambda_D, \omega) = (1, 1)$ stands for

the best case whose formation is fully stimulated so that its total pore volume is covered by the fracture system. All other cases are located between these two extremes, as illustrated in **Fig. 5.19**.

After depleting a fractured reservoir for a while, many unpropped conductive fracture would lose their high conductivity from the initial hydraulic fracturing, which makes ω become smaller and smaller during the depletion. This is where the re-fracturing would make a great difference. Thus, ω can be used as the indicator for selecting the re-fracturing candidates. A potential candidate is supposed to experience significant drop of ω during the production. This is the first scenario of re-fracturing candidate.

According to **Fig. 5.19**, there is another scenario of potential re-fracturing candidate. Take the cumulative curve of $\omega = 0.3$ as an example. From 0.01% EUR to 1% EUR, the time needed is about 2 log cycles, which almost equals the best case with $(\lambda_D, \omega) = (1, 1)$ since the curve of $\omega = 0.3$ is "compressed" very close to the best case curve in this interval. However, for further recovery from 1% EUR to 10% EUR, $\omega = 0.3$ curve would take about 2.5 log cycles, while the best case in this interval would only take less than 2 log cycles. In other words, the effective stimulation on one interval is unnecessary to be effective on another one. In order to improve the production performance from 1% EUR to 10% EUR, $\omega = 0.3$ needs to be further increased. This example demonstrates another scenario of potential re-fracturing candidate. That is, even though the fractures have not experienced significant conductivity loss and ω keeps almost the same as that right after the initial fracturing treatment, the current value of ω will not be efficient enough for the further depletion so that re-fracturing is suggested for increasing ω to a higher level.

5.3.2.6. Effects of σ

$\alpha = 0.7$ is used to generate the type curves with different values of σ in this subsection. With the similar reason mentioned in the last subsection, the type curves are made at $\lambda_D = 1.0$.

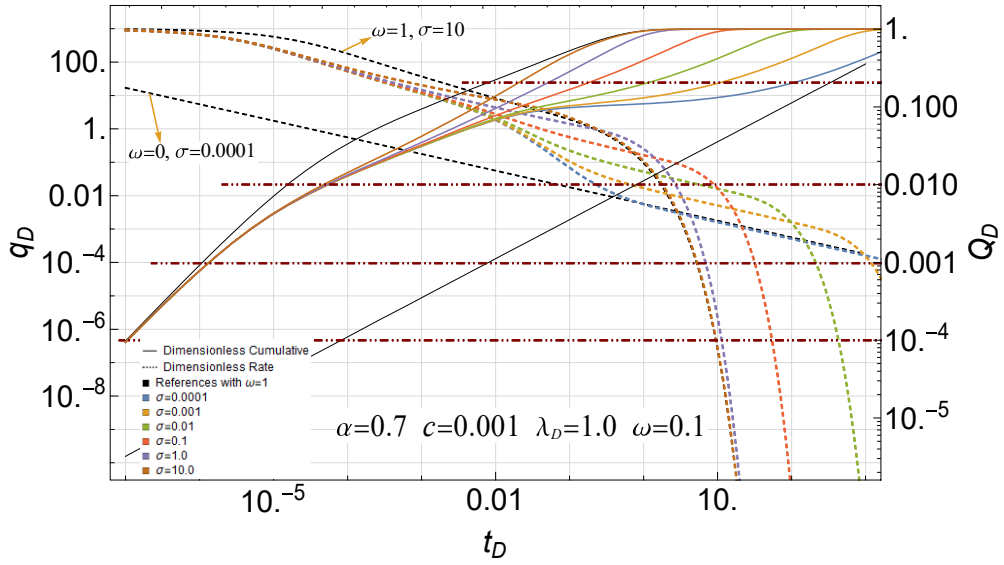

Figure 5.20 – Type curves of Model II with $\alpha = 0.7$, $c = 0.001$, and $\omega = 0.1$

The resulting curves are displayed in **Fig. 5.20**. The curves colored black are the reference curves of $(\omega, \sigma) = (1, 10)$ and $(\omega, \sigma) = (0, 0.0001)$, respectively.

In contrast to the rate curves with different ω in **Fig. 5.19**. the curves with different σ have the same early-time stem and then deviate from it at a time correlated with the value of σ. A smaller value of σ corresponds to a latter transition to the half-slope regime and a latter beginning of the late exponential decline. Regarding the late exponential decline, besides σ has control over its start point, there seems to be another factor also having impact, because the late exponential decline of the cases of $\sigma = 1.0$ and 10.0 are much closer to each other than to other curves. This additional factor is very likely to be the magnitude of λ_D, which corresponds to the time at which the fracture exponential decline begins.

As indicated in **Fig. 5.18** to **Fig. 5.20**, the late exponential decline happens only if both the fracture system and the matrix have reached exponential decline. The exponential decline of the fracture system is dictated by λ_D, while that of the matrix by σ. Consequently, this start point of the late exponential decline is qualitatively determined by the relatively smaller one between λ_D

and σ regarding some criterion undetermined yet. Furthermore, speaking of the transfer to late exponential decline, a popular technique related to this for the development of unconventional reservoirs is decline curve analysis with modified hyperbolic decline curve. Compared with our model, what this technique does is roughly approximating transient regimes of two power-law trends with a hyperbolic curve and then tailing it with the late exponential decline. Since λ_D hardly has impact on the slope according to **Fig. 5.18**, the correspondence between the two sets of parameters can be roughly summarized as that the initial decline rate D_i is related to (α, c), the b factor to (α, ω, σ), and D_{lim} or q_{lim} to the relatively smaller one between λ_D and σ mentioned above.

Similar to the previous subsections. the auxiliary lines are made to analyze the cumulative curves. Starting almost at the same point, the interval of $\sigma = 10.0$ is roughly 5 log cycles while that of $\sigma = 0.001$ is about 8 log cycles. The latter would take around 1000 times as much time as the former to increase the recovery from 0.01% EUR to 20% EUR! Such a superior behavior of the cases with large σ is right related to the slower decline in the early-to-intermediate time due to the greater support by the matrix with relatively better conductivity. There are various ways for improving the relative conductivity of the matrix. The first feasible way is to enable hydraulic fracturing to induce and re-activate small-scale fractures, which would effectively decrease L_m, thus increase σ. Another possible way is probably improving the matrix conductivity by the relevant chemicals. Though, as mentioned above, the rock beyond the conductive fracture network is hardly stimulated during the slick-water fracturing, if some relevant chemicals are added into the fracturing fluid without much increasing the viscosity but capable of "loosening" the matrix by reaction, we would achieve a larger η_m. By the definition of σ, the value of σ would increase,

if other parameters are assumed to be unchanged. In this case, the development by the fracturing fluid with such chemicals is expected to beat the other one stimulated by slick water.

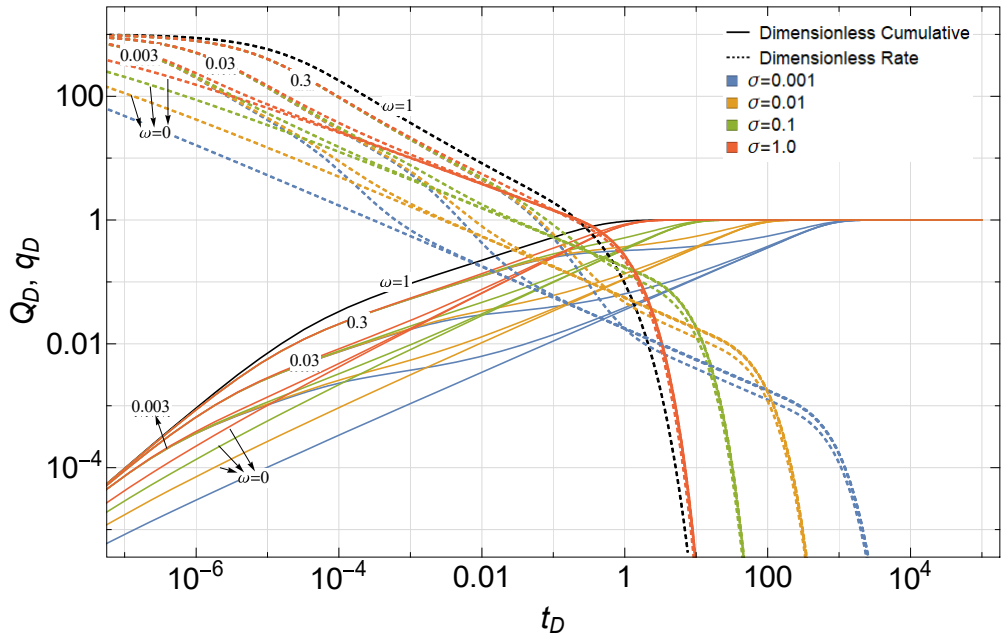

Figure 5.21 – Type curves of Model II with $\alpha = 0.7$, $c = 0.001$, and $\lambda_D = 1.0$

5.3.2.7. Sampled Type Curves and Relevant Discussion

To comprehensively display the effect of ω and σ, a set of type curves stems sampled with $(\alpha, c, \lambda_D) = (0.7, 0.001, 1)$ is generated and shown in **Fig. 5.21**.

According to **Fig. 5.21** and the discussions made in the last 2 subsections, using the cumulative curve with $\omega = 1$ as the reference of the best case, the period when ω has a greater effect on improving the production performance close to the best case is different from that of σ. By the cumulative curves **Fig. 5.21**, it is apparent that in the early time, all stems with non-zero ω are "compressed" to the best case, which means that a relatively small increase to ω during this

time would make a great difference to accelerate the early-time recovery. In contrast, in the late time, the cumulative curves approach the unity converging to a set of new stems characterized by σ. The larger value is σ, the closer is the corresponding curve to the best case. Consequently, this observation probably sets the reasonable goals for the initial fracturing and re-fracturing. The primary goal for the initial fracturing is increasing the value of ω by massive treatments, while that for the re-fracturing is increasing the value of σ perhaps by re-activating the fractures in smaller scales or "loosening" matrix rock using some edge-cutting techniques.

Concretely, combining the above discussions and the discussions about c in Section 5.2.3, the major goals of hydraulic fracturing in unconventional reservoirs is supposed to be reducing the values of c and increasing ω and σ, according to our model. c is lowered by creating and propping hydraulic fractures near perforations, and ω is increased by inducing and re-activating more fractures deep into the formation to create a connected conductive fracture network. This is perhaps the theoretical explanation for the success of slick-water hydraulic fracturing in unconventional reservoirs. Compared to conventional techniques using crosslinked water or guar gel, though slick water can only transport proppants to a shorter distance (which is already enough for lowering c), the less viscous slick water is easier for flowing deep into the formation to induce and re-activate more fractures resulting to a much greater ω than fracturing with viscous fluid. Slick-water fracturing also has the positive effect of increasing σ by split the whole chunk of formation into separate blocks (lowering L_m). However, in our opinion, the primary effect of slick-water fracturing is increasing ω according to Raterman et al. (2017), so that it is a proper technique for the initial fracturing. In order to further increasing σ, people may resort to other methods.

It should be pointed out that the effects of ω and σ on accelerating the recovery from fractured tight formations are attributed to the nature of the classic dual-porosity model, while in

the setting of our models both ω and σ are subject to the variations due to massive fracturing treatments, instead of being the pure formation properties

At last, based on the type curves in **Fig. 5.19** to **Fig. 5.21**, the initial trend (the slope of the first power-law regime) displayed by Model II curves is basically subject to little impact of λ_D, ω, and σ. Therefore, regarding interpreting the production data, it seems to be an effective way where the early-time production data is firstly fitted by Model I to get preliminary values of α and c. Then a more complicated data-fitting using Model II is performed based on these preliminary values. This sequential data-fitting workflow is expected to resolve the issue of non-uniqueness for using the five-parameter Model II directly.

5.4. Section Summary

1. Two well-based fractional production decline models are developed by considering an infinite conductivity horizontal well draining a complex fracture network with a fractional-flux related skin. Model I only considers the flow in the fracture system during the initial period, and Model II considers the finiteness of the fracture system as well as a normal-diffusion influx from the matrix;
2. The Model I is successfully used in both synthetic and field cases, which indicates its capability of averagely describing the transient flow regime in the extremely heterogeneous fracture networks;
3. The production of single-phase flow through heterogeneous fractured media can be characterized by seven parameters, α, c, λ_D, ω, σ, τ, and EUR. And the resulting constant bottom-hole solution is ready to be used as the kernel for modeling the cases of variable bottom-hole pressure;

4. The effects of these parameters on the production performance have been discussed extensively, based on which some insights about the practice of developing unconventional reservoirs are provided:

    - The essence of using hydraulic fracturing for economic development of unconventional reservoirs is reducing the values of c while increasing ω and σ, assuming α and λ_D are determined by the characteristics of the formation and cannot be largely altered;
    - Two scenarios of potential re-fracturing candidates are identified. One is for the conductivity loss of the initially re-activated fractures due to the depletion. The other is for the insufficiently increased ω or σ for the further recovery;
    - According to the relative extent to which the parameters ω and σ can improve the production performance in different periods of production, the primary goal for the initial production is mainly increasing ω, while that for the re-fracturing is increasing σ.
    - The feasibility of the empirical modified hyperbolic decline curve can be theoretically explained by our model.

6. CONCLUSIONS AND RECOMMENDATIONS

This dissertation presents a comprehensive study for modeling the production and characterizing the well performance for the fractured horizontal well in unconventional reservoirs, especially shale and tight sands. Based on the different fundamental governing equations utilized, standard diffusivity equation for normal diffusion or fractional diffusivity equation for sub-diffusion, our work is separated into two main parts.

In the first part, from our study originated from some time-invariant features of the stabilized flow in a bounded reservoir described by standard diffusivity equation, the following conclusions can be derived:

- By using the algorithm of combining the FEM with Richardson extrapolation, the stabilized productivity index for an infinite conductivity fracture in a rectangular drainage area can be calculated accurately and correlated to the geometry of the drainage area (aspect ratio A_r and penetration ratio I_x).
- The proposed section-based optimization is ready to provide a preliminarily optimized development plan only according to the total resources for the fracturing treatment in a section and some typical parameters of hydraulic fractures with an employed treatment technique.
- In the setting of standard diffusivity equation, the dimensionless total fracture length (l_{fD}) and the feasible range of fracture half-length are the two most important input parameters dictating the number of columns and rows of the optimum fracture array. Other parameters (lateral spacing, cluster spacing, individual fracture penetration) all follow from these main decisions.

- In the development plan of unconventional reservoirs, the amount of proppant available for the whole section is more important than the number of laterals. In fact, the productivity potential is determined first of all by the dimensionless total fracture length l_{fD}. The required number of laterals is basically determined by the technologically feasible range of infinite conductivity fracture half-length.

In the second part, we account for the heterogeneity stemming from the complex conductive fracture network in unconventional reservoirs using subdiffusion-backed fractional diffusivity equation. The following conclusions can be derived from the work of this part:

- According to our qualitative revisit for the physical background of the single-phase diffusivity equation and the demonstration by simulating the particle-wise diffusion on complex fracture networks using a Markov-chain-based model, the topology of a complex fracture network is formally verified to be a major source of anomalous diffusion (including sub-diffusion) in the reservoir scale, so that the fractional diffusivity equation have gained supportive argument for characterizing flow and production in highly fractured unconventional reservoirs.
- In the traditional framework of a horizontal well with multi-stage planar fractures, a fractional production decline model is developed, which results in a set of type curves with three parameters (A_r, I_x, and α). The consistency and robustness of applying the type curves to perform data-fitting based on approximated (A_r, I_x) is confirmed. And The trace of anomalous diffusion is identified by applying this fracture-based model to interpret the synthetic production data of deliberate reservoir simulations. However, the issue of non-uniqueness for applying this model is also found, which to some extent

implies the limitations of such a traditional framework and motivates the exploration for a more effective one for fractured horizontal wells.

- By considering an infinite conductivity horizontal well draining a complex fracture network with a fractional-flux related skin, the first well-based fractional production decline model without accounting for the influx from matrix (Model I) is developed, which results in a set of universal type curves with four two parameters (α, c). Model I is successfully applied to interpret both synthetic and field production data leading to the estimated EURs comparable to the true corresponding true values of the reservoir simulation models, whose heterogeneity only comes from the complex fracture networks. It indicates the fractional models' capability of describing the transient flow regime in the extremely heterogeneous fracture networks.
- As showcased by the application to field data, Model I is ready to interpret the production data during the flow-back period when only liquid flow happens subsurface. And due to the "self-consistency" of this model, some more relevant parameters, such as the SRV range (y_e), the anomalous permeability of the system (k^*), and the range of the convergence region (y_c), can only be estimated after combining the interpreted parameters from our model and the relevant information from other sources.
- After incorporating a tempering factor and a normal-diffusion influx from the matrix into Model I, a new model (Model II) is obtained which is supposed to describe the whole sequence of flow regimes for the production of the slightly compressible flow through fractured horizontal wells. This production performance turns out to be characterized by seven parameters, α, c, λ_D, ω, σ, τ, and EUR. And the resulting

constant bottom-hole solution is ready to be used as the kernel for modeling the cases of variable bottom-hole pressure.

- By investigating the effects of the dimensionless parameters on production performance, some insights about the practice of developing unconventional reservoirs are provided: (a) The essence of using hydraulic fracturing for economic development of unconventional reservoirs is reducing the values of c while increasing ω and σ, assuming α and λ_D are determined by the characteristics of the formation and cannot be largely altered; (b) Two scenarios of potential re-fracturing candidates are identified. One is for the conductivity loss of the initially re-activated fractures due to the depletion. The other is for the insufficiently increased ω or σ for the further recovery; (c) According to the relative extent to which the parameters ω and σ can improve the production performance in different periods of production, the primary goal for the initial production is mainly increasing ω, while that for the re-fracturing is increasing σ; (d) The feasibility of the empirical modified hyperbolic decline curve can be theoretically explained by our model. The effects of ω and σ on speeding-up the recovery from fractured tight formations are attributed to the nature of the classic dual-porosity model, while in the setting of our models both ω and σ are subject to the significant variations due to massive fracturing treatments, instead of the pure formation properties.
- In the setting of our models based on fractional diffusivity equation, the above statement about amount of proppant and well spacing (the last item in the first part) is still basically valid. Large amount of proppant is strongly related to a small value of c.

And an ideal well spacing should be $2y_e$, which is also determined by the employed fracturing techniques, similar to the feasible range of fracture half-length.

- Even though seeming to be sort of trivial, we would like to emphasize again that the fractional models in this dissertation have been developed from a view of "mapped" pressure, which is only a *proxy* in the ideal homogeneous domains for the actual pore pressure in the highly heterogeneous formation, including both the fracture system and the matrix. And this "mapped" pressure only physically makes sense for describing the global or macroscopic performance with respect to the scale of interest, while it is of little physical significance point-wisely.

Based on the results reported for this dissertation, we have several recommendations for future works:

- Though the topology of complex fracture networks as a source of anomalous diffusion has been verified formally in Section 3 and the corresponding continuum models have been validated by comparing with the relevant synthetic and field cases in Section 4 and 5, a rigorous mathematical theory behind needs to be found or even created and then linked back to the practical objects, especially in reservoir engineering.
- Extensions of the fractional models to single-phase compressible flow (by pseudo-pressure) and multi-phase flow (by a novel type of reservoir simulator, whose flux depends on pressure history) are suggested to gain more handles on the flow and production from fractured unconventional reservoirs.
- Model II can be generalized to considering the influx of sub-diffusion by introducing more parameters.

REFERENCES

Abdassah, D., and Ershaghi, I. 1986. Triple-Porosity Systems for Representing Naturally Fractured Reservoirs. *SPE Form Eval* **1** (2): 273-280. SPE-13409-PA

Acuna, J.A., and Yortsos, Y. C. 1991. Numerical Construction and Flow Simulation in Networks of Fractures Using Fractal Geometry. Presented at the SPE Annual Technical Conference and Exhibition, Dallas, Texas, 6-9 October. SPE-22703-MS

Acuna, J.A., Ershaghi, I., and Yortsos, Y. C. 1995. Pressure Practical Application of Fractal Pressure Transient Analysis of Naturally Fractured Reservoirs. *SPE Formation Evaluation* **10** (03): 173-179. SPE-24705-PA

Acuna, J. A., and Yortsos, Y. C. 1995. Application of fractal geometry to the study of networks of fractures and their pressure transient. *Water Resources Research* **31** (3): 527-540

Adams, E. E., and Gelhar, L. W. 1992. Field study of dispersion in a heterogeneous aquifer: 2. Spatial moments analysis. *Water Resources Research* **28** (12): 3293-3307

Albinali, A., Holy, R., Sarak, H., and Ozkan, E. 2016. Modeling of 1D Anomalous Diffusion in Fractured Nanoporous Media. *Oil & Gas Science and Technology – Revue d'IFP Energies Nouvelles* **71** (4), 56

Albinali, A., and Ozkan, E. 2016. Anomalous Diffusion Approach and Field Application for Fractured Nano-Porous Reservoirs. Presented at the SPE Annual Technical Conference and Exhibition, Dubai, UAE, 26-28 September. SPE-181255-MS

Aniemena, C., and Vera, F. 2018. RTA Assisted Production Forecasting in Shale Reservoir Development. Presented at the SPE/AAPG/SEG Unconventional Resources Technology Conference, Unconventional Resources Technology Conference, Houston, Texas, 23-25 July. URTEC-2870785-MS

Ataei, A., Motaei, E., Yazdi, M. E., Masoudi, R., and Bashir, A. 2018. Rate Transient Analysis RTA and Its Application for Well Connectivity Analysis: An Integrated Production Driven Reservoir Characterization and a Case Study. Presented at the SPE Asia Pacific Oil and Gas Conference and Exhibition, Brisbane, Australia, 23-25 October. SPE-192046-MS

Balankin, A. S. 2018. Mapping physical problems on fractals onto boundary value problems within continuum framework. *Physics Letters A* **382** (4): 141-146

Beier, R.A. 1994. Pressure Transient Model of a Vertically Fractured Well in a Fractal Reservoir. *SPE Formation Evaluation* **9** (02): 122-128. SPE-20582-PA

Bello, R. O., and Wattenbarger, R. A. 2008. Rate Transient Analysis in Naturally Fractured Shale Gas Reservoirs. Presented at the CIPC/SPE Gas Technology Symposium 2008 Joint Conference, Calgary, Alberta, Canada, 16-19 June. SPE-114591-MS

Beohar, A., Verma, S. K., Sabharwal, V., Kumar, R., Shankar, P., and Gupta, A. K. 2017. Integrating Pressure Transient and Rate Transient Analysis for EUR Estimation in Tight Gas Volcanic Reservoirs. Presented at the SPE Oil and Gas India Conference and Exhibition, Mumbai, India, 4–6 April. SPE-185376-MS

Berkowitz, B., and Scher, H. 1997. Anomalous transport in random fracture networks. *Physical review letters* **79** (20): 4038

Berkowitz, B., and Scher, H. 2001. The Role of Probabilistic Approaches to Transport Theory in Heterogeneous Media. *Transport in Porous Media* **42** (1-2): 241-263

Blas, J. 2018, December 6. The U.S. Just Became a Net Oil Exporter for the First Time in 75 Years. *Bloomberg.* Retrieved from https://www.bloomberg.com/news/articles/2018-12-06/u-s-becomes-a-net-oil-exporter-for-the-first-time-in-75-years

Blasingame, T. A. and Lee, W. J. 1986. Properties of Homogeneous Reservoirs, Naturally Fractured Reservoirs, and Hydraulically Fractured Reservoirs from Decline Curve Analysis. Presented at the Permian Basin Oil and Gas Recovery Conference, Midland, Texas, 13-15 March. SPE-15018-MS

Blasingame, T. A. and Lee, W. J. 1986. Variable-Rate Reservoir Limits Testing. Presented at the Permian Basin Oil and Gas Recovery Conference, Midland, Texas, 13-15 March. SPE-15028-MS

Blasingame, T. A., Johnston, J. L., and Lee, W. J. 1989. Type-Curve Analysis Using the Pressure Integral Method. Presented at the SPE California Regional Meeting, Bakersfield, California, 5-7 April. SPE-18799-MS

Blasingame, T. A. and Lee, W. J. 1989. Pressure-Buildup Test Analysis- Variable-Rate Case: A

New Approach. *SPE Form Eval* **4** (2): 273-280. SPE-17052-PA

Boulis, A., Jayakumar, R., and Rai, R. 2013. A New Approach for Well Spacing Optimization and Its Application to Various Shale Gas Resources. Presented at the International Petroleum Technology Conference, Beijing, China, 26-28 March. IPTC-17150-MS

Brown, M., Ozkan, E., Raghavan, R., et al. 2011. Practical Solutions for Pressure-Transient Responses of Fractured Horizontal Wells in Unconventional Shale Reservoirs. *SPE Reservoir Evaluation & Engineering* **14** (06): 663–676. SPE-125043-PA

Brown, S. P., and Yücel, M. K. 2013. The shale gas and tight oil boom: U.S. states' economic gains and vulnerabilities. *Council on Foreign Relations*. Retrieved from https://www.cfr.org/report/shale-gas-and-tight-oil-boom

Burg, C., and Erwin, T. 2009. Application of Richardson extrapolation to the numerical solution of partial differential equations. *Numerical Methods for Partial Differential Equations* **25** (4): 810-832

Camacho Velazquez, R., Fuentes-Cruz, G., and Vasquez-Cruz, M. A. 2008. Decline-Curve Analysis of Fractured Reservoirs with Fractal Geometry. *SPE Reservoir Evaluation & Engineering* **11** (03): 606-619. SPE-104009-PA

Chang, J., and Yortsos, Y. C. 1990. Pressure transient analysis of fractal reservoirs. *SPE Formation Evaluation* **5** (01): 31-38. SPE-18170-PA

Chen, C.-C., and Raghavan, R. 1997. A Multiply-Fractured Horizontal Well in a Rectangular Drainage Region. *SPE Journal* **2** (04): 455–465. SPE-37072-PA

Chen, C., and Raghavan, R. 2015. Transient flow in a linear reservoir for space–time fractional diffusion. *Journal of Petroleum Science and Engineering* **128**: 194–202

Chow, V. T. 1952. On the determination of transmissibility and storage coefficients from pumping test data. *Transactions, American Geophysical Union* **33** (3): 397

Chu, W., Pandya, N., Flumerfelt, R. W., and Chen, C. 2017. Rate-Transient Analysis Based on Power-Law Behavior for Permian Wells. Presented at the SPE Annual Technical Conference and Exhibition, San Antonio, Texas, 9-11 October. SPE-187180-MS

Chu, W., Scott, K., Flumerfelt, R., and Chen, C.-C. 2018. A New Technique for Quantifying Pressure Interference in Fractured Horizontal Shale Wells. Presented at the SPE Annual Technical Conference and Exhibition, Dallas, Texas, 24-26 September. SPE-191407-MS

Cinco L., H., Samaniego V., F., and Dominguez A., N. 1978. Transient Pressure Behavior for a Well with a Finite-Conductivity Vertical Fracture. *SPE Journal* **18** (4): 253-264. SPE-6014-PA

Cinco-Ley, H., & Samaniego-V., F. 1981. Transient Pressure Analysis for Fractured Wells. *Journal of Petroleum Technology* **33** (09): 1,749-1,766. SPE-7490-PA

Clark, J. B. 1949. A Hydraulic Process for Increasing the Productivity of Wells. *Journal of Petroleum Technology* **1** (01): 1–8. SPE-949001-G

Clarkson, C. R. and Pedersen, P. K. 2010. Tight Oil Production Analysis: Adaptation of Existing Rate-Transient Analysis Techniques. Presented at the Canadian Unconventional Resources and International Petroleum Conference, Calgary, Alberta, Canada, 19-21 October. SPE-137352-MS

Cossio, M., Moridis, G., and Blasingame, T. A. 2013. A Semianalytic Solution for Flow in Finite-Conductivity Vertical Fractures by Use of Fractal Theory. *SPE Journal* **18** (01): 83-96. SPE-153715-PA

Dake, L. P. 1983. *Fundamentals of reservoir engineering*. Amsterdam, The Netherlands: Elsevier.

de Swaan, A. 1978. Theory of Waterflooding in Fractured Reservoirs. *SPE Journal* **18** (2): 117-122. SPE-5892-PA.

Eburi, S., Padmakar, A. S., Wilson, K., Banki, R. et al. 2014. Well Spacing Optimization of Liquid Rich Shale Plays Using Reservoir Simulation. Presented at the SPE Annual Technical Conference and Exhibition, Amsterdam, Netherlands, 27-29 October. SPE-170833-MS

Einstein, A. 1905. Über die von der molekularkinetischen Theorie der Wärme geforderte Bewegung von in ruhenden Flüssigkeiten suspendierten Teilchen. *Annalen der physik* **322** (8): 549-560

Energy Information Administration. 2016. *Trends in U.S. Oil and Natural Gas Upstream Costs*. Retrieved from https://www.eia.gov/analysis/studies/drilling/pdf/upstream.pdf

Energy Information Administration. 2017. *Annual Energy Outlook 2017 with projections to 2050*. Retrieved from https://www.eia.gov/outlooks/aeo/pdf/0383(2017).pdf

Energy Information Administration. 2018, March 8. *How much shale (tight) oil is produced in the United States?*. Retrieved from https://www.eia.gov/tools/faqs/faq.php?id=847&t=6

Energy Information Administration. 2018. *Annual Energy Outlook 2018 with projections to 2050*. Retrieved from https://www.eia.gov/outlooks/aeo/pdf/AEO2018.pdf

Fan, D., and Ettehadtavakkol, A. 2017. Semi-analytical modeling of shale gas flow through fractal induced fracture networks with microseismic data. *Fuel* **193**: 444-459

Fisher, M. K., Heinze, J. R., Harris, C. D. et al. 2004. Optimizing Horizontal Completion Techniques in the Barnett Shale Using Microseismic Fracture Mapping. Presented at the SPE Annual Technical Conference and Exhibition, Houston, Texas, 26-29 September. SPE-90051-MS

Flamenco-Lopez, F., and Camacho Velazquez, R. 2003. Determination of Fractal Parameters of Fracture Networks Using Pressure-Transient Data. *SPE Reservoir Evaluation & Engineering* **6** (01): 39-47. SPE-82607-PA

Flores, C. P., Holditch, S. A., and Ayers, W. B. 2011. Economics and Technology Drive Development of Unconventional Oil and Gas Reservoirs: Lessons Learned in the United States. Presented at the SPE Annual Technical Conference and Exhibition, Denver, Colorado, 30 October-2 November. SPE-146765-MS.

Fuentes-Cruz, G. and Valko, P. P. 2015. Revisiting the Dual-Porosity/Dual-Permeability Modeling of Unconventional Reservoirs: The Induced-Interporosity Flow Field. *SPE Journal* **20** (1): 124-141. SPE-173895-PA

Gale, J. F., Laubach, S. E., Olson, J. E., and et al. 2014. Natural fractures in shale: A review and new observations. *AAPG bulletin* **98** (11): 2165-2216

Grechishnikova, A. (2017). Niobrara discrete fracture networks: From outcrop surveys to subsurface reservoir models. Presented at the 2017 SEG International Exposition and Annual Meeting, Society of Exploration Geophysicists, Houston, Texas, 24-29 September

Gringarten, A. C., Ramey, H. J., and Raghavan, R. 1974. Unsteady-State Pressure Distributions Created by a Well with a Single Infinite-Conductivity Vertical Fracture. *SPE Journal* **14**

(4): 347-360. SPE-4051-PA

Guo, X., Wu, K., and Killough, J. 2018. Investigation of Production-Induced Stress Changes for Infill-Well Stimulation in Eagle Ford Shale. *SPE Journal* **23** (04): 1,372-1,388. SPE-189974-PA

Hagberg, Aric A., Schult, Daniel A., and Swart, Pieter J. 2008. Exploring network structure, dynamics, and function using NetworkX. In Gäel Varoquaux, Travis Vaught, and Jarrod Millman (Eds), *Proceedings of the 7th Python in Science Conference (SciPy2008)*, Pasadena, California, Aug 2008

Hagoort, J. 2009. The Productivity of a Well with a Vertical Infinite-Conductivity Fracture in a Rectangular Closed Reservoir. *SPE Journal* **14** (04): 715–720. SPE-112975-PA

Hagoort, J. 2010. Production Performance of a Constant-Pressure Well in an Orthogonally Fractured Reservoir. *SPE Reservoir Evaluation & Engineering* **13** (3): 523-537. SPE-120228-PA

Haubold, H. J., Mathai, A. M., & Saxena, R. K. 2011. Mittag-Leffler functions and their applications. *Journal of Applied Mathematics* **2011** (298628)

Havlin, S., and Ben-Avraham, D. 1987. Diffusion in disordered media. *Advances in Physics* **36** (6): 695-798

Holy, R. W., and Ozkan, E. 2016. Numerical Modeling of Multiphase Flow Toward Fractured Horizontal Wells in Heterogeneous Nanoporous Formations. Presented at the SPE Annual Technical Conference and Exhibition, Dubai, UAE, 26-28 September. SPE-181662-MS

Itô, K., and McKean, K. 1996. *Diffusion processes and their Sample Paths*. Berlin/Heidelberg, Germany: Springer

Jahandideh, A., and Jafarpour, B. 2014. Optimization of Hydraulic Fracturing Design Under Spatially Variable Shale Fracability. Presented at the SPE Western North American and Rocky Mountain Joint Meeting, Denver, Colorado, 17-18 April. SPE-169521-MS

Kazemi, H. 1969. Pressure Transient Analysis of Naturally Fractured Reservoirs with Uniform Fracture Distribution. *SPE Journal* **9** (4): 451-462. SPE-2156-PA

Kelly, J. F., Bolster, D., Meerschaert, M. M., Drummond, J. D., and Packman, A. I. 2017. FracFit: A robust parameter estimation tool for fractional calculus models. *Water Resources Research* **53** (3): 2559–2567

King, G. E. 2012. Hydraulic Fracturing 101: What Every Representative, Environmentalist, Regulator, Reporter, Investor, University Researcher, Neighbor and Engineer Should Know About Estimating Frac Risk and Improving Frac Performance in Unconventional Gas and Oil Wells. Presented at the SPE Hydraulic Fracturing Technology Conference, Woodlands, Texas, 6-8 February. SPE-152596-MS

Larsen, L., and Hegre, T. M. 1991. Pressure-Transient Behavior of Horizontal Wells with Finite-Conductivity Vertical Fractures. Presented at the International Arctic Technology Conference, Anchorage, Alaska, 29-31 May. SPE-22076-MS

Larsen, L., and Hegre, T. M. 1994. Pressure Transient Analysis of Multifractured Horizontal Wells. Presented at the SPE Annual Technical Conference and Exhibition, New Orleans, Louisiana, 25-28 September. SPE-28389-MS

Lee, S.-T., and Brockenbrough, J. 1983. A New Analytic Solution for Finite Conductivity Vertical Fractures With Real Time and Laplace Space Parameter Estimation. Presented at the SPE Annual Technical Conference and Exhibition, San Francisco, California, 5-8 October. SPE-12013-MS

Lin, Q., and Xie, R. 1987. Error expansions for finite element approximations and their applications. In Y.-I. Zhu & B. Guo (Eds.), *Numerical Methods for Partial Differential Equations* (pp. 98–112). Berlin/Heidelberg, Germany: Springer

Liu, X., Chen, Z., and Jiang, L. 1987. Exact Solution of Double-Porosity, Double-Permeability Systems Including Wellbore Storage and Skin Effect. Presented at the SPE Annual Technical Conference and Exhibition, Dallas, Texas, 27-30 September. SPE-16849-MS

Ma, X., Plaksina, T., and Gildin, E. 2013. Optimization of Placement of Hydraulic Fracture Stages in Horizontal Wells Drilled in Shale Gas Reservoirs. Presented at the Unconventional Resources Technology Conference, Denver, Colorado, 12-14 August. URTEC-1580378-MS

Mainardi, F. 2014. On some properties of the Mittag-Leffler function $E_\alpha(-t^\alpha)$, completely monotone for $t > 0$ with $0 < \alpha < 1$. *Discrete & Continuous Dynamical Systems-B*, **19** (7): 2267-2278

Malinowska, A. B., Odzijewicz, T., and Torres, D. F. 2015. *Advanced methods in the fractional calculus of variations*. Berlin/Heidelberg, Germany: Springer.

McKoy, and M. L. 1997, October 1. Tight gas reservoir simulation: Modeling discrete irregular strata-bound fracture network flow, including dynamic recharge from the matrix [Article]. Retrieved February 10, 2019, from https://digital.library.unt.edu/ark:/67531/metadc690581/

Meerschaert, M. M., Zhang, Y., and Baeumer, B. 2008. Tempered anomalous diffusion in heterogeneous systems. *Geophysical Research Letters* **35** (17)

Meerschaert, M., Nane, E., and Vellaisamy, P. 2013. Transient anomalous sub-diffusion on bounded domains. *Proceedings of the American Mathematical Society* **141** (2): 699–710

Metzler, R., Glöckle, W. G., and Nonnenmacher, T. F. 1994. Fractional model equation for anomalous diffusion. *Physica A: Statistical Mechanics and its Applications* **211** (1): 13-24

Meyer, B. R., Bazan, L. W., Jacot, R. H. et al. 2010. Optimization of Multiple Transverse Hydraulic Fractures in Horizontal Wellbores. Presented at the SPE Unconventional Gas Conference, Pittsburgh, Pennsylvania, 23-25 February. SPE-131732-MS

Moghanloo, R. G., Yuan, B., Ingrahama, N. et al. 2015. Applying macroscopic material balance to evaluate interplay between dynamic drainage volume and well performance in tight formations. *Journal of Natural Gas Science and Engineering* **27**: 466-478

Moler, C., and Van Loan, C. 2003. Nineteen dubious ways to compute the exponential of a matrix, twenty-five years later. *SIAM review* **45** (1): 3-49

Moridis, G. J., and Blasingame, T. A. 2014. Evaluation of Strategies for Enhancing Production of Low-Viscosity Liquids From Tight/Shale Reservoirs. Presented at the SPE Latin America and Caribbean Petroleum Engineering Conference, Maracaibo, Venezuela, 21-23 May. SPE-169479-MS

Mukherjee, H., and Economides, M. J. 1991. A parametric comparison of horizontal and vertical well performance. *SPE Formation Evaluation* **6** (02): 209-216. SPE-18303-PA

Olorode, O. M., Akkutlu, I. Y., and Efendiev, Y. 2017. Compositional Reservoir Flow Simulation for Organic-Rich Gas Shale. Presented at the SPE Reservoir Simulation Conference,

Montgomery, Texas, 20-22 February. SPE-182667-MS

O'Shaughnessy, B., & Procaccia, I. 1985. Analytical Solutions for Diffusion on Fractal Objects. *Physical Review Letters* **54** (5): 455–458

Ozcan, O., Sarak, H., Ozkan, E., and Raghavan, R. S. 2014. A Trilinear Flow Model for a Fractured Horizontal Well in a Fractal Unconventional Reservoir. Presented at the SPE Annual Technical Conference and Exhibition, Amsterdam, The Netherlands, 27-29 October. SPE-170971-MS

Ozkan, E., and Raghavan, R. 1988. Some New Solutions to Solve Problems in Well Test Analysis: Part 1 - Analytical Considerations. SPE-18615-MS

Ozkan, E., Brown, M. L., Raghavan, R. S., and Kazemi, H. 2009. Comparison of Fractured Horizontal-Well Performance in Conventional and Unconventional Reservoirs. Presented at the SPE Western Regional Meeting, San Jose, California, 24-26 March. SPE-121290-MS.

Qanbari, F., and Clarkson, C. R. 2016. Rate-Transient Analysis of Liquid-Rich Tight/Shale Reservoirs Using the Dynamic Drainage Area Concept: Examples from North American Reservoirs. Presented at the SPE Low Perm Symposium, Denver, Colorado, 5-6 May. SPE-180230-MS

Prats, M. 1961. Effect of Vertical Fractures on Reservoir Behavior-Incompressible Fluid Case. *SPE Journal* **1**(2): 105-118. SPE-1575-G

Raghavan, R. S., Chen, C.-C., and Agarwal, B. 1997. An Analysis of Horizontal Wells Intercepted by Multiple Fractures. *SPE Journal* **2** (03): 235–245. SPE-27652-PA

Raghavan, R. 2011. Fractional derivatives: application to transient flow. *Journal of Petroleum Science and Engineering* **80** (1): 7-13

Raghavan, R., and Chen, C. 2013. Fractional diffusion in rocks produced by horizontal wells with multiple, transverse hydraulic fractures of finite conductivity. *Journal of Petroleum Science and Engineering* **109**: 133–143

Raghavan, R., and Chen, C. 2017. Addressing the Influence of a Heterogeneous Matrix on Well Performance in Fractured Rocks. *Transport in Porous Media* **117** (1): 69-102

Raghavan, R., and Chen, C. 2017. Rate decline, power laws, and subdiffusion in fractured rocks. *SPE Reservoir Evaluation & Engineering* **20** (03): 738-751. SPE-180223-PA

Raghavan, R., & Chen, C. 2018. Time and Space Fractional Diffusion in Finite Systems. *Transport in Porous Media* **123** (1): 173–193

Raghavan, R., and Chen, C. 2019. The Theis solution for subdiffusive flow in rocks. *Oil & Gas Science and Technology – Revue d'IFP Energies Nouvelles* **74**: 6

Raterman, K. T., Farrell, H. E., Mora, O. S., et al. 2017. Sampling a Stimulated Rock Volume: An Eagle Ford Example. Presented at the SPE/AAPG/SEG Unconventional Resources Technology Conference, Austin, Texas, 24-26 July. URTEC-2670034-MS

Rogers, L. C. G., and Williams, D. 1994. Diffusions, Markov processes and martingales: Volume 2, Itô calculus. Cambridge, United Kingdom: Cambridge University press

Roussel, N. P., and Sharma, M. M. 2011. Optimizing Fracture Spacing and Sequencing in Horizontal-Well Fracturing. *SPE Production & Facilities* **26** (2): 173-184. SPE-127986-PA

Russell, D. G., and Truitt, N. E. 1964. Transient Pressure Behavior in Vertically Fractured Reservoirs. *Journal of Petroleum Technology* **16** (10): 1159-1170. SPE-967-PA

Sabzikar, F., Meerschaert, M. M., and Chen, J. 2015. Tempered fractional calculus. *Journal of Computational Physics* **293**: 14–28

Salami, O. 2014. Synthesis and Working Mechanism of Humic Acid Graft Copolymer Fluid Loss Additives Suitable for Cementing High Pressure / High Temperature Oil and Gas Wells. (Doctoral Dissertation). Retrieved from https://www.researchgate.net/publication/264391238_Synthesis_and_Working_Mechanism_of_Humic_Acid_Graft_Copolymer_Fluid_Loss_Additives_Suitable_for_Cementing_High_Pressure_High_Temperature_Oil_and_Gas_Wells/references

Sidje, R. B. 1998. Expokit: a software package for computing matrix exponentials. *ACM Transactions on Mathematical Software (TOMS)* **24** (1): 130-156

Soliman, M. Y., Hunt, J. L., and Azari, M. 1999. Fracturing Horizontal Wells in Gas Reservoirs. *SPE Production & Facilities* **14** (4): 277-283. SPE-59096-PA

Soroushian, A. 2010, Pseudo convergence and its implementation in engineering approximate computations, Proceedings of the International Conference from Scientific Computing to Computational Engineering, 4th IC-SCCE, Athens, Greece, 7-10 July.

splichte. 2013. *lsi*. In GitHub repository. Retrieved from https://github.com/splichte/lsi

Transition rate matrix. (n.d.). In Wikipedia. Retrieved January 20, 2019, from https://en.wikipedia.org/wiki/Transition_rate_matrix

Valdes-Perez, A. R., and Blasingame, T. A. 2018. Pressure-Transient Behavior of Double Porosity Reservoirs with Transient Interporosity Transfer with Fractal Matrix Blocks. Presented at the SPE Europec featured at 80th EAGE Conference and Exhibition, Copenhagen, Denmark, 11-14 June. SPE-190841-MS

Valdes-Perez, A. R., Larsen L., and Blasingame, T. A. 2018. Pressure-Transient Behavior of a Horizontal Well with a Finite-Conductivity Fracture within a Fractal Reservoir. Presented at the SPE Canada Unconventional Resources Conference, Calgary, Alberta, Canada, 13-14 March. SPE-189814-MS

Valkó, P.P. and Abate, J. 2004. Comparison of Sequence Accelerators for the Gaver Method of Numerical Laplace Transform Inversion. *Computers and Mathematics with Application* **48** (3-4): 629-636

Vilaseca, E., Isvoran, A., Madurga, S., and et al. 2011. New insights into diffusion in 3D crowded media by Monte Carlo simulations: effect of size, mobility and spatial distribution of obstacles. *Physical Chemistry Chemical Physics* **13** (16), 7396-7407

Vlahos, L., Isliker, H., Kominis, Y., et al. 2008. Normal and Anomalous Diffusion: A Tutorial. Retrieved from https://arxiv.org/abs/0805.0419

Wang, J., Wei, Y., and Qi, Y. 2016. Semi-Analytical Modeling of Flow Behavior in Fractured Media with Fractal Geometry. *Transport in Porous Media* **112** (3): 707–736

Wang, W., Su, Y., Sheng, G., Cossio, M., and Shang, Y. 2015. A mathematical model considering complex fractures and fractal flow for pressure transient analysis of fractured horizontal wells in unconventional reservoirs. *Journal of Natural Gas Science and Engineering* **23**: 139-147.

Wang, W., Shahvali, M., and Su, Y. 2015. A semi-analytical fractal model for production from

tight oil reservoirs with hydraulically fractured horizontal wells. *Fuel* **158**: 612-618.

Warren, J. E. and Root, P. J. 1963. The Behavior of Naturally Fractured Reservoirs. *SPE Journal* **3**(3): 245-255. SPE-426-PA

Wattenbarger, R. A., El-Banbi, A. H., Villegas, M. E., et al. 1998. Production analysis of linear flow into fractured tight gas wells. Presented in the SPE rocky mountain regional/low-permeability reservoirs symposium, Denver, Colorado, 5-8 April. SPE-39931-MS

Weng, X., Kresse, O., Chuprakov, D., et al. 2014. Applying complex fracture model and integrated workflow in unconventional reservoirs. *Journal of Petroleum Science and Engineering* **124**: 468–483

Wilson, K. C., and Durlofsky, L. J. 2013. Optimization of shale gas field development using direct search techniques and reduced-physics models. Journal of Petroleum Science and Engineering **108**: 304–315

Wolfram Research, Inc. 2018. Mathematica (Version 11.3), Champaign, IL

Wu, K., and Olson, J. E. 2015. Simultaneous multifracture treatments: fully coupled fluid flow and fracture mechanics for horizontal wells. *SPE journal* **20** (02): 337-346. SPE-167626-PA

Xiong, H., Liu, S., Feng, F., et al. 2019. Optimize Completion Design and Well Spacing with the Latest Complex Fracture Modeling & Reservoir Simulation Technologies – A Permian Basin Case Study with Seven Wells. Presented at the SPE Hydraulic Fracturing Technology Conference and Exhibition, Woodlands, Texas, 5-7 February. SPE-194367-MS

Yang, X. 2018. Tempered Fractional Derivative: Application to Linear Flow (Master's theses). Texas A&M University, College Station, Texas. Retrieved from The OAKTrust digital repository at Texas A&M (2019-01-18T14:55:27Z)

Yu, W., and Sepehrnoori, K. 2013. Optimization of Multiple Hydraulically Fractured Horizontal Wells in Unconventional Gas Reservoirs. Presented at the SPE Production and Operations Symposium, Oklahoma City, Oklahoma, 23-26 March. SPE-164509-MS

Yuan, B., Zhang, Z., and Clarkson, C. R. 2018. Distance-of-Investigation Could be Misused in Unconventional Heterogeneous Reservoirs with Non-Static Properties. Presented at the SPE Annual Technical Conference and Exhibition, Dallas, Texas, 24-26 September. SPE-

Zhang, Y., Meerschaert, M. M., and Baeumer, B. 2008. Particle tracking for time-fractional diffusion. *Physical Review E* **78** (3): 036705.

APPENDIX A

STABILIZED PRODUCTIVITY INDEX OF THE BOUNDARY-DOMINATED STATE

To derive the expression of the stabilized PI for BDS (Eq. (2.5)), we solve the system of Eq. (2.3a) to Eq. (2.3g), which is copied below as Eq. (A1)

$$\frac{\partial^2 P_D}{\partial x_D^2}+\frac{\partial^2 P_D}{\partial y_D^2}=\frac{\partial P_D}{\partial t_D} \quad \text{(A1a)}$$

$$t_D=0: P_D=1 \quad \text{(A1b)}$$

$$x_D=\sqrt{A_r}, 0\le y_D\le \frac{1}{\sqrt{A_r}}: \frac{\partial P_D}{\partial x_D}=0 \quad \text{(A1c)}$$

$$y_D=\frac{1}{\sqrt{A_r}}, 0\le x_D\le \sqrt{A_r}: \frac{\partial P_D}{\partial y_D}=0 \quad \text{(A1d)}$$

$$x_D=0, 0\le y_D\le \frac{1}{\sqrt{A_r}}: \frac{\partial P_D}{\partial x_D}=0 \quad \text{(A1e)}$$

$$y_D=0, I_x\sqrt{A_r}\le x_D\le \sqrt{A_r}: \frac{\partial P_D}{\partial y_D}=0 \quad \text{(A1f)}$$

$$y_D=0, 0\le x_D\le I_x\sqrt{A_r}: P_D=0 \quad \text{(A1g)}$$

The above problem, Eq. (A1), is a typical linear PDE with an initial condition and homogeneous boundary conditions. So, it can be solved by the method of variable separation. Assume that P_D is the product of two functions which are the function of spatial variables and temporal variable respectively.

$$P_D(t_D, x_D, y_D)=G(t_D)\varphi(x_D, y_D) \quad \text{(A2)}$$

Then, Eq. (A2) can be rearranged into the form

$$\frac{1}{\varphi}\left(\frac{\partial^2\varphi}{\partial x_D^2}+\frac{\partial^2\varphi}{\partial y_D^2}\right)=\frac{1}{G}\frac{\partial G}{\partial t_D}=-\lambda \quad \text{(A3)}$$

Here λ is the eigenvalue for the system.

After splitting Eq. (A3) and solving for F and G respectively, for each specified λ_i, we have

$$G = C_1 exp(-\lambda_i t_D) \quad \text{(A4)}$$

$$\varphi = C_2 \varphi_i(x_D, y_D) \quad \text{(A5)}$$

where C_1 and C_2 are the constants of integration with arbitrary values, and φ_i is the eigenfunction corresponding to λ_i.

The general solution for the dimensionless problem is written like Eq. (A6).

$$P_D(t_D, x_D, y_D) = \sum_{i=1}^{\infty} A_i \exp(-\lambda_i t_D)\varphi_i(x_D, y_D) \quad \text{(A6)}$$

Since the solution includes the temporal exponential term, from the perspective of physics the parameter before time t_D must be a non-negative number, otherwise p_D would increase exponentially to infinity. In addition, $\lambda = 0$ corresponds to a φ_i which represents the dimensionless pressure distribution at $t_D = \infty$. According to the feature of constant pressure production and the definition of the dimensionless group, $P_D(t_D = \infty, x_D, y_D) = 0$. That is, the φ_i corresponding to $\lambda = 0$ is 0. Therefore, all the nontrivial eigenvalues are positive. Without losing any generality, λ_i are arranged in the order of ascendant absolute value with i increasing from 1 to infinity.

In the quarter of the reservoir, the flow rate can be expressed as Eq. (A7).

$$\frac{q_{sc}B}{4} = H\int_0^{x_f}(-v)\,dx = H\int_0^{x_f}\frac{k}{\mu}\frac{\partial p}{\partial y}dx = \frac{kH}{\mu}\int_0^{x_f}\frac{\partial P}{\partial y}dx \quad \text{.....(A7)}$$

According to the definition of dimensionless groups, the dimensionless flow rate can be derived from Eq. (A7), as Eq. (A8) shows.

$$q_{scD} = \frac{\mu B q_{sc}}{2\pi kh(P_i - P_w)} = \frac{2}{\pi}\int_0^{x_f}\frac{\partial P_D}{\partial y}dx = \frac{2}{\pi}\int_0^{x_{fD}}\frac{\partial P_D}{\partial y_D}dx_D = \frac{2}{\pi}\int_{\Gamma_D}\left(-\frac{\partial P_D}{\partial n}\right)ds$$

$$= -\frac{2}{\pi}\int_{\Gamma_D}\nabla P_D\cdot\vec{n}\,ds \quad \text{.....(A8)}$$

By using the divergence theorem, Eq. (A8) can be written as

$$q_{scD} = -\frac{2}{\pi}\int_{\Gamma_D}\nabla P_D\cdot\vec{n}\,ds = -\frac{2}{\pi}\int_{\Omega_D}\nabla\cdot\nabla P_D\,dX_D = -\frac{2}{\pi}\int_{\Omega_D}\nabla^2 P_D\,dX_D \quad \text{.....(A9)}$$

As the definition of the dimensionless PI shows,

$$J_D = \frac{q_{scD}}{\overline{P_D} - P_{wD}} = \frac{q_{scD}}{\overline{P_D}} = -\frac{2}{\pi}\frac{\int_{\Omega_D}\nabla^2 P_D\,dX_D}{\int_{\Omega_D}P_D\,dX_D}$$

$$= -\frac{2}{\pi}\frac{\int_{\Omega_D}\nabla^2\sum_{i=1}^{\infty}A_i\exp(-\lambda_i t_D)\varphi_i(x_D,y_D)\ \mathrm{d}X_D}{\int_{\Omega_D}\sum_{i=1}^{\infty}A_i\exp(-\lambda_i t_D)\varphi_i(x_D,y_D)\ \mathrm{d}X_D}$$

$$= -\frac{2}{\pi}\frac{\sum_{i=1}^{\infty}A_i\exp(-\lambda_i t_D)\int_{\Omega_D}\nabla^2\varphi_i(x_D,y_D)\ dX_D}{\sum_{i=1}^{\infty}A_i\exp(-\lambda_i t_D)\int_{\Omega_D}\varphi_i(x_D,y_D)\ dX_D}$$

$$= -\frac{2}{\pi}\frac{A_1\exp(-\lambda_1 t_D)\int_{\Omega_D}\nabla^2\varphi_1\,dX_D + \sum_{i=2}^{\infty}A_i\exp(-\lambda_i t_D)\int_{\Omega_D}\nabla^2\varphi_i\ dX_D}{A_1\exp(-\lambda_1 t_D)\int_{\Omega_D}\varphi_1\ dX_D + \sum_{i=2}^{\infty}A_i\exp(-\lambda_i t_D)\int_{\Omega_D}\varphi_i\ dX_D} \quad \text{.....(A10)}$$

From the above discussions, we know that $\lambda_i > 0$ and when $i > 1$, $|\lambda_i| > |\lambda_1|$. Thus, when $i > 1$, $\lambda_i - \lambda_1 > 0$. Finally, we can get the expression for the dimensionless PI for BDS.

$$J_{D,BDS} = -\frac{2}{\pi}\lim_{t_D\to\infty}\frac{A_1\int_{\Omega_D}\nabla^2\varphi_1\,dX_D + \sum_{i=2}^{\infty}A_i\exp(-(\lambda_i-\lambda_1)t_D)\int_{\Omega_D}\nabla^2\varphi_i\,dX_D}{A_1\int_{\Omega_D}\varphi_1\,dX_D + \sum_{i=2}^{\infty}A_i\exp(-(\lambda_i-\lambda_1)t_D)\int_{\Omega_D}\varphi_i\,dX_D}$$

$$= -\frac{2}{\pi}\frac{\int_{\Omega_D} \nabla^2 F_1 \, dX_D}{\int_{\Omega_D} F_1 \, dX_D} = \frac{2}{\pi}\lambda_1 \quad \text{.....(A11)}$$

The above derivation shows that the BDS dimensionless PI can be expressed by the minimum eigenvalue of the original time-dependent system. Furthermore, it will be proved that only a relevant time-independent eigensystem needs to be solved to get the eigenvalues of the original problem.

All the λ_i and φ_i are determined from the time-independent part of Eq. (A3), which is shown in Eq. (A12a), plus some appropriate boundary conditions.

$$\frac{\partial^2 \varphi}{\partial x_D^2} + \frac{\partial^2 \varphi}{\partial y_D^2} = -\lambda\varphi \quad \text{.....(A12a)}$$

Substitute Eq. (A2) into the original boundary conditions Eq. (A1c) to Eq. (A1g), take the temporal function $G(t_D)$ out of the spatial partial derivative and eliminate it. Then we can get

$$x_D = \sqrt{A_r}, 0 \le y_D \le \frac{1}{\sqrt{A_r}} : \frac{\partial \varphi}{\partial x_D} = 0 \quad \text{.....(A12b)}$$

$$y_D = \frac{1}{\sqrt{A_r}}, 0 \le x_D \le \sqrt{A_r} : \frac{\partial \varphi}{\partial y_D} = 0 \quad \text{.....(A12c)}$$

$$x_D = 0, 0 \le y_D \le \frac{1}{\sqrt{A_r}} : \frac{\partial \varphi}{\partial x_D} = 0 \quad \text{.....(A12d)}$$

$$y_D = 0, I_x\sqrt{A_r} \le x_D \le \sqrt{A_r} : \frac{\partial \varphi}{\partial y_D} = 0 \quad \text{.....(A12e)}$$

$$y_D = 0, 0 \le x_D \le I_x\sqrt{A_r} : \varphi = 0 \quad \text{.....(A12f)}$$

Eq. (A12) is the time-independent eigensystem to be solved for getting the eigenvalues and eigenfunctions of the original problem. In fact, to solve Eq. (A12) is a main step in the variable separation method. That is, the eigenvalues and eigenfunctions of the system Eq. (A12) are

equivalent to those of the original system Eq. (A1). In the computations, only this simple time-independent system is solved to get the BDS dimensionless PI.

APPENDIX B

STABILIZED PRODUCTIVITY INDEX OF THE PSEUDO-STEADY STATE

The general governing equation in dimensional domain for the constant rate case is the same as that for the constant pressure (Eq. (2.1)).

During the PSS, each point in the reservoir shares the same rate of pressure change, so does the average pressure of the whole reservoir.

$$\frac{\partial P}{\partial t} = \frac{\partial \bar{P}}{\partial t} \quad \text{(B1)}$$

With the material balance of a quarter of the reservoir, Eq. (B2),

$$c_t AH(P_i - \bar{P}) = \frac{q_{sc}}{4} Bt \quad \text{(B2)}$$

the time derivative term in Eq. (2.1) can be written as

$$\frac{\partial P}{\partial t} = \frac{\partial \bar{P}}{\partial t} = -\frac{q_{sc} B}{4 c_t AH} \quad \text{(B3)}$$

Combining Eq. (2.1) and Eq. (B3), the governing equation for the pseudo steady state is obtained, like Eq. (B4).

$$\frac{\partial^2 P}{\partial x^2} + \frac{\partial^2 P}{\partial y^2} = -\frac{\mu q_{sc} B}{4kAH} \quad \text{(B4)}$$

For an infinite-conductivity fracture centrally located in a closed reservoir, the boundary conditions in a quarter of the reservoir are as Eq. (2.2b) to Eq. (2.2e), Eq. (2.2g) and Eq. (2.2h) show.

After substituting the corresponding dimensionless group in Section 2.2.1.1 the PSS problem can be defined as

$$\frac{\partial^2 P_D}{\partial x_D^2} + \frac{\partial^2 P_D}{\partial y_D^2} = -\frac{\pi}{2} \quad \text{(B5a)}$$

$$x_D = \sqrt{A_r}, 0 \le y_D \le \frac{1}{\sqrt{A_r}} : \frac{\partial P_D}{\partial x_D} = 0 \quad \text{(B5b)}$$

$$y_D = \frac{1}{\sqrt{A_r}}, 0 \le x_D \le \sqrt{A_r} : \frac{\partial P_D}{\partial y_D} = 0 \quad \text{(B5c)}$$

$$x_D = 0, 0 \le y_D \le \frac{1}{\sqrt{A_r}} : \frac{\partial P_D}{\partial x_D} = 0 \quad \text{(B5d)}$$

$$y_D = 0, I_x\sqrt{A_r} \le x_D \le \sqrt{A_r} : \frac{\partial P_D}{\partial y_D} = 0 \quad \text{(B5e)}$$

$$y_D = 0, 0 \le x_D \le I_x\sqrt{A_r} : P_D = 0 \quad \text{(B5f)}$$

At last, according to the definition of dimensionless PI,

$$J_{D,PSS} = \frac{q_{scD}}{\overline{P_D} - P_{scD}} = \frac{1}{\overline{P_D}} = \frac{A_D}{\int_{\Omega_D} P_D dX} = \frac{1}{\int_{\Omega_D} P_D dX}. \quad \text{(B12)}$$

APPENDIX C

FRACTIONAL FLUX LAW FROM FRACTIONAL DIFFUSIVITY EQUATION

To derive the fractional flux law, we take advantage of the specific property of the fractional calculus (Malinowska et al., 2015), as shown in Eq. (C1).

$$\left({}_0I_t^{\alpha} \circ \frac{d^{\alpha}}{dt_D^{\alpha}} \right)[f](t) = f(t) \quad \text{(C1)}$$

where ${}_0I_t^{\alpha} f(t)$ is the Riemann-Liouville fractional integral, which is defined when $0 < \alpha \leq 1$ in Eq. (C2).

$${}_0I_t^{\alpha} f(t) := \frac{1}{\Gamma(\alpha)} \int_0^t \frac{f(\tau)}{(t-\tau)^{1-\alpha}} d\tau \quad \text{(C2)}$$

Comparing the above definition with the definition in Eq. (4.7), it is evident that

$$\frac{d^{\alpha}}{dt^{\alpha}} f(t) = \frac{d}{dt}\ {}_0I_t^{1-\alpha} f(t) \quad \text{(C3)}$$

Performing Riemann-Liouville fractional integral on both sides of Eq. (4.6), we obtain

$$P = \eta^*\ {}_0I_t^{\alpha}(\Delta P) \quad \text{(C4)}$$

Then taking first order time derivative on both sides of Eq. (C4) yields

$$\frac{\partial}{\partial t} P = \eta^* \frac{\partial}{\partial t}\ {}_0I_t^{\alpha}(\Delta P) \quad \text{(C5)}$$

or

$$\phi c_t \frac{\partial}{\partial t} P = \frac{k^*}{\mu} \frac{\partial}{\partial t}\ {}_0I_t^{\alpha}(\nabla \cdot \nabla P) \quad \text{(C6)}$$

Since $\frac{\partial}{\partial t}$ and ${}_0I_t^{\alpha}$ only operates with respect to t, they hold the commutative property along with the spatial operator $\nabla \cdot$. Thus, we have

$$\phi c_t \frac{\partial}{\partial t} P = \nabla \cdot \left[\frac{k^*}{\mu} \frac{\partial}{\partial t} \, {}_0I_t^{\alpha} (\nabla P) \right] \quad \text{(C7)}$$

Using the relation in Eq. (C3), Eq. (C7) can be written as

$$\phi c_t \frac{\partial}{\partial t} P = \nabla \cdot \left[\frac{k^*}{\mu} \frac{\partial^{1-\alpha}}{\partial t^{1-\alpha}} (\nabla P) \right] \quad \text{(C8)}$$

Comparing Eq. (C8) with the general conservation law, we can obtain the fractional flux law as Eq. (C9) shows.

$$\vec{v} = -\frac{k^*}{\mu} \frac{\partial^{1-\alpha}}{\partial t^{1-\alpha}} \nabla P \quad \text{(C9)}$$

APPENDIX D

SOLUTION OF FRACTIONAL DIFFUSIVITY EQUATION BY THE METHOD OF SEPARATION VARIABLES

With the definition in Eq. (4.7), even though the fractional order time derivative is included, the problem, Eq. (4.10), is a typical linear partial differential equation PDE supplemented by a uniform initial condition and homogeneous boundary conditions. So, the method of variable separation is employed to obtain the solution.

Assume that P_D is the product of two functions which are the function of spatial variables and temporal variable respectively.

$$P_D(t_D, x_D, y_D) = G(t_D)\varphi(x_D, y_D) \quad \text{(D1)}$$

Then, Eq. (4.10a) can be rearranged into the form

$$\frac{1}{\varphi}\left(\frac{\partial^2\varphi}{\partial x_D^2} + \frac{\partial^2\varphi}{\partial y_D^2}\right) = \frac{1}{G}\frac{\partial^\alpha G}{\partial t_D^\alpha} = -\lambda \quad \text{(D2)}$$

Here λ is the eigenvalue for the system.

To solve φ, the governing equation only regarding φ is obtained from Eq. (D2) and the pertinent boundary conditions by substituting Eq. (D1) into Eq. (4.12c) to Eq. (4.12g), which leads to the following eigenvalue problem.

$$\frac{\partial^2\varphi}{\partial x_D^2} + \frac{\partial^2\varphi}{\partial y_D^2} = -\lambda\varphi \quad \text{(D3a)}$$

$$x_D = \sqrt{A_r}, 0 \le y_D \le 1/\sqrt{A_r} : \frac{\partial\varphi}{\partial x_D} = 0 \quad \text{(D3b)}$$

$$y_D = 1/\sqrt{A_r}, 0 \le x_D \le \sqrt{A_r} : \frac{\partial \varphi}{\partial y_D} = 0 \quad \text{(D3c)}$$

$$x_D = 0, 0 \le y_D \le 1/\sqrt{A_r} : \frac{\partial \varphi}{\partial x_D} = 0 \quad \text{(D3d)}$$

$$y_D = 0, I_x\sqrt{A_r} < x_D \le \sqrt{A_r} : \frac{\partial \varphi}{\partial y_D} = 0 \quad \text{(D3e)}$$

For a specified eigenvalue λ_i, φ is expressed as Eq. (D4).

$$\varphi = C_{1i}\varphi_i(x_D, y_D) \quad \text{(D4)}$$

where C_{1i} is the constants of integration with arbitrary values, and φ_i is the eigenfunction corresponding to λ_i.

Regarding G, another eigenvalue problem, shown by Eq. (D5), out of Eq. (D2) is to be solved.

$$\frac{\partial^\alpha G}{\partial t_D^\alpha} = -\lambda G \quad \text{(D5)}$$

By Mainardi (2014), the solution for an equation in the form of Eq. (D5) with a specified λ_i is expressed as

$$G = C_{2i}E_\alpha(-\lambda_i t_D^\alpha) \quad \text{(D6)}$$

where C_{2i} is the constants of integration with arbitrary values, and E_α is the corresponding Mittag-Leffler function with one parameter.

After combining the solution in Eq. (D4) and Eq. (D6) and performing superposition on the solutions of all possible λ_i, the general solution is written like Eq. (D7).

$$P_D(x_D, y_D, t_D) = \sum_{i=1}^{\infty} C_i E_\alpha(-\lambda_i t_D^\alpha)\varphi_i(x_D, y_D) \quad \text{(D7)}$$

where $C_i = C_{1i}C_{2i}$.

To solve for the integration constants A_i, Eq. (D7) is evaluated at the initial time combined with the initial condition, Eq. (4.10b), as shown in Eq. (D8).

$$1 = \sum_{i=1}^{\infty} C_i \varphi_i(x_D, y_D) \quad \text{.....(D8)}$$

By the orthogonality of the eigenfunction $\varphi_i(x_D, y_D)$, C_i is expressed as Eq. (D9) if $\varphi_i(x_D, y_D)$ is normalized.

$$C_i = \int_{\Omega} \varphi_i(x_D, y_D) dX_D \quad \text{.....(D9)}$$

In all, the solution of the problem, Eq. (4.10), is

$$P_D(x_D, y_D, t_D) = \sum_{i=1}^{\infty} E_\alpha(-\lambda_i t_D^\alpha) \varphi_i(x_D, y_D) \int_{\Omega} \varphi_i(x_D, y_D) dX_D \quad \text{.....(D10)}$$

APPENDIX E

RELATIONSHIP BETWEEN THE PRESSURE INTEGRATION AND THE PRODUCTION RATE

In the setting of fractional decline, the relationship between flow rate and time derivative of pressure integral isn't as apparent as that of the regular case. It is derived in the following steps.

Within the dimensional domain, the flow rate is expressed as Eq. (E1).

$$q = h_f \int_0^{x_f} v \, dx \quad \text{..... (E1)}$$

By the fractional flux law in Eq. (4.11), we can get

$$q = h_f \int_0^{x_f} -\frac{k^*}{\mu} \frac{\partial^{1-\alpha}}{\partial t^{1-\alpha}} \nabla P \cdot \vec{n} \, dx \quad \text{..... (E2)}$$

where $\vec{n}$ is the unit normal vector of the corresponding parts of boundary. Eq. (E2) can be written into Eq. (E3) by the commutative property between spatial and temporal operators.

$$q = -h \frac{k^*}{\mu} \frac{d^{1-\alpha}}{dt^{1-\alpha}} \int_0^{x_f} \nabla P \cdot \vec{n} \, dx \quad \text{..... (E3)}$$

Due to the zero Neumann boundary condition on the other parts of the domain, the integral in Eq. (E3) is extended to the whole boundary as shown in Eq. (E4).

$$q = -h \frac{k^*}{\mu} \frac{d^{1-\alpha}}{dt^{1-\alpha}} \int_{\partial\Omega} \nabla P \cdot \vec{n} \, ds \quad \text{..... (E4)}$$

Using divergence theorem to the integral term in Eq. (E4), we can get

$$q = -h \frac{k^*}{\mu} \frac{d^{1-\alpha}}{dt^{1-\alpha}} \int_{\Omega} \Delta P \, dX_D \quad \text{..... (E5)}$$

According to Eq. (4.6), ΔP can be replaced by the fractional order time derivative of P, as shown in Eq. (E6).

$$q = -h\frac{k^*}{\mu}\frac{d^{1-\alpha}}{dt^{1-\alpha}}\int_{\Omega}\frac{1}{\eta^*}\frac{\partial^{\alpha}}{\partial t^{\alpha}}P\,dX_D \quad \text{..... (E6)}$$

That is,

$$q = -h\frac{k^*}{\mu\,\eta^*}\frac{d^{1-\alpha}}{dt^{1-\alpha}}\frac{d^{\alpha}}{dt^{\alpha}}\int_{\Omega}P\,dX_D \quad \text{..... (E7)}$$

With the property of the fractional calculus (Malinowska et al., 2015), Eq. (E7) is simplified as

$$q = -h\frac{k^*}{\mu\,\eta^*}\frac{d}{dt}\int_{\Omega}P\,dX_D \quad \text{..... (E8)}$$

which means that the regular relation between the flow rate and the ordinary first order time derivative of the pressure integral holds even in the fractional setting. This is consistent with the material balance over the whole domain.

After substituting the dimensionless groups into Eq. (E8), the corresponding dimensionless form is obtained.

$$q_D(t_D) = -\frac{d}{dt_D}\int_{\Omega}P_D(x_D, y_D, t_D)dX_D \quad \text{..... (E9)}$$

Then by substituting the solution of P_D (Eq. (4.12)) into Eq. (E9), q_D can be further expressed as Eq. (E10).

$$q_D(t_D) = -\sum_{i=1}^{\infty}\frac{dE_{\alpha}(-\lambda_i t_D^{\alpha})}{dt_D}\left(\int_{\Omega}\varphi_i(x_D, y_D)dX_D\right)^2 \quad \text{..... (E10)}$$

$E_{\alpha}(z)$ has the recurring property (Haubold et al., 2011) as Eq. (E11) shows with the definition of the Mittag-Leffler function of two parameters in Eq. (E12).

$$\frac{d}{dz}E_{\alpha}(z) = \frac{1}{\alpha}E_{\alpha,\alpha}(z) \quad \text{..... (E11)}$$

$$E_{\alpha,\beta}(z) := \sum_{k=0}^{\infty} \frac{z^k}{\Gamma(\alpha k + \beta)} \quad \text{..... (E12)}$$

Using the above property, Eq. (E10) is further simplified as Eq. (E13).

$$q_D(t_D) = \frac{1}{t_D^{1-\alpha}} \sum_{i=1}^{\infty} \lambda_i E_{\alpha,\alpha}(-\lambda_i t_D^{\alpha}) A_i \quad \text{..... (E13)}$$

APPENDIX F

EXTRA PRESSURE DROP DUE TO HEMISPHERICAL STABILIZED DARCY'S FLOW

The extra pressure drop in the thin convergence region is approximated by assuming stabilized Darcy's flow in a hemispherical region of radius r_c between two parallel cross sections with radius of r_c and r_p, respectively (Fig. 5.3 (c)). Such problem is solved in a coordinate shown in Fig. 5.3 (d).

In the coordinate, the pressure is kept constant at $X = 0$ as P_e and at $X = \sqrt{r_c^2 - r_p^2}$ as P_w. Because of stabilized flow, on an arbitrary intermediate cross section of $X = x$ the flow rate is also a constant of q_p, as shown in Eq. (F1).

$$q_p = -\frac{k_f}{\mu}\frac{dP}{dx}\,\pi(r_c^2 - x^2) \quad \text{.....(F1)}$$

After separating the variables in Eq. (F1), we can get

$$-dP = \frac{q_p \mu}{\pi k_f}\frac{dx}{(r_c^2 - x^2)} \quad \text{.....(F2)}$$

Integrate both sides of Eq. (F2) over the whole range, as shown in Eq. (F3).

$$-\int_{P_e}^{P_f} dP = \frac{q_p \mu}{\pi k_f}\int_0^{\sqrt{r_c^2 - r_p^2}} \frac{dx}{(r_c^2 - x^2)} \quad \text{.....(F3)}$$

Finally, we can obtain the relation between the extra pressure drop and the flow rate (Eq. (F4)).

$$\Delta P_c = P_e - P_w = q_p \frac{\mu}{\pi k_f r_c}\operatorname{arctanh}\left(\sqrt{1 - \frac{r_p^2}{r_c^2}}\right) \quad \text{.....(F4)}$$

APPENDIX G

SOLUTION OF THE 1-D BOUNDARY VALUE PROBLEM IN LAPLACE DOMAIN

In this appendix, the boundary value problems of Eq. (5.6), Eq. (5.29), and Eq. (5.35) are solved in a uniform way. The generalized form of these three systems can be written as Eq. (G1).

$$\left(f(\alpha,\lambda_D,s)g(\omega,\sigma,s)\right)^2\widetilde{P_D}=\frac{\partial^2}{\partial y_D^2}\widetilde{P_D} \quad \text{.....(G1a)}$$

$$\frac{\partial\widetilde{P_D}}{\partial y_D}(y_D=1)=0 \quad \text{.....(G1b)}$$

$$\widetilde{P_D}(y_D=0)=\frac{1}{s}+\frac{c\,s}{\left(f(\alpha,\lambda_D,s)\right)^2}\left(\frac{\partial\widetilde{P_D}}{\partial y_D}\right)_{y_D=0} \quad \text{.....(G1c)}$$

In Eq. (5.6), $f(\alpha,\lambda_D,s)=s^{\frac{\alpha}{2}}$ and $g(\omega,\sigma,s)=1$. In Eq. (5.29), $f(\alpha,\lambda_D,s)=\sqrt{(s+\lambda_D)^\alpha-{\lambda_D}^\alpha}$ and $g(\omega,\sigma,s)=\sqrt{1+\omega\tanh\left(\sqrt{s/\sigma}\right)/\sqrt{s/\sigma}}$. And in Eq. (5.35), $f(\alpha,\lambda_D,s)=\sqrt{(s+\lambda_D)^\alpha-{\lambda_D}^\alpha}$ and $g(\omega,\sigma,s)=\sqrt{1+\omega\sqrt{\sigma}/\sqrt{s}}$.

The general solution of Eq. (G1a) is shown in Eq. (G2).

$$\widetilde{P_D}=C_1\exp(fgy_D)+C_2\exp(-fgy_D) \quad \text{.....(G2)}$$

where C_1 and C_2 are the constants of integration with arbitrary values.

Taking the derivative of Eq. (G2) with respect to y_D, we can get

$$\frac{\partial\widetilde{P_D}}{\partial y_D}=C_1fg\exp(fgy_D)-C_2fg\exp(-fgy_D) \quad \text{.....(G3)}$$

Substituting Eq. (G2) and (G3) into the boundary conditions Eq. (G1b) and (G1c), a system of equations with respect to C_1 and C_2 is obtained, as shown in Eq. (G4).

$$\begin{cases} fg\exp(fg)\,C_1 - fg\exp(-fg)\,C_2 = 0 \\ \left(1 - c\,s\frac{g}{f}\right)C_1 + \left(1 + c\,s\frac{g}{f}\right)C_2 = \frac{1}{s} \end{cases} \quad \text{.....(G4)}$$

By solving Eq. (G4), C_1 and C_2 are expressed as Eq. (G5).

$$\begin{cases} C_1 = \dfrac{\frac{f}{s}}{-g\,c\,s + g\,c\,s\exp(2\,fg) + f + f\exp(2\,fg)} \\ C_2 = \dfrac{\frac{f}{s}\exp(2\,fg)}{-g\,c\,s + g\,c\,s\exp(2\,fg) + f + f\exp(2\,fg)} \end{cases} \quad \text{.....(G5)}$$

Substituting Eq. (G5) into Eq. (G2), we can get

$$\widetilde{P_D} = \frac{\frac{f}{s}\exp(fg\,y_D) + \frac{f}{s}\exp(fg(2 - y_D))}{-g\,c\,s + g\,c\,s\exp(2\,fg) + f + f\exp(2\,fg)} \quad \text{.....(G6)}$$

After doing some further simplifications to Eq. (G6), finally we can obtain $\widetilde{P_D}$ (Eq. (G7)).

$$\widetilde{P_D} = \frac{\cosh\left(fg\,(y_D - 1)\right)}{s\cosh(fg) + c\,s^2\sinh(fg)\frac{g}{f}} \quad \text{.....(G7)}$$